Geophysical Parameter Estimation with a Passive Microwave Spectrometer at 54/118/183/425 GHz

by

R.Vincent Leslie

B.S. Electrical Engineering
Boston University (1998)

S.M. Electrical Engineering
Massachusetts Institute of Technology (2000)

Submitted to the Department of Electrical Engineering and Computer Science
in partial fulfillment of the requirements for the degree of

Doctor of Science in Electrical Engineering

at the

MASSACHUSETTS INSTITUTE OF TECHNOLOGY

June 2004

Author ....
Department of Electrical Engineering and Computer Science
y 21, 2004

Certified by..
David H. Staelin
Professor of Electrical Engineering
esis Supervisor

Accepted by..
thur C. Smith
Chairman, Department Committee on Graduate Students

Geophysical Parameter Estimation with a Passive Microwave Spectrometer at 54/118/183/425 GHz

by

R.Vincent Leslie

Submitted to the Department of Electrical Engineering and Computer Science
on May 21, 2004, in partial fulfillment of the
requirements for the degree of
Doctor of Science in Electrical Engineering

Abstract

The National Polar-orbiting Operational Environmental Satellite System (NPOESS) Aircraft Sounder Testbed - Microwave, or NAST-M, includes passive microwave spectrometers operating near the oxygen lines at 50-57 GHz, 118.75 GHz, and 424.76 GHz, and a spectrometer centered on the water vapor absorption line at 183.31 GHz. All four of the spectrometers' antenna horns are colocated, have 3-dB (full-width at half-max) beamwidths of 7.5°, and are directed at a single mirror that scans cross-track beneath the aircraft with a swath up to 100-km wide. The 183.31- and 424.76-GHz systems were developed as part of this thesis. The calibration techniques for two high-altitude airborne platforms are described and validated for two recent deployments.

During these two deployments, various precipitation phenomena were imaged by NAST-M's radiometric and video instruments. Retrieval methods were developed and tested for single-pixel rain rate, precipitation cell-top altitude, and cloud-top altitude retrievals of convective cells. The basis of the single-pixel retrievals is a simplified convective-cell hydrometeor-profile model used with a radiative transfer solution that included absorption by atmospheric gases and by hydrometeor absorption and scattering. Two retrieval techniques were used to relate the simulated brightness temperatures to the actual brightness temperatures from the deployments. Case studies are presented from each deployment.

In addition, a technique for estimating the cell-wide aggregate rain rate ($km^2 \cdot mm/hr$) is presented based on the microwave radiometric signature. The cumulative 3-decibel perturbation areas of convective cells in the four frequency bands are shown to be related to their aggregate rain rates. A simple three-dimensional model of a convective cell is presented that provides a physical basis for this relationship.

Thesis Supervisor: David H. Staelin
Title: Professor of Electrical Engineering

Acknowledgments

I would like to start by thanking Prof. Staelin for making the NAST-M instrument a reality. His patience was enormous, and his guidance and support were invaluable.

Thanks to Phil Rosenkranz for his valuable assistance with questions regarding simulations and thoughtful suggestions as a thesis reader. Thanks to Bill Blackwell for his valued technical assistance with upgrading the NAST-M instrument, insightful thesis suggestions as a thesis reader, and for bequeathing me NAST-M and a set of golf clubs.

I would like to thank Jack Barrett, Lou DiPalma, and Mike McGuirk for their valuable engineering support and know-how in installing the new spectrometers. I would like to give a special thanks to Prof. Jeffrey Hesler (University of Virginia), Chris Eurvard (Millitech), and their associates for answering my seemingly endless receiver questions.

Thanks to the numerous people who have supported the upgrade and deployment of NAST-M. I'll try to mention everyone, but forgive me if I don't remember everyone. Thanks to graduate students Andrew Sanchez and Jessica Loparo for their help with the instrumentation, data reduction, and field work. I would also like to thank Lou DiPalma, Mike Doucette, and Fred Chen for their field work. I'd like to thank Andy Gallant, Peter Morley, and the machinists at the MIT Central Machine Shop for making my drawings and paper mock-ups a reality. Thanks to the technicians at MIT's Lincoln Laboratories and Center for Space Research for making us proud to open our electronics in public. Thanks to Al McGurl, Bill Gibbs, and Scott Bressler for bending over backwards to get us in and out of Building 26. Thanks to everyone in the RLE front office for their help and ability to answer my questions politely the second and third time around. Thanks to the employees of Dryden Flight Research Center and Scaled Composites, especially to the engineers and pilots (who were sometimes the same person). Thanks to the people in the field who saved us more than once with either spare parts or manpower, especially to the NASA Langley and University of Wisconsin folks.

I dedicate this thesis to my wonderful wife, Anne, and I would like to thank her for her patience, devotion, and love. Also, I would like to thank my family for their support and patience.

This thesis has been funded in part by the U.S. Department of Commerce/NOAA under contract No. DG133E-02-CN-0011. Opinions, interpretations, conclusions, and recommendations are those of the author and are not necessarily endorsed by the United States Government.

Contents

List of Figures

List of Tables

Chapter 1

Introduction

The National Polar-orbiting Operational Environmental Satellite System (NPOESS) monitors global environmental conditions. The NPOESS Aircraft Sounder Testbed (NAST) program uses high-altitude aircraft as a testbed for future Polar-orbiting Operational Environmental Satellites (POESs) by simulating potential instruments (*e.g.*, Cross-track Infrared Sounder (CrIS) and Advanced Technology Microwave Sounder (ATMS)), evaluating retrieval algorithms, previewing data products, and providing flight validations. NAST is made up of a high-resolution infrared Michelson interferometer (NAST-I) [15] and a complementary microwave spectrometer suite (NAST-M), which simulates the CrIS and ATMS instruments for the NPOESS Preparatory Project (NPP). The NAST aircraft flies at altitudes between 17 to 20 km, compared to the POES's 800 km. ATMS has 22 channels with center frequencies ranging from 23.8 GHz to 183 GHz, while NAST-M has four colocated spectrometers near the 50-56 GHz oxygen absorption band, the 118.75 and 424.76 GHz oxygen absorption lines, and the 183.31-GHz water vapor absorption line. The National Oceanic and Atmospheric Administration (NOAA), which oversees the POESs and the Geostationary Operational Environmental Satellites (GOESs), sponsored the addition to NAST-M of a spectrometer at the 424.76-GHz oxygen absorption line. The 183- and 425-GHz spectrometers were first calibrated during this research.

When comparing GOES and POES orbits, geosynchronous orbits have better temporal coverage, but polar orbits (sun-synchronous orbits) have global coverage and a higher spatial resolution. Another advantage the POESs have over the GOESs is their use of the microwave spectrum to cloud-clear infrared radiances in order to retrieve temperature and humidity profiles in atmospheres that would otherwise be opaque at infrared and visible wavelengths (*e.g.*, [8, 9]). Microwaves are generally more successful than infrared or visible wavelengths for precipitation estimation, because they can penetrate cloud structure to sense hydrometeors, where as infrared instruments gain precipitation information from cloud area and from the cloud-top's altitude and temperature. There are techniques that use data from both low earth orbit (LEO) and geostationary earth orbit (GEO) platforms (*e.g.*, [44]). Future geostationary satellites hope to gain the benefits of the microwave spectrum. In order for the microwave wavelengths to have a useful spatial resolution on a GOES platform, the size of the lower-frequency antennas would be too cumbersome (800-km POES altitude versus a 36,000-km GOES altitude). Naturally, an interest in the higher-frequency spectrometers arises to maintain the same spatial resolution with a more manageable antenna size. A similar system to the NAST-M 425-GHz system is under consideration for the GEM/GOMAS (GEostationary Microwave observatory/Geostationary Observatory for Microwave Atmospheric Sounding) proposal [6] with a nominal two-meter diameter parabolic antenna. The NAST-M spectrometer suite provides empirical data, as opposed to simulated data, to help determine the utility of the geosynchronous application.

1.1 Thesis Overview

The thesis continues with a background chapter (Chapter 2) that covers some of the fundamentals used throughout the thesis. Chapter 3 presents the system integration of the two new spectrometers into the established NAST-M instrument. System integration includes the design and manufacture of the front-end receivers, intermediate frequency (IF) filter banks, and upgraded data acquisition system. Chapter 3 also presents the calibration technique for both of the aircraft platforms, which are the ER-2 (www.dfrc.nasa.gov) and the Proteus (www.scaled.com). The calibration onboard the ER-2 is a three-point calibration that closely follows the previous publications [36, 7, 8]. The Proteus requires a two-point calibration, because of NAST-M's configuration in the aircraft, but otherwise remains the same. To date, the upgraded 4-band NAST-M has flown in some capacity in four campaigns. They are the International H_2O Project (IHOP 2002), the Cirrus Regional Study of Tropical Anvils and Cirrus Layers-Florida Area Cirrus Experiment (CRYSTAL-FACE 2002), Pacific THOR*pex* (THe Observing-system Research and *p*redictability *ex*periment) Observing System Test (PTOST 2003), and the Atlantic THOR*pex* Observing System Test (ATOST 2003). Chapter 4 validates the calibration of CRYSTAL-FACE and PTOST by entering atmospheric measurements of temperature and humidity into radiative transfer solution and comparing the results with the calibrated brightness temperatures. These two deployments contained the majority of the precipitation imagery. IHOP and ATOST will be validated in another publication, but the calibration technique would remain unchanged.

During CRYSTAL-FACE and PTOST, various precipitation phenomena were imaged by NAST-M's radiometric and video instruments. Chapter 5 presents single-pixel rain rate, precipitation cell-top altitude, and cloud-top altitude retrievals of the convective cells. The basis of the single-pixel retrievals is a simplified convective-cell hydrometeor-profile model used with a radiative-transfer solution that included absorption by atmospheric constituents and by hydrometeor absorption and scattering. Simulations using the simplified hydrometeor profile with different characteristics (*e.g.*, cell-top altitude) form a training ensemble of brightness temperatures. Two techniques were used to relate the simulated brightness temperatures to the actual brightness temperatures from the deployments. The first technique is a constant-coefficient polynomial estimator that was optimized in a mean-squared error sense. The second technique involved comparing the actual brightness temperatures with the brightness temperatures in the training ensemble and choosing a simulation (and therefore a rain rate, *etc.*) by minimizing an error metric (a lookup approach). The error metric was the weighted sum of the squared brightness temperature discrepancies for each channel. Case studies are presented from each deployment.

Chapter 6 presents a technique for estimating the cell-wide aggregate rain rate ($km^2 \cdot mm/hr$) based on the microwave radiometric signature. The radiometric signature was based on the brightness-temperature perturbation induced by the convective cell when compared to nearby clear air. The perturbation area is the surface area within a contour defined by a value that is half of the maximum perturbation value. The sum of the 3-dB perturbation areas, one area from each spectrometer, is shown to be related to the aggregate rain rate based on fourteen convective cells from the two deployments. A simple three-dimensional model of a convective cell is discussed for the purpose of presenting a physical basis for the relationship between the perturbation area and the aggregate rain rate. Also, the fourteen cells were classified into one of three main stages of a typical convective-cell life cycle, which are growing, mature, and dissipating. Microwave signature characteristics are discussed from each stage, and how they relate to the regression between cumulative area and aggregate rain rate.

1.2 Prior Work

Under the sponsorship of the NPOESS Integrated Program Office (IPO), NAST tests remote sensing instruments developed at the Massachusetts Institute of Technology's Lincoln Laboratories, MIT's Research Laboratory of Electronics, University of Wisconsin-Madison, and NASA. One of these instruments is the NAST-M passive microwave spectrometer, which was designed and built at the MIT's Research Laboratory of Electronics in the Remote Sensing and Estimation Group [7]. NAST-M had its origins in the microwave temperature sounder (MTS) [24, 52]. The original NAST-M suite has been used in a variety of remote sensing applications, including atmospheric profile retrievals (*e.g.*, temperature [36] and water vapor [35]), cloud-parameter estimation (*e.g.*, precipitation cloud-top altitude [57]), and cloud-clearing of coincident infrared data [8].

Presently, precipitation estimation can be divided into three general areas. They are the indirect methods that measure infrared or visible radiation emerging from the top of clouds, the direct methods of passively measuring the scattering, absorption, and thermal emission of hydrometeors at micro- and millimeter wavelengths, and radar techniques that infer rainfall parameters from backscattering. A good review of satellite rainfall estimation over land can be found in Petty [49]. There is a history of precipitation mapping at microwave frequencies ranging from 10.7 GHz to 183 GHz [10], and even higher frequencies are contemplated. Quantitative validation of accuracy is very difficult for all rain-rate estimation techniques [14]. Within the passive microwave retrieval category, there are two general approaches to rain-rate estimation. The empirical approach is to derive a single-pixel statistical retrieval through coincidental measurements of rain-rate from radar (*e.g.*, NEXRAD) or rain gauges [13]. The other standard approach is to base the retrieval on the convective cell physics. The physically-based approach uses radiative-transfer models of the scattering and absorption of hydrometeors within storm models [53, 26, 55, 25, 66]. One set of storm models are the cloud resolving models (CRM) that use sophisticated and realistic representations of cloud microphysical processes and try to resolve the time evolution and structure of clouds and cloud systems (*e.g.*, [63]). The CRM needs a set of initial conditions to start the simulation. A stochastic-process storm model randomly forms convective storms, which then follow the large-scale movements and evolutions of storms determined by random distributions with physical constraints [2]. This differs from the CRM because the CRM determines the cloud evolution from the internal physics, while the stochastic model imposes large-scale cloud evolutional trends in order to model the internal physics. These two types of storm simulations determine most of inputs necessary for the radiative transfer calculations, but some further models are necessary (*e.g.*, drop size distributions).

The simplified convective-cell hydrometeor-profile model in Chapter 5 was compared to the actual data from CRYSTAL-FACE and PTOST. This allowed the simulations involving the radiative-transfer solution and storm model to be compared with actual storm brightness temperatures. Other airborne passive microwave instruments have had this opportunity [1, 71], but they were limited to two polarizations at 18 and 37 GHz, one channel at 92 GHz, and a 183-GHz system with channels at ±2,

±5, and ±9 GHz.

The relationship between a convective cell's area and rainfall has long been recognized (*e.g.*, [11]), and a family of precipitation estimation methods, called the life-history methods [49], have been developed to estimate the average rain rate over the lifetime of the convective cell [20]. Techniques have also been developed to nowcast the rain volume to be potentially used in flash flood warnings [18]. The life-history methods typically rely on geostationary platforms because of the relatively high temporal sampling, and therefore have utilized visible or infrared wavelengths [19, 4, 49].

Chapter 2

Background

The general purpose of the NAST-M instrument is to measure the intensity of atmospheric radiation so that geophysical parameters can be retrieved from post-processed radiometric data. This chapter gives brief explanations for many of the fundamental concepts used to meet this purpose. Section 2.1 describes the fundamentals of the instrumentation that NAST-M uses to collect the radiometric data, while Section 2.2 reviews the atmospheric physics encountered in retrieving geophysical parameters. Atmospheric models, using atmospheric physics and an atmospheric profile, simulate the intensity that NAST-M would measure. Section 2.3 explains the basics of the atmospheric model, and Section 2.4 reviews the fundamentals of constant-coefficient estimators used to retrieve geophysical parameters.

2.1 General Radiometry Instrumentation

All of NAST-M's radiometers are total-power radiometers, which use a superheterodyne configuration to downconvert the frequencies of interest to a more manageable intermediate frequency (IF). Further, the measured power is divided by frequencies into channels, which make NAST-M's receivers spectrometers. This section reviews some of the fundamentals of the NAST-M instrumentation.

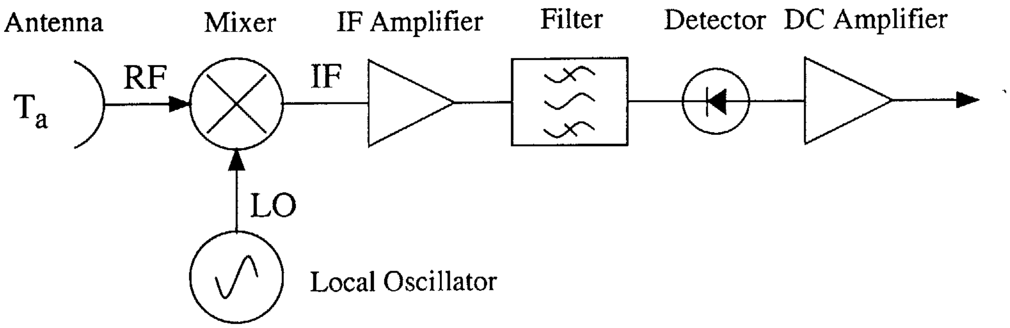

Figure 2-1: A total-power radiometer schematic

2.1.1 Radiometer with Periodic Absolute Calibration

A fundamental instrument used in passive remote sensing of atmospheric radiation is the total-power radiometer. A schematic of a standard total-power radiometer is shown in Figure 2-1 from Janssen [32]. The microwave frequencies that NAST-M measures are too difficult to amplify, therefore a superheterodyne system is used to downconvert the frequencies to an intermediate frequency so that off-the-shelf RF amplifiers can be used. Then a spectrometer configuration is implemented by having the IF segregated through a filterbank made up of RF amplifiers, power dividers, and bandpass filters. Each specific passband of a RF filter is called a channel and defines a particular atmospheric weighting function. Note that the figure only shows one "channel." After the filterbank, a square law device converts the power incident on the device to a proportional voltage. The square law device used on NAST-M is the tunnel diode detector, which is very linear with power when it is at a good operating point. The detector's output voltage from each channel is converted to a digital signal, after amplification and filtering, by an analog-to-digital converter. Through digital signal processing, the signal is integrated (equivalent to a lowpass filter) and expressed as "counts."

Calibration consists of relating the counts to the correct brightness temperature measured by the antenna. Brightness temperature will be defined in Section 2.2.1. The radiometric counts fluctuate because of overall gain and baseline changes (*e.g.*, IF amplifiers have temperature coefficients for gain and noise figure), and therefore periodic looks at two temperature-controlled targets are needed to calibrate the intervening nadiral scene. The targets, or calibration loads, are designed to be as close to blackbodies as possible, and their physical temperature is measured and recorded during instrument operation. This is called periodic absolute calibration and the theory is discussed more in Section 2.1.3.

2.1.2 Radiometer Performance

Attributes of a radiometer include the antenna's directional response, the spectral response, and the radiometric sensitivity [58]. Within the microwave spectrum, it is common to express power in terms of temperature using the Rayleigh-Jeans approximation (Section 2.2.1). The antenna temperature is

$$T_a(f) = \frac{1}{4\pi} \int_{4\pi} T_b(f,\theta,\phi)\, G(f,\theta,\phi)\; d\Omega \;\; [Kelvin]. \tag{2.1}$$

Equation 2.1 shows that the antenna temperature integrates or accounts for the brightness temperature, T_b, over the entire gain pattern of the antenna, $G(f,\theta,\phi)$. Therefore, $G(f,\theta,\phi)$ gives the directional response of the radiometer. Spectral response is mainly controlled by the RF filters' frequency response and the other RF components in the filter bank. NAST-M's spectral response is presented in Chapter 3.

In radio astronomy and remote sensing, a common radiometric-sensitivity metric is ΔT_{rms}, which is in Kelvin. This metric measures the uncertainty of the instrument to measure an absolute brightness temperature. In the next section, ΔT_{rms} will be investigated further for its importance in calibrating radiometric instruments. Kraus [33] and Staelin [59] derived the equation for ΔT_{rms}, under idealized conditions, to be:

$$\Delta T_{rms} = \frac{V_{out_{rms}}}{\frac{\partial V_{out}}{\partial T_a}} = \frac{T_a + T_r}{\sqrt{B\tau}} \;\; [Kelvin]. \tag{2.2}$$

The variables are V_{out}, the output voltage of the total-power radiometer; B, the bandwidth of the channel [Hertz]; τ, the boxcar integration time [second]; T_r, the noise temperature of the receiver; and T_a is the antenna temperature. The receiver noise temperature is from the internally generated thermal noise.

2.1.3 Evaluation of Radiometric Sensitivity

A metric for radiometric sensitivity is the noise equivalent temperature difference between truth and observed, often termed ΔT_{rms}. In Hersman and Poe [29], ΔT_{rms} is reduced into its independent components. They present it as $\Delta T_{rms}^2 = \delta_{sc}^2 + \delta_{cal}^2 + \delta_{gf}^2$. The δ_{sc}^2 is the fluctuation due to broad-band "white" noise and is inherent in any total-power radiometer (see Equation 2.2). Typically, the calibration is considered 'ideal' and only the δ_{sc}^2 component is mentioned, but calibration does introduce an additional source of error, δ_{cal}^2. The final term, δ_{gf}^2, is due to the receiver gain fluctuations and electronic $1/f$ noise. The total ΔT_{rms} can be viewed in a 'variance' space with each of these sources of noise as an orthogonal contributor. A superior calibration technique will reduce the total ΔT_{rms} with post-flight signal processing. Section 3.3 explains the calibration techniques used for NAST-M.

The lowest theoretical limit of ΔT_{rms}^2 comes from the δ_{sc}^2 contribution. The δ_{cal}^2 component of ΔT_{rms}^2 is introduced by the calibration technique, which was considered to be equal to zero in Equation 2.2. $V_{cal}(t)$ is the estimate of the true calibration-load voltage. It is an estimate because the radiometer takes only periodic measurements of the calibration load and those are inherently noisy because of δ_{sc}^2. The period between calibration-load measurements is t_c. If the instrument's gain and the load's physical temperature were completely stable, then every measurement of the calibration load during the duration of flight could be used in the estimate of the calibration-load voltage, and therefore increase the accuracy of the estimate. This is not realizable because of varying receiver gain. Nonetheless, an estimate of the $V_{cal}(t_o)$ will use several measurements of the calibration load at times close to t_o. This estimate of V_{cal} is written mathematically as

$$V_{cal} = \sum_k w(t - kt_c) \cdot V(kt_c) \quad k = 0, \pm 1, \pm 2, \ldots, \tag{2.3}$$

with the proper constraint that

$$\sum_k w(t - kt_c) = 1. \tag{2.4}$$

The $w(t - kt_c)$ are the weights of the calibration measurements. Hersman and Poe [29] give this final expression of ΔT_{rms} when considering an imperfect calibration as

$$\Delta T_{rms} = (T_a + T_r)\sqrt{\frac{1}{B\tau} + \frac{1}{B\tau}\sum_k w^2(t - kt_c)} \tag{2.5}$$

and the

$$\delta_{cal} = (T_a + T_r)\sqrt{\frac{1}{B\tau}\sum_k w^2(t - kt_c)}. \tag{2.6}$$

The power spectrum of the receiver noise has two primary components. There is a flat "white" component that is due to δ_{sc}, or, in other words, the fundamental performance of the total-power radiometer. The other component is the gain fluctuation, or $1/f$ noise. These components add to give a power spectral density that is represented by the curve in Figure 2-2. The calibration technique can be considered a transfer function, $H(f)$, multiplied by the instrument's power spectral density, $S_r(f)$, which gives the ΔT_{rms} as

$$(\Delta T_{rms})^2 = c^2 \int_0^\infty S_r(f)\, H(f)\, df, \tag{2.7}$$

where c is a constant radiometer scale factor [Kelvin/Volt]. The mathematical expression for the effective calibration filter is:

$$H(f) = \left| \frac{\sin(\pi f \tau_s)}{\pi f \tau_s} - \frac{\sin(\pi f \tau_c)}{\pi f \tau_c} \sum_k w(t - kt_c) e^{-j2\pi f(t-kt_c)} \right|^2, \tag{2.8}$$

where τ_s and τ_c are the integration time for the scene and calibration load, respectfully.

The noise spectra can be separated into the flat portion intrinsic to a total-power radiometer, $S_i(f)$, and the $1/f$ portion that is due to gain fluctuations, $S_g(f)$. The

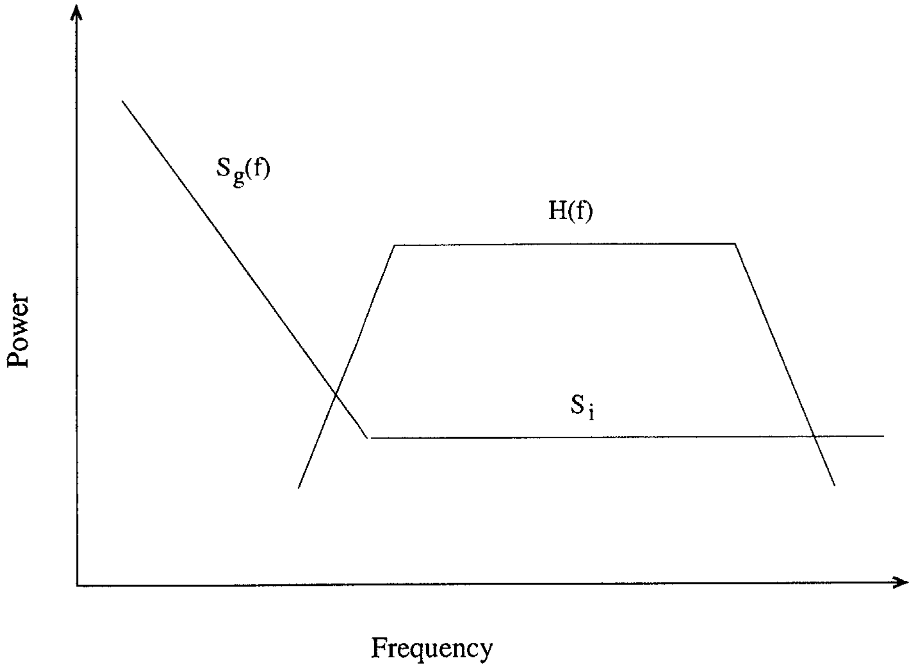

Figure 2-2: Receiver power spectral density with equivalent calibration filter $H(f)$

$(\Delta T_{rms})^2$ contribution due to gain fluctuations is

$$\delta_{gain}^2 = c^2 \int_0^\infty S_g(f)\, H(f)\, df. \tag{2.9}$$

The period between calibrations, t_c, is chosen to filter out as much gain-related noise as possible. It can be seen from Figure 2-2 that the calibration technique ($H(f)$) effectively filters out the gain-drift noise by reducing the contribution of $S_g(f)$ in the ΔT_{rms}^2 equation. Therefore, from Equation 2.8, it is important to choose $w(t)$, the weights of the nearby calibration measures, to include as much information as possible for the V_{cal} estimation.

The calibration technique of NAST-M uses a linear interpolation of the two nearest calibration points, which is the best of the simple techniques to reduce the affect of $1/f$ noise, but there are optimal techniques [48]. In this application, the optimal did not offer significant improvement [8]. The linear interpolation technique gives a weight function ($w(t)$) that is triangular in shape with the peak at the spot being calibrated and the two corners at the two nearest calibration points (see [29].

2.2 Atmospheric Physics of Thermal Radiation

The physics defines the atmospheric transmittance model that is used to transform atmospheric profiles into radiances (see Section 2.3.3), which will be important for calibration and for creating training ensembles. The fundamentals are presented here, and more in-depth references include Stephens and Ulaby *et al.* [61, 67]. The numerical solution to the radiative transfer equation and atmospheric model will be described in Section 2.3.

2.2.1 Brightness Temperature

Matter emits electromagnetic energy or radiation. A theoretical body of matter that absorbs all incident radiation is called a blackbody. The intensity emitted by a body at uniform temperature, T, is defined by Kirchhoff's law:

$$I_f = \kappa_a \cdot B_f(T) \; \left[\frac{W}{m^2 \cdot Hz \cdot Ster}\right]. \tag{2.10}$$

The absorption coefficient, κ_a, has a value between 0 and 1 and is frequency dependent. Having $\kappa_a = 0$ means that the matter neither emits or absorbs electromagnetic energy, while a $\kappa_a = 1$ is the theoretical blackbody. Max Planck derived a radiation formula for radiation intensity in units of power per area-hertz-steradian. Planck's radiation law is as follows

$$B_f(T) = \frac{2hf^3}{c^2(e^{hf/kT} - 1)} \; \left[\frac{W}{m^2 \cdot Hz \cdot Ster}\right] \tag{2.11}$$

with T, temperature in Kelvin; f, frequency in Hertz; h, Planck's constant; k, Boltzmann's constant; c, speed of light in the medium. The power series expansion $e^x = \sum_{k=0}^{\infty} \frac{x^k}{k!}$ can be approximated when $x \ll 1$ as $e^x = 1 + x$. This approximation is the Rayleigh-Jeans limit and gives

$$B_f(T) = \frac{2kT}{\lambda^2} \; \left[\frac{W}{m^2 \cdot Hz \cdot Ster}\right], \tag{2.12}$$

only when $hf \ll kT$. This is true in the microwave region of the electromagnetic spectrum for temperatures greater than 50 Kelvin.

A very common term in microwave remote sensing is brightness temperature. Kirchhoff's law is in units of intensity, and when intensity is expressed in units of temperature, then it is termed brightness temperature. Rayleigh-Jeans law, Equation 2.12, can be rearranged to give the equivalent temperature for a given intensity:

$$T_b = \frac{\kappa_a B_f(T) \cdot \lambda^2}{2k} = \frac{I_f \cdot \lambda^2}{2k}. \tag{2.13}$$

This equation is only appropriate if all the conditions for the Rayleigh-Jeans limit are met.

2.2.2 Radiative Transfer Equation

The radiative transfer equation, RTE, defines the physics of the thermal radiation between a source, an intervening medium, and a receiver. In this section, the RTE is defined for an incremental piece of atmosphere. Section 2.3.1 will extend the equation to a scenario where the terrestrial atmosphere is the medium, the earth's surface is the source, and NAST-M is the receiver. A more in-depth explanation of radiative transfer can be found in [12, 3].

Figure 2-3 shows the geometry of a planar-stratified atmosphere, with the surface of the earth at the bottom. The antenna is pointing toward the surface from somewhere within the atmosphere. The exchange of radiation in an incremental piece of the atmosphere (ds) is

$$dI_f = dI_{emission} + dI_{extinction} + dI_{scattering}. \tag{2.14}$$

The $dI_{extinction}$ comes from Lambert's law, which states

$$dI_{extinction} = -\alpha_e \cdot I_f \; ds. \tag{2.15}$$

The α_e is the extinction coefficient and it is the sum of the absorption coefficient, κ_a, and the scattering coefficient, κ_s.

Kirchhoff's law states that, in thermodynamic equilibrium, emission is equal to absorption, and therefore:

$$dI_{emission} = \kappa_a \cdot B_f(T)\ ds. \tag{2.16}$$

Furthermore, the $dI_{scattering}$ term is electromagnetic energy that is scattered into the direction of the incremental distance ds, as opposed to κ_s term in Equation 2.15 where the energy is scattered away from the ds direction. The source of the electromagnetic energy that is scattered into the ds direction could have many sources, which are lumped into the scattering source function (J_s). The scattering source function equation is:

$$J_s = \frac{1}{4\pi} \iint\limits_{4\pi} \psi(s, \acute{s})\ B_f(T, \acute{s})\ d\Omega, \tag{2.17}$$

which determines the contributions of the scattered energy from all directions ($\acute{s}$) in 4π steradians. $B_f(T, \acute{s})$ is the incident radiation from the $\acute{s}$ direction, and $\psi(s, \acute{s})$ is the phase function. The brightness temperature simulations in this thesis use the Henyey-Greenstein [28] model for the phase function. The $dI_{scattering}$ is:

$$dI_{scattering} = \kappa_s \cdot J_s\ ds. \tag{2.18}$$

The distance along the s direction can be approximated as $z \cdot \sec(\theta)$. The optical depth, or opacity, is defined as

$$\begin{aligned} \tau(z) &= \int_{z}^{z''} \alpha_e(z)\ dz. \\ \tau(s) &= \sec(\theta)\ \tau(z) \end{aligned} \tag{2.19}$$

Putting Equation 2.15, Equation 2.16, and Equation 2.18 into Equation 2.14 results in

$$\frac{dI_f}{ds} = \kappa_a B_f(T) - \alpha_e I_f + \kappa_s J_s. \tag{2.20}$$

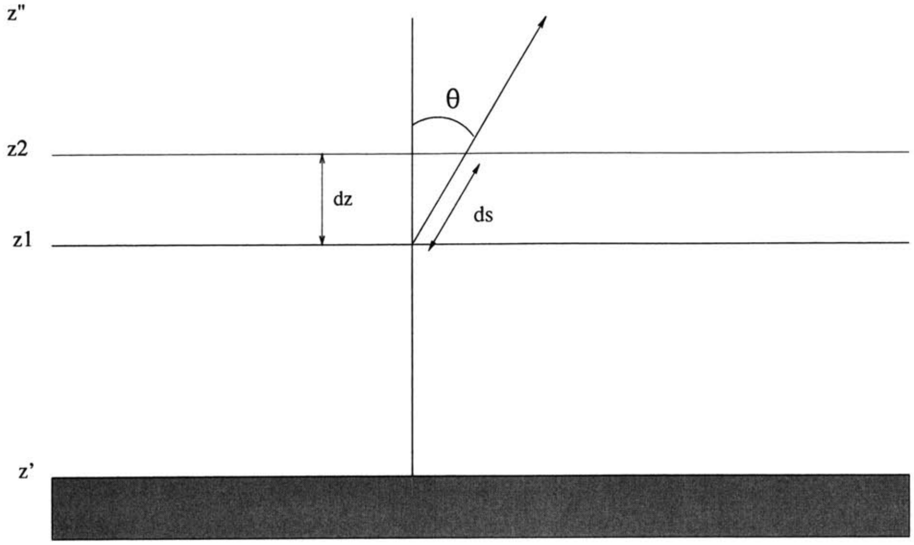

Figure 2-3: Geometric layout for plane stratified atmosphere

For now, the rest of the radiative-transfer-equation derivation will ignore scattering, but the precipitating numerical solution will pick it up again in Section 2.3.5. Multiplying both sides by $e^{\tau(z)}$ and integrating from z' to z'' in Equation 2.20 results in the intensity at the antenna:

$$I_f(z'') = I_f(z') \cdot e^{-[\tau(z')-\tau(z'')]\sec(\theta)} + \int_{z'}^{z''} \sec(\theta) B_f(z) e^{-[\tau(z)-\tau(z'')]\sec(\theta)} \alpha_e(z)\, dz. \quad (2.21)$$

2.2.3 Scattering Coefficient

The volume scattering coefficient (κ_s) determines the power scattered within the atmosphere (units of Nepers/m). The scatterers (*e.g.*, rain drops) have no coherent phase relationship, because they are assumed to be randomly distributed within the volume. Also, the density of scatterers is assumed to be low enough that particles do not overshadow one another. These two assumptions lead to this equation, from Ulaby [67, pg 305]:

$$\kappa_s = \int_{r=0}^{r=\infty} p(r) Q_s(r) dr. \quad (2.22)$$

Where $p(r)$ is the drop-size distribution, which is the number of drops per m^3 per unit increment of r with dimensions of m^{-4}, and $Q_s(r)$ is the scattering cross-section

Where $p(r)$ is the drop-size distribution, which is the number of drops per m^3 per unit increment of r with dimensions of m^{-4}, and $Q_s(r)$ is the scattering cross-section of a sphere of radius (r) with dimensions of m^2. Modeling of $p(r)$ is described in Section 2.3.4. Scattering efficiency, $\xi_s = Q_s/\pi r^2$, and the parameter Chi, $\chi = 2\pi r/\lambda_o$, can be used to rearrange the scattering coefficient equation as:

$$\kappa_s = \frac{\lambda_o^3}{8\pi^2}\int_o^\infty \chi^2 p(\chi)\xi_s(\chi)d\chi. \tag{2.23}$$

Mie [46] found the solution for the scattering (ξ_s) and absorption (ξ_a) efficiencies for a dielectric sphere of radius, r. The complete solutions are in Ulaby [67, pg 290], and the equation for the scattering efficiency is repeated here:

$$\xi_s(n,\chi) = \frac{2}{\chi^2}\sum_{l=1}^{\infty}(2l+1)(|a_l|^2 + |b_l|^2). \tag{2.24}$$

The variables are the complex index of refraction (n) and the Mie coefficients (a_l and b_l). For a more in-depth explanation of the theory behind hydrometeor scattering, please see Gasiewski [32, Ch. 3] or Ulaby *et al.* [67, Ch. 5].

2.2.4 Absorption Coefficient

The absorption coefficient (κ_a) value increases because the density of atmospheric molecular absorbers or hydrometeors increases. Molecular constituents have three different mechanisms that absorb incident electromagnetic energy. An easy molecule to visualize is a diatomic one, and the visualization can be carried over to more complicated molecules. The energy of a diatomic molecule can be stored in electronic states within the atoms, in the vibrations of the two atoms, or in the rotation of the atoms around a center of gravity. Depending on the incident-radiation's wavelength, each of these sources of energy can be excited. In the visible and ultra-violet regimes, the absorption occurs when electrons are excited to a higher electron state. At the larger wavelengths of the mid- to near infrared frequencies, the principal absorption is from vibration of inter-atomic spacing. Lastly, the microwave and far-infrared frequencies, which are the frequencies most pertinent to this thesis, are mainly absorbed by rotational transitions. For a more in-depth explanation, please see Rosenkranz [32, Chap. 2].

Hydrometeors can also absorb electromagnetic energy. A hydrometeor is condensed atmospheric water vapor, and, if the hydrometeor is large enough, it will scatter microwave electromagnetic energy. The absorption of hydrometeors follows the same reasoning as the scattering presented in Section 2.2.3. Equation 2.23 is of the same form as the equation for the absorption of hydrometeors, but ξ_s is replaced with ξ_a. For a more in-depth explanation, please see Ulaby [67, pg 288].

2.2.5 Surface Emissivity

The surface emissivity defines the amount of power that is absorbed by the surface. Radiation incident on the surface is either reflected or transmitted. The relationship between emissivity, ε_s, and reflectivity, ρ_s, is:

$$\varepsilon_s + \rho_s = 1. \tag{2.25}$$

Emissivity can be derived from Maxwell's equations and the refractive index of the two materials at the boundary [65, 67]. Under thermal equilibrium, the fraction of radiation absorbed is also the fraction radiated, therefore the brightness temperature from the surface is:

$$T_{b_{\text{surf}}} = \varepsilon_s \cdot T_{\text{surface}}. \tag{2.26}$$

2.3 Atmospheric Model and Simulation

From the radiative transfer equation (Equation 2.21) in Section 2.2, numerical solutions can determine, along with an atmospheric profile (*e.g.*, a radiosonde), the brightness temperatures that the airborne NAST-M instrument would observe. This section will describe the atmospheric model and the numerical solutions used in this thesis, and will explain the necessary assumptions and approximations.

2.3.1 Airborne Microwave RTE

This section adapts Equation 2.21 to be used in an airborne microwave application. The first step is to replace the intensity (I_f) with the brightness temperature (see Equation 2.13). Next, the position at the surface is set to zero ($z' = 0$) and $\tau(z'') = 0$, which gives

$$T_b = T_{b_{\text{surf}}} e^{-\tau(0)\sec(\theta)} + T_{b_u} \tag{2.27}$$

$$T_{b_u} = \int_0^{z''} T(z) e^{-\tau(z)} \alpha_e(z) \sec(\theta)\, dz. \tag{2.28}$$

The intensity from the surface, $I_f(0)$, is replaced by the brightness temperature of the surface (Equation 2.26). Equation 2.27 only accounts for the thermal radiation from the surface and the intervening atmosphere. To complete the airborne equation, two additional sources are included, which comes from the downwelling radiation and cosmic background radiation that is reflected by the surface. The complete microwave-frequency airborne RTE is

$$T_b = T_{b_u} + [T_{b_{\text{surf}}} + (1 - \varepsilon_s) T_{b_d}] e^{-\tau(0)\sec(\theta)}. \tag{2.29}$$

The ε_s is the surface emissivity, and T_{b_d} is

$$T_{b_d} = T_{\text{cosmic}}\, e^{-\tau(0)\sec(\theta)} + \sec(\theta) \int_0^{z''} T(z) \alpha_e(z)\, e^{-[\tau(0)-\tau(z)]\sec(\theta)}\, dz. \tag{2.30}$$

2.3.2 Weighting Functions

A convenient tool for understanding how spectrometers sound the atmosphere is the concept of temperature weighting functions. Taking Equation 2.29 and combining the integrals at nadir gives:

$$T_b = \varepsilon_s T_{\text{surf}}\, e^{-\tau(0)} + \rho_s T_{\text{cosmic}} e^{-2\tau(0)} + \int_0^{z''} \alpha_e(z)(1 + \rho_s e^{-2[\tau(0)-\tau(z)]}) e^{-\tau(z)} T(z)\, dz. \tag{2.31}$$

Everything within the integral, except the temperature profile, can be placed into a weighting function.

$$W(z) = \alpha_e(z)(1 + \rho_s e^{-2[\tau(0)-\tau(z)]\sec(\theta)})e^{-\tau(z)\sec(\theta)}. \tag{2.32}$$

If α_e is great enough to ignore the contributions of the surface and cosmic background, then Equation 2.31 can be written as a Fredholm integral equation of the first kind:

$$T_b = \int_0^{z''} W(z)T(z)\, dz. \tag{2.33}$$

This is the principal equation behind temperature profile sounding.

2.3.3 Constituent Absorption Modeling

In the microwave spectrum, the atmospheric model is described by the radiative transfer equation from Section 2.2.2. The absorption coefficient, κ_a, from atmospheric gases is modeled with a line-by-line model called the Millimeter-wave Propagation Model (MPM). Liebe *et al.* developed the line-by-line model [37, 38, 39, 42, 52], which accounts for the absorption lines of the molecular constituents pertinent to the frequencies of interest. The primary molecules accounted for are oxygen, O_2; nitrogen, N_2; ozone, O_3; water vapor, H_2O; and liquid water drops that are too small to scatter microwave radiation. The absorption coefficient is a function of the height above the surface, water vapor profile, pressure profile, and temperature profile. The simulated absorption coefficient is used to solve for the brightness temperature in Equation 2.21.

2.3.4 Hydrometeor Modeling

As mentioned in Section 2.2, hydrometeors both absorb and scatter in the atmospheric model used in this thesis. The equations are the same for κ_s and κ_a, with the exception of the efficiencies. A model for the drop-size distribution and a Mie coefficient algorithm are needed to numerically solve for κ_a and κ_s.

To calculate the scattering or absorption cross-section of hydrometeors, the hydrometeors are assumed to be a dielectric spheres, which leads to the use of the Mie solutions mentioned in Section 2.2.3. The scattering and absorption efficiency factors (ξ_s and ξ_a) are determined from the Mie coefficients (Equation 2.24). Deirmendjian developed an iterative procedure for calculating the Mie coefficients [17]. When $|n\chi| \ll 1$, the Mie coefficients are calculated using the Rayleigh approximation, and the particular algorithm used by the atmospheric model is from Wiscombe [70].

There are several ways to model the drop-size distribution ($p(r)$). A staple distribution used for modeling rain is the Marshall-Palmer [43]. Marshall and Palmer measured surface drop-size distributions to formulate this expression:

$$p(r) = N_o \, e^{-2br}, \text{ with } b = 4100 \, R_r^{-0.21}. \tag{2.34}$$

The drop-size distribution is in units of number of drops of radius (r meters), per unit volume per unit drop-radii interval (m^{-4}) and has a constant $N_o = 8.0 \times 10^6 \ m^{-4}$. The b function is related to the rain rate (R_r) in units of mm/hr.

2.3.5 Numerical Solutions to the Airborne RTE

There are two RTE solutions used in this thesis for calculating NAST-M brightness temperatures. One is used under clear-air or non-precipitating cloud conditions, while the other solution includes scattering for hydrometeors. Other techniques exist.

Non-precipitating Solution

Tbarray is a software program, written by Philip W. Rosenkranz [51], which calculates the microwave emission and transmission for a given atmospheric profile. The Tbarray program does not include scattering and assumes a planar-stratified atmosphere, which is useful in situations with either clear air or non-precipitating clouds. The input profiles include temperature, pressure, water vapor, liquid water, and ozone. Tbarray calls subroutines to determine the absorption coefficients by using the line-by-line model described in Section 2.3.3. The airborne brightness temperature is computed outside the program by using the Tbarray-computed transmittance, Tbarray-computed emission, cosmic background radiation, surface emissivity, and Equation 2.29. All of NAST-M's antenna have 3-dB beamwidths of 7.5°, and each spot's beamwidth is modeled as a Gaussian function of angle with nine sample points about the peak. Also, the frequency response of all channels was measured in the lab (*e.g.*, Section 3.4.1). The simulation then weights frequencies with a higher response accordingly.

Tbarray arranges the atmosphere into slabs, for which boundaries are defined by the discrete profile inputs. An "absorption-of-averages" method is used to determine the absorption coefficient of each slab [52, pg 84]. The arithmetic mean was used to determine the temperature, water vapor, liquid water, and ozone of the slab, but used a geometric mean for the pressure. Then the integral in Equation 2.21 is approximated through successive slabs:

$$T_{b_i} = T_{b_{i-1}} e^{-\tau_{slab}\sec(\theta)} + T_{slab}(1 - e^{-\tau_{slab}\sec(\theta)}) \tag{2.35}$$

$$\tau_{slab} = \Delta H \cdot \kappa_a \tag{2.36}$$

ΔH is the height of the slab. A summary of the simulation can be found in Appendix B.1.

Precipitating Solution

Tbscat is also a program written by Rosenkranz, and his radiative transfer solution is described in [50]. This algorithm differs from Tbarray because it includes multistream scattering, but both algorithms assume a planar-stratified atmosphere. The algorithm starts with Equation 2.20, and separates it into:

$$\cos(\theta_i)\frac{dI_i(z)}{dz} = -\alpha_e(z)I_i(z) + \kappa_a B_f(z) + \kappa_s \sum_{j=1}^{2N} \tilde{p}_{ij}(z) I_j(z) \tag{2.37}$$

for each stream $i = 1, \ldots, 2N$. The $\tilde{p}_{ij}(z)$ ($\psi(s, \acute{s})$ in Eq. 2.20) is the normalized phase function, where the Henyey-Greenstein [28] model is used. At the top of the atmosphere, N streams are going down into the atmosphere and N streams are returning from the surface. These streams describe a system of $2N$ coupled first-order differential equations, and the algorithm approaches the solution as an initial-value problem. The radiation above the sensor, from cosmic background radiation and any atmosphere above the aircraft, are used as the initial conditions for the N downward propagating streams, and the N unknown output radiances are the initial conditions for the upward propagating streams. The backward Euler method of finite difference equations begins at the top of the atmosphere, and all $2N$ solutions are propagated toward the surface. At the surface, the N upward propagating streams are matched with the N downward propagating streams using the specular surface reflectivity and the surface temperature, which allows the initially unknown output radiances to be algebraically solved. When the opacity (see Equation 2.19), at some altitude above the surface, is high enough, then the atmosphere below this altitude is considered a blackbody (the reflectivity is set to zero), and the output radiances are immediately solved for. This allows the calculation of the final solution to avoid unnecessary computations. The condition to determine if the opacity is great enough is:

$$\int_{z_1}^{z_{max}} \kappa_a(z) + \frac{1 - g(z)}{2} \kappa_s(z)\, dz > 4 \tag{2.38}$$

where $g(z)$ is the asymmetry factor, *i.e.*, one-third times the first-order coefficient in a spherical harmonic expansion of the normalized phase function [50, pg 1890]. The weight on the scattering coefficient, $\frac{1-g(z)}{2}$, is a way to account for only the backscattering energy. For this reason and for other advantages mentioned in [50], the algorithm can be considered a rapid solution to the RTE. A summary of the simulation can be found in Appendix B.2.

2.4 Bayesian Constant-coefficient Estimators

Retrievals of geophysical parameters in the thesis use the non-linear constant coefficient statistical estimator. The next several sections present the linear least-squares estimator (LLSE) from formulation of the Bayesian theory to the practical implementation of the estimator through statistical inference. The LLSE can be adapted to the non-linear case by including polynomials, and the review presented here can be easily extended to the polynomial case (Constant-Coefficient Polynomial Estimator or CCPE). The theory presented here is also applicable to the calibration routines in Section 3.3.

The Bayesian framework minimizes the expected value of a cost function in order to determine the performance of an estimator. There are several standard cost functions, and a few examples are the minimum absolute error (MAE), maximum a posteriori (MAP), or the minimum mean-squared error (MMSE). The cost function used throughout this thesis is the mean-squared error, which is also called the least-squares criterion:

$$\hat{Y}(X) = \arg\min_{\hat{a}(\cdot)} E[(Y - \hat{a}(X))^2]. \tag{2.39}$$

Bayesian methods of estimation use *a priori* information when choosing the optimal estimator. The general solution to Equation 2.39 is:

$$\hat{Y}_{MMSE} = E[Y|X]. \tag{2.40}$$

2.4.1 Linear Least-Squares Estimator

The optimal estimator that estimates Y based on $\mathbf{X}$, with the MMSE criterion, is

$$\hat{Y}_{MMSE} = E[Y|X_1 = x_1, \ldots, X_L = x_L] = \int_{-\infty}^{\infty} y \cdot p_{y|\mathbf{x}}(y|x)\, dy. \tag{2.41}$$

Where x is a realization of the random vector $\mathbf{X}$. It can be difficult to determine the complete statistical characterization of the relationship between X and Y. Also, the relationship between X and Y may be nonlinear. To help get around these two shortcomings (but still suboptimal), an estimator will have an additional constraint that it is an affine function of the measured random variables:

$$\hat{Y}(\mathbf{X}) = \alpha + \beta^T \cdot \mathbf{X}. \tag{2.42}$$

One technique for finding the minimum of Equation 2.39, with Equation 2.42 in the place of $\hat{a}(\mathbf{X})$, is to take the derivative with respect to each coefficient and set it equal to zero. For example,

$$\frac{\partial}{\partial \alpha} E[(Y - \alpha - \sum_i \beta_i X_i)^2] = 0 \tag{2.43}$$

$$-2(E[Y] - \alpha - \sum_i \beta_i E[X_i]) = 0 \tag{2.44}$$

that gives the solution:

$$\alpha = E[Y] - \sum_i \beta_i E[X_i]. \tag{2.45}$$

A similar approach to the other coefficients allows the formation of a set of equations called the normal equations:

$$Cov_{\mathbf{X}} \cdot \beta = Cov_{\mathbf{X}Y}. \tag{2.46}$$

The resulting suboptimal estimator is the linear least-squares estimator:

$$\hat{Y}(X) = E[Y] + (Cov_{\mathbf{X}}^{-1} \cdot Cov_{\mathbf{X}Y})^T \cdot (X - E[X]). \tag{2.47}$$

2.4.2 Statistical Inference

A practical consideration when using a LLSE is determining the covariance matrix. The sample variance is an estimator for the population variance, which converges to the true variance when there are enough samples, N. The sample variance formula is

$$S_x^2 = \frac{\sum_{i=1}^{N} (x_i - M_x)^2}{N}, \tag{2.48}$$

with M_x being the sample mean:

$$M_x = \frac{\sum_{i=1}^{N} x_i}{N}. \tag{2.49}$$

The expected value of the sample mean is the mean of X and the variance of the sample mean is $\frac{\delta_x^2}{N}$. As N goes to infinity, the variance of the estimator goes to zero. The sample variance has an expected value of:

$$E[S_x^2] = \frac{N-1}{N}\delta_x^2, \tag{2.50}$$

which also gives the true variance of X when N is large. Another important inference is the sample covariance:

$$S_{xy}^2 = \frac{\sum_{i=1}^{N}(x_i - M_x)(y_i - M_y)}{N}. \tag{2.51}$$

2.4.3 Linear Regression

Linear regression is the practical application of the LLSE. Samples from the relationship between the random variables are given in ordered pairs (x_i, y_i). If the given variable is X (called the regressor variable), then the response variable is Y. Multivariate linear regression has slope parameters for each regressor variable. X is assumed to be measured without error and Y will have the following relationship with X:

$$y_i = \alpha + \beta \cdot x_i + \epsilon_i. \tag{2.52}$$

The error ϵ_i is introduced from imperfect measurements or from random variations. If each ordered pair holds equal validity in representing the linear relationship (equal variance and independent), then a linear system can be formed:

$$\mathbf{y}_N = \mathbf{A} \cdot \mathbf{p}, \tag{2.53}$$

where

$$\mathbf{y}_N = \begin{bmatrix} y_1 \\ y_2 \\ \vdots \\ y_N \end{bmatrix} \quad \mathbf{A} = \begin{bmatrix} x_1 & 1 \\ x_2 & 1 \\ \vdots & \vdots \\ x_N & 1 \end{bmatrix} \quad \mathbf{p} = \begin{bmatrix} \hat{\alpha} \\ \hat{\beta} \end{bmatrix}. \tag{2.54}$$

Equation 2.53 can be rewritten in the more familiar form of

$$\mathbf{A} \cdot \mathbf{x} = \mathbf{b}. \tag{2.55}$$

In the linear regression situation, we have an overdetermined system. Therefore, Equation 2.55 can be solved in a manner that satisfies Equation 2.39, which involves choosing an error criterion that minimizes the mean-squared error between the regressor and the response variable. Minimizing $E[(x - \hat{x})^2]$ is the same as using the least squares approximation. From linear algebra, the familiar form is

$$\hat{\mathbf{x}} = (\mathbf{A}^{\mathbf{T}} \cdot \mathbf{A})^{-1} \cdot \mathbf{A}^{\mathbf{T}} \cdot \mathbf{b}. \tag{2.56}$$

Therefore, the least-squares solution or the linear regression is

$$\hat{\beta} = \frac{N \cdot \sum_{i=1}^{N} x_i y_i - \left(\sum_{i=1}^{N} x_i\right)\left(\sum_{i=1}^{N} y_i\right)}{N \cdot \sum_{i=1}^{N} x_i^2 - \left(\sum_{i=1}^{N} x_i\right)^2} = \frac{S_{xy}^2}{S_x^2}, \tag{2.57}$$

$$\hat{\alpha} = \frac{\left(\sum_{i=1}^{N} y_i - \hat{\beta}\sum_{i=1}^{N} x_i\right)}{N} = M_y - \hat{\beta}\ M_x. \tag{2.58}$$

The LLSE estimator (Equation 2.47) and least squares approximation (Equation 2.56) are the same thing with one important difference. The linear regression is the statistically inferred form of the LLSE estimator based on a finite training data set.

Chapter 3

NAST-M Instrumentation and Calibration

This chapter covers the various aspects of the NAST-M instrumentation from hardware to calibration. The hardware portion consists of a review of the airborne platforms and the NAST-M suite prior to the installation of the new spectrometers. The scan pattern is discussed to gain an understanding of the brightness temperature imaging. The new spectrometer's hardware is then presented, as are the resulting weighting functions. The calibration techniques for each platform are presented and are followed by laboratory validation.

3.1 NAST Platforms

Currently, the platforms of the National Polar-orbiting Operational Environmental Satellite System (NPOESS) Aircraft Sounder Testbed - Microwave (NAST) are the ER-2 high-altitude aircraft, which is a modified U-2 aircraft on loan to NASA from the United States Air Force, and the Proteus, which is a custom-made high-altitude aircraft designed and built at Scaled Composites for numerous high-altitude applications. NAST flies in one of the ER-2 superpods, which lies under the wings of the ER-2 aircraft (see Figure 3-1 and Figure 3-2(b)). The superpods allow views of both nadir and zenith, where the zenith view is used for calibration. The ER-2 has a

NASA Dryden Flight Research Center Photo Collection
http://www.dfrc.nasa.gov/gallery/photo/index.html
NASA Photo: EC99-45225-1 Date: October 1999 Photo by: Jim Ross

Lockheed ER-2 #809 high altitude research aircraft in flight

NASA Dryden Flight Research Center Photo Collection
http://www.dfrc.nasa.gov/gallery/photo/index.html
NASA Photo: EC99-45225-3 Date: October 1999 Photo by: Jim Ross

Lockheed ER-2 #809 high altitude research aircraft in flight

(a) ER-2 - Bottom View

(b) ER-2 - Side View

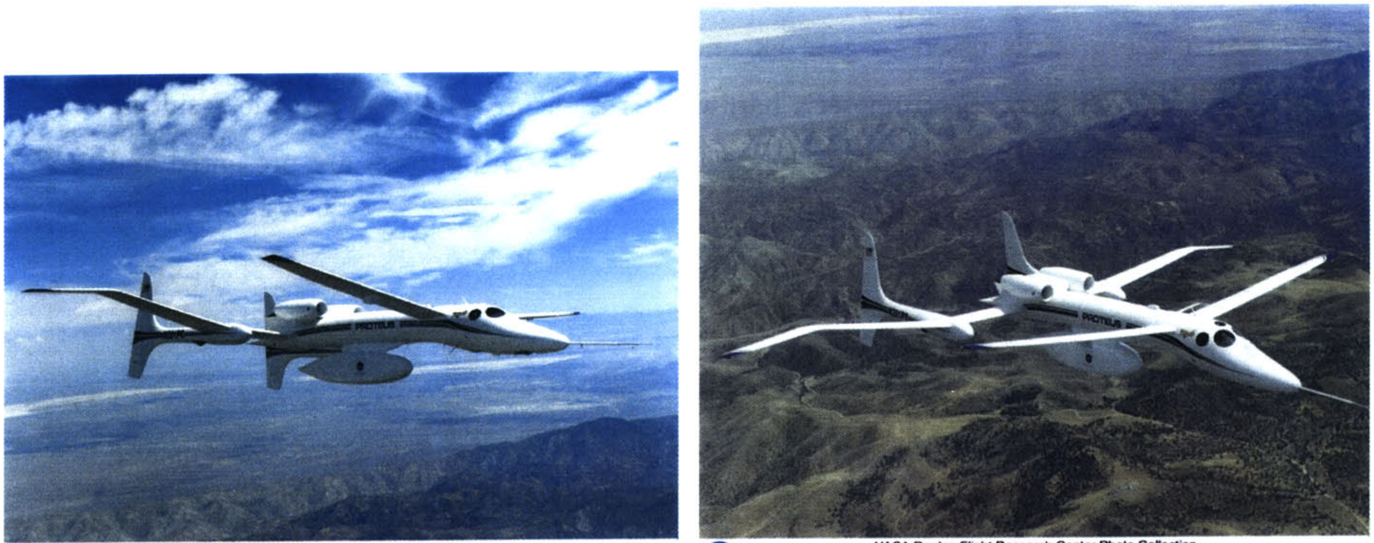

NASA Dryden Flight Research Center Photo Collection
http://www.dfrc.nasa.gov/gallery/photo/index.html
NASA Photo: EC99-45110-11 Date: July 26, 1999 Photo by: Patrick Wright

ERAST Program Proteus Aircraft in Flight over the Mojave Desert in California

NASA Dryden Flight Research Center Photo Collection
http://www.dfrc.nasa.gov/gallery/photo/index.html
NASA Photo: EC99-45110-8 Date: July 26, 1999 Photo by: Patrick Wright

ERAST Program Proteus Aircraft in Flight

(c) Proteus - Side View

(d) Proteus - Top View

Figure 3-1: Pictures of NAST's Current High-Altitude Platforms.

(a) Proteus

(b) ER-2

Figure 3-2: NAST-M installed on NAST platforms.

maximum cruising altitude of 20 km at a speed of 410 knots (211 m/s), while Proteus cruises at 17 km at a speed of 160 knots (82 m/s). In Proteus, NAST flies in a pod underneath the fuselage and lacks the zenith view that it has on the ER-2's superpod (see Figure 3-1 and Figure 3-2(a)). Both the Proteus' pod and the NAST-M's portion of the ER-2's superpod are unpressurized. The loss of the zenith port reduces the three-point calibration to a two-point calibration, but also reduces leakage of zenith cold-space radiation into the antenna during calibration.

3.2 NAST-M Instrumentation

The NAST-M instrument consists of four independent total-power microwave spectrometers that share a scanning reflector. The original suite had two spectrometers near the oxygen lines at 50-57 GHz (single sideband) and the oxygen line at 118.75 GHz (double sideband) [7]. The two new spectrometers are double-sideband superheterodyne systems, one centered on the 183.31-GHz water vapor absorption line (183-GHz system) and the other centered on the 424.76-GHz oxygen absorption line (425-GHz system).

Passive microwave retrievals of temperature and water vapor profiles involve mea-

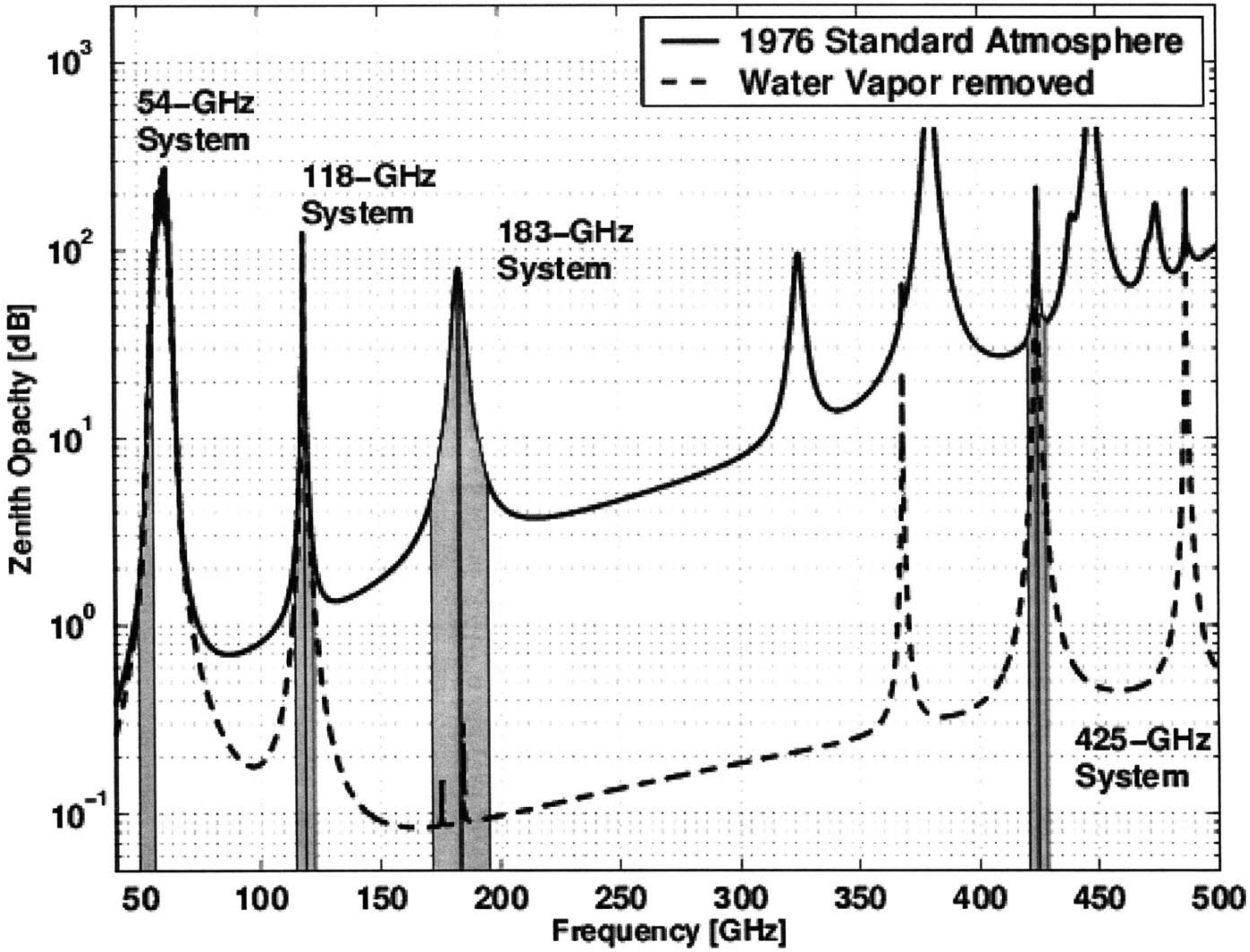

Figure 3-3: Zenith opacity for the U.S. 1976 standard atmosphere with the NAST-M frequency coverage.

surements of brightness temperatures near known absorption lines of oxygen and water vapor molecules. Figure 3-3 shows the zenith opacity due to oxygen, nitrogen, and water vapor as a function of frequency; the NAST-M spectral coverage is overlaid. Zenith opacity is the integrated atmospheric attenuation from the terrestrial surface to the top of the atmosphere. For this simulation, the U.S. 1976 standard atmosphere was used with the Millimeter-wave Propagation Model [MPM] [42]. Hydrometeors (*e.g.*, rain) both absorb and scatter electromagnetic waves.

The instrument's spectral response is determined by the LO frequency and IF filterbank and defines the temperature weighting functions of NAST-M. The mathematical formula defining the weighting function is described in Section 2.3.2, and an example appears in Figure 3-11. The shapes of the weighting functions are determined by the absorption coefficient (see Equation 2.32). The weighting functions are somewhat Gaussian in shape when looking into the atmosphere from high altitudes, with the peak of the Gaussian distribution located near an optical depth of unity, determined by the frequency affect from the absorption line or lines. As the transmittance decreases, the altitude of the peak of the Gaussian curve increases. There is a high degree of correlation between most weighting functions, which can cause the inversion to become unstable. Yet, the correlation is important for the statistical estimators commonly used in parameter estimation. A compromise between performance and diminishing returns is chosen when the weighting functions of a sounder are designed.

The NAST-M spectrometer flies together with NAST-Infrared (NAST-I), an 8500-channel infrared interferometric spectrometer scanning wavelengths of 3.6 to 16.1 microns with 2.6-km resolution at an altitude of 20 km over $\pm 48^o$ swath [15]. The NAST system is testing and validating measurement concepts essential to the success of the NPOESS global environmental satellite system. The new 183-GHz spectrometer, combined with the existing 50-57 GHz spectrometer, is validating concepts utilized by the Advanced Microwave Sounding Unit (AMSU) on the operational National Oceanic and Atmospheric Administration (NOAA) satellites, a precursor to the NPOESS Advanced Technology Microwave Spectrometer (ATMS) and the Conical scanning Mi-

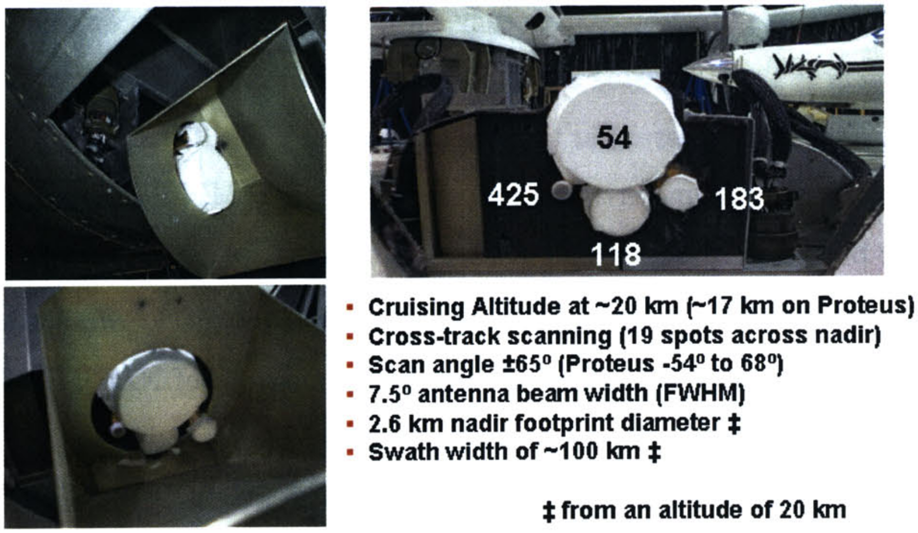

- Cruising Altitude at ~20 km (~17 km on Proteus)
- Cross-track scanning (19 spots across nadir)
- Scan angle ±65° (Proteus -54° to 68°)
- 7.5° antenna beam width (FWHM)
- 2.6 km nadir footprint diameter ‡
- Swath width of ~100 km ‡

‡ from an altitude of 20 km

Figure 3-4: Pictures of NAST-M's reflector and antenna horns.

crowave Imaging System (CMIS) planned for NPOESS (npoess.noaa.gov).

3.2.1 Scan Pattern

The scan assembly remained unchanged from the original suite, but there were some deployment-specific changes to the scan pattern. NAST-M's scanning reflector gives the radiometers the ability to image a swath that extends to the right and left of the aircraft. The scan uses a "step and stare" method, and the resulting swath is illustrated in Figure 3-5(a). The design of the new spectrometers required the receiver front ends to be right next to receiver horns of the 54- and 118-GHz systems. The completed spectrometers, reflector, calibration loads, and motor are pictured in Figure 3-6. All of the radiometers' horns (see Figure 3-4) are fixed facing the rotating reflector, and the reflector's motor and encoder are controlled by the onboard flight computer. The reflector steps 360 degrees in approximately 5.5 seconds. The mirror's rotation allows the onboard loads to be viewed for calibration. A total of 25 pauses are made where the instrument takes a measurement. These measurements, or "spots,"

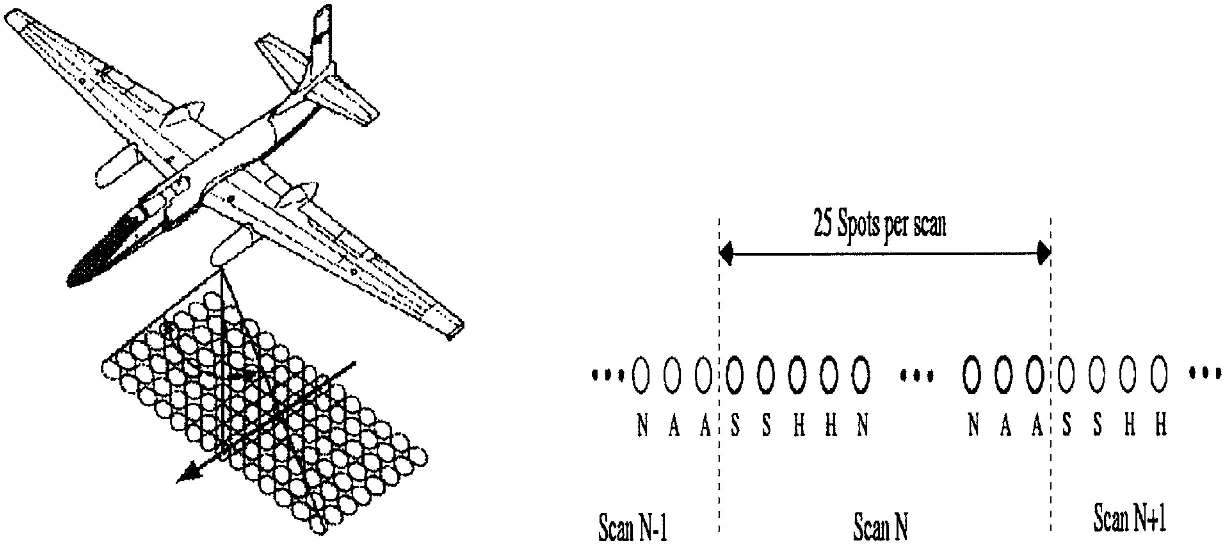

(a) field of view

(b) Scan pattern: H - heated load, A - ambient load, S - zenith port, N - an view towards nadir

Figure 3-5: NAST-M ER-2 scan pattern and illustration of swath.

are divided between the target and the calibration loads. The scan pattern varied depending on the aircraft and deployment. Figure 3-5(b) illustrates the scan pattern on board the ER-2. On the ER-2, the scan starts at zenith with two measurements through the zenith port, and then the reflector's orientation moves to the heated load for another two measurements. The two spots on the heated load are at different angles, which were optimized for the different antenna-beam patterns. The optimization consisted of choosing the angle with the peak brightness temperature, which was assumed to be the angle where the calibration load was best covered by the antenna beam. The first spot, *i.e.*, angle, is optimized for the large 54-GHz antenna beams, while the second angle is optimized for the other smaller wavelength spectrometers (see Section 3.4.2). The Proteus lacks the zenith port, and the two zenith spots were shifted with one going to each calibration load. The onboard calibration loads are described in detail in Blackwell [8, pg. 195]. The next 19 spots are off nadir by ±64.8 degrees. On board the Proteus, the viewing angle is $-54°$ to $68°$. When the cruising altitude is 20 km (typically 17 km for the Proteus), the swath width is approximately

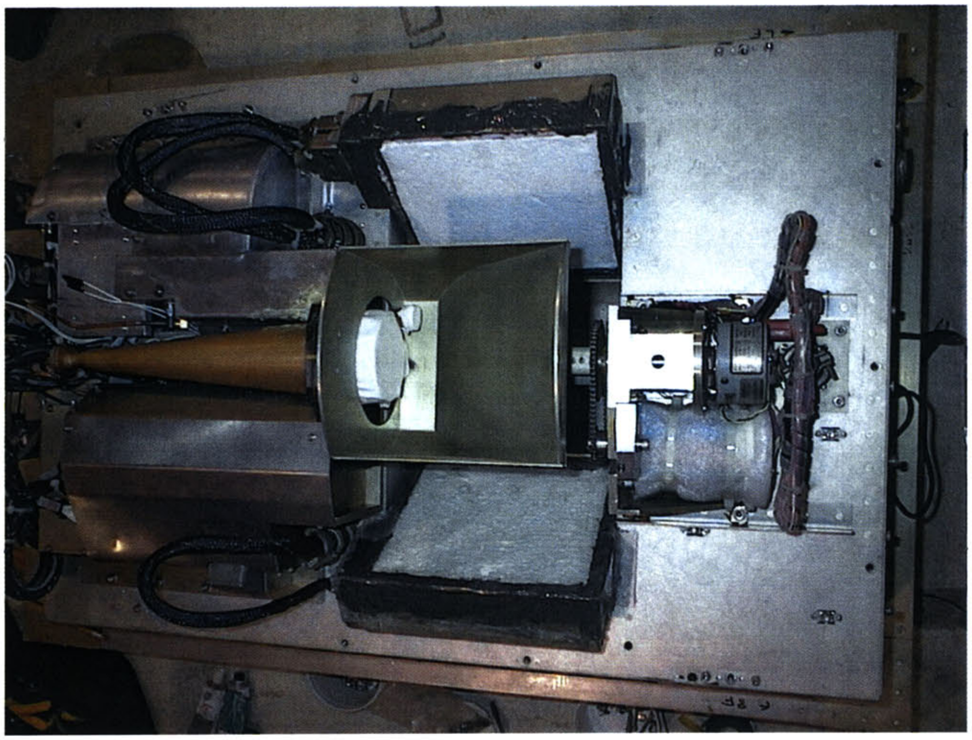

Figure 3-6: Top view of NAST-M horns, reflector, and onboard calibration loads

100 km. The most extreme ER-2 angles have footprints on the surface that are 14-km long in the crosstrack direction (*e.g.*, see Figure 3-18). At nadir, the cross-track spatial resolution is 2.6 km on the ER-2 from 20 km, and the resolution goes down slightly to 2.2 km at an altitude of 17 km. The NAST-M scan pattern was originally designed for the ER-2 at a speed of 210 m/s, and the nadir surface antenna footprints overlapped. The footprints were designed to overlap above the surface to fully resolve clouds. The Proteus air speed is significantly slower and there is considerable overlap between nadir footprints from one scan to another. To end the scan pattern rotation, two measurements of the ambient calibration load are taken at the same angle for all spectrometers. A single scan lasts approximately 5.5 seconds and includes views of two or three thermal calibration sources. The most extreme angles have footprints on the surface that are 14-km long in the crosstrack direction, and the two most extreme angles on each side are left out in most NAST-M imagery, which gives an effective swath width of 55 km. Figure 3-5 is an illustration of the instrument's field of view on the surface along with an illustration of the scan pattern while on the ER-2.

A practical problem with radiometers is time-varying gain. The active RF components and extreme environmental conditions that the instrument experiences are the principal sources of the fluctuations. The periodic views of the calibration loads are designed to alleviate this problem by recalibrating the instrument on every scan. During the time between calibrations, we assume that the gain fluctuations are linear or at least monotonic. Spectral estimation can determine the contribution of the $1/f$ noise, to determine if this is true. This assumption allows simple interpolations between calibration points to determine the gain and baseline at a particular time during the scan. Section 2.1.1 reviewed the periodic absolute calibration, and Figure 3-6 is a picture of the scanning assembly that implements the periodic scan. It can be seen that the horns face the rotating mirror, and the mirror views the two onboard calibration loads that are covered in Styrofoam. In the photo, the zenith port is underneath the mirror and between the onboard loads.

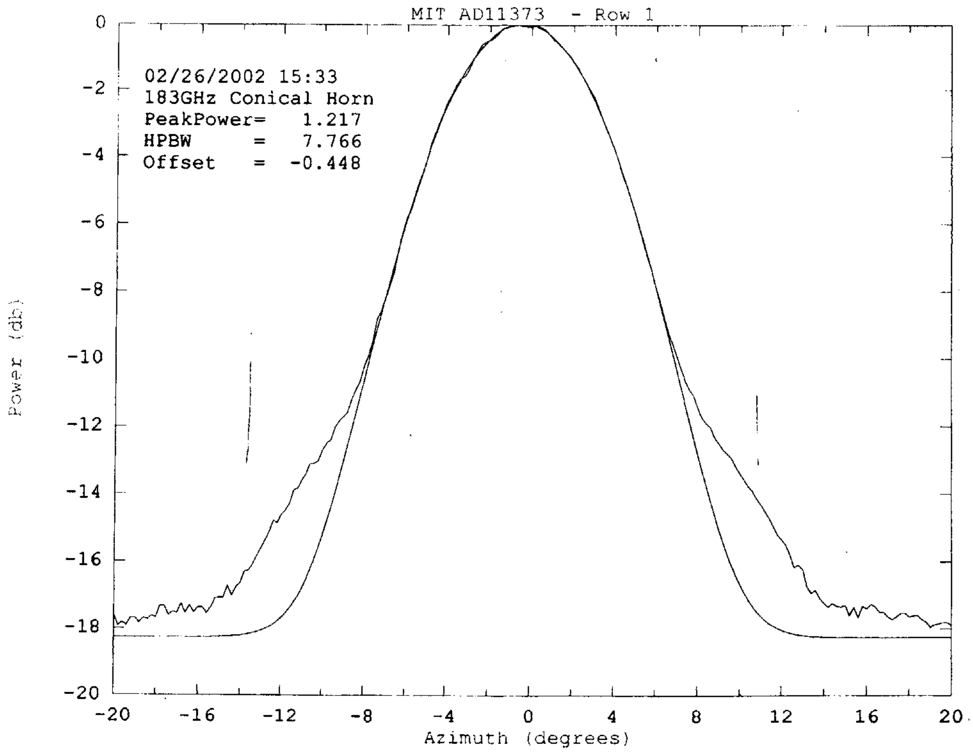

Figure 3-7: Millitech-supplied antenna beam measurement for the 183-GHz radiometer. The abscissa is azimuth in degrees, and the ordinate is power in decibels. The half power beamwidth is 7.766 degrees with a -0.448 degree offset.

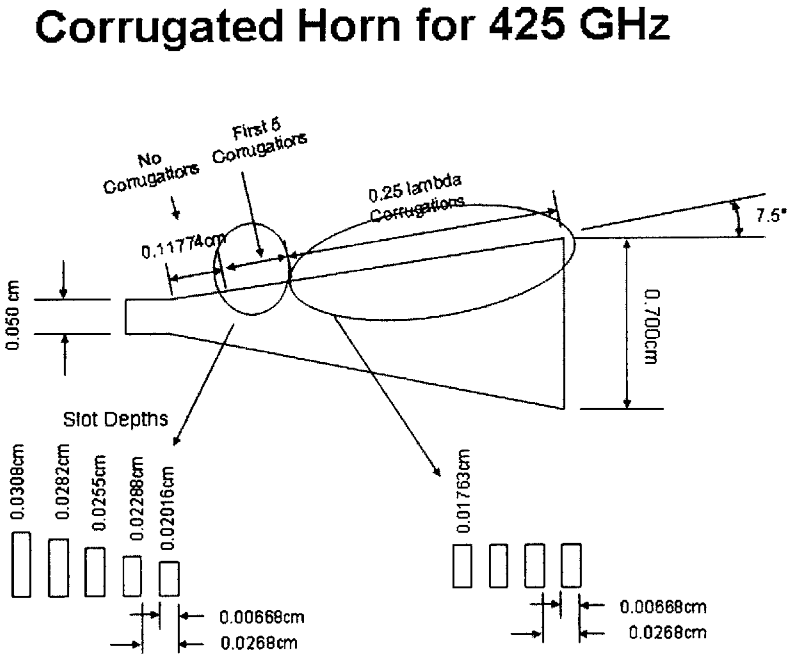

Figure 3-8: The 425-GHz scalar-feed horn dimensions. Proved by Prof. J. L. Hesler from the University of Virginia.

The spectrometer's directional response is defined by the antenna-beam pattern. Millitech supplied a measurement of the 183-GHz conical horn's antenna beam and the results are presented in Figure 3-7. Unfortunately, there is not a similar measurement for the 425-GHz scalar-feed horn, but there is an illustration of the horn's design in Figure 3-8. Figure 3-9 is an illustration of NAST-M's antenna horns, which gives the orientation of each spectrometer's polarization. Images of the actual horns and position in relation to the reflector are in Figures 3-4 and 3-6.

Using the aircraft navigation data, NAST-M's antenna and scan specifications, and MathWork's Matlab software, NAST-M's brightness temperatures can be imaged on a geographic map with the appropriate antenna footprint. Figure 3-10 is a sample of the NAST-M antenna-footprint imaging code, which illustrates a transparent surface-sensitive channel over the Hawaiian Islands. The MathWork's Mapping Toolbox has data for the island's boundaries, which is an independent test of the imaging code that shows very good agreement. As the aircraft gains altitude in the

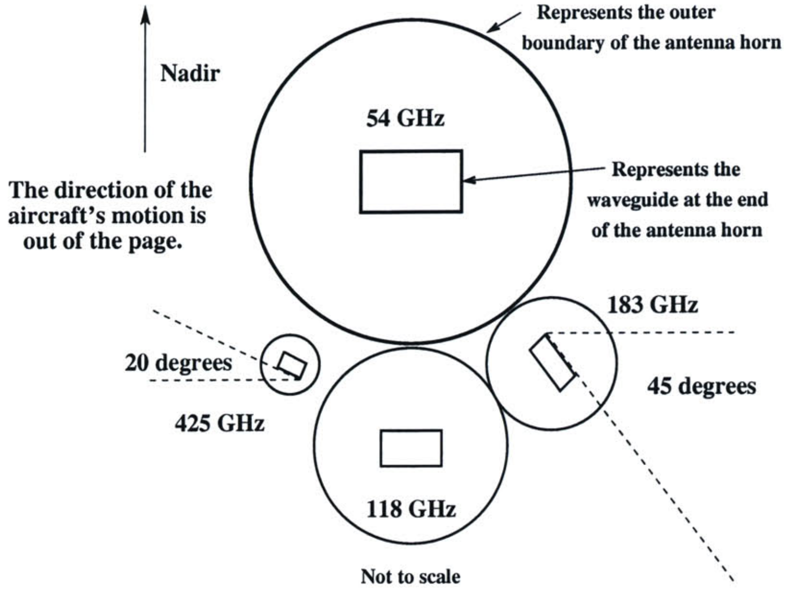

Figure 3-9: Illustration of NAST-M's antenna horns and the resulting polarization. Each measures a single linear polarization that is perpendicular to the long section of the waveguides, which are represented by rectangles. The illustration is in the same orientation as the image in the upper right-hand corner of Figure 3-4, but is not to scale.

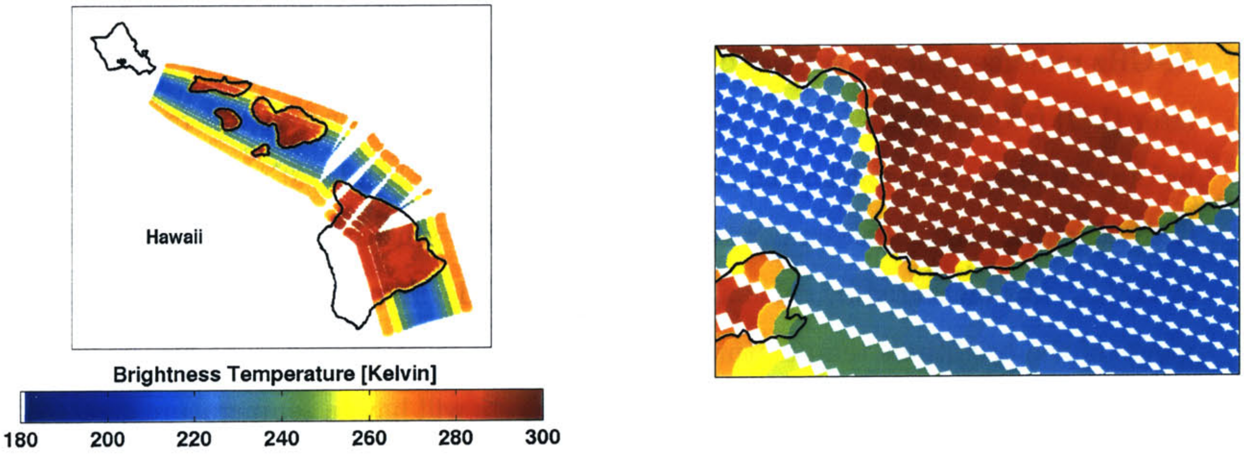

(a) Lower Hawaiian Islands

(b) Close up view of West Maui's southern coastline.

Figure 3-10: NAST-M brightness temperature data within antenna footprints along with island boundaries.

Table 3.1: Spectral Description of the NAST-M 54-GHz System

54-GHz System SSB (LO = 46 GHz) τ = 100 msec				
Chan.	RF (GHz)	IF (MHz)	BW (MHz)	ΔT_{rms}
1	50.21-50.39	4210-4390	180	0.1879
2	51.56-51.96	5560-5960	400	0.1274
3	52.6-53	6600-7000	400	0.1084
4	53.63-53.87	7630-7870	240	0.1474
5	54.2-54.6	8200-8600	400	0.1248
6	54.74-55.14	8740-9140	400	0.1528
7	55.335-55.665	9335-9665	330	0.1754
8	55.885-56.155	9885-10155	270	0.2321

northwestern portion of Figure 3-10(a), the surface swath width correctly increases. Channel one of the 54-GHz system allows easily comparison of the land-sea boundaries. This code will be very useful in imaging convective cells, where accurate areal metrics will be used in storm-wide parameter retrievals.

3.2.2 Previous Instrumentation

The original NAST-M suite, which includes the 54- and 118-GHz systems, is presented in [7, 8]. A brief portion is repeated here for convenience and continuity. The 54-GHz radiometer has a single-sideband superheterodyne receiver with a local oscillator (LO) frequency at 46 GHz. Table 3.1 is a list of the 54-GHz system's frequencies before and after downconversion, along with the resulting bandwidths. Also included is the channel brightness temperature sensitivity. The sensitivity of the instrument, or ΔT_{rms}, was measured by calculating the standard deviation of one of the measurements of the brightness temperature on the heated calibration load. The heated load is the "worst case" scenario since no practical targets will have a temperature greater than the heated load, *i.e.*, the heated load has the highest antenna temperature. The values of ΔT_{rms} in Table 3.1 and Table 3.2 were calculated from a flight during the WINTEX deployment in March 1999. The 118-GHz radiometer is a double-sideband superheterodyne receiver with an LO frequency at 118.75 GHz. Table 3.2 lists the passbands for the 118-GHz system. Figure 3-11 plots the nadir weighting functions

Table 3.2: Spectral Description of the NAST-M 118-GHz System

118-GHz System DSB (LO = 118.75 GHz) τ = 100 msec					
Chan.	LSB (GHz)	USB (GHz)	IF (MHz)	BW (MHz)	ΔT_{rms}
1	114.75-115.75	121.75-122.75	3000-4000	1000	0.1922
2	115.95-116.45	121.05-121.55	2300-2800	500	0.2436
3	116.45-116.95	120.55-121.05	1800-2300	500	0.2066
4	116.95-117.35	120.15-120.55	1400-1800	400	0.2679
5	117.35-117.75	119.75-120.15	1000-1400	400	0.3002
6	117.75-118.15	119.35-119.75	600-1000	400	0.3814
7	118.15-118.45	119.05-119.35	300-600	300	0.6080
8	118.45-118.58	118.92-119.05	170-300	130	0.8930
9	118.58-118.68	118.82-118.92	70-170	100	1.1545

for the 54- and 118-GHz systems using the U.S. 1976 standard atmosphere and the Millimeter-wave Propagation Model [42] assuming a surface emissivity of unity. Both spectrometers view O_2 lines or line.

3.2.3 New Instrumentation

Figure 3-12 presents blowups of the zenith opacity shown in Figure 3-3 around the frequency of interest for the two new spectrometers. Each spectrometer's channels are marked in the figures. The following sections introduce the new spectrometers with block diagrams and photos. Figure 3-6 is a picture of both new spectrometers installed into the NAST-M suite.

183-GHz Spectrometer

One of the two new spectrometers is centered around the water vapor absorption line at 183.31 GHz (183-GHz system). The principal purpose of the 183-GHz system is to enable the NAST-M instrument to retrieve humidity profiles and precipitation, along with the temperature profiles. The receiver front end was designed at Millitech under the Millimeter-Wave Products Division. On campus, the receiver was completely repackaged to endure the harsh environment of the high-altitude platforms. Figure 3-14(a) shows the receiver front end before and after reconfiguration.

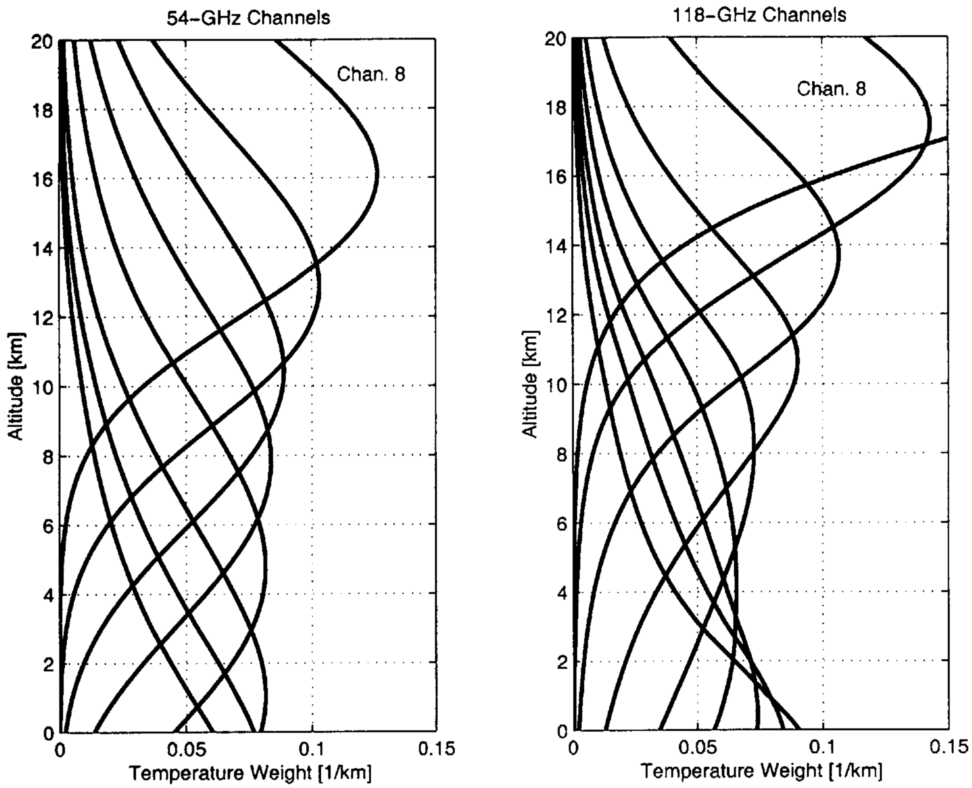

Figure 3-11: Nadir temperature weighting functions with a blackbody surface.

The 183-GHz receiver front end is a double-sideband total-power radiometer. Figure 3-13 is a block diagram for the 183-GHz system. The local oscillator (LO) source is a dielectric resonance oscillator (DRO). The DRO and the RF amplifiers are thermally isolated and temperature controlled by thermoelectric controllers (TEC). The PID controller used to control and drive the TECs was a Wavelength Electronics MPT-2500. The RF amplifiers are temperature controlled to reduce gain fluctuations from temperature changes at 60,000 feet ($\sim -40°C$). The DROs have a frequency-temperature coefficient of 3 ppm/degree C, but the temperature control will minimize any shift in DRO frequency. Some of the LO chain uses MMIC technology, which has a strict supply voltage requirement. A classic crowbar circuit and power regulator were used to maintain the power requirements for the MMIC and other components. Pictures of installed circuits, LO plate, and MMIC are in Figure 3-14(b).

The 183-GHz receiver front end downconverts the signal to an IF frequency of 0.7 to 12 GHz, which is then filtered to six channels with bandwidths from 500 MHz to

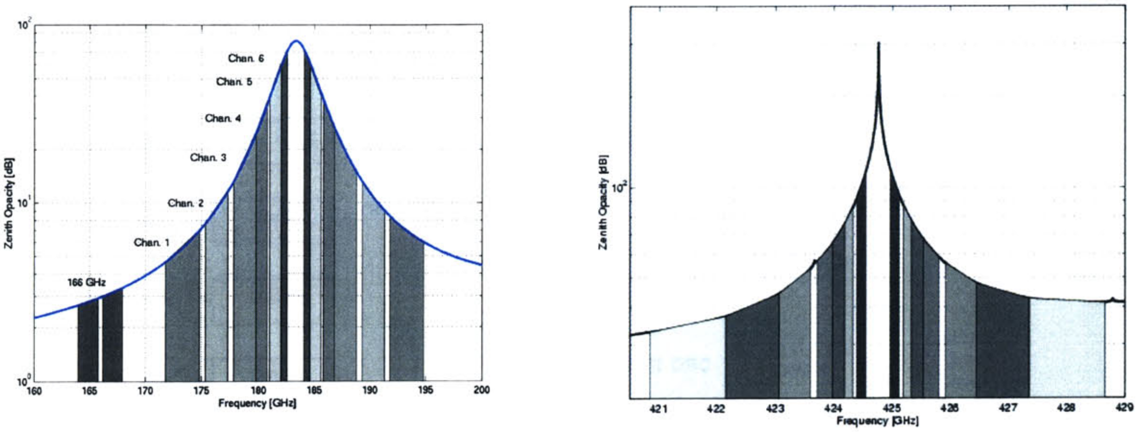

(a) 183-GHz System

(b) 425-GHz System

Figure 3-12: The new spectrometer's passbands against zenith opacity.

3 GHz. The spectral response is overlaid on the zenith opacity in Figure 3-12(a) and the resulting temperature weighting functions are plotted as a function of altitude and water vapor burden in Figure 3-15. The 183-GHz system's water vapor-burden weighting functions peak at 15, 8, 4.5, 2.5, 1.2, and 0.5 mm. The most transparent channels of the 118-GHz system and the 425-GHz system supplement the water vapor-burden peaks with peaks at 50 mm and 3 mm, respectively. The RMS sensitivities of the 183-GHz system range from 0.4 to 0.8 Kelvin. The spectral response and sensitivities are summarized in Table 3.3. The sensitivities were calculated by computing the standard deviation of the calibrated brightness temperatures on the heated load during mid-flight. The receiver temperature was determined from measurements of the radiometer's output power when it viewed LN_2-submerged and ambient Eccosorb targets. An IF filter limited the output frequencies to be between 500 to 12,000 MHz, and the resulting receiver temperature was 3000 K.

The 183-GHz system has a computer-controlled RF switch in order to change the LO frequency between DROs. The other LO frequency was to "look" at a transparent window next to the 183.31 GHz absorption line at 166 GHz. Unfortunately, at the present time the Millitech mixer has had difficulty optimizing an acceptable noise temperature at both LO frequencies. Only the 183 LO is operational.

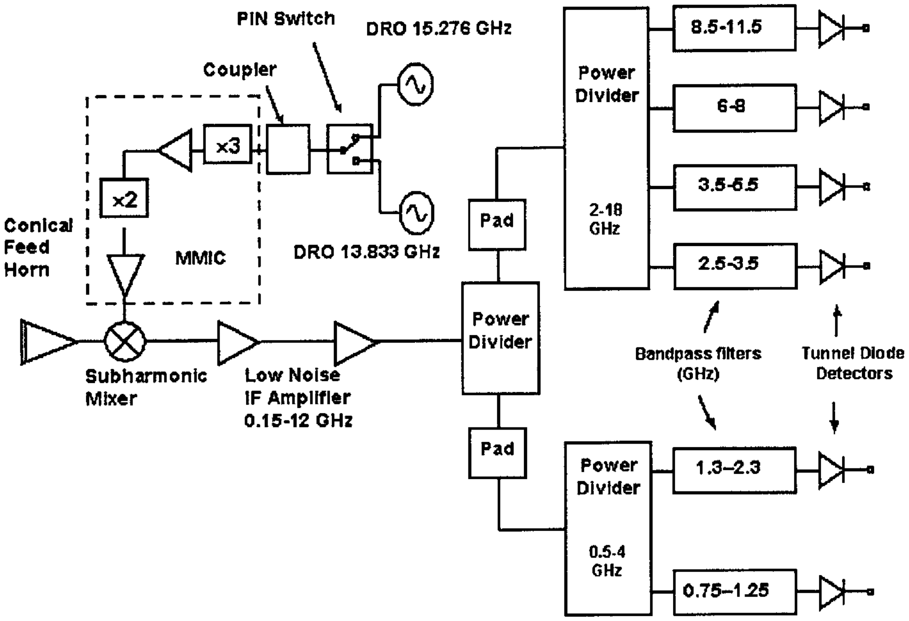

Figure 3-13: Block Diagram of the 183-GHz Spectrometer

Table 3.3: Spectral description of the NAST-M 183-GHz system

183-GHz System DSB (LO = 183.31 GHz) τ = 100 msec						
Chan.	CF(GHz)	LSB (GHz)	USB (GHz)	IF (MHz)	BW (MHz)	ΔT_{rms}
1	10	171.81-174.81	191.81-194.81	8500-11500	3000	0.38
2	7	175.31-177.31	189.31-191.31	6000-8000	2000	0.47
3	4.5	177.81-179.81	186.81-188.81	3500-5500	2000	0.54
4	3	179.81-180.81	185.81-186.81	2500-3500	1000	0.58
5	1.8	181.01-182.01	184.61-185.61	1300-2300	1000	0.79
6	1	182.06-182.56	184.06-184.56	750-1250	500	1.5

Based on the PTOST 01Mar03 flight.

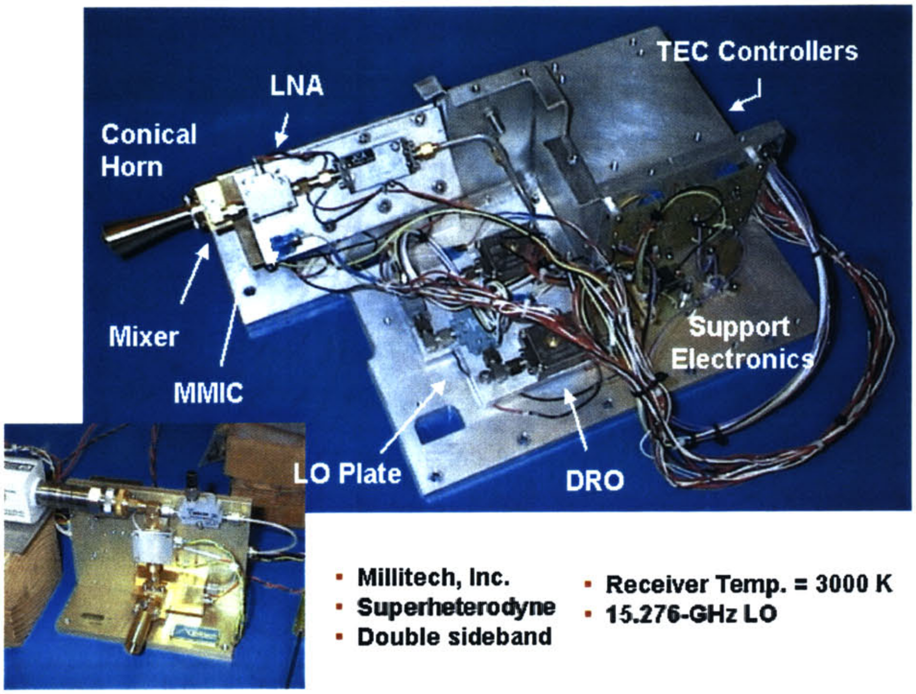

- Millitech, Inc.
- Superheterodyne
- Double sideband
- Receiver Temp. = 3000 K
- 15.276-GHz LO

(a) Overview with before (bottom left) and after (top) pictures

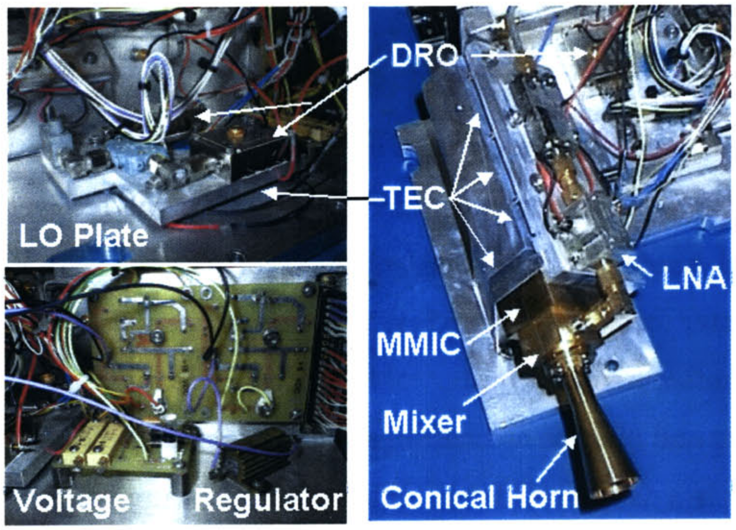

(b) Close up of key components

Figure 3-14: Pictures of the 183-GHz receiver front end.

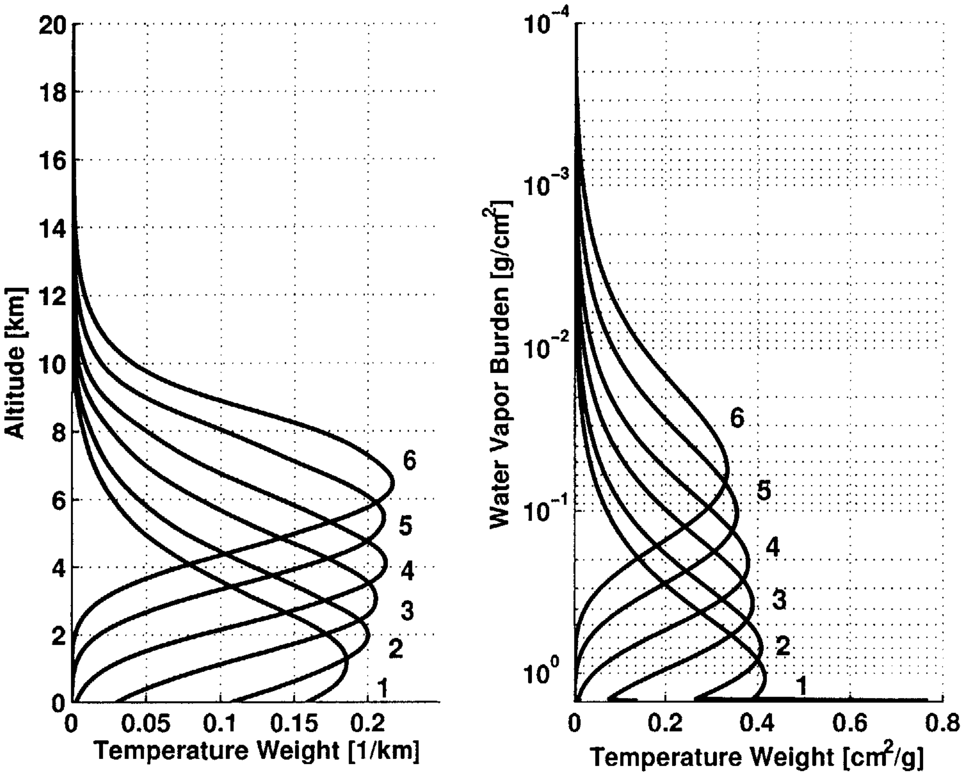

Figure 3-15: 183-GHz temperature weighting functions as a function of water vapor burden

425-GHz Spectrometer

A block diagram of the 425-GHz radiometer system is shown in Fig. 3-17(a) and the passbands are shown in Figure 3-12(b). The 425-GHz system is also a total-power spectrometer with a double-sideband superheterodyne receiver. The receiver was designed and bench-tested at the University of Virginia and Virginia Diodes, Inc. [30]. The Center for Space Research at the Massachusetts Institute of Technology designed and manufactured the housing for the 425-GHz receiver. A labeled picture of the receiver before and after the reconfiguration is in Figure 3-17(b). The LO for the 425-GHz receiver is a Gunn oscillator, which is temperature controlled to maintain its frequency. The Gunn is set at 106.19 GHz and a varactor doubler upconverts the frequency, which then drives the subharmonic mixer. The 425-GHz receiver has a separate subharmonic mixer for measuring the LO frequency. Any deviations of the Gunn oscillator from the absorption line frequency can cause the opaque temperature

Table 3.4: Spectral Description of the NAST-M 425-GHz System

425-GHz System DSB (LO = 424.76 GHz) $\tau = 100$ msec						
Chan.	CF(GHz)	LSB (GHz)	USB (GHz)	IF (MHz)	BW (MHz)	ΔT_{rms}
1	3.250	420.86-422.16	427.36-428.66	2600-3900	1300	0.49
2	2.150	422.16-423.03	426.46-427.36	1700-2600	900	0.47
3	1.430	423.06-423.60	425.92-426.46	1160-1700	540	0.58
4	0.910	423.72-423.98	425.54-425.80	780-1040	260	0.85
5	0.680	423.98-424.18	425.34-425.54	580-780	200	0.96
6	0.505	424.18-424.33	425.19-425.34	430-580	150	1.2
7	0.285	424.40-424.55	424.97-425.12	210-360	150	1.2

Based on the PTOST 01Mar03 flight.

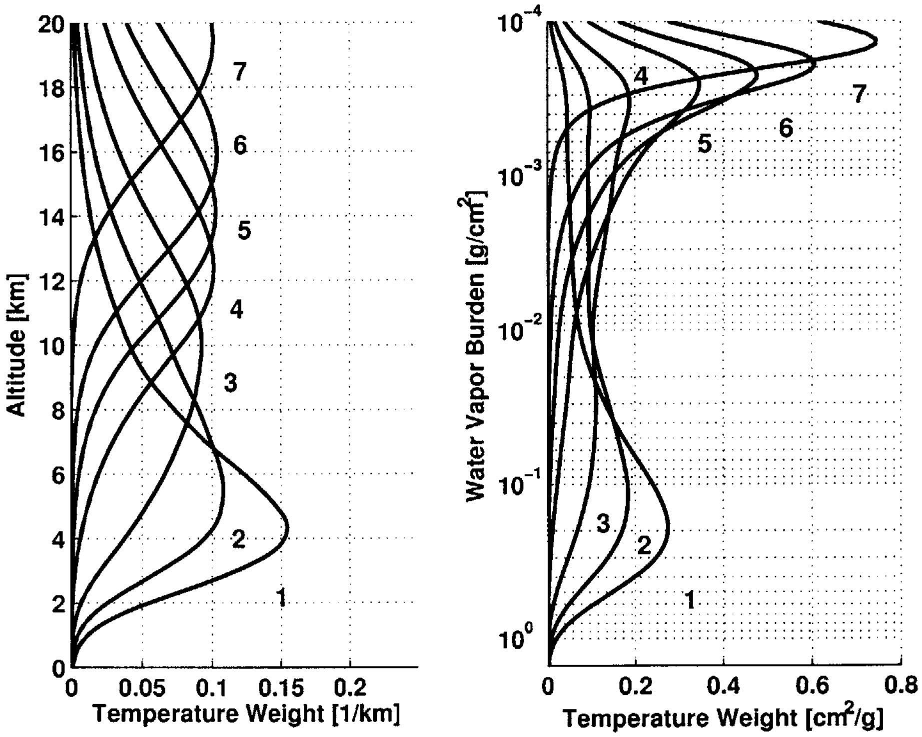

Figure 3-16: 425-GHz Spectrometer's nadir temperature weighting functions as a function of altitude and water vapor burden.

weighting functions to have two peaks instead of the desired bell shape.

The 425-GHz system has an IF frequency ranging from 270 MHz to 3.9 GHz, which is filtered to seven channels with bandwidths of 150 MHz to 1.3 GHz, and the RMS sensitivities range from 0.4 to 1 Kelvin. The values are summarized in Table 3.4. The sensitivities were calculated by computing the standard deviation of the calibrated brightness temperatures on the heated load during mid-flight. The receiver temperature was determined from measurements of the radiometer's output power when it viewed LN_2-submerged and ambient Eccosorb targets. An IF filter limited the output frequencies to be between 200 to 4,000 MHz, and the resulting receiver temperature was 4000 K. The 425-GHz system has temperature weighting functions with peaks at 600, 500, 300, 200, 150, 100, and 60 millibar. Temperature weighting functions for the 425-GHz system are shown in Fig. 3-16. The 425-GHz channels furthest from the absorption line are sufficiently sensitive to water vapor because of the water vapor continuum that they do not sense the surface. For example, channel one of the 425-GHz system has a weighting function very similar to channel four of the 183-GHz system, except that the 425-GHz channel is more sensitive to hydrometeors; it typically peaks near 4 km or 0.2 g/cm^2.

3.3 Calibration

Instrument calibration involves finding the most accurate and concise method to quantify the raw measurement data. For NAST-M, the calibrated data is the target brightness temperature, with the "target" being the atmospheric brightness temperature within the antenna pattern. The raw data comes from the analog output voltage of the tunnel diode detectors, which has been quantized by the A/D converter. Due to the design of a total-power radiometer, the output voltage, and therefore the counts, are related to the brightness temperature in an affine manner (assuming instrument linearity), but the gain and baseline (slope and y-intercept) are unknown and constantly changing. This section explains the technique and necessary background to calibrate the NAST-M data. The two aircraft platforms made it necessary to have two

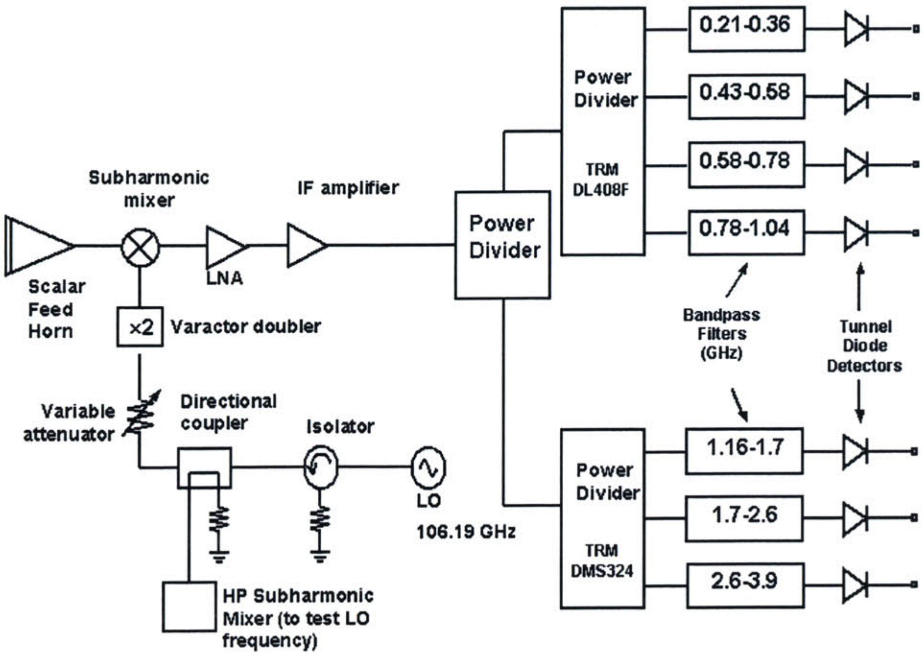

(a) Block Diagram

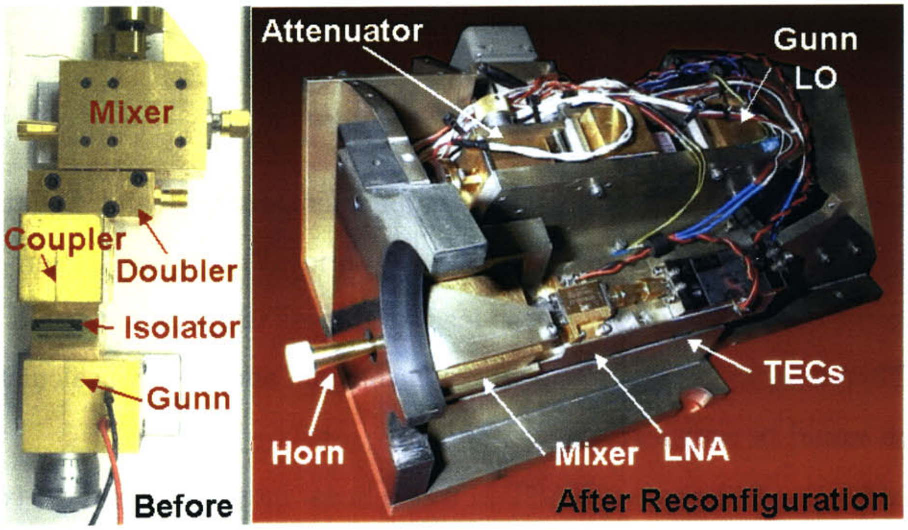

(b) Receiver Front End

Figure 3-17: Picture and block diagram of the 425-GHz Spectrometer.

calibration techniques. The instrument configuration on the Proteus limited the calibration to a two-point technique, while the ER-2 allowed a more desirable three-point calibration technique.

3.3.1 Ideal Two-point Calibration

We estimate the gain and baseline from the calibration load measurements in order to calibrate the radiance measurements.

$$\hat{T_b}(ch_i, sc_j, sp_k) = b(ch_i, sc_j, sp_k) + g(ch_i, sc_j, sp_k) \cdot c(ch_i, sc_j, sp_k) \tag{3.1}$$

$\hat{T_b}$ is the abbreviation for the estimated brightness temperature. The b is called the bias, baseline, or y-intercept, and g is the gain or slope. $\hat{T_b}$, c, g, and b are all discrete functions of channel (ch_i $i \in \{1, \ldots, 30\}$), scan index (sc_j $j \in \{1, \ldots, max.\ scan\}$), and spot index ($sp_k$ $k \in \{1, \ldots, 25\}$). If only two calibration loads are used, which is the minimum information needed to determine a gain and baseline, then the simple formulas are:

$$gain = \hat{\mathrm{g}} = \frac{T_H - T_A}{C_H - C_A}, \tag{3.2}$$

$$baseline = \hat{\mathrm{b}} = T_A - gain \cdot C_A \tag{3.3}$$

where T_H and T_A are the hot and ambient load temperatures and C_H and C_A are the hot and ambient load radiance counts. In an ideal instrument, there would be no instrument noise and the calibration load brightness temperature would be known exactly. Therefore, we would have no error in the gain and baseline calculations, and calibration would be very straight forward.

The calibration technique of NAST-M uses a linear interpolation of the two nearest calibration points, which is the best of the simple techniques used to reduce the affect of $1/f$ noise, but there are optimal techniques [48]. In this application, the optimal technique did not offer significant improvement [8]. The linear interpolation technique gives a weight function ($w(t)$ from Equation 2.3) that is triangular in shape with the peak at the spot being calibrated and the two corners at the two nearest calibration points. The counts of the calibration loads are filtered with a triangular filter of length seven before the interpolation is performed.

3.3.2 Three-point Calibration

While the NAST-M is on board the ER-2, the calibration can use three points. The resistive thermal devices (RTD) from the onboard loads give the temperature of two calibration points, and an estimate of the zenith-view brightness temperature comes from the radiative transfer equation (RTE). The three radiance counts are coupled with their related brightness temperatures to give three calibration points in which the linear relationship between counts and brightness temperature can be determined.

Typically, a straight line solution that goes through all three noisy calibration points can not be found. In linear algebra terms, the A matrix (from Equation 2.53) has a solution in the two-point case but has no solutions in the overconstrained case. The technique of linear regression determines the gain and baseline that minimizes the mean squared error between estimated brightness temperature and actual brightness temperature for the three calibration points.

In statistical terms, the variable that is estimated is called the response, and the variable that is used to estimate the response is called the predictor. In this case, the counts (c) are the predictor, and the brightness temperature is the response variable. Linear regression of counts to brightness temperature is greatly complicated by the fact that both the predictor and response have noise. Most rudimentary linear regression literature deals only with noise in the measurement of the response, not the predictor. Weisberg [68, p. 76] warns that care must be taken when trying to remove the noise in the predictor. If the application of the regression will use noisy inputs, which is true in this case because of the instrument noise, then it is better to do a linear regression with the noisy predictors than with noise-free predictors. In this case, the noise statistics for each of the calibration loads are not the same. The ΔT_{rms} that is intrinsic to radiometers is dependent on the target's temperature. Therefore, the noise variance is greater for the hotter calibration loads. The zenith view, which has a brightness temperature that is approximately $3\,K$ for the transparent channels, would have the least noise variance. Unfortunately, another error is introduced in the measurement of cosmic background radiation because the actual temperature profile above the aircraft is unknown. The U.S. 1976 standard atmosphere is used in the RTE model to estimate the brightness temperature seen through the zenith view. The hot load at $\sim 334\,K$ has the higher noise variance, followed by the ambient load ($\sim 240\,K$). Standard linear regression assumes the noise in the predictor variables are equal for each sample point. To circumvent this difficulty, weighted-least-squares is used instead of the usual least-squares solution. Weighted-least squares normalize the noise in each sample point before calculating the slope and y-intercept. Least-squares estimation minimizes the expected value of the error squared. The technique of weighted least squares can correct the error introduced by the unequal noise variance. When a system is overdetermined, the linear least squared solution is:

$$\hat{x} = (A^T A)^{-1} A^T b, \tag{3.4}$$

which is derived from

$$A^T A x = A^T b \quad \text{or} \quad Ax = b. \tag{3.5}$$

Here the symbols are for the general cases where x is a response vector and b is a predictor vector. Specific to the calibration of NAST-M data, the $Ax = b$ is:

$$\begin{bmatrix} C_{\mathrm{S}} & 1 \\ C_{\mathrm{A}} & 1 \\ C_{\mathrm{H}} & 1 \end{bmatrix} \begin{bmatrix} \hat{\mathrm{g}} \\ \hat{\mathrm{b}} \end{bmatrix} = \begin{bmatrix} T_{\mathrm{S}} \\ T_{\mathrm{A}} \\ T_{\mathrm{H}} \end{bmatrix} \tag{3.6}$$

or

$$\check{\mathbf{C}} \cdot \bar{x} = \bar{T}, \text{ instead of } \mathbf{A}\bar{x} = \bar{b}. \tag{3.7}$$

The mathematical explanation will continue with the $Ax = b$ notation, because it is the notation used in the reference [62].

Weighted least squares does a matrix multiplication of a weight matrix before a least square solution is found. The weight matrix allows certain calibration loads to gain more emphasis in the regression. For example, in the NAST-M calibration application, the calibration load with the least amount of variance should be weighed more than a noise calibration load. The weighted regression starts as:

$$WAx = Wb \quad \text{or} \quad A^T W^T W A x = A^T W^T W b. \tag{3.8}$$

Now the solution is:

$$x = (A^T W^T W A)^{-1} A^T W^T W b = (A^T C A)^{-1} A^T C b \text{ with } C = W^T W. \tag{3.9}$$

The optimal weight matrix, C, is the inverted covariance matrix of the error. The error is $e = b - Ax$, and the error covariance matrix is $\mathbf{V} = E[ee^T]$. A mathematical proof can be found in Strang [62, p. 144].

A thoughtful approach to the error covariance matrix starts with a simple noise analysis of the calibration regression. In the ideal case there is no instrument or RTD noise, the atmosphere above the aircraft is equal to the standard atmosphere, and the instrument is linear. Therefore, the error is be zero, and $\bar{x}$ is invertible in Equation 3.7. With the addition of instrument noise, the true atmosphere above the aircraft, and RTD noise, the system of equations becomes:

$$\begin{bmatrix} C_{\mathrm{S}} + \upsilon_{\mathrm{S}} & 1 \\ C_{\mathrm{A}} + \upsilon_{\mathrm{A}} & 1 \\ C_{\mathrm{H}} + \upsilon_{\mathrm{H}} & 1 \end{bmatrix} \begin{bmatrix} \hat{\mathrm{g}} \\ \hat{\mathrm{b}} \end{bmatrix} = \begin{bmatrix} T_{\mathrm{Z}} + \epsilon_{\mathrm{Z}} \\ T_{\mathrm{A}} + \epsilon_{\mathrm{A}} \\ T_{\mathrm{H}} + \epsilon_{\mathrm{H}} \end{bmatrix} \tag{3.10}$$

where υ is the additive noise of the radiometer, and ϵ_{A} and ϵ_{H} are the additive noise of RTDs. Also, ϵ_{H} consists of error due to the temperature gradient across the calibration load, which is absent on the ambient load ([8, pg. 96] or [36, pg. 54]). The noise on the zenith view calibration brightness temperature, ϵ_{Z}, is different from the other two loads. This noise represents the error in the simulation that arises from assuming the standard atmosphere above the aircraft. For any particular flight to which the calibration is applied, the ϵ_Z is a bias resulting from the difference between the actual temperature profile above the aircraft and the standard atmosphere. Statistics of this bias are determined from simulations between the TIGR radiosonde ensemble and the standard atmosphere in a manner very similar to Blackwell [8, pg. 93]. After replacing the matrixes and vectors with symbols, Equation 3.10 becomes:

$$(\check{\mathbf{C}} + \boldsymbol{\Upsilon}) \cdot \bar{x} = \bar{T} + \bar{\epsilon} \tag{3.11}$$

with

$$\boldsymbol{\Upsilon} = \begin{bmatrix} v_\mathrm{Z} & 0 \\ v_\mathrm{A} & 0 \\ v_\mathrm{H} & 0 \end{bmatrix} = [\bar{v}\ \bar{0}] \tag{3.12}$$

and

$$\bar{\epsilon} = [\epsilon_\mathrm{Z}\ \epsilon_\mathrm{A}\ \epsilon_\mathrm{H}]^T. \tag{3.13}$$

After some algebra, the error is:

$$\bar{e} = \bar{T} - \check{\mathbf{C}} \cdot \bar{x} = \hat{g}\bar{v} + \bar{\epsilon} \tag{3.14}$$

The RTDs are filtered before calibration, and the $\hat{g}\bar{v}$ term dominates. The variance of $\hat{g}\bar{v}$ is the ΔT_{rms} at that particular calibration load's temperature. The errors between calibration loads are independent and uncorrelated. In other words, the error covariance matrix is diagonal. Therefore, the error covariance matrix is:

$$\mathbf{V} = \begin{bmatrix} (\Delta T_{rms}^{\mathrm{zenith}})^2 + \delta_Z^2 & 0 & 0 \\ 0 & (\Delta T_{rms}^{\mathrm{ambient}})^2 + \delta_{gradient}^2 & 0 \\ 0 & 0 & (\Delta T_{rms}^{\mathrm{heated}})^2 + \delta_{gradient}^2 \end{bmatrix} \tag{3.15}$$

The additional error on the zenith port (δ_Z) comes from the standard deviation computed between the standard atmosphere and the TIGR ensemble. Note that there are techniques that estimate the profile above the aircraft using the brightness temperatures measured when viewing the atmosphere beneath the aircraft, but those techniques were not investigated here. The gradient standard deviations that were added to the ambient load was 0.2 K and 1.5 K to the heated load.

Proteus Two-point Calibration

As previously mentioned, NAST-M lacks a zenith port while flying aboard the Proteus aircraft. Therefore, the three-point calibration technique is unavailable, but some aspects that were introduced in the three-point calibration can still be used. Essentially, the three-point calibration is reduced to weighted two-point least-squares regression. For example, the error covariance matrix becomes:

$$\mathbf{V} = \begin{bmatrix} (\Delta T_{rms}^{\text{ambient}})^2 + \delta_{gradient}^2 & 0 \\ 0 & (\Delta T_{rms}^{\text{heated}})^2 + \delta_{gradient}^2 \end{bmatrix}. \tag{3.16}$$

3.3.3 Calibration and Validation

Validation consisted of laboratory experiments and comparisons between radiometric and simulated data. Laboratory measurements revealed differences between the estimated temperatures of the onboard calibration loads and independently-calibrated measurements of the onboard calibration loads. Corrections were determined and validated through measurements of a target submerged in liquid nitrogen (see Section 3.4.2), and further validated in the NAST-M validation chapter (see Chapter 4). In a separate experiment, the optimal view-angle of the calibration loads was confirmed by stepping through all angles and choosing the angle with the maximum brightness-temperature value.

To validate the NAST-M calibration, dropsondes and radiosondes measured the temperature and humidity profiles in approximately the same area and time interval. These profiles were entered into a software program written to simulate brightness temperatures specifically for the NAST-M instrument; it used the Millimeter-wave Propagation Model [42]. These simulated brightness temperatures were then compared with the actual coincidental brightness temperatures measured by the instrument.

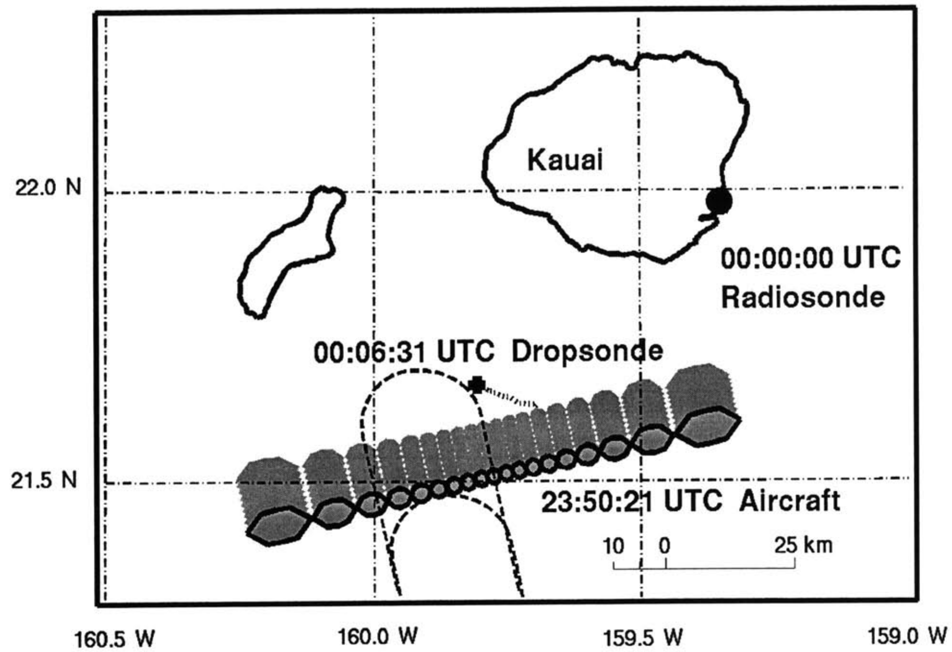

Figure 3-18: A map with an example of the aircraft's position in relation to dropsonde and radiosonde release points. Also included are the UTC times of these releases, the aircraft's time of overpass, and the dropsonde's trajectory.

Fig. 3-18 is a flight map illustrating a typical profile comparison. The footprints of the radiometric data are plotted, and the footprints of the last scan are outlined in black. The footprints were projected from the altitude of the ER-2 to a flat surface, taking into account the scan angle. The dropsonde drop site is plotted, along with the trajectory of the dropsonde, as it fell from an altitude of 14 km. To supplement the atmospheric data above the dropsonde, data was used from a radiosonde launched on the island of Kauai, Hawaii, approximately 100 km away. Ten sequential spots at each angle were averaged to reduce the effect of noise, and then validation is done by subtracting this averaged brightness temperature from the simulated brightness temperature calculated with the radiosonde/dropsonde profiles.

Due to errors in position, time, assumed ancillary simulation inputs (*e.g.*, surface temperature), and other sources, a single profile comparison can be misleading. Ideally, as many profile comparisons as possible are used and their statistics are calculated. The results for two deployments are presented in Chapter 4.

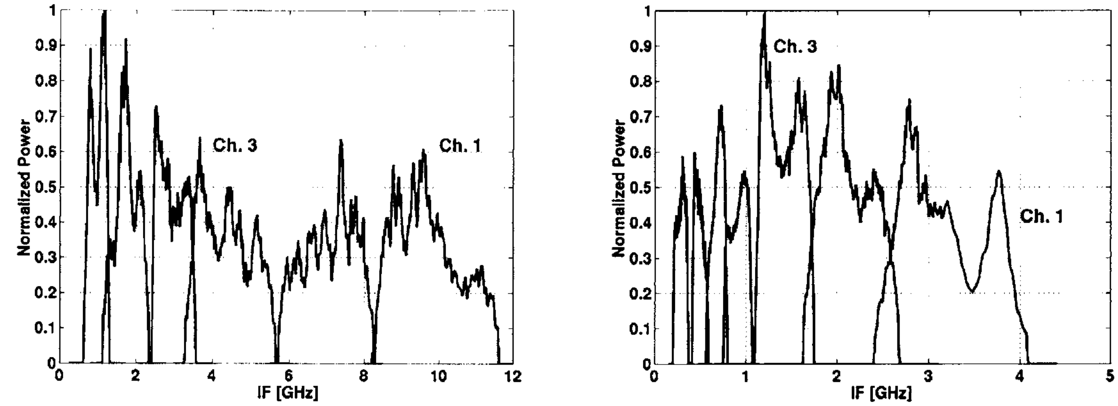

(a) 183-GHz passbands

(b) 425-GHz passbands

Figure 3-19: Passbands measurements of the two new spectrometers.

3.4 Laboratory Measurements

After the recent deployments of CRYSTAL-FACE and THORpex, several laboratory experiments were done to determine the accuracy of the new spectrometers.

3.4.1 Passband Measurements

Accurate measurement of the frequency response was needed for validation purposes in Chapter 4 and Section 3.3.3. In the laboratory, the reflector viewed a room temperature target as a source and a spectrum analyzer measured the power spectral density for each of the channels. The data points were saved to a file and loaded into Matlab. Figure 3-19 has the normalized frequency responses measured for the 183-GHz and 425-GHz systems.

3.4.2 Calibration Load Evaluation

This experiment used the NAST-M radiometers and independent calibration sources to measure the brightness temperature of the onboard calibration loads. The independent measurements of the calibration load's brightness temperature were then compared with the onboard temperature sensors. Any bias could then be removed in

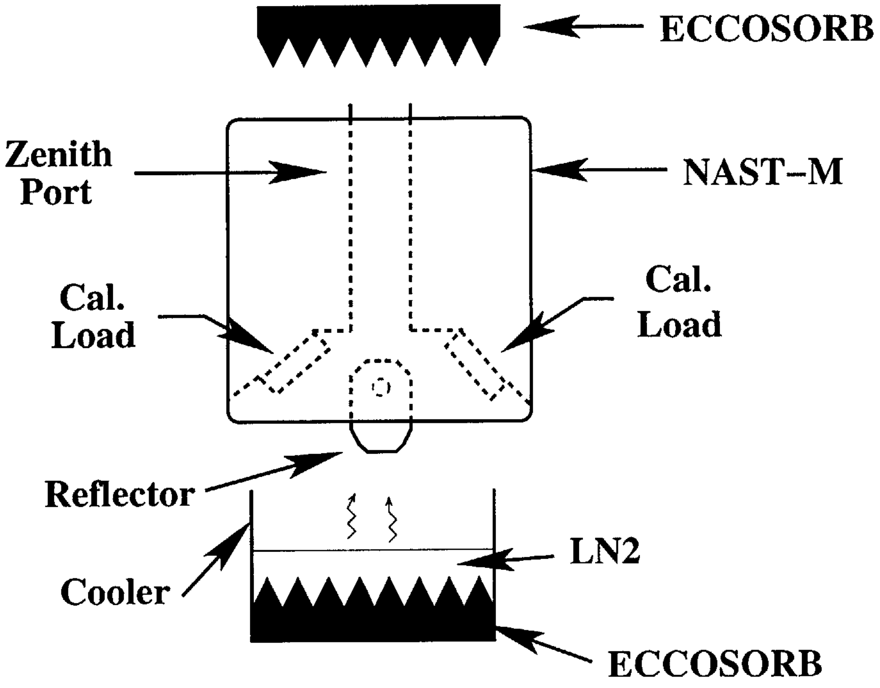

Figure 3-20: Illustration of calibration.

the standard NAST-M calibration routine.

The typical scan pattern was modified to periodically step through approximately twenty angles viewing the onboard calibration loads. In between these load-image sweeps, the scan pattern viewed two external calibration loads. One was a single piece of Eccosorb situated on top of the zenith port with a temperature sensor placed about half an inch into the target. The temperature of this ambient load was measured by a Lakeshore silicon-diode temperature sensor, but when the Lakeshore temperature was compared with the measurement from the onboard ambient load's temperature and there was a six Kelvin difference. This is not surprising because the onboard load's temperature is affected by heat dissipated throughout the instrument, but the radiometric counts only revealed a four Kelvin difference between the internal and external ambient loads. The first option assumes that the error comes from a combination of the Lakeshore sensor problems and because of temperature gradients on the external Eccosorb target. Therefore, two Kelvin were added to the Lakeshore temperature reading in order to reduce the six Kelvin temperature difference to a four Kelvin difference. The other option would be subtract two degrees from both the onboard heated and ambient calibration loads. This option was less persuasive because of the extensive calibration of the NAST-M temperature measurement system [8, pg. 207], but the onboard temperature system could use a recalibration. The rest of this calibration used the adjusted temperature of the external ambient load (*i.e.*, the first option). In Chapter 4, validation of the calibration revealed that the comparison between simulated and actual brightness temperatures was improved by using the Lakeshore-measured temperature, *i.e.*, the second option, which confirms the need to recalibration NAST-M's temperature measurement system. The second external load was an Eccosorb target submerged in liquid nitrogen. The temperature of the LN_2 load was modeled as:

$$T_{ln} = \rho \cdot T_{amb} + (1 - \rho) \cdot T_{bp}. \tag{3.17}$$

The T_{ln} is the estimated temperature of the liquid nitrogen target, T_{amb} is the ambient background temperature of the room (295 Kelvin), T_{bp} is the boiling-point temperature of liquid nitrogen (77 Kelvin), and ρ is the surface reflectivity of the liquid nitrogen-air boundary (0.008). Figure 3-20 is an illustration of the experiment setup. There were three 100-msec views of the external ambient load through the zenith port, nineteen 1.8° steps past the NAST-M heated load, three measurements of the LN_2 load at nadir, three more LN_2 views after a full 360° rotation, and finally 22 1.8° steps pass the NAST-M ambient load. The 360° rotation was a matter of coding necessity, and the LN_2 measurements closest in time to the NAST-M load measurements were used in the calibration.

Figure 3-21 are the results of using external LN_2-submerged and ambient Eccosorb targets to measure the brightness temperatures of the onboard heated and ambient calibration loads, respectively. In Figure 3-21(a), the red horizontal line is the temperature that the calibration load's resistive temperature devices (RTDs) measured the load to be. There are seven RTDs on the heated load, and they are weighted as derived in [8, pg. 96]. The vertical black lines represent the angles that the standard scan pattern views the calibration loads. The solid line was intended for the 54-GHz

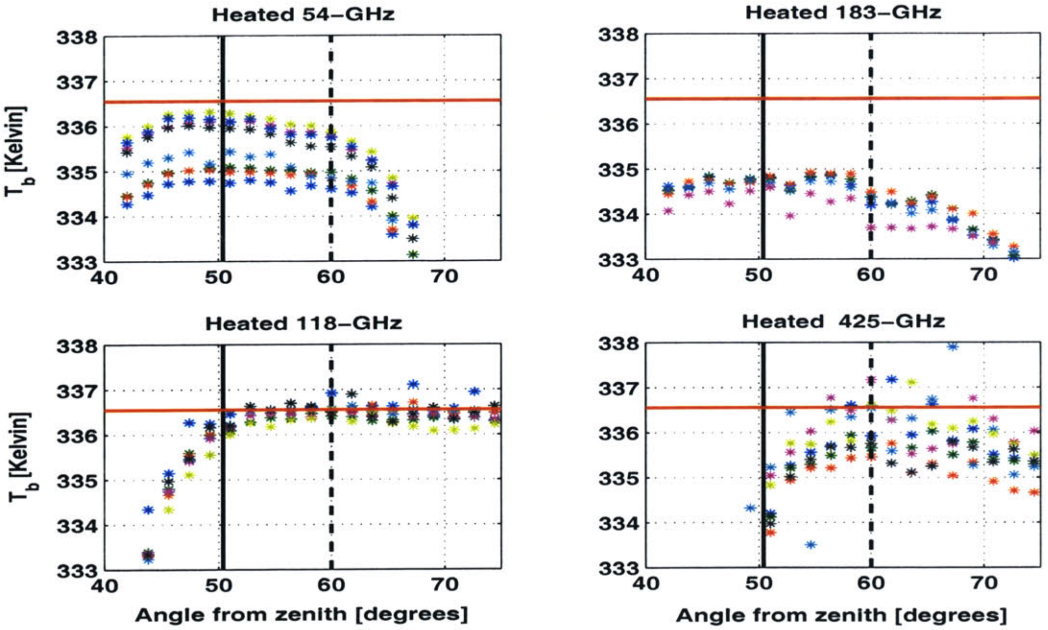

(a) Externally calibrated T_b image of the heated load: Red line is the NAST-M's measurement of the internal heated load's temperature. The solid black line is the angle that 54-GHz system uses to measure the heated load temperature, while the black dashed line is the angle the other systems use.

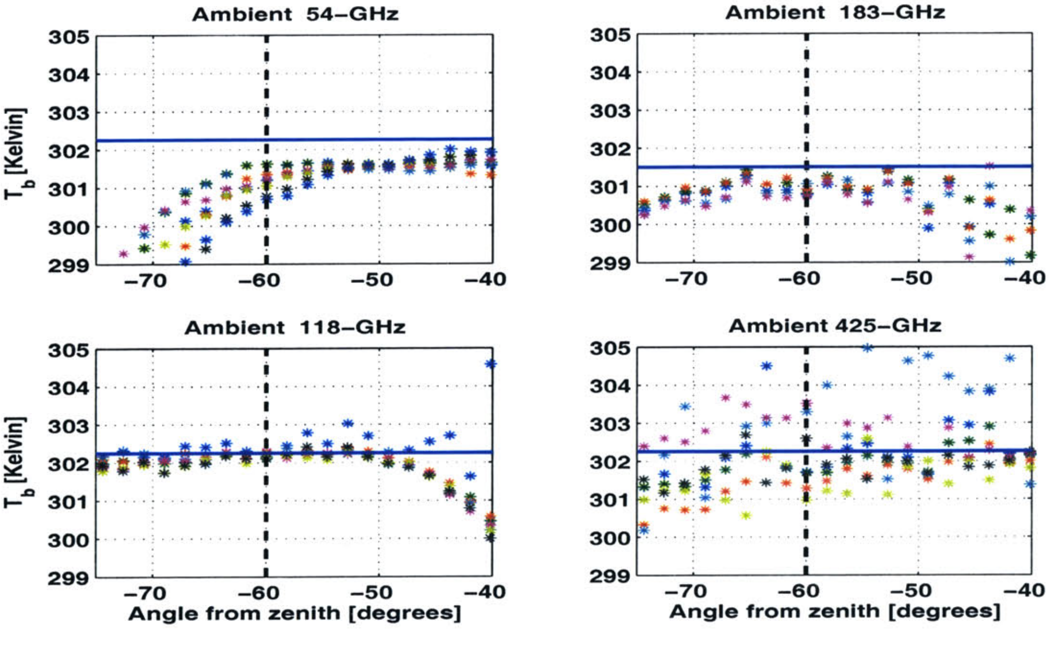

(b) Externally calibrated T_b image of the ambient load: Blue line is the NAST-M's measurement of the internal ambient load's temperature. The black dashed line is the angle used by all spectrometers to measure the ambient load's temperature.

Figure 3-21: Results from imaging the NAST-M calibration loads.

system, and the dashed line was to be used by the other three spectrometers. These angles were determined from previous imaging of the calibration loads at 54 and 118 GHz. The angles were chosen because they were at the maximum brightness temperature of the two spectrometers. The 54-GHz channels have a problem with the antenna beam spilling over the calibration load's surface [8, pg. 211]. The spillover was quantified for each load and for all 54-GHz channels. The effects of the spillover can be seen in Figure 3-21(a). The spillover reduced the 54-GHz channels' brightness temperatures varying degrees depending on the amount of spillover. This phenomena is well documented in Blackwell [8] and will not be discussed further here. The routine calibration technique does correct for 54-GHz antenna-beam spillover.

In Figure 3-21(b), the blue horizontal line is the temperature that the calibration load's RTDs measured the load to be. The five RTDs on the ambient load are averaged together. Again, the vertical black lines represent the angle that the standard scan pattern viewed the ambient calibration load. All of the spectrometers used the same ambient-load angle.

For the 183- and 425-GHz systems only, a bias was determined that would adjust the calibration. The results from Figure 3-21 are converted to a bias that is added to the calibration load's temperatures. In other words, it moves the red and blue lines in Figure 3-21 down to the brightness temperatures. In all cases, the bias is a negative value, and the effect on the regression between counts and calibrated brightness temperatures is illustrated in Figure 3-22. The difference between the heated and ambient load determines the amount of leverage at the LN_2 brightness temperature. T^A_{bias} and T^H_{bias} are given in Table 3.5. The source of the discrepancy is mostly likely nonlinearity of the instrument, and further analysis will be done in another publication.

3.4.3 Liquid Nitrogen Measurements

A common validation technique involves measuring the brightness temperature of Eccosorb submerged in liquid nitrogen, which is lowered to 77 K. The apparatus setup has several important points. The liquid nitrogen level must always cover the

Table 3.5: Calibration Load Bias Adjustment

Ch. No.	183 GHz				425 GHz			
	heated load (K)		ambient load (K)		heated load (k)		ambient load (K)	
	1st	2nd	1st	2nd	1st	2nd	1st	2nd
1-6	-2	-4	-0.5	-2.5	-1	-2.75	0.0	-2.0
7	N/A	N/A	N/A	N/A	"	"	"	"

1st and 2nd refer to calibration options described in text

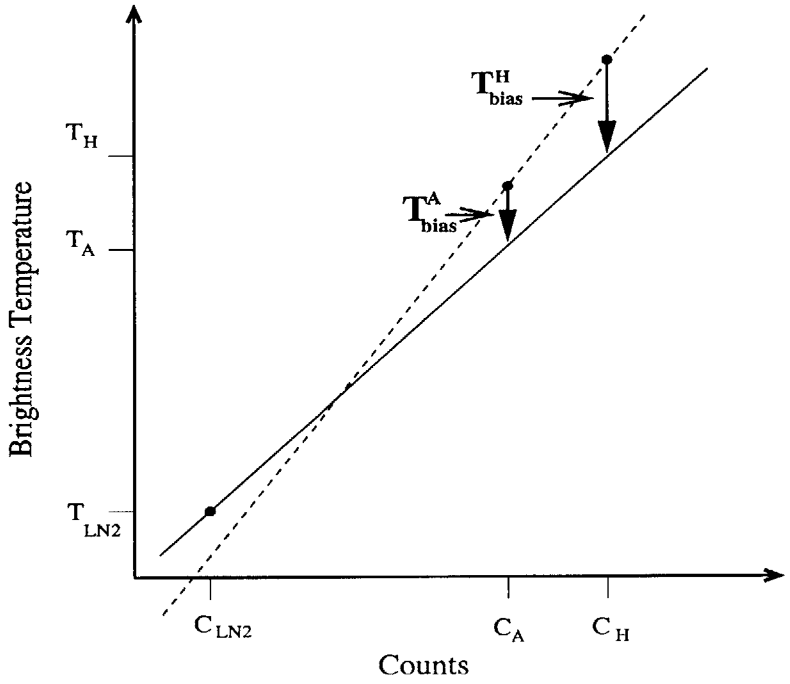

Figure 3-22: Illustration of the bias adjustment.

Eccosorb, especially the tips. The insulated cooler and Eccosorb were not quite big enough to contain all of the spurious sidelobes, so metallic plates were placed along the outsides of the cooler in an attempt to fill the entire antenna pattern with the submerged target. This adjustment was noticeable in the radiometric data.

The radiometric data viewing the nadir LN_2 target was calibrated using the internal calibration loads and the corrections in Table 3.5. The results are presented in Figure 3-23. The 118-GHz channels measured the brightness temperature to be around 79 K, and the estimated brightness temperature of the target, when modeling the LN_2-air surface to have a reflectivity of 0.008, is 78.75 K. This is not surprising considering there is negligible spillover on the 118-GHz system. The 54-GHz system ranges from 72 to 84 K, and the differences are credited to the antenna-beam spillover, which was not corrected for in Figure 3-21. With the corrections from Table 3.5, the 183-GHz system measures the LN_2 to be approximately 80 K. The 425-GHz system has very high noise during ground measurements, which are symptoms of the LO drift discussed in Chapter 4. The noise caused the LN_2 measurements to fluctuate in Figure 3-23.

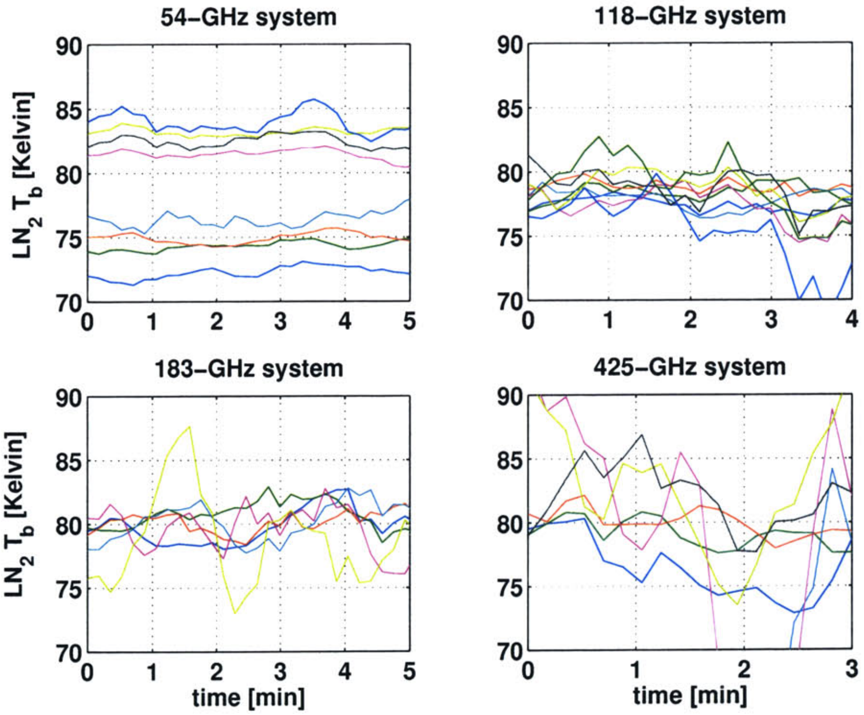

Figure 3-23: Calibration corrected measurements of LN_2.

Chapter 4

Field Deployment Validation

This chapter covers the validation of NAST-M flight data for two recent deployments, and they are the Cirrus Regional Study of Tropical Anvils and Cirrus Layers-Florida Area Cirrus Experiment (CRYSTAL-FACE 2002) and the Pacific THOR*pex* (THe Observing-system Research and *p*redictability *ex*periment) Observing System Test (PTOST 2003). The 183-GHz system was operational during the International H2O Project (IHOP 2002), but the validation of this deployment will be presented in a future publication. The Atlantic THORPEX Observing Systems Test (ATOST) finished in December of 2003 and will also be presented in a future publication.

The deployments presented here have three validation days each, in which flight data is compared with simulated brightness temperatures from coincidental measurements of the atmospheric profile. The mean and standard deviation over all the profile comparisons are used to quantify the success of the calibration for each deployment.

4.1 CRYSTAL-FACE 2002

The deployment was based in Key West, FL for the month of July in 2002. NAST flew on the Proteus aircraft, and Table A.1 summarizes the CRYSTAL-FACE flights. The 183-GHz system was installed before CRYSTAL-FACE, but the 425-GHz system was installed during the deployment and yielded limited data. Table A.1 also has notes on the performance of NAST-M for each of the flights.

Table 4.1: CRYSTAL-FACE Atmospheric Profile Observations

No.	Distance difference [km]	Release time [UTC]	Time difference [min]	Maximum altitude [km]	Map symbol	Instrument type
July 9, 2002						
1	9.37	16:01	15	19.97	△	dropsonde
2	6.07	16:44	17	20.4	△	”
3	4.82	19:54	98	21.24	△	”
s	400-800	18:00	120	23	◇	radiosonde - KW
s	150-700	12:00	4-8 hrs	16	◇	radiosonde - Belize
July 13, 2002						
4	1.98	18:39	11	20.24	△	dropsonde
5	3.80	21:49	58	20.94	△	”
6	5.64	22:06	6	21.24	△	”
s	150-350	21:00	150	29.99	◇	radiosonde - Miami
July 19, 2002						
7	49.86	18:11	20	20.13	△	dropsonde
8	39.64	21:13	4	21.01	△	”
9	41.21	22:22	3	21.11	△	”
10	10.5	22:55	11	21.24	△	”
s	175-200	18:00	0.1-4 hrs	32.29	◇	radiosonde - Miami

NOTE: s marks a supplemental profile

4.1.1 Mission Overview

Six aircraft were involved in this deployment, and the flight paths of the various aircraft were coordinated to coincide with ground truth measurements (*e.g.*, radiosonde) or satellite overpasses. The official CRYSTAL-FACE website states (http://cloud1.arc.nasa.gov/crystalface/):

> CRYSTAL-FACE is a measurement campaign designed to investigate tropical cirrus cloud physical properties and formation processes. Understanding the production of upper tropospheric cirrus clouds is essential for the successful modeling of the Earth's climate. These measurements will be compared with ground based radars, satellites, and the results of advanced atmospheric models, in order to improve our ability to forecast future climate change. This large multi-agency experiment will unite seven NASA

centers, NOAA, National Science Foundation, Department of Energy, Office of Naval Research, U.S. Weather Research Program, Universities and other government weather researchers in this well coordinated study of our environment.

4.1.2 CRYSTAL-FACE Validation

Simulations using the radiative transfer equation and the atmospheric profiles allow the calibrated brightness temperatures to be validated. Differences are expected as the profiles aren't completely coincidental or colocated. Also, the simulation has some approximations like the planar-stratified atmosphere and Gaussian antenna beam, which introduce errors at the extreme angles. As mentioned in Section 3.3.3, multiple profiles are compared and the statistics are calculated to average the errors in order to reveal any systematic bias. The purpose of the validation is to validate the calibration techniques and to identify any calibration issues such as LO frequency drift. Auxiliary information such as sea surface temperature and surface wind speed can be gathered from buoys at the National Data Buoy Center (www.ndbc.noaa.gov).

Table 4.1 has the information on ten of the atmospheric profiles that were available during CRYSTAL-FACE for brightness temperature comparisons. The information includes the spatial and temporal proximity of the comparisons and any supplemental data from a nearby radiosonde. The validation days are outlined below. During CRYSTAL-FACE, the dropsondes were dropped from the ER-2 aircraft, while NAST was aboard the Proteus. This was advantageous for brightness temperature comparisons because the ER-2 typically flew three kilometers higher than the Proteus. Some radiosondes collect data as high as thirty kilometers, and the data at the highest altitude could be used to augment the atmospheric profile. This will be more pertinent for the PTOST deployment where the dropsondes were launched at 13 km.

The simulation used in this section is more detailed than the simulations used to train the estimators of geophysical parameters, where computation limitations require the simulation to have more approximations or simplifications. For this chapter, each channel had thousands of frequency sample points in order to model the passbands measured in the laboratory (see Section 3.4.1) accurately. Also, the antenna pattern was modeled at each "spot" as a Gaussian beam with seven sample points. The emissivity was calculated for each frequency and angle within the antenna beam. The profile's altitude resolution was 200 meters for the lowest twenty kilometers, then it had 1-km resolution up to 30-km altitude. The additional complexity in the simulation is necessary to make the simulation results as accurate as possible.

July 9, 2002

The flight on July 9^{th} took the ER-2 and the Proteus from Florida to the coastline of the Yucatan Peninsula and back. The ER-2 dropped six dropsondes as it flew out into the Caribbean Sea, but the Proteus only passed over three of the six drop sites. Figure 4-1 is a map with the Proteus flight path and the dropsonde-launch locations. Table 4.1 summarizes the distance and time differences between the launch site/time and the aircraft's overpass. The NAST-M video camera was inoperable during CRYSTAL-FACE, but the MODIS airborne simulator is a high-resolution imager sensitive to visible wavelengths, and it was used to determine clear-air conditions at the drop sites. The MODIS airborne simulator, which flew on the ER-2, showed low-altitude "popcorn" clouds at the northern drop sites, but it was mostly clear air. The lower drop site was clear air. The clouds were small compared to the 2.5-km antenna footprint, but they do introduce noise. The error introduced by a cloud in one profile brightness-temperature comparison will be reduced when it is averaged with several other profile comparisons.

July 13, 2002

There were three dropsondes during this flight off the coast of Florida, and the Proteus was close to all three of them. Figure 4-2(a) is a map of the flight path along with dropsonde and radiosonde locations. The first steps in a profile comparison is to determine the atmospheric profile's integrity and whether or not the launch site had relatively clear weather. Two figures that are helpful in determining the usefulness of an atmospheric profile are Figure 4-2(b) and Figure 4-3. Figure 4-2(b) is an

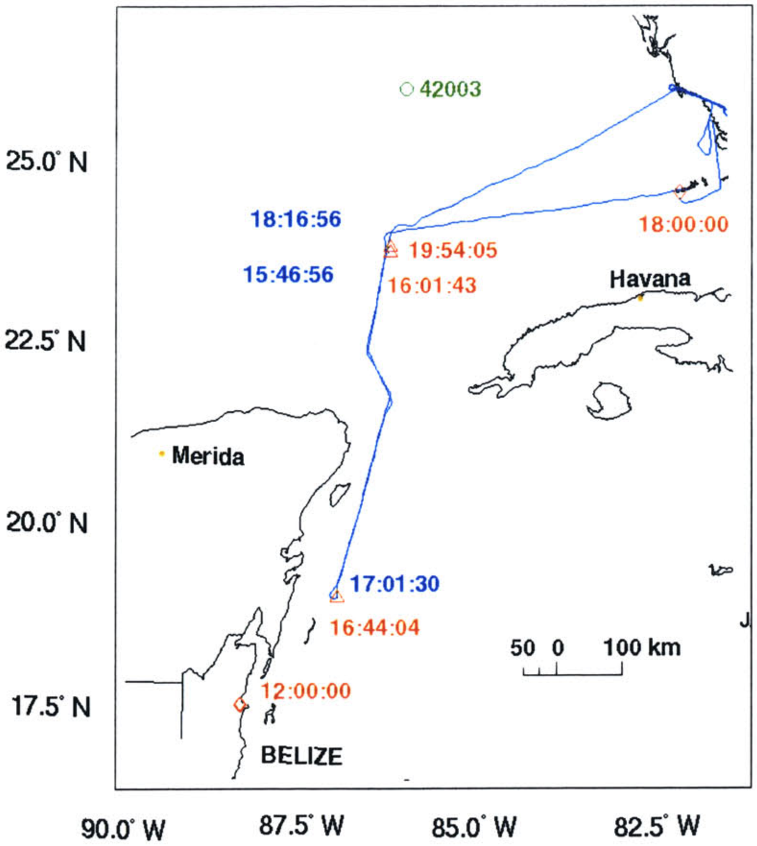

Figure 4-1: Validation Map for July 9, 2002. The blue line marks the flight path of the aircraft. Red triangles are dropsonde locations and the launch timestamps are next to them in red. The blue timestamps are the times when the aircraft crosses over the dropsonde dropsite. The red diamonds are radiosonde launch sites with their launch times. The green circles are buoy locations.

example of the atmospheric profiles measured on July 13, 2003, which went through quality control check (*e.g.*, outliers were removed). The radiosonde can be useful in filling in areas of the profile that are missing in the dropsonde profile. Figure 4-3 is a GOES-8 image from the archives of the Cooperative Institute for Meteorological Satellite Studies at the University of Wisconsin-Madison Space Science and Engineering Center. The images were archived at one-hour intervals during this deployment. Checking the 1-km resolution GOES image allows the first run in determining the clear-air conditions. If the GOES image suggests clouds like the one in Figure 4-3, then the MODIS airborne simulator's data is used to determine the extent of the cloud coverage. Once again, the averaging of the profiles reduces the affect of any

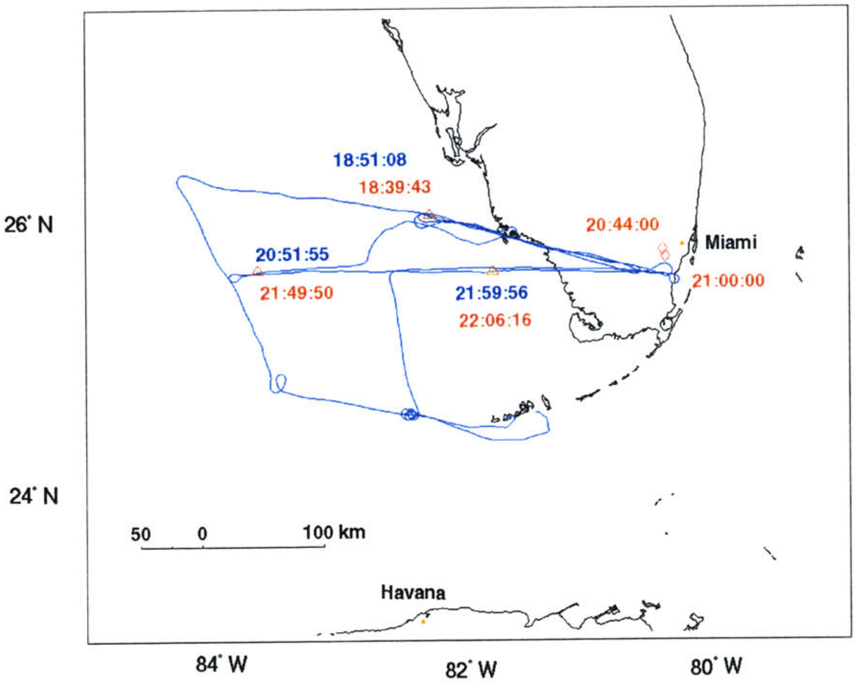

(a) Map

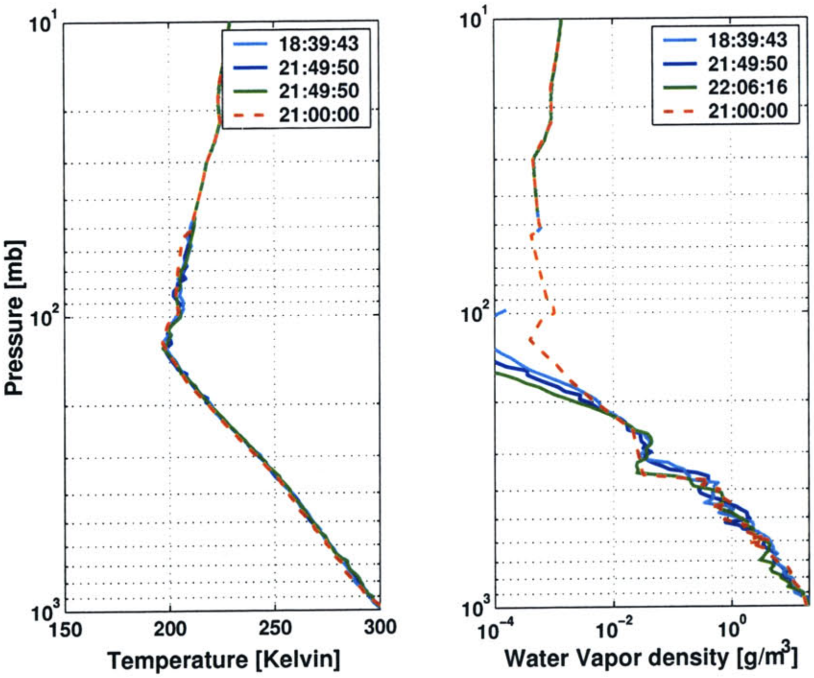

(b) Dropsonde and radiosonde profiles

Figure 4-2: Validation map and profiles for July 13, 2002

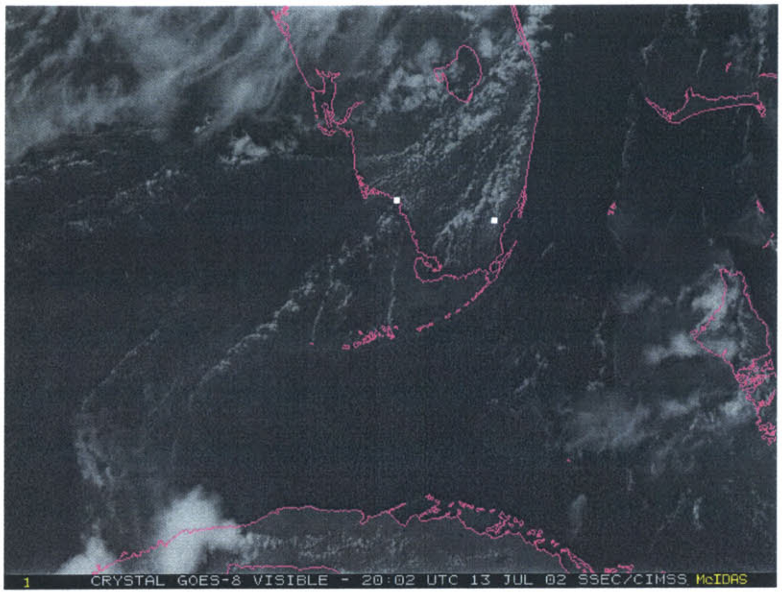

Figure 4-3: GOES-8 image from July 13, 2002 at 20:02 UTC

cloud-induced noise.

Typically, profile comparisons over land are avoided because of the difficulty in determining the surface emissivity. This is especially difficult over the marshes of the Everglades, which cover much of southern Florida. There are surface emissivity models (*e.g.*, fastem [22]) that used sea surface temperature and wind speed as inputs. These inputs come from either buoys or satellite data.

July 19, 2002

The flight path crisscrossed the southern coastline of the Florida peninsula. While over the Gulf of Mexico, the ER-2 dropped four dropsondes and one additional one off the eastern coastline. The Proteus was within reasonable reach of three of the dropsondes in the Gulf of Mexico and the one off the eastern coastline of Florida. The MODIS airborne simulator showed high-altitude cirrus clouds at the first dropsonde location off the eastern coast of Florida, while the other three drop sites were clear air. The Proteus made 360° turns around two of the dropsonde release points and did not level off for dozens of kilometers, and the Proteus inertial navigation system failed for this flight. Therefore, the brightness temperature comparisons for these two locations were made at the nearest level portion of the flight. The spatial and

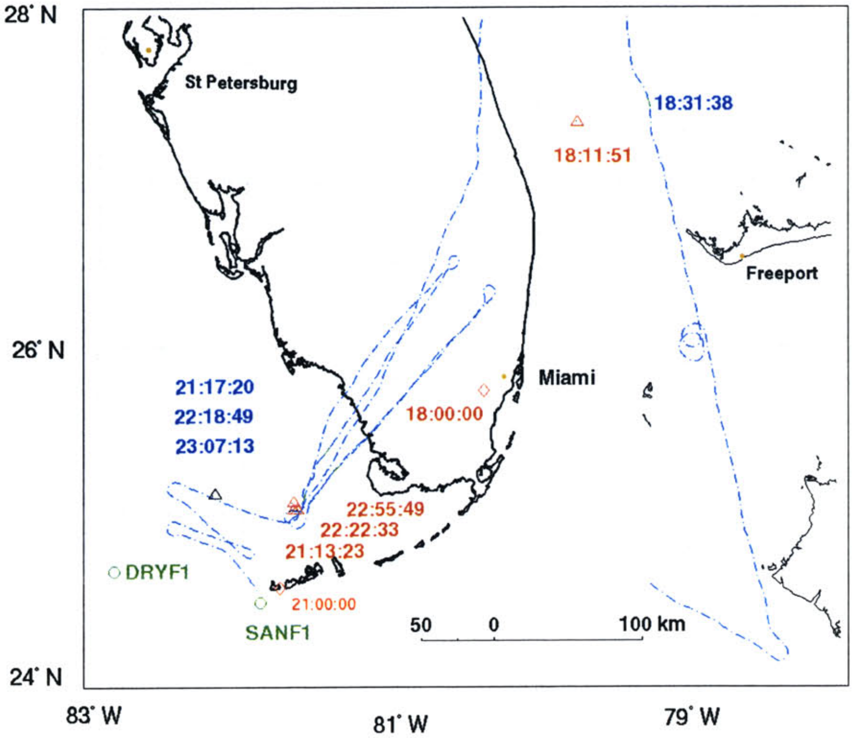

Figure 4-4: Validation map for July 19, 2002

temporal differences are also summarized in Table 4.1.

Comparison Statistics

All of the profiles from Table 4.1 are compared with the nearest level-flight NAST-M data and the statistics are presented in the following figures. The 183-GHz system was inoperable on July 9th and are not included in the statistics. Also, July 13th has the only clear-air profile comparisons for the 425-GHz system. At the time only the four most-transparent 425-GHz channels were operational, but the fourth had considerable noise and was deemed unusable. As mentioned in Section 3.4.2, using the "second option" for correcting the measured and radiometric temperature differences produced better results. The following figures use the corrections from Table 3.5, which uses the "first option," but the mean from the second option is included in red as a dash-dot-dot line. The first option consisted of adding two degrees to the Lakeshore temperature measurement of the external ambient load, while the second option reduced the onboard heated and ambient load's by two Kelvin.

The validation figures are presented in Section 4.3. In Figure 4-11, the mean of the difference between the seven profile comparisons of the 183-GHz system is the solid black line (using the first option). The black dashed lines mark one standard deviation above and below the mean value. During this mission there seems to be a negative bias on the 183-GHz system, which could be an artifact of the high degree of variability of the humidity profile. The mean of the second option gives the red dash-dot-dot line, which gives a similar bias, but in the positive direction.

In Figure 4-12, the mean of the difference between the three profile comparisons of the 425-GHz system is the solid black line. The black dashed lines mark one standard deviation above and below the mean value. The fourth channel was deemed useless because of extremely high noise. Similar to the 183-GHz system, both options were about equal when dealing with the temperature difference.

In Figure 4-9, the mean of the difference between the ten profile comparisons is the solid black line for the 54-GHz system. The black dashed lines mark one standard deviation above and below the mean value. The 54-GHz channels were corrected for the beam spillover, but on board the Proteus, the spillover effect is reduced because the zenith port is plugged with a piece of Eccosorb, which typically reaches 240 K during the flight. The bias of the transparent channels could be from a combination of errors in surface emissivity model and sea surface temperature (the second option helps but cannot explain the entire bias). Using the simulation software and a radiosonde from July 9^{th}, the sensitivity of the simulated brightness temperature to inputs such as sea surface temperature (T_s) and surface emissivity (ε_s) can be calculated. The nadiral sensitivity due to sea surface temperature at 50.3 GHz is

$$\begin{aligned}
T_b(\varepsilon_s, T_s) &= \varepsilon_s(T_s) \cdot [T_s \cdot tr - tr^2 \cdot T_{cosmic} - tr \cdot T_b^{dwl}] + constant && (4.1)\\
\frac{\partial T_b}{\partial T_s} &= \frac{\partial \varepsilon_s}{\partial T_s} \cdot [T_s \cdot tr - tr^2 \cdot T_{cosmic} - tr \cdot T_b^{dwl}] + \varepsilon_s(T_s) \cdot tr && (4.2)\\
\left[\frac{\partial T_b}{\partial T_s}\right]_{T_s=295K} &\cong 0.146. && (4.3)
\end{aligned}$$

tr is the one-way transmittance between the aircraft and the surface, and T_b^{dwl} is the downwelling brightness temperature that will reflect off of the surface. $\frac{\partial \varepsilon_s}{\partial T_s}$ was approximated as -0.0021 and is based on computations using fastem with input sea surface temperatures that ranged over 280 to 305 K. The nadiral sensitivity of brightness temperature due to surface emissivity is

$$\frac{\partial T_b}{\partial \varepsilon_s} = [T_s \cdot tr - tr^2 \cdot T_{cosmic} - tr \cdot T_b^{dwl}] \tag{4.4}$$

$$\left[\frac{\partial T_b}{\partial \varepsilon_s}\right]_{T_s=295K} \cong 116. \tag{4.5}$$

This means that the brightness temperature would be perturbed equally by a seven Kelvin change in sea surface temperature as it would be by a 0.008 change in surface emissivity. The surface emissivity is also a function of surface wind speed (W).

$$\frac{\partial T_b}{\partial W} = \frac{\partial T_b}{\partial \varepsilon_s} \cdot \frac{\partial \varepsilon_s}{\partial W} \tag{4.6}$$

$$\left[\frac{\partial T_b}{\partial W}\right]_{T_s=295K} \cong 116 \cdot 0.0025 = 0.3. \tag{4.7}$$

$\frac{\partial \varepsilon_s}{\partial W}$ was approximated as 0.0025 and is based on computations using fastem with input wind speeds that ranged over 0 to 16 m/s at 300 K.

The fastem model used in these simulation is an approximation to a full geometric optics emissivity model. Geometric optics models assume the sea surface is composed of randomly oriented facets. This is an improvement over specular surface models when simulating brightness temperatures over oceans because waves perturb the ocean's surface. Fastem includes Bragg scattering and sea foam adjustments. An evaluation of the fastem model for the AMSU window channels determined that the fastem approximation to a full geometric optics emissivity model is poor [16]. The report compared the 23.8, 31.4, 50.3, 52.8, 89, and 150 GHz frequencies at wind speeds of 0, 3, 7, 14, and 20 m/s, and determined that the largest bias was 7 K with a standard deviation of 2.6 K. The surface wind speed was estimated from either buoys readings or by using the last couple of readings from the dropsonde. The range of wind speeds for CRYSTAL-FACE was one to four meters per second.

In Figure 4-10, the mean of the difference between the ten profile comparisons is the solid black line for the 118-GHz system. The black dashed lines mark one standard deviation above and below the mean value. The 118-GHz system has LO leakage that affects the three most opaque channels, and this explains their large bias. Also, the temperature stabilization was altered because of the addition of the 183- and 425-GHz systems, and it wasn't corrected until after the deployment. This temperature shift changed the LO frequency to 117.9 GHz, and the shift is accounted for in these simulation comparisons.

4.1.3 CRYSTAL-FACE Summary

Based on the statistics from Figures 4-9, 4-10, 4-11, and 4-12, the validation of the CRYSTAL-FACE deployment is satisfactory and ready for further analysis, *e.g.*, geophysical parameter estimation. The 425-GHz data for this mission will only be used for precipitation parameter estimation and not profile estimation. As mentioned in Section 3.3.2, the Proteus calibration used a two-point weighted least-squares technique along with the corrections in Table 3.5 from Section 3.4.2. Table 4.2 summarizes the nadir bias and standard deviation of the 183- and 425-GHz systems for the CRYSTAL-FACE deployment. It includes results from calibrations using both the first and second option in dealing with the calibration load discrepancy. The frequency drift of the 118-GHz LO during this deployment was quantified for this mission by adjusting the simulation LO frequency until all of the 118-GHz channels were reasonable in Figure 4-10. For this mission, the 118-GHz LO was at 117.9 GHz. A more sophisticated technique was used for the PTOST mission, which flew on the ER-2 and had the zenith port.

4.2 PTOST 2003

The Pacific THOR*pex* (THe Observing-system Research and *p*redictability *ex*periment) Observing System Test (PTOST 2003) flew sorties out of Hickam Air Force Base (Oahu, HI) during February and March of 2003. This mission had two aircraft, the NASA ER-2 and the NOAA Gulfstream IV. The Gulfstream IV coordinated flights with the ER-2, but had a ceiling of 45,000 ft (12 km) and a speed of 440 knots (240

Table 4.2: C-F: Calibration Bias

Channel No.	183-GHz Spectrometer			425-GHz Spectrometer		
	mean difference [K]		standard deviation [RMS K]	mean difference [K]		standard deviation [RMS K]
	1^{st} option	2^{nd} option		1^{st} option	2^{nd} option	
1	-1.00	1.50	0.50	-2.0	0.50	0.50
2	-0.90	1.50	0.50	-1.5	0.75	0.25
3	-1.90	0.50	0.50	-1.0	0.50	1.00
4	-1.80	0.50	0.50	-20	-20	10
5	-1.80	0.50	0.50	N/A	N/A	N/A
6	-0.50	1.80	1.00	N/A	N/A	N/A
7	N/A	N/A	N/A	N/A	N/A	N/A

m/s). During this mission, the Gulfstream launched the dropsondes, and NAST was installed on the ER-2. Table A.2 summarizes the PTOST flights with notes on the performance of NAST-M during this deployment.

4.2.1 Mission Overview

This mission description comes from the official PTOST website (www-angler.larc.nasa.gov/thorpex/):

> The 2003 Pacific THOR*pex* Observing System Test is the first in a series of Pacific and Atlantic observation campaigns in support of the WWRP/USRP THOR*pex* Program. THOR*pex* - a Global Atmospheric Research Program, is a 10 year international research program under the auspices of the World Meteorological Organization/World Weather Research Program (WMO/WWRP) to accelerate improvements in short range (up to 3 days), medium range (3-7 days) and extended range (two week) weather predictions and the societal value of advanced forecast products. THOR*pex* will examine predictability and observing system issues, and establish the potential to produce significant statistically-verifiable improvements in forecasts of high impact weather. The program builds upon and coordinates advances being made in the operational forecasting and

basic research communities.

4.2.2 Local Oscillator Frequency Test

The frequencies of the 118- and 425-GHz local oscillators (LO) drifted during flight. Most commonly, it is caused by not maintaining a constant LO temperature, but this was only the case for the 118-GHz LO during this mission. The 425-GHz LO has had problems on the bench, and the receiver's temperature sensors revealed that the temperature was correct. An experiment was devised to determine the LO frequency for either the 118- or 425-GHz systems. There is very little oxygen above the aircraft, but there is enough to significantly warm the brightness temperature of the more opaque channels against the very cold background radiation. If there is a deviation in the LO frequency, as it was suspected for the 425-GHz system during PTOST, then the passbands would be shifted over the absorption line (see Figure 3-12(b)) and the channel's brightness temperatures will be affected. The LO frequency test consists of varying the LO frequency in simulations of the zenith-view brightness temperatures until the numerical simulations matched the actual flight data. Figure 4-5 is an example from March 1, 2003 with a frequency step size of 5 MHz. The estimated frequency of the LO would be the frequency that minimized the error metric. In this case, the error metric was the sum of the absolute difference between the actual brightness temperature (calibrated with the "second option" 2-point calibration) and the simulated brightness temperature. From this test, it was determined that the 425-GHz LO frequency was off the absorption line by at least 0.56 GHz. The frequency shifts were incorporated in the following validation simulations and summarized in Table 4.3.

In an attempt to determine the robustness of the test, the simulations were repeated with additional approximations or intentional errors. In the ideal case, a radiosonde would give the atmospheric profile above the aircraft to be included in the simulations, but rarely does a radiosonde measure the profile above the altitude of the aircraft. For the example in Figure 4-5, there was a coincidental radiosonde, but it only had readings up to 31 km, so the radiosonde was augmented with the

Table 4.3: LO Measurements

Date	425-GHz LO freq. [GHz]	118-GHz LO freq. [GHz]
1-Mar-03	106.01	118.12
3-Mar-03	106.05	118.19
11-Mar-03	105.95	118.12

standard 1976 tropical atmosphere. It should be noted that the closest portion of the profile above the aircraft is the most important because that that region is where most of the zenith absorption arises. GPS gave the altitude of the aircraft as 19.95 km. Using the GPS altitude and the radiosonde/standard atmosphere in the simulations produced the red diamonds in the Figure 4-5. The first robustness test was to change the aircraft's altitude, and see the resulting change in Figure 4-5. The radiosonde/standard atmosphere combination was simulated with a lower altitude of 19.3 km, and those results are the blue squares. The second test consisted of removing the radiosonde portion of the atmospheric profile and replacing it entirely with the standard atmosphere. The results of using the correct altitude and only the standard atmosphere are the red asterisks. The worst-case scenario is when the incorrect 19.3 km altitude and standard atmosphere are used, and those profiles are the blue circles. The result from the graph in Figure 4-5 shows that the experiment is very robust and gives a good indication of the LO frequency even when the exact altitude and profile are unknown. This test probably works the best for the systems that view a single oxygen absorption line. It was assumed that the test would not work for the 183-GHz system, because there is very little water vapor above the aircraft.

4.2.3 PTOST Validation

The PTOST validation follows the same guidelines as the CRYSTAL-FACE validation. There are also three validation days, and the profile-comparison statistics are presented.

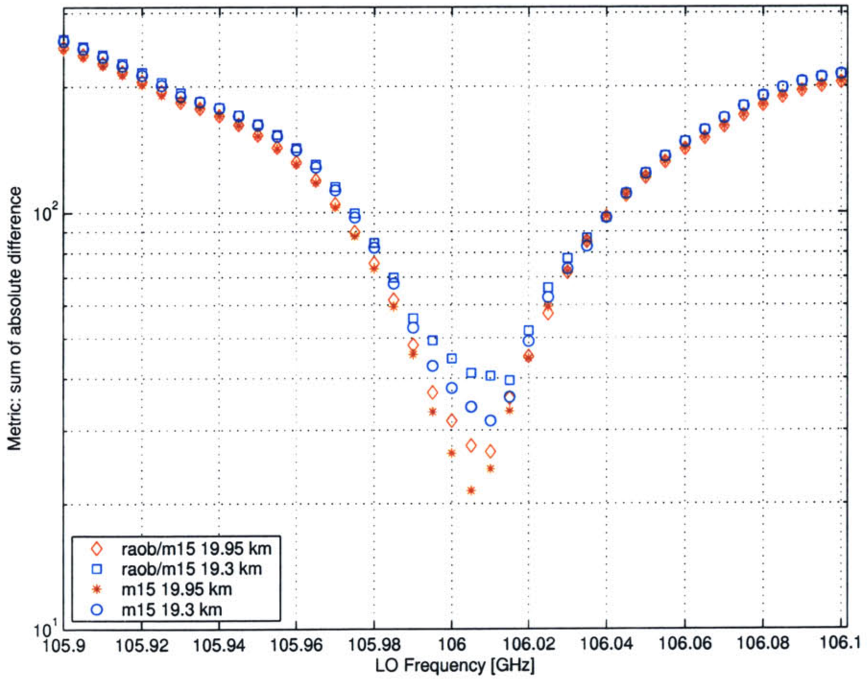

Figure 4-5: Error analysis of the test to determine the LO frequency through the zenith port. Red symbols indicate the simulation used the correct altitude of 19.95 km. The blue symbols are the results of the intentional introduction of an altitude error of 650 meters. The difference between the two symbols of the same color are whether the standard tropical atmosphere was used or the standard tropical atmosphere augmented by a coincidental radiosonde.

March 1, 2003

On this day, there were two dropsondes dropped from an altitude of 13.7 km as the ER-2 flew overhead at 20 km. The release points of the dropsondes were 1.23 and 4.75 km away from the aircraft's position. The aircraft flew over the region between 2:03 to 2:11 UTC, and the dropsondes were released at 1:53 and 2:02 UTC. A radiosonde launched at midnight (UTC) from Lihue on the island of Kauai filled in the atmospheric profile between the dropsonde's release altitude and the aircraft's altitude. The radiosonde was approximately 200 km away and rose to an altitude of 31.2 km, but the large distance was not a concern because the most dynamic portion of the atmosphere is under 12 km, particularly for the humidity profile. Figure 4-6 has a map with the ER-2 flight path, and a plot of the profiles used in the March 1^{st} comparison. In Figure 4-6(a), the red triangles are the Gulfstream IV dropsonde-launch locations. The green circles are the buoy's locations and were supplied by the National Data Buoy Center (www.ndbc.noaa.gov), and they supplied the surface sea temperature and wind conditions for the surface emissivity model, which were approximately 25° Celsius and seven meters per second for March 1, 2003. The radiosonde-launch location is marked with a red diamond. Times related to the release locations or the aircraft's position were also included.

March 3, 2003

There are four profile comparisons on March 3, 2003. The flight path is drawn in Figure 4-7 as the blue dash-dot line. The comparisons were made at both ends and within the middle of the "race track" pattern. The two in the middle were at separate times during the flight, but the release points were very close to each other. The spatial and temporal differences are given in Table 4.4. The spatial distance is the distance between the dropsonde release point and the closest aircraft position. The dropsondes typically fall at a rate of 1 km per minute. The buoy readings indicated wind speeds at approximately six meters per second and a water temperature of around 25 ° Celsius.

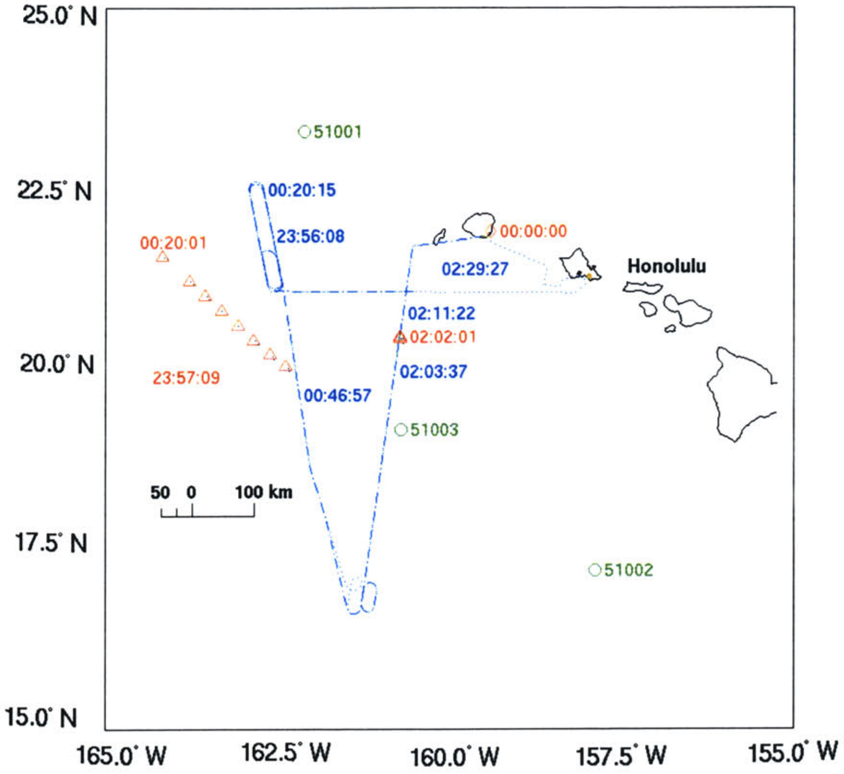

(a) Map

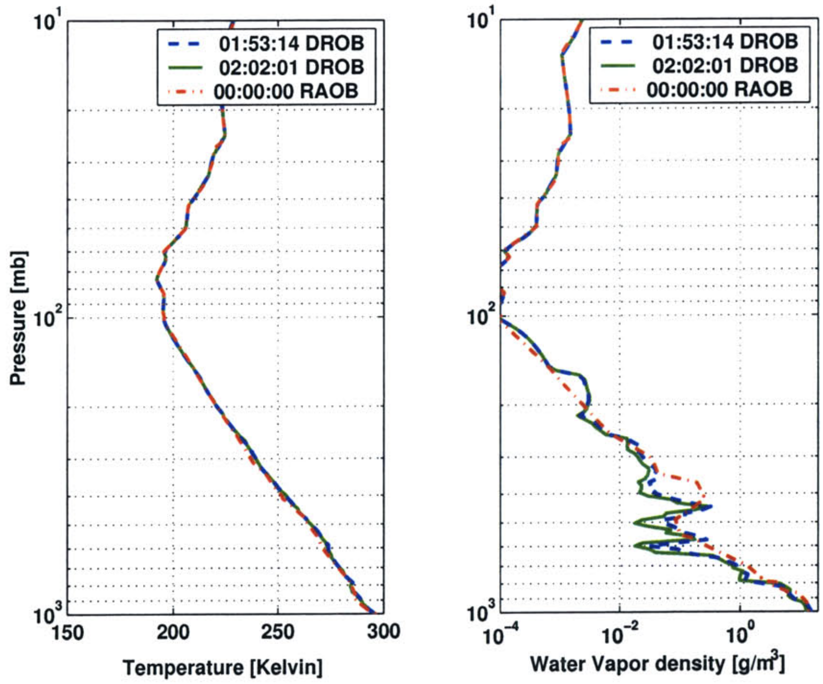

(b) Dropsonde and radiosonde profiles

Figure 4-6: Validation on March 1, 2003

Table 4.4: Profile Measurements 3-Mar-03

No.	Spatial dist. [km]	Release time [UTC]	Temporal dist. [min]	Maximum altitude [km]	Map symbol	Instrument type
1	5.14	23:50	21	12.9	△	dropsonde
2	13.29	23:58	1.5	12.9	◇	”
3	0.16	00:06	16	12.9	□	”
4	0.15	00:27	0.5	12.9	○	”
5	50-200	00:00	10-27	31.3	○	radiosonde

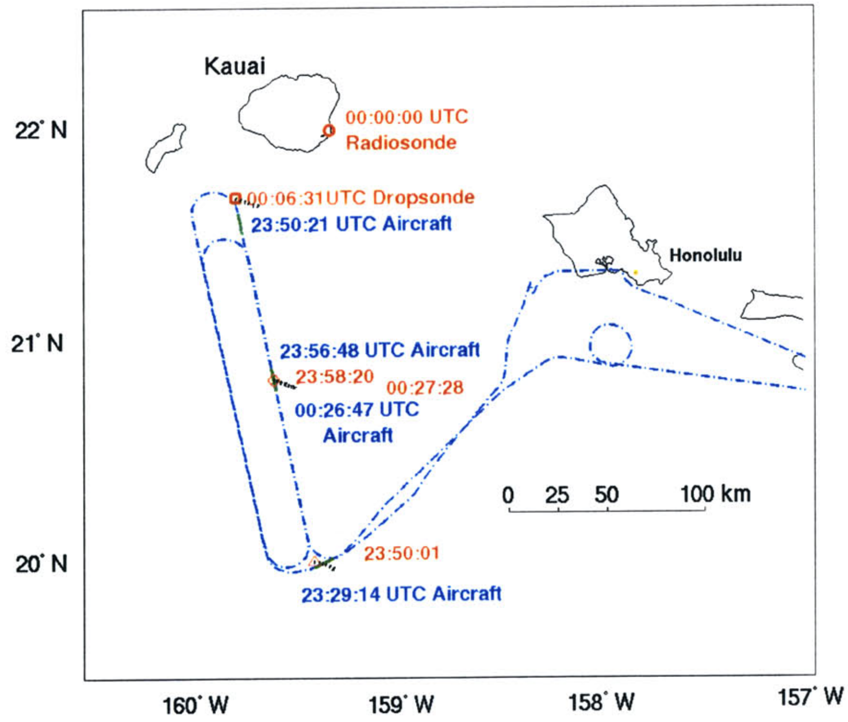

Figure 4-7: Validation on March 3, 2003

Table 4.5: Profile Measurements 11-Mar-03

No.	Spatial dist. [km]	Release time [UTC]	Temporal dist. [min]	Maximum altitude [km]	Map symbol
1	6.71	00:49	22	13.3	△
2	17.94	00:56	22	13.3	□
3	33.57	01:06	30	13.3	◇
4	19.29	01:12	28	13.3	x
5	15.50	01:56	33	13.4	∘
6	17.64	02:03	34	13.4	⋆
7	39.65	02:10	36	13.3	∗

March 11, 2003

The flight on this validation day was 1500 km away from the Hawaiian Islands, which made a Hawaiian radiosonde comparison pointless. The flight went back and forth across a weather front, but the northwest corner of Figure 4-8 is confirmed to be completely clear air by the NAST-M video camera. There were seven dropsondes and the labels and details are described in Table 4.5. There were no buoys in this location, but the dropsondes include wind speed, and the wind speed values closest to the surface were around eleven meters per second. Without a radiosonde to augment the atmospheric profile, this flight was exclusively used for the 183-GHz system, which has weighting functions that peak well below the 13 km release altitude (see Figure 3-15).

Comparison Statistics

Using the correct LO frequencies found in Section 4.2.2 and the calibration adjustments from Section 3.4.2, dropsondes from this deployment were compared with brightness temperatures calibrated with the three-point calibration from Section 3.3.2. The comparison was made for all four spectrometers and are presented as a function of scan angle in Figures 4-13, 4-14, 4-15, and 4-16. The 183-GHz system and the first three most-transparent channels of the 54- and 118-GHz systems utilized thirteen dropsonde comparisons and used the profiles from all three validation days. The

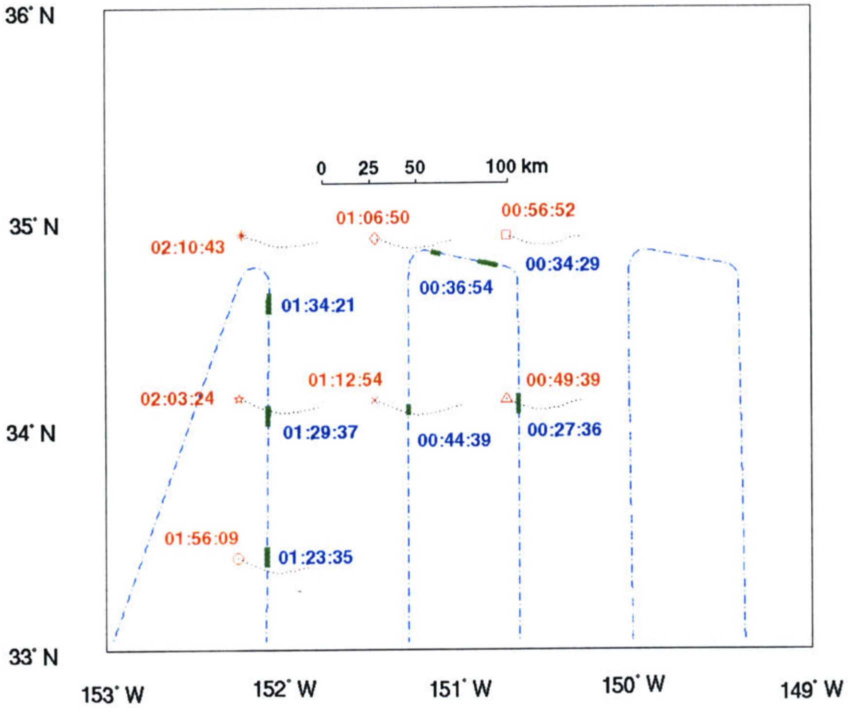

Figure 4-8: Validation on March 11, 2003

other 54- and 118-GHz channels and the 425-GHz system computed statistics utilizing six radiosonde/dropsonde comparisons between March 1^{st} and 3^{rd}. Once again, the second option for handling the temperature difference has its mean value drawn in the figures as a red dash-dot-dot line.

The biases of the transparent 54-GHz channels are larger than the ones recorded for CRYSTAL-FACE, but are still credited to the emissivity model, or to the model's input parameters. The 118-GHz system had several serious problems during PTOST, which resulted in a serious LO frequency shift. The shift is caused by a combination of a change in the room-temperature operating frequency of the LO and from a temperature stabilization problem. The room-temperature operating frequency can be adjusted by moving the position of a sapphire rod inside the Gunn oscillator. The temperature stabilization was not corrected until the ATOST deployment, so during PTOST the LO frequency would slowly decreasing as the LO's temperature decreased. The 118-GHz system has its own LO leakage that effected the calibration of the opaque channels, but after the installation of the 183-GHz system, it was found that the 183-GHz DRO also leaks into the 118-GHz system. A harmonic of the 15.276-GHz dielectric resonance oscillator (DRO) escapes out of the 183-GHz horn and is reflected off the calibration loads and back into the 118-GHz antenna horn. The harmonic initially corrupts the calibration of the first channel of the 118-GHz system, but as the LO's temperature becomes colder (*i.e.*, as its frequency shifts), the corruption would shift to the second 118-GHz channel. This is the reason why the second channel in Figure 4-14 has such a large bias. The corruption of the first channel had already passed by the time of the data comparison. The 183-GHz corruption of the 118-GHz system was avoided during the IHOP and CRYSTAL-FACE deployments because an extra calibration load measurement was made in which the 183-GHz DRO was shut off. Unfortunately, the NAST-M scanning assembly sometimes misses commands from the computer to move the reflector and this would completely ruin the 183-GHz data because the LO would be shut off for certain measurements of the calibration loads. It was decided that the 183-GHz system had higher priority, so the corruption of the 118-GHz system was deemed an acceptable loss for this mission.

4.2.4 PTOST Summary

The near-nadir mean and standard deviation statistics per channel for the 183-GHz and 425-GHz systems are summarized in Table 4.6. The 425-GHz system did not operate as it was designed because of the frequency shift.

The shift altered the shape of the temperature weighting functions. Since the shift has been quantified, the retrieval of atmospheric profiles using the 425-GHz system will still be attempted.

The validation has identified and quantified the major calibration issues of the PTOST 2003 deployment, and the data is prepared for the geophysical parameter estimation in the remaining chapters. The issues are:

- 425-GHz LO frequency shift
- 118-GHz LO frequency shift
- 118-GHz LO leakage that effects opaque 118-GHz channels

Table 4.6: PTOST: Calibration Bias

Channel No.	183-GHz Spectrometer mean difference [K]		183-GHz Spectrometer standard deviation [RMS K]	425-GHz Spectrometer mean difference [K]		425-GHz Spectrometer standard deviation [RMS K]
	1^{st} option	2^{nd} option		1^{st} option	2^{nd} option	
1	-3.00	-0.75	1.00	-2.80	-0.80	0.60
2	-2.10	0.00	1.00	-2.50	-0.80	0.50
3	-2.00	0.00	1.10	-2.50	-0.75	0.25
4	-2.10	0.20	1.00	-1.00	-0.50	2.00
5	-1.40	0.80	1.00	-1.40	-0.25	0.50
6	-3.20	-1.5	1.00	0.00	1.50	1.20
7	N/A	N/A	N/A	-2.50	-1.00	1.50

- 183-GHz LO leakage that effects transparent 118-GHz channels

- Potential 183- and 425-GHz nonlinearity

The 425-GHz LO shift will require re-engineering the LO chain of the receiver's front end. High-frequency high-power RF oscillators are not being produced anymore. A new system will include a lower frequency high-power oscillator with RF upconverters. As previously mentioned, the 118-GHz LO drift can be remedied by stable temperature control and adjustment of the mechanical frequency tuner, *i.e.*, the sapphire rod. Several attempts were made to alleviate the 183-GHz LO leakage, but all attempts degraded the performance of the 183-GHz system. They consisted of rotating the polarization of the 118-GHz radiometer to be orthogonal to the 183-GHz polarization, adding a small adapter between the horn and mixer to attenuate the spurious frequencies, and the insertion of a high-pass filter before the LO frequency enters the mixer in attempt to eliminate the signal before it is upconverted. Other solutions must be investigated. From the beginning, the 118-GHz LO leakage was mitigated by inserting a lowpass filter into the IF waveguide, but the residuals are still apparent. Further laboratory experiments are needed to evaluate the linearity of the rear end (bandpass filter to A/D converter), also the onboard temperature measurement system needs to be recalibrated.

4.3 Validation Figures

The descriptions are presented in Section 4.1.2 and 4.2.3. The solid black line is the mean of the simulated minus observed brightness temperatures using the first calibration correction option. The gray dashed line are one standard deviation above and below this mean. The red dash-dot line is the mean using the second calibration correction option (see Section 3.4.2).

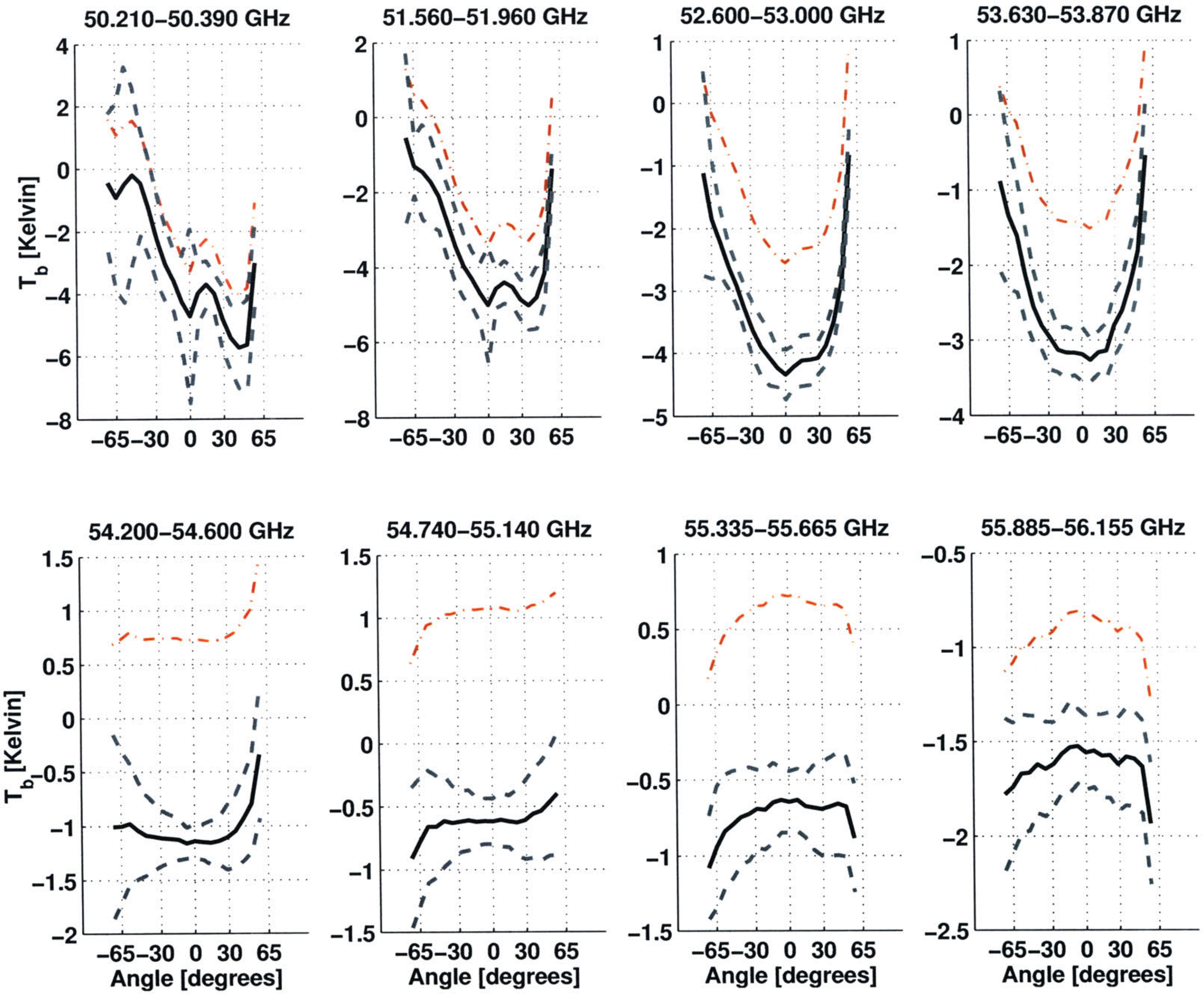

Figure 4-9: C-F: Validation of 54-GHz system (Simulated minus Observed)

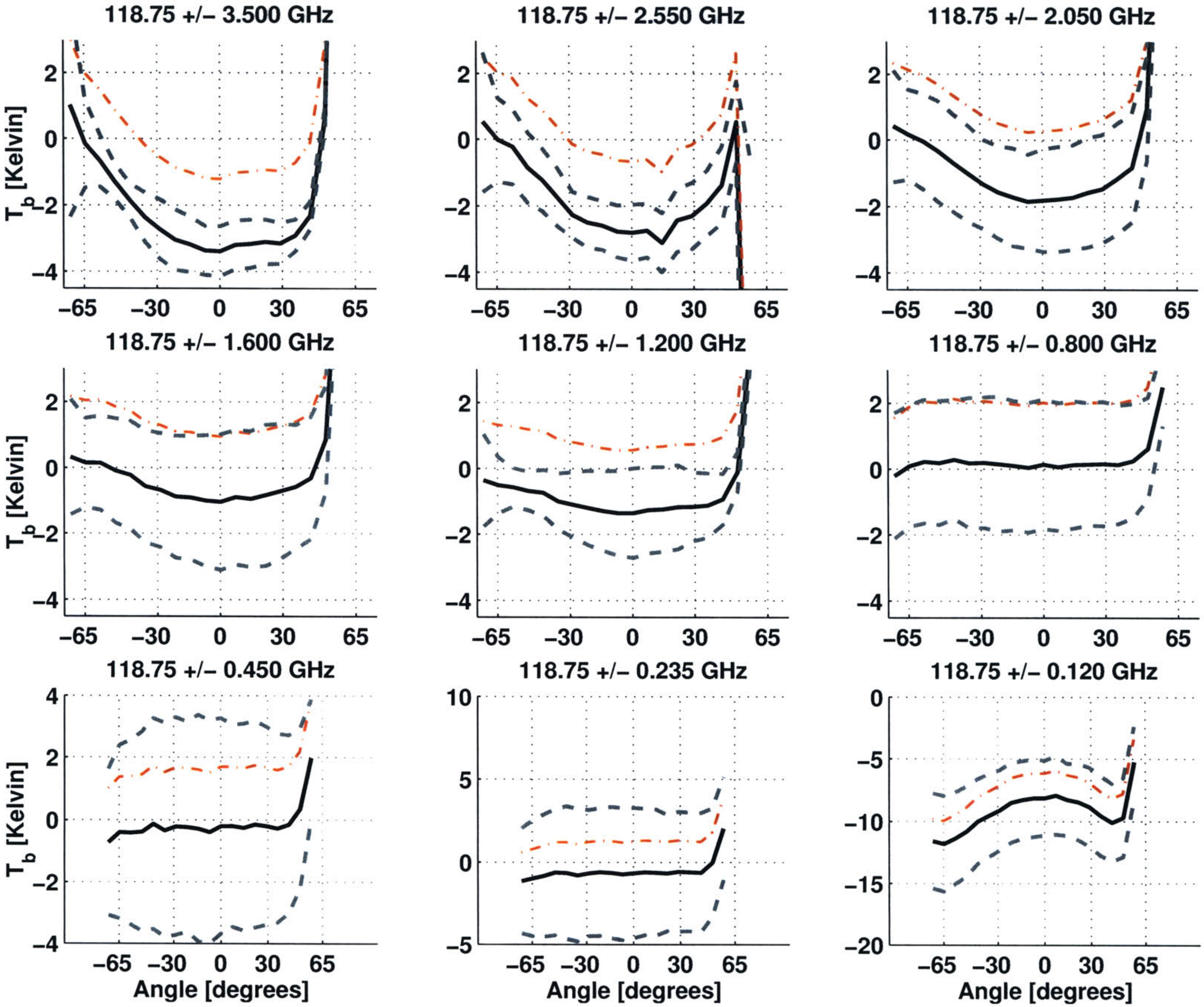

Figure 4-10: C-F: Validation of 118-GHz system (Simulated minus Observed)

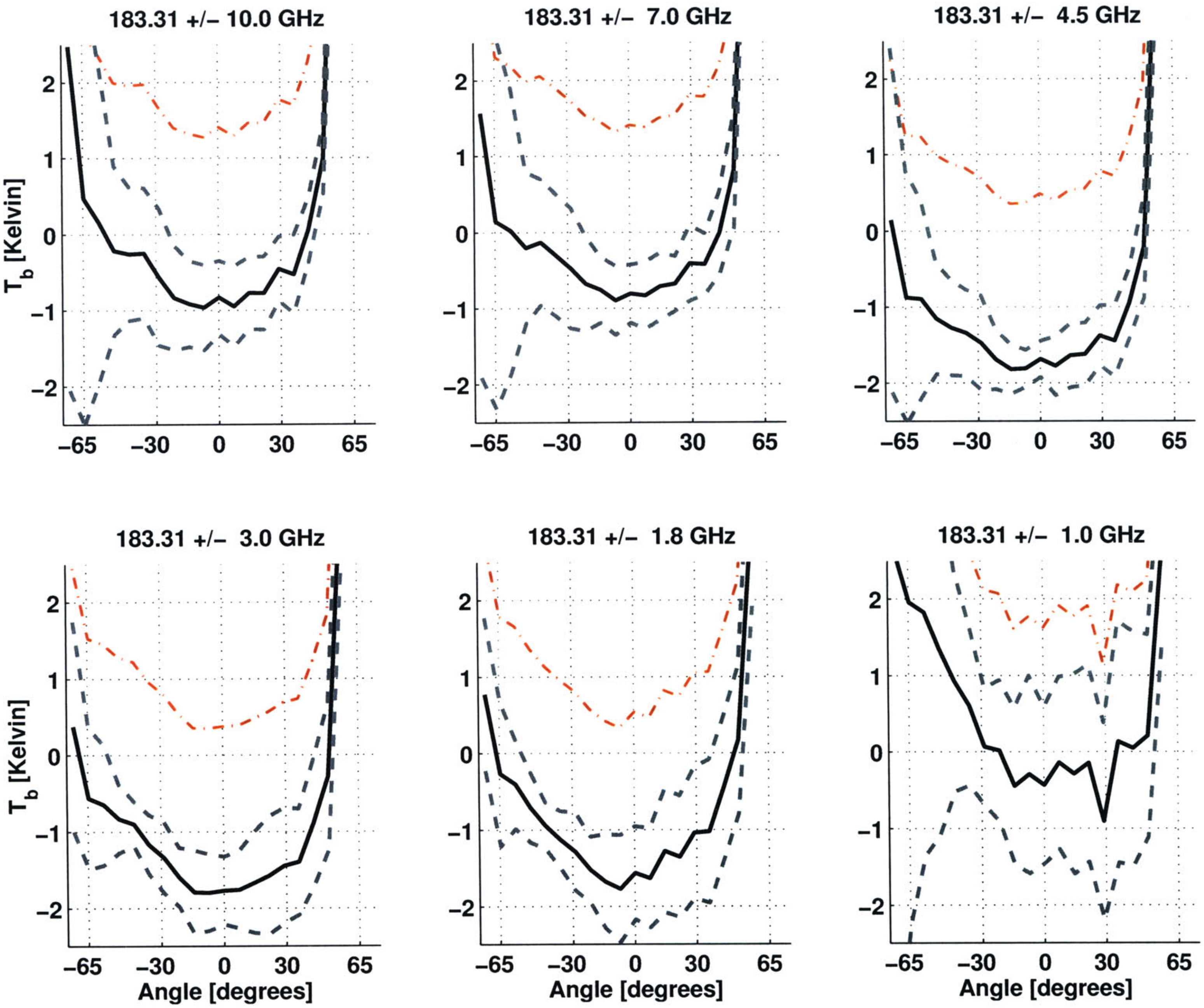

Figure 4-11: C-F: Validation of 183-GHz system (Simulated minus Observed)

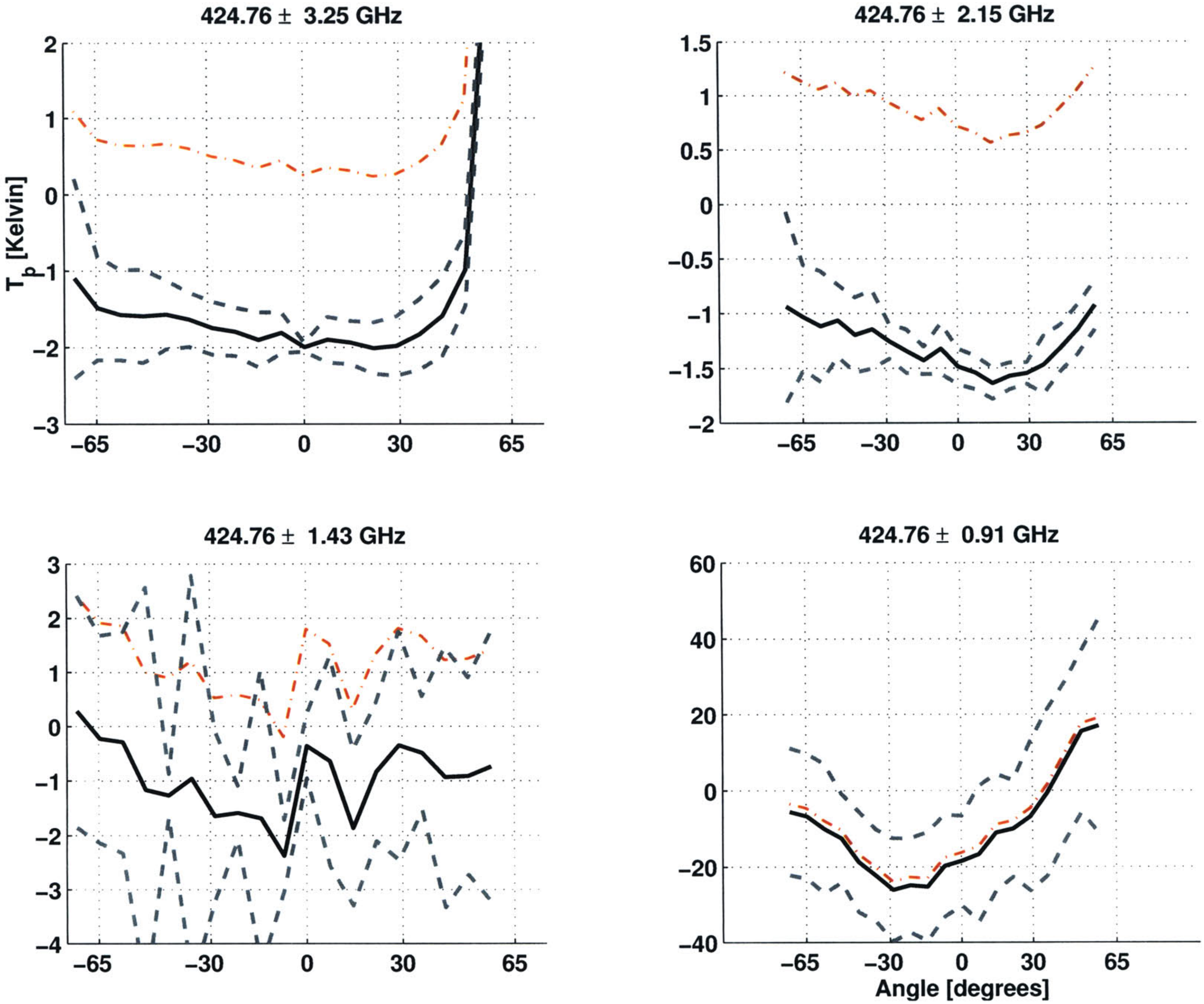

Figure 4-12: C-F: Validation of 425-GHz system (Simulated minus Observed)

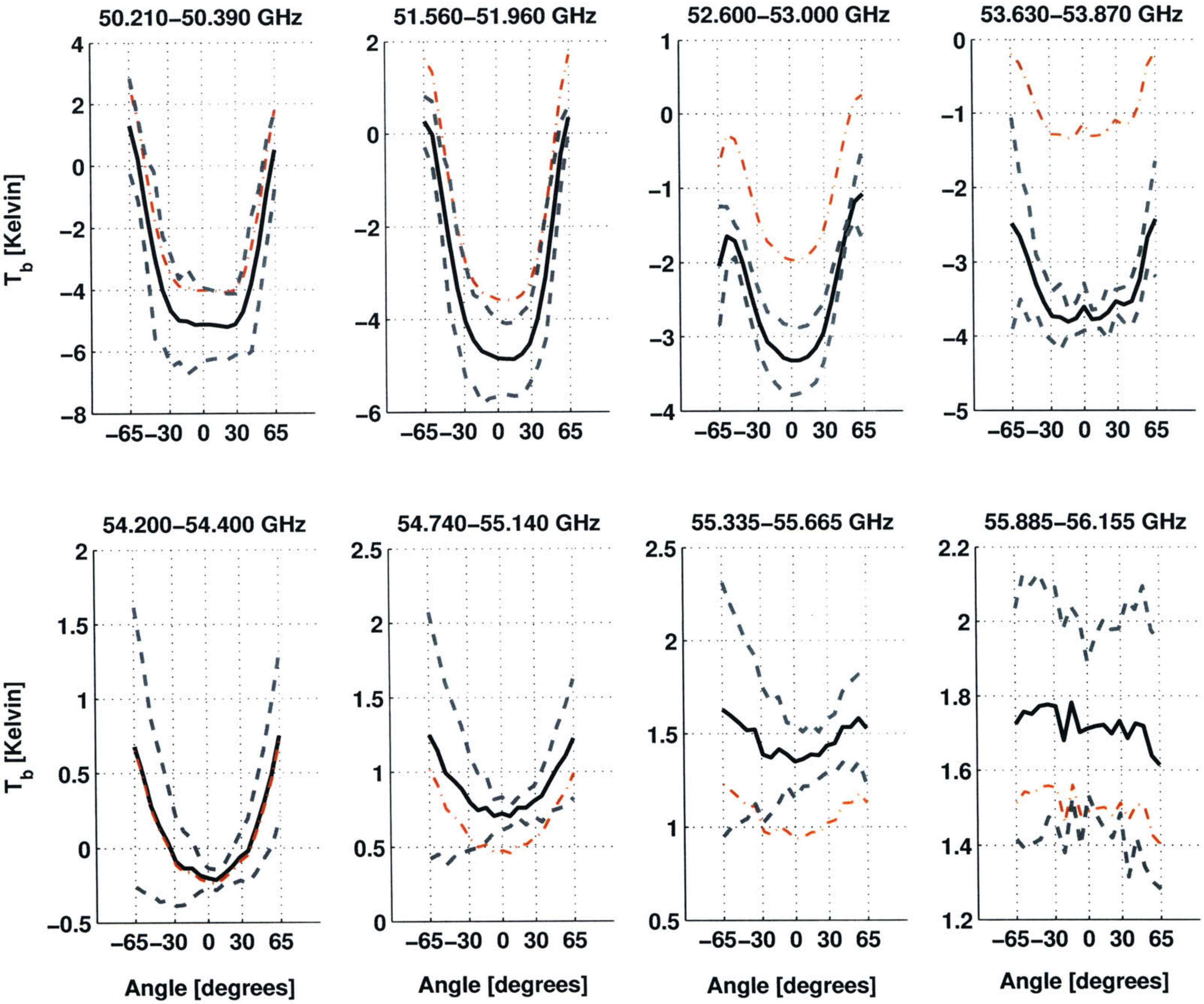

Figure 4-13: PTOST: Validation of 54-GHz system (Simulated minus Observed)

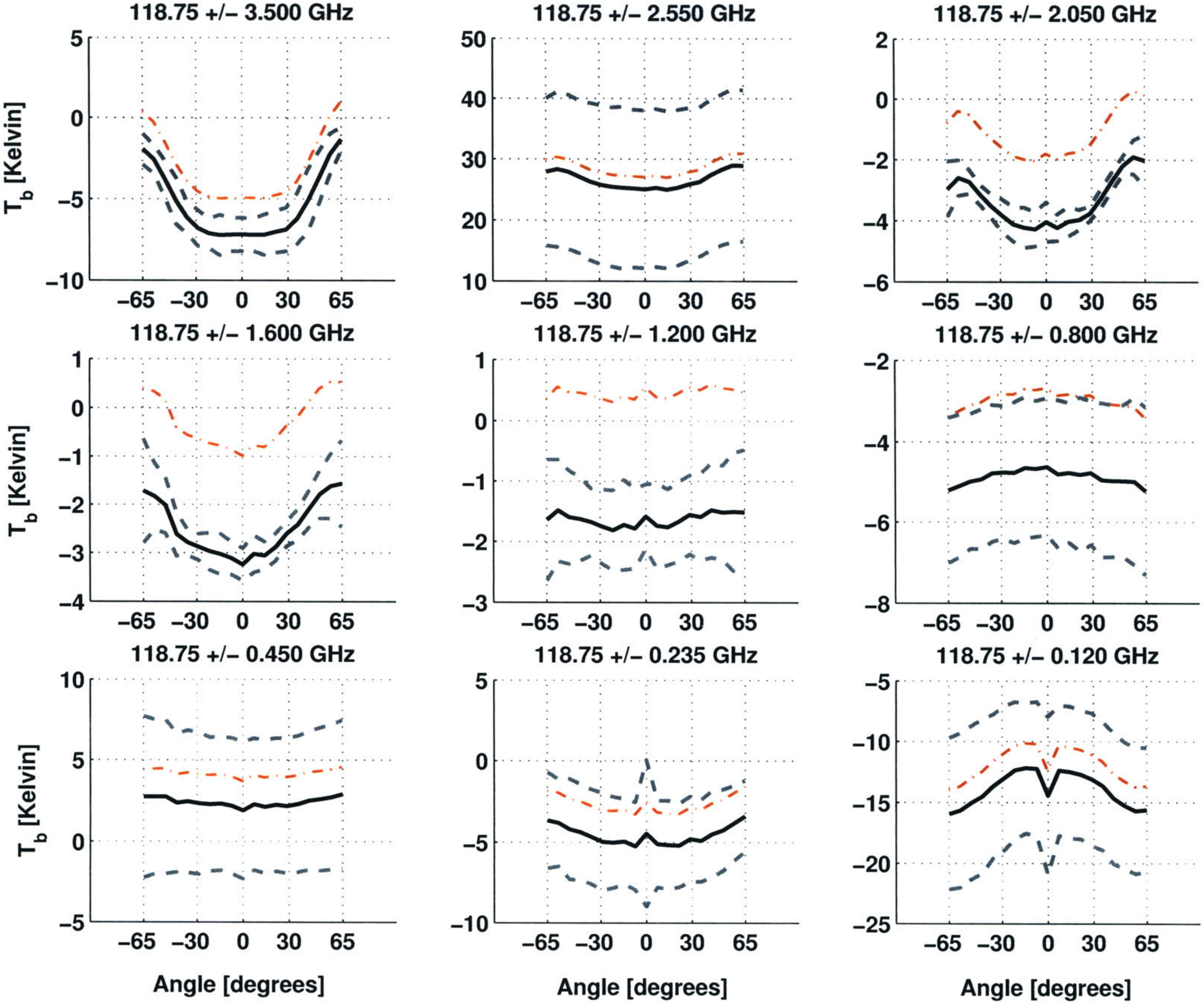

Figure 4-14: PTOST: Validation of 118-GHz system (Simulated minus Observed)

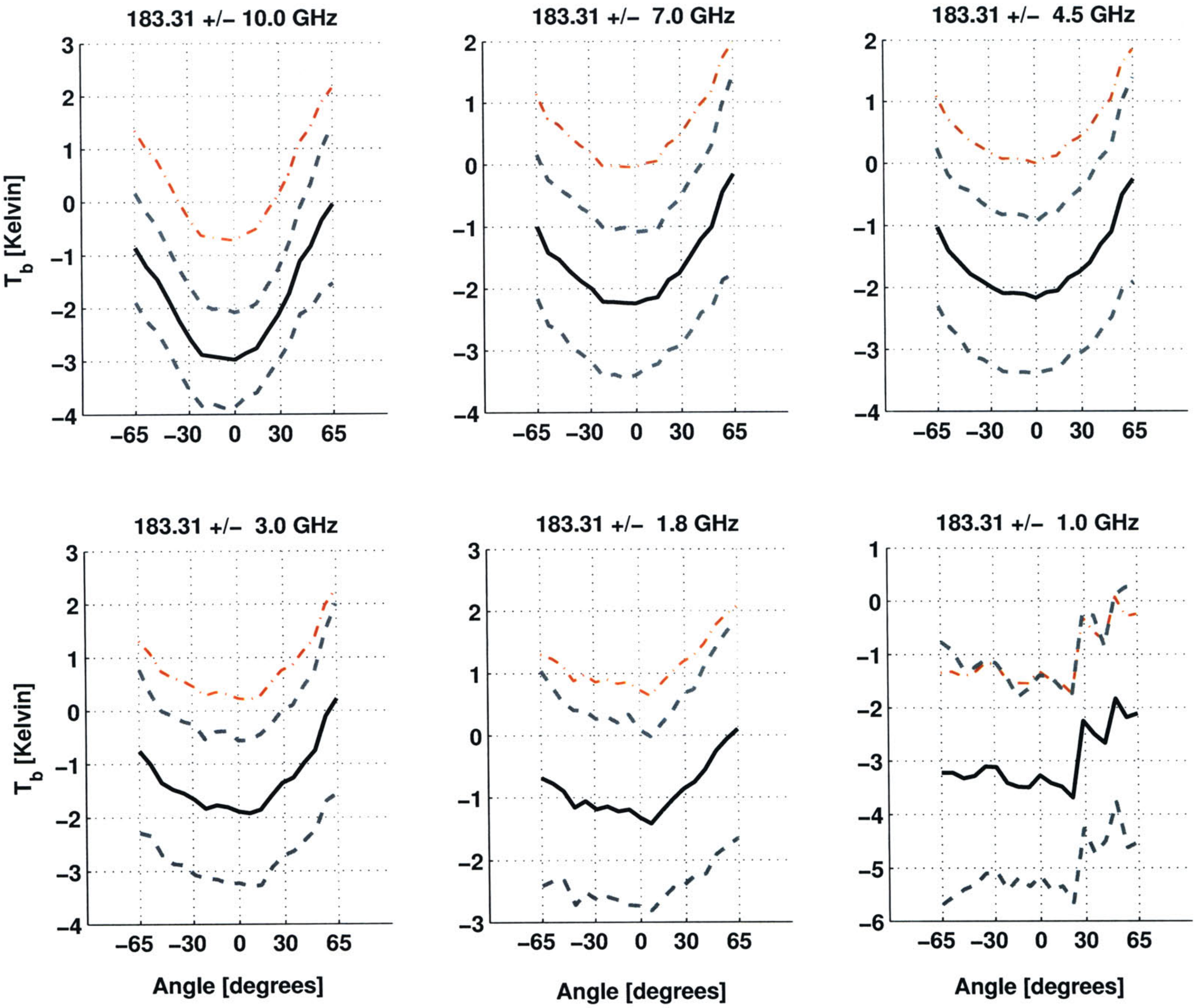

Figure 4-15: PTOST: Validation of 183-GHz system (Simulated minus Observed)

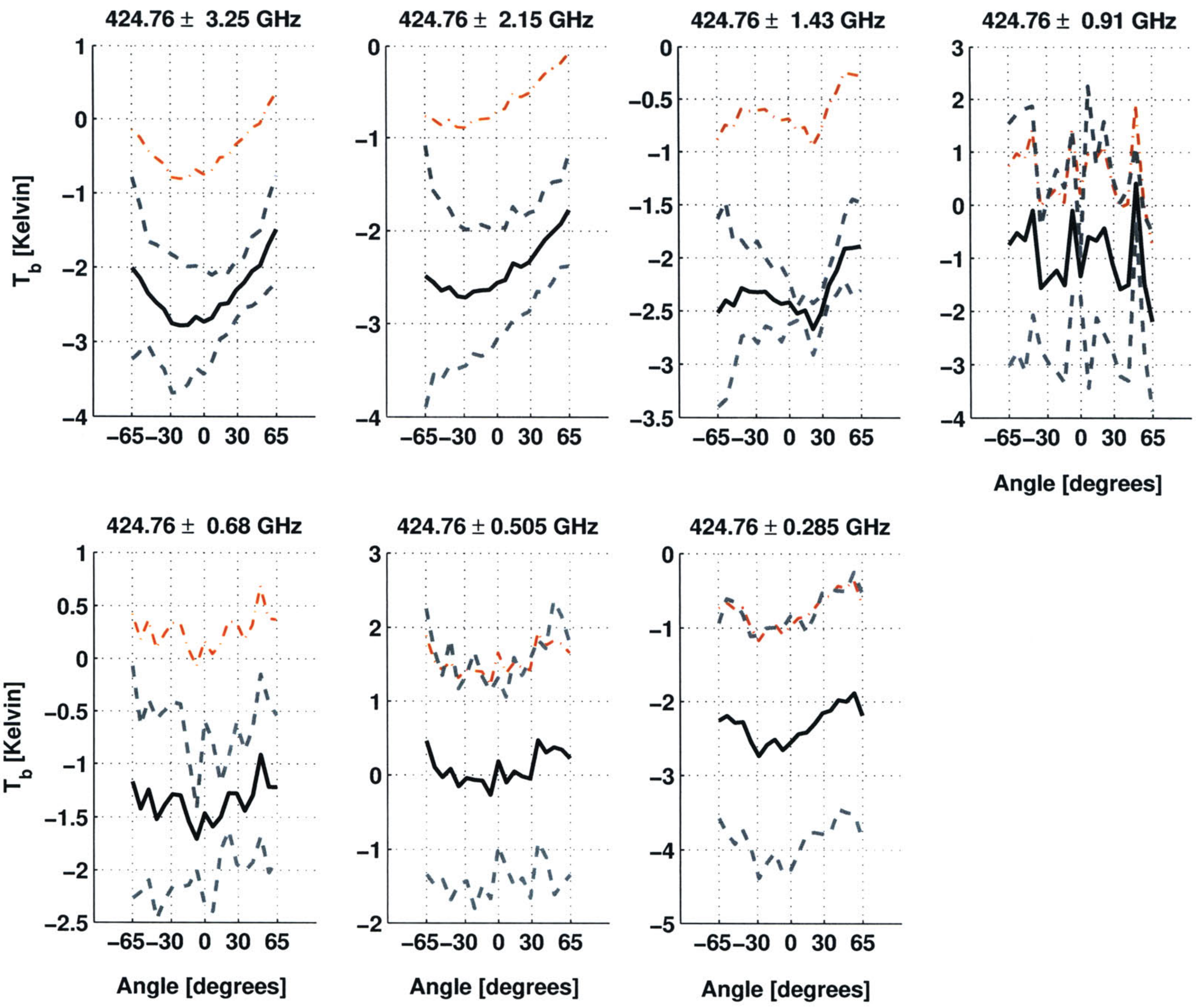

Figure 4-16: PTOST: Validation of 425-GHz system (Simulated minus Observed)

Chapter 5

Single-Pixel Precipitation Parameter Estimation

Precipitation estimation is an extremely difficult problem due in no small part to rainfall's spatial and temporal variability and to the lack of direct measurement techniques. Presently, precipitation estimation can be divided into three general areas. They are: 1) the indirect methods that measure infrared or visible radiation emerging from the top of clouds, 2) the direct methods of passively measuring the scattering, absorption, and thermal emission of hydrometeors at the micro- and millimeter frequencies, and 3) radar techniques that infer rainfall parameters from backscattering. Rainfall ground validation consists of rain gauges, which are highly accurate but severely undersample the area covered, and radar techniques that cover a wide area, but lack accuracy.

The passive microwave NAST-M instrument is novel in its wide-frequency range and the breadth of its weighting function peaks throughout the lower atmosphere. These unique attributes give NAST-M the potential to retrieve precipitation parameters, and this chapter investigates NAST-M's ability to retrieve these parameters through a pixel-by-pixel technique.

5.1 Prior Work

This section gives a very brief synopsis of the rainfall retrieval techniques aboard the Aqua spacecraft under the Earth Observing System (EOS) [47], which gives a good overview and represents the present standard in single-pixel spaceborne retrievals of rainfall. This standard consists of two subcategories of passive microwave rainfall estimators, which are the physically-based retrievals that use simulations of complex storm models, and empirical techniques that use coincidental microwave brightness temperature with independent rainfall measurements to derive an estimator.

The two microwave systems that retrieve rain rate aboard Aqua are the Advanced Microwave Scanning Radiometer - Earth Observing System (AMSR-E) and the Advanced Microwave Sounding Unit/Humidity Sounder for Brazil (AMSU/HSB) combination. AMSR-E is similar to other satellite instruments (*e.g.*, Special Sensor Microwave/Imager (SSM/I) or the Tropical Rainfall Measuring Mission (TRMM) Microwave Imager (TMI)), which use passive radiometers at microwave window frequencies (< 90 GHz) to retrieve rainfall. Over oceans, the reflective surface allows physical retrievals using the absorption and scattering of hydrometeors based on a radiative-transfer and storm model, but over land the retrieval technique is empirical because the absorption of the hydrometeors is confused with variations in the surface emissivity, and there is insufficient scattering at these low frequencies. Over land, the AMSR-E rainfall retrievals rely on the 85-GHz scattering perturbations (perturbations compared to an estimated clear-air 85-GHz channel from the 19- and 22-GHz channels), where the perturbation was related to the rain rate through ground-based radar measurements [69]. The AMSU/HSB microwave sounding suite can retrieve rain rates through either the lower channels at 23.8, 31.4, and 89 GHz or the 54- and 183-GHz spectrometers, which include opaque channels used for temperature- and humidity-profile retrievals. Chen and Staelin describe an empirical technique that uses the 54- and 183-GHz systems and is valid over land or ocean. The technique centers around a multilayer feedforward neural network trained on ground-based radar measurements of rain rates [13].

The technique presented in this chapter shares instrumentation similar to AMSU/HSB, but uses a physical retrieval technique most similar to the AMSR-E technique over ocean (or to [55]). As previously mentioned, NAST-M is a sounding instrument with a wide-frequency range with spectrometers at 54, 118, 183, and 425 GHz. NAST-M shares similar 54- and 183-GHz systems with AMSU/HSB, but lacks the channels at 23.8, 31.4, and 89 GHz, which are principally used for water vapor and precipitation measurements. The NAST-M technique is reviewed in this chapter.

5.2 Brief Overview of Convective Cells

There are two basic types of precipitation, which are convective and stratiform. Convective precipitation is usually identified by strong updrafts with velocities greater than several meters per second. Convective precipitation is localized in cells that are isolated or are in series (squall line). Under the correct upper atmospheric conditions, a convective cell can turn into a supercell, which is identified by its distinct anvil shape where the anvil cloud can reach heights of 15 km (50 kft). A few components of a thunderstorm, *i.e.*, convective cell, are updraft and downdraft, vertical wind shear, out-flow phenomena, and wall clouds [27]. The impetus of precipitation comes from warm moist air parcels rising into the atmosphere, while expanding and becoming cooler aloft. The colder air temperatures causes the vapor pressure of water (evaporation rate) to decrease, which in turns allows condensation to occur on small dust particles, *i.e.*, clouds form. The condensation releases heat and the air continues to rise higher into the atmosphere. Various processes such as accretion or aggregation cause larger droplets to form, and they fall to the earth as precipitation in a number of forms, *e.g.*, rain or snow. Under the right conditions, *i.e.*, an unstable atmosphere, a strong convective updraft can form. The updraft will eventually stifle itself as the cold air sinks back down, but a high-altitude vertical wind shear can blow the cold air off the top of the updraft and it will sink back to the surface nearby (causing a downdraft). Along with the cold air, all but the heaviest hydrometeors are blown toward the downdraft. The hydrometeors have different masses, which is related to

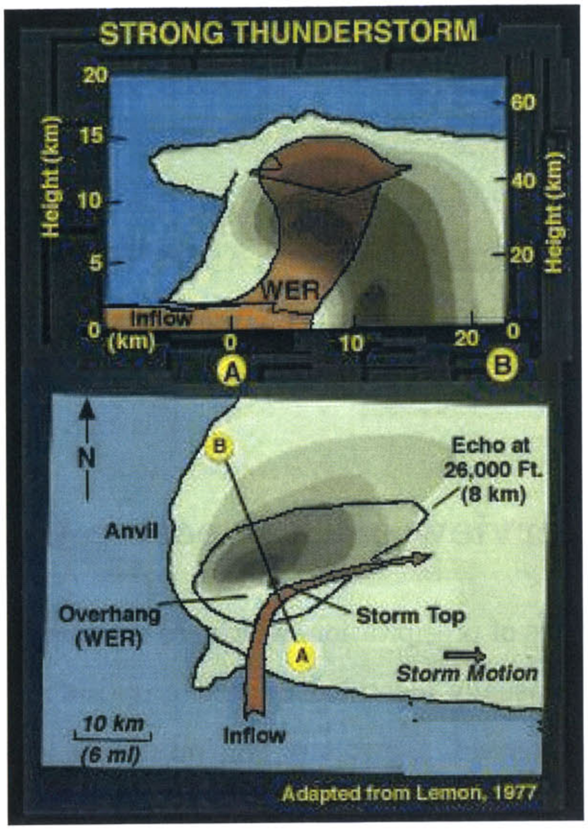

Figure 5-1: Schematic of Severe Thunder Storm. Image from the University of Illinois WW2010 Project [27]

their diameters. The mass density depends on the composition of the hydrometeor, *e.g.*, liquid or ice. Because of the vertical wind shear, the larger particles fall closer to the updraft, but the lighter particles are carried by the out-flow phenomena further away from the updraft. Figure 5-1 is a schematic of a strong thunderstorm. The top schematic in the figure is a vertical cross-section from point A to point B in the bottom schematic. The orange arrow in both the top and bottom schematic represents the air flow associated with the storm. The air flow starts at the bottom of the cell with the inflow and then goes straight up where it is called an updraft. The updraft is cut off by the high-altitude vertical wind shear at the top of the anvil and becomes the outflow. The figure uses contours of gray to represent VIP gradients (Digital Video Integrater and Processor), which is related to the reflectivity (dBZ) and therefore the rain. Note that WER stands for weak echo region.

Taking note of the VIP gradient in the bottom schematic of Figure 5-1, the decreasing radar return is an indication that the distribution of hydrometeor drop-sizes is decreasing. The larger particles fall closer to the overhang and the smaller particles travel the furthest distance due to the vertical wind shear. It should also be noted that this is a general case and there are many forms of thunderstorms, but this case is representative of convective cells. Figure 5-2 is a vertical schematic of the two extreme cases of updraft and downdraft strength. The left-hand schematic is more representive of stratiform precipitation as two temperature fronts collide, and the right-hand schematic is a supercell (local aggregation of convective cells).

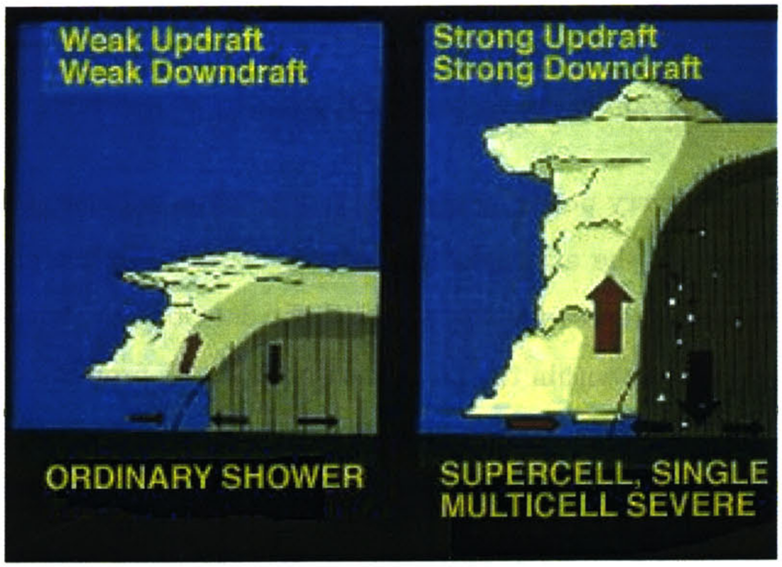

Figure 5-2: Vertical Profiles of the updraft and downdraft. Image from the University of Illinois WW2010 Project [27]

5.3 Retrieval Technique

The estimator for this retrieval technique follows the Bayesian methodology reviewed in Section 2.4 and described in Section 5.3.1. Bayesian methodology uses the cross-covariance between brightness temperature and precipitation parameters, and this is derived using the cloud simulation model in Section 5.3.2. Figure 5-3 illustrates the sample spaces involved in this technique. The ensemble of all possible atmo-

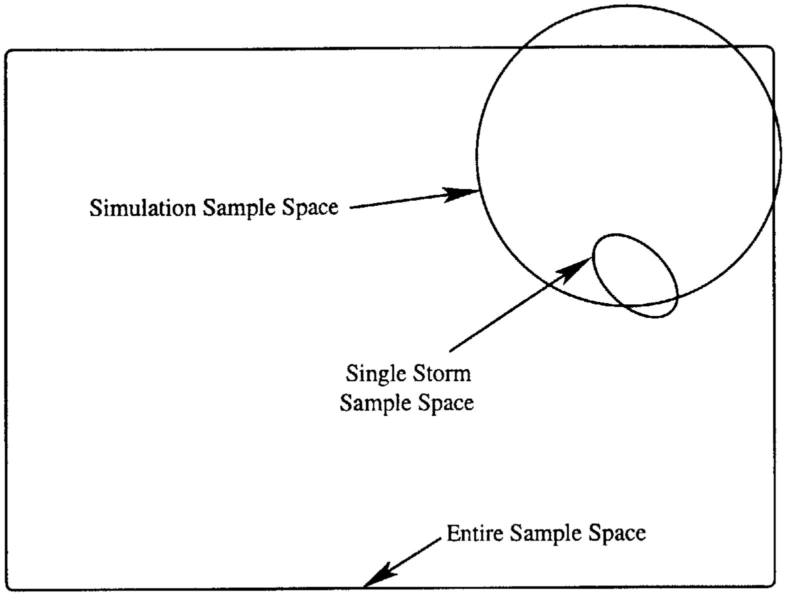

Figure 5-3: Venn diagram of the atmospheric, simulation, and flight data ensemble.

spheric profiles with every potential precipitation scenario is illustrated by the outer box. The circle covers the atmospheric conditions covered in the cloud simulation model, and the ellipse represents the actual flight data to be retrieved. Note that the ellipse will always be within the box (when NAST-M is properly calibrated), but rarely completely within the circle. The circle's "position" and shape will change by adjusting the simulation model. The statistics used in the Bayesian estimator are inferred from the cloud-simulation-model sample space, *e.g.*, the cross-covariance between the precipitation parameters and NAST-M's brightness temperatures. The Venn diagram gives insight into a practical consideration where the simulation model mean will most likely not equal the flight data mean. From experience in analyzing the case studies in Section 5.4, the local clear-air mean of the flight data was used in all calculations which required the brightness temperature mean. The mean is calculated from the closest available clear air in vicinity of the convective cell being retrieved. This requires that the estimator (specifically, the **C** and **D** of Section 5.3.1) to be recalculated for each new section of flight data (the simulations do not have to be recalculated). One of the estimator's prime advantages is its simplicity and very low computational load.

The NAST-M has a digital video system that helps identify atmospheric and surface conditions and is used to determine the visible cloud-top altitude, which will invariably differ from the estimated precipitation cloud-top altitude, but will give a maximum bound. The optical stereoscopic technique used on NAST-M video data was evaluated against coincidental Cloud Physic Lidar (CPL) data [45], with agreement being within one kilometer. The NAST-M images and optical stereoscopy were used to confirm the rough accuracy of the cloud-top retrieval; see examples discussed in Section 5.4.1.

5.3.1 Nonlinear Constant-coefficient Estimator

The technique estimates a precipitation "state" vector ($\hat{S}$) that contained precipitation cell-top altitude [km], rain rate [mm/hr], and cloud top altitude [km]. The estimator is a weighted sum of first- and second-order polynomials of the difference between the observed and background (clear air) brightness temperatures, where the weights minimize the mean-square error over a training set. Third-order polynomials offered no discernible improvement. The non-cloud background temperatures are easily determined from the NAST-M observations, use of the NAST-M camera, or from GOES-8 imagery. Each estimator was trained for either ocean or land retrievals, but a mixed surface model was necessary for the Florida marshlands in the CRYSTAL-FACE case study.

For each pixel, the retrieved state vector S of dimension three is simply related to the brightness perturbation vector $B - M$, where $(b_i - m_{b_i})$ is the i^{th} vector element of $B - M$ corresponding to channel i, b_i is the observed brightness temperature, and m_{b_i} is the observed neighboring mean background (clear air) brightness temperature:

$$\begin{aligned} \hat{S} &= \mathbf{C} \cdot (B - M) + \mathbf{D} \cdot P \qquad (5.1) \\ P &= [(b_1 - m_{b_1})^2, (b_2 - m_{b_2})^2, \ \ldots \ , (b_N - m_{b_N})^2]^T \end{aligned}$$

The variable N is the number of channels used in the estimation. The maximum N is the total complement of channels on board the NAST-M. For various reasons, *e.g.*, a bad channel during the flight, a subset is usually used in practice. A single element of the $\hat{S}$ vector is:

$$\hat{s}_k = \sum_{i=1}^{N} c_{ki} \cdot (b_i - m_{b_i}) + \sum_{j=1}^{N} d_{kj} \cdot (b_j - m_{b_j})^2. \tag{5.2}$$

5.3.2 Simulation Model

The statistical relationship between brightness temperature and convective precipitation is required to determine the optimal weights found in **C** and **D**, in the minimum mean-squared-error sense. A simple precipitating-cloud model was devised in order to simulate brightness temperatures, which use a simplified hydrometeor profile. In general, the simplified hydrometeor profile approach is usually avoided [69] because of the excessive degrees of freedom within convective precipitation, *i.e.*, the many different profiles involved. One example of a simplified-profile technique is given in Kummerow *et al.* [34]. The success of the retrieval technique presented in this chapter shows that certain assumptions and approximations make the simplified hydrometeor-profile technique very competitive.

First, the Goddard Cumulus Ensemble [63] gives insight into the limits of the profile parameters found in the structure of the convective cell. Then this knowledge is adapted to a simplified model that is used in the radiative-transfer-solution software. Section 5.3.3 evaluates the performance of the single-pixel retrieval by entering the simulated training set into the retrieval and comparing with the true precipitation values. A qualitative test of the retrieval is made by simulating select parts of the GCE model, which are then used to retrieve rain rates that are compared to the model's surface rain rate.

Profile Basis: Goddard Cumulus Ensemble Model

The Goddard Cumulus Ensemble Model is a cloud resolving model that uses sophisticated and realistic representations of cloud microphysical processes and tries to resolve the time evolution, structure, and life cycles of clouds and cloud systems. Output from this model will shape the form and range of values used in the approximated hydrometeor profiles used in this retrieval technique.

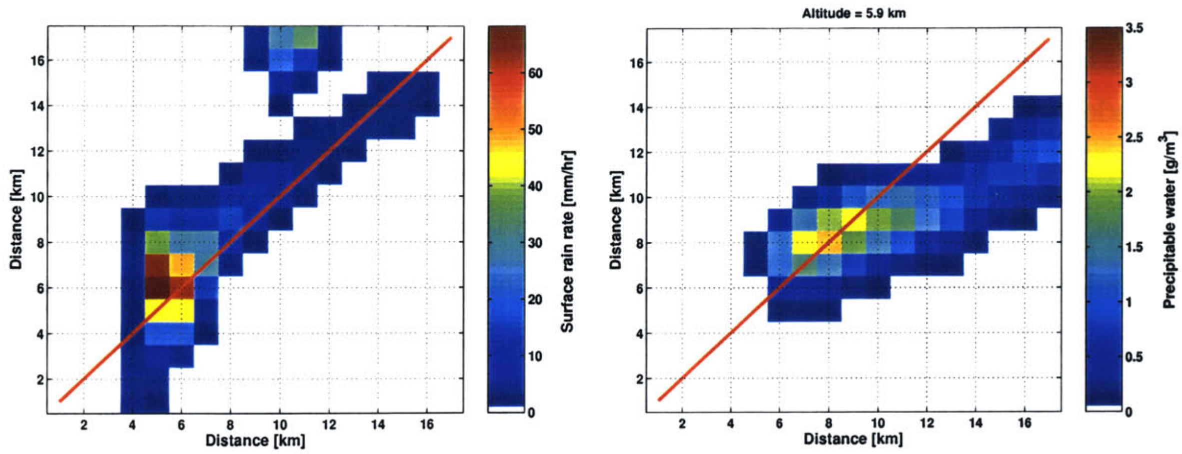

(a) Surface Rain Rate

(b) Total Water Content: Horizontal Slice

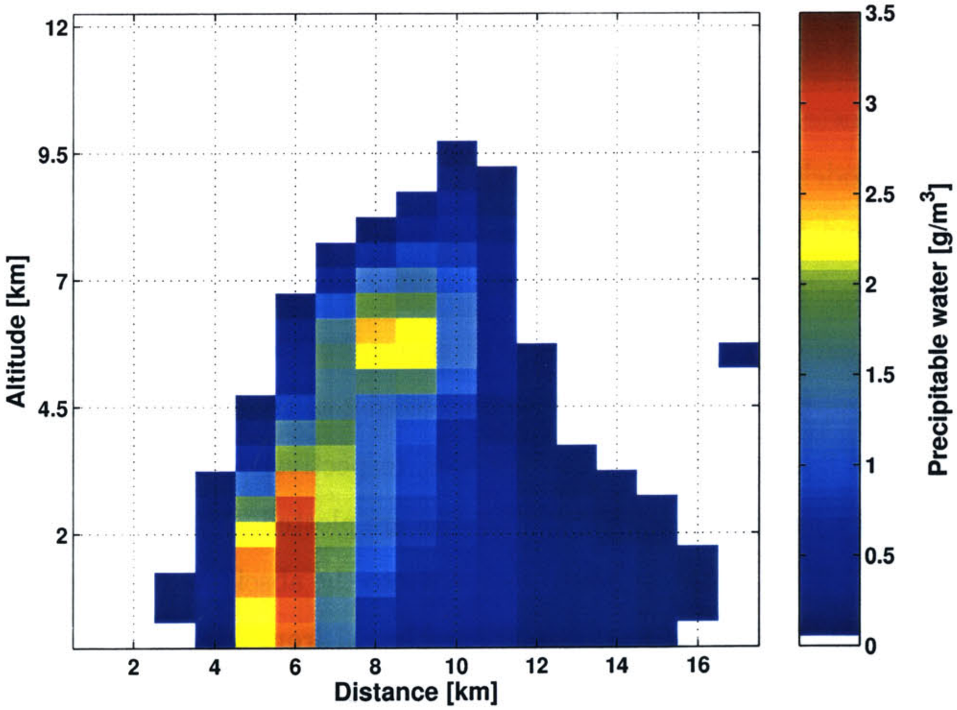

(c) Total Water Content: Vertical Slice

Figure 5-4: Typical Convective cell profile from the Goddard Cumulus Ensemble Model.

First, a subsection of the storm six hours into the hurricane simulation is presented in Figure 5-4. This part of the simulation was chosen because it was a single mature convective cell with a strong anvil blowoff, which is a paradigmatic example. Notice that the images are very similar to the sketch presented in Figure 5-1 of the strong thunderstorm. Figure 5-4(a) is an areal plot of the surface rain rate. A strong convective core is apparent at six kilometers into the abscissa and ordinate. Moving higher into the atmosphere, Figure 5-4(b) is the total precipitating water at a 6-km altitude. Precipitating water includes three states, which are raindrops, snowflakes, or graupel/hail. Clouds particles make up a second category of water (liquid or ice) in the atmosphere, but the droplet sizes are very small ($< 50\ \mu m$ radius). Figure 5-4(c) is a vertical slice down the cell, and the location of the slice is illustrated in Figure 5-4(a) and Figure 5-4(b) by the red line. The convective core is even more apparent at six kilometers, but now the vertical wind shear has pushed the precipitation to the right of Figure 5-4(c).

Two hydrometeor profiles from this cell will help illustrate the principal categories that will be modeled in the next section. Figure 5-5(a) presents the hydrometeor, temperature, and humidity profiles from the convective core (at the 6-km abscissa and ordinate mark). The solid black line is the precipitable water profile, which is the summation of the dashed lines that represents the rain, snow, and graupel profiles. The non-precipitating cloud profiles consist of the solid red and cyan lines, which represent liquid and ice-crystal particles, respectively. On the right-hand side, the matching temperature and humidity profiles are plotted. The second hydrometeor profile (Figure 5-5(b)) is located ten kilometers into the abscissa and seven kilometers into the ordinate. This profile represents the blowoff from the top of the convective core. At this point in the storm's evolution, the precipitation has not reached the surface. The third example in Figure 5-6, which is not part of the above mentioned GCE convective cell, is a very strong convective-core profile that gives an idea on how intense the storms can become.

These examples, and a review of the other profiles in the GCE data set, suggest that the hydrometeor profile can be simplified for use in a radiative transfer solution

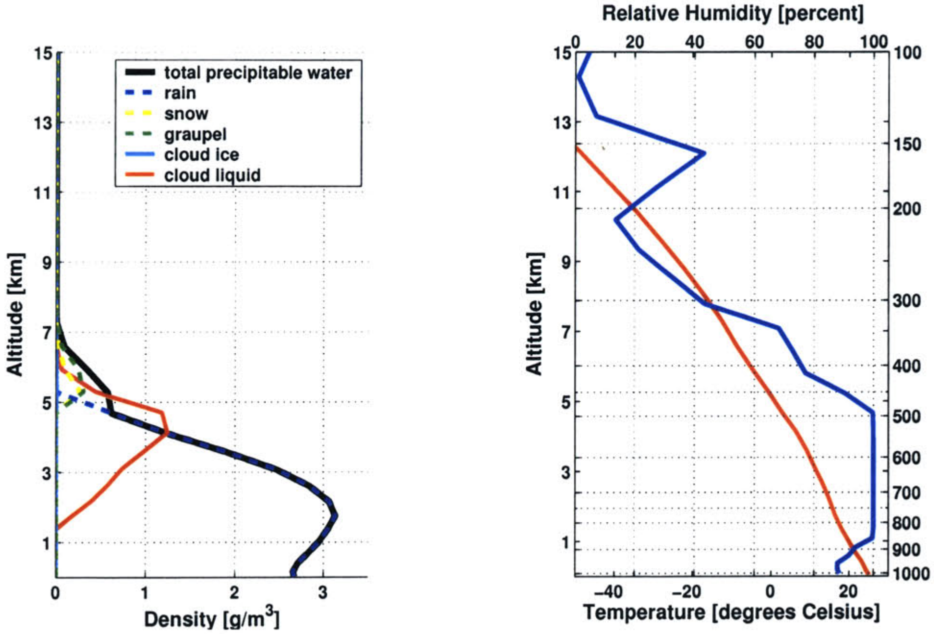

(a) Convective Core

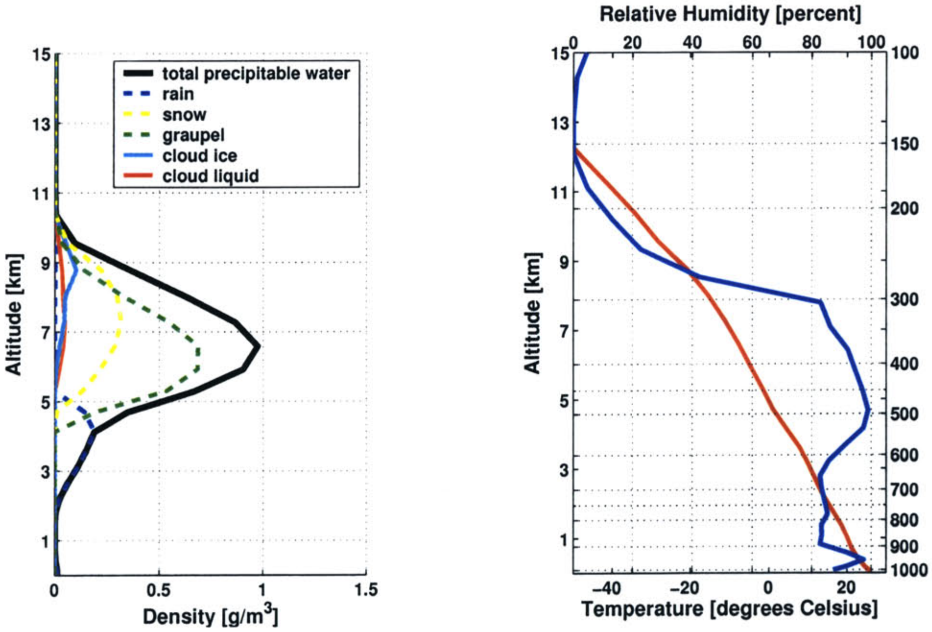

(b) Anvil Blowoff

Figure 5-5: Typical Convective cell profile from Goddard Cumulus Ensemble. In the right-hand figures, red is the temperature profile and blue is the humidity profile.

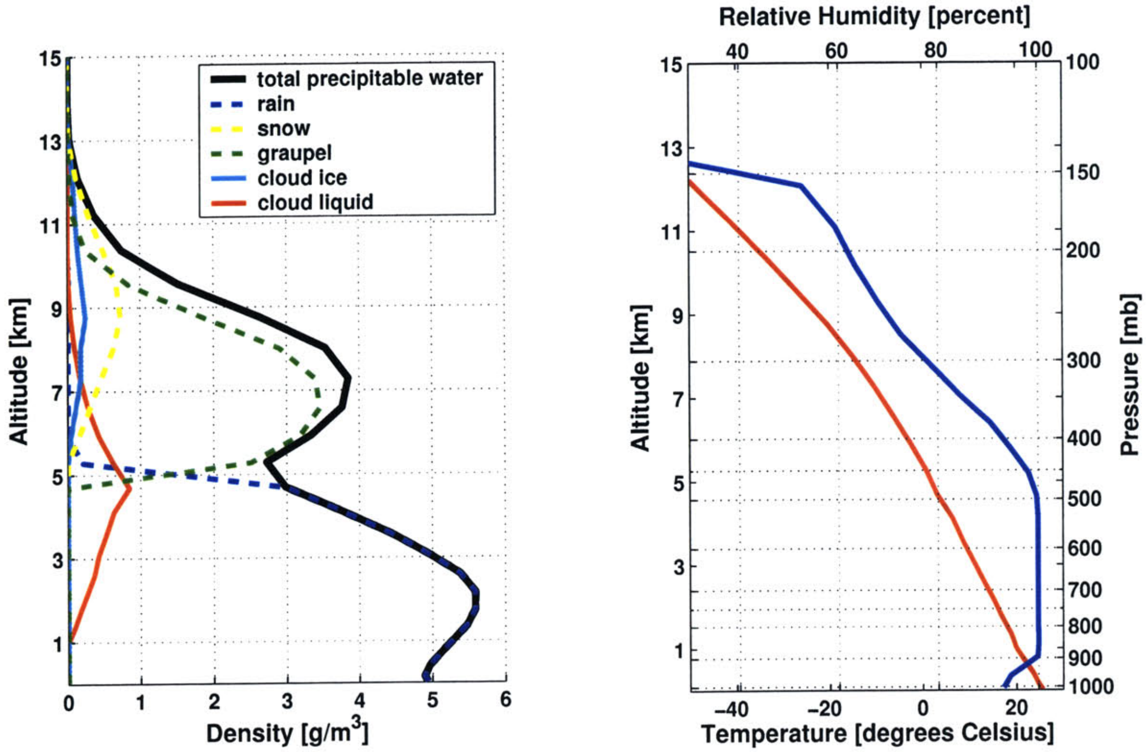

Figure 5-6: Typical Convective cell profile from Goddard Cumulus Ensemble. In the right-hand figures, red is the temperature profile and blue is the humidity profile.

that includes scattering. The next section examines how a large range of convective cell profiles can be simulated in order to derive the statistics necessary for estimating precipitation parameters.

Approximated Convective Storms

The approximation has several important parts. The first part is the radiative transfer solution, which introduces several approximations, *e.g.*, in geometry. The next part involves the simulation's auxiliary parameters, *e.g.*, surface emissivity. Then the hydrometeor profile characteristics are introduced, which leads to how the precipitable water in the hydrometeor profile is related to the parameters in the state vector.

There are several numerical methods for determining brightness temperature from atmospheric profiles [56]. The simulations use a less computation-intensive radiative transfer (RT) solution [50], which uses absorption coefficients from Liebe *et al.* [42]. The solution assumes a planar-stratified atmosphere, as illustrated in Figure 2-3, with an eighteen stream maximum and was given an altitude resolution of 500 meters. This RT solution technique is described in Section 2.3.5. Each stream is given a separate angle θ (θ as shown in Figure 2-3) and assumes azimuthal independence. The stream angles (θ) were at nadir, 60°, and each of the first seven NAST-M scan angles from nadir. This allowed an individual estimator to be implemented for scan angles ranging from nadir to $\pm 50.6°$. Scan angles greater than $\sim 50°$ were discarded. The RT solution uses a two-phase approach to the density of the precipitation. When the temperature is above freezing, the precipitation is treated as liquid water. Below freezing, the precipitation is given a density ranging from snow (0.1 g/cm^3) to ice (1 g/cm^3), and the density is known as the ice factor. The output of the RT solution is given for horizontal and vertical polarization, but it should be noted that there is no mixing of polarizations within the solution. The polarizations were combined using this formula:

$$T_b(\theta) = T_b^V \cdot \sin^2(\theta) + T_b^H \cdot \cos^2(\theta). \tag{5.3}$$

T_b^H is the horizontal polarization, and T_b^V is the vertical polarization.

The approximation requires temperature, pressure, and humidity profiles. The temperature and pressure profiles were the same regardless of the precipitation state. The precipitating- or non-precipitating-cloudy humidity profile was based on the clear-air humidity profile, except that the relative humidity was raised to 100 percent when a cloud was present. The clear-air profiles were chosen to closely match the deployment conditions. This was accomplished by either using a nearby radiosonde, and when the radiosonde was unavailable, by averaging a subset of the TIGR3 radiosonde ensemble [23]. The subset was chosen from the TIGR3 radiosondes by matching the latitude and month of the deployment. When simulating clear-air or non-precipitating cloudy profiles, the temperature and humidity profiles were perturbed to simulate the natural variation of atmospheric conditions. Approximately 300 clear-air variant profiles were included in the training set. Surface emissivity was computed for three conditions, which were water (ocean), marshland (water and land mixture), and land. The water surface emissivity was calculated using the fast emissivity model (fastem [22]), which is frequency dependent. The land surface emissivity was modeled as a Gaussian random variable with a mean of 0.92 and a standard deviation of 0.05. The land surface emissivity was kept equal to or below unity and was frequency independent. Marshland was modeled as a weighted sum of the water and land surface emissivity, where the land portions ranged from 40 to 70 percent. The surface temperature came from the radiosonde or a NOAA oceanic surface water temperature map. A Gaussian zero-mean two-Kelvin-standard-deviation random variable was added to the surface temperature for the clear-air simulations.

The most crucial aspect of the approximation is the hydrometeor profile. The hydrometeor profile is the volumetric density of water (precipitating or non-precipitating), or total water content (TWC), as a function of altitude in grams per cubic meter (g/m^3). The water is assumed to be spheres of different diameters, and the diameters can range from the smallest cloud particles ($< 100\ \mu m$) to large raindrops ($\sim 4\ mm$). The simplified hydrometeor profiles are illustrated in Figure 5-7. The hydrometeor profile model has a constant total water content (g/m^3) up to the precipitation cell-top altitude. The profile is varied by changing the highest altitude of the precipitation (precipitation cell-top altitude), a single value of rain rate, and the density for the frozen water above the freezing point (ice factor [g/cm^3]). The Marshall-Palmer model [43] relates the total water content to rain rate, R_r (see Section 2.3.4):

$$TWC = \frac{8\,\pi}{(4100\,R_r^{-0.21})^4}\ \left[\frac{g}{m^3}\right]. \tag{5.4}$$

A single rain rate value determined the TWC of the entire profile, which is marked "total precipitating water" in Figure 5-7(a). The rain rate also determines the drop-size distribution for the entire column through Equation 2.34, but when the M-P model was compared to flight data, the Marshall-Palmer distribution lacked larger radii [64]. For the strong convective mission CRYSTAL-FACE, the M-P was modified to include larger radii and the rain rate ranged between 0.1 mm/hr to 100 mm/hr. The modification moved the peaks of the M-P distributions in Figure 5-9(a) toward the right. The shift was increased linearly from 0.01 to 0.15 mm as the rain rate

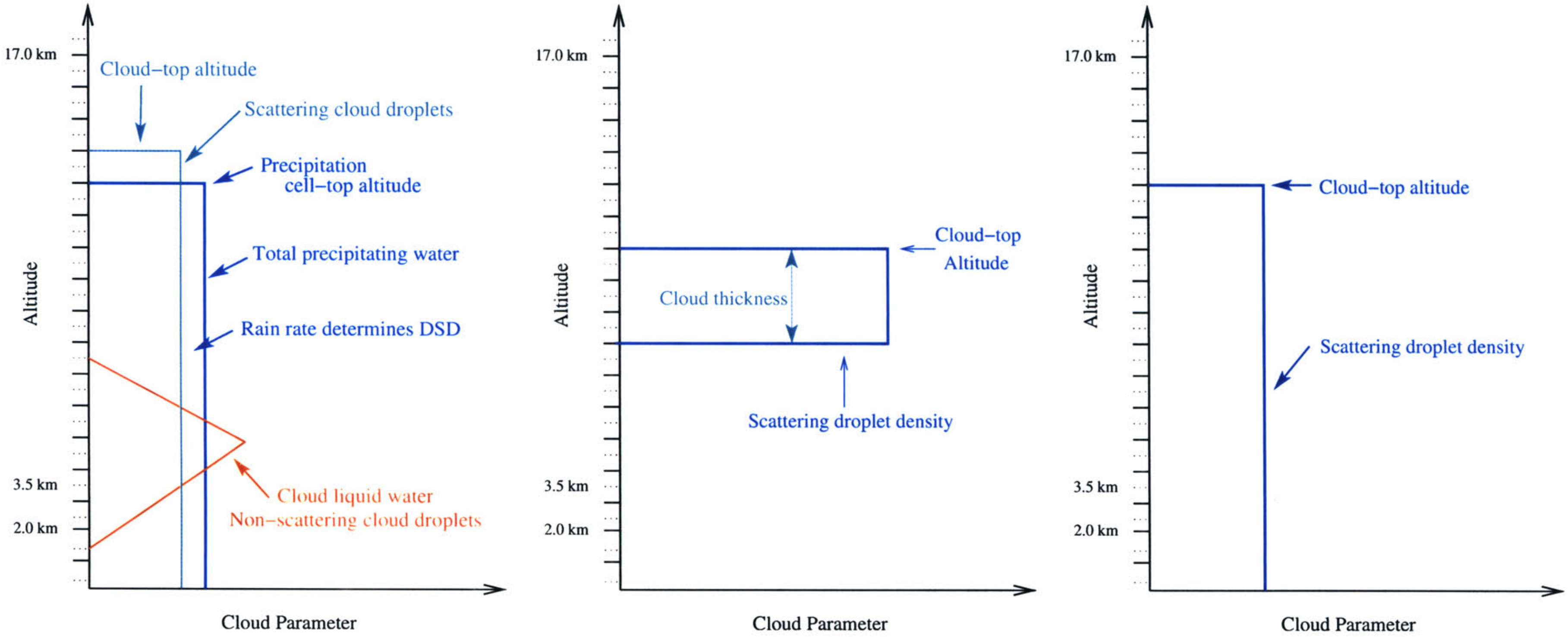

(a) precipitating-cloud profile.

(b) non-precipitating-cloud profile.

(c) anvil-cloud profile.

Figure 5-7: Illustrations of the simplified hydrometeor-profile model. See code in Appendix C.3 and C.4.

increased. The modification makes Equation 2.34 become:

$$p(r) = N_o \, e^{-\frac{2\,b}{1+c2b}\,r} \text{ and } b = 4100\, R_r^{-0.21}. \tag{5.5}$$

The c was dependent on the rain rate (These were the rain rates used for the CRYSTAL-FACE simulations):

Rain rate	0	0.5	0.8	1	2	3	4	5	8	10
c	0	0.01	0.02	0.02	0.03	0.03	0.04	0.05	0.05	0.06
Rain rate	12	15	18	22	25	35	50	75	100	
c	0.06	0.07	0.08	0.09	0.09	0.1	0.12	0.14	0.15	

Two examples are presented in Figure 5-8. For the squall lines in PTOST, the M-P remained unchanged and the rain rate ranged from 0.1 to 35 mm/hr. The drop-size distribution is plotted in Figure 5-9(a). The cell-top heights ranged uniformly from 2 km to 17 km in 1-km increments. Each profile was simulated with an ice factor of 0.1, 0.4, 0.7, and 1 g/cm^3. This model roughly fulfills a range of convective-cell conditions encountered in the field. For a sample of more realistic convective-cell profiles measured by ground based radar, see [54].

The tbscat software [50] divides hydrometeors into two regimes, and the difference is whether the droplet scatters or not. The non-scattering droplets, which have very small diameters, are included in the variable called cloud liquid water and labeled in Figure 5-7(a). The 425-GHz system is sensitive to very small droplets and so most of the cloud droplets were in the scattering regime. The scattering cloud droplets are also marked in all three profile types, but the cloud drop-size distribution has much smaller radii [67, pg. 306] than the precipitating radii. Like the precipitating hydrometeors, the scattering droplets were characterized in terms total water content per radius $\left(\frac{g/m^3}{mm}\right)$. The cloud distribution is also presented in Figure 5-9(a) and is the same for either the precipitating or non-precipitating clouds. The third profile is an attempt to model the anvil blowoff of a convective cell (Figure 5-7(c)). As the the larger hydrometeors fall out of the vertical wind shear, the drop-size distribution consists smaller and smaller radii. This is represented in a different drop-size distribution

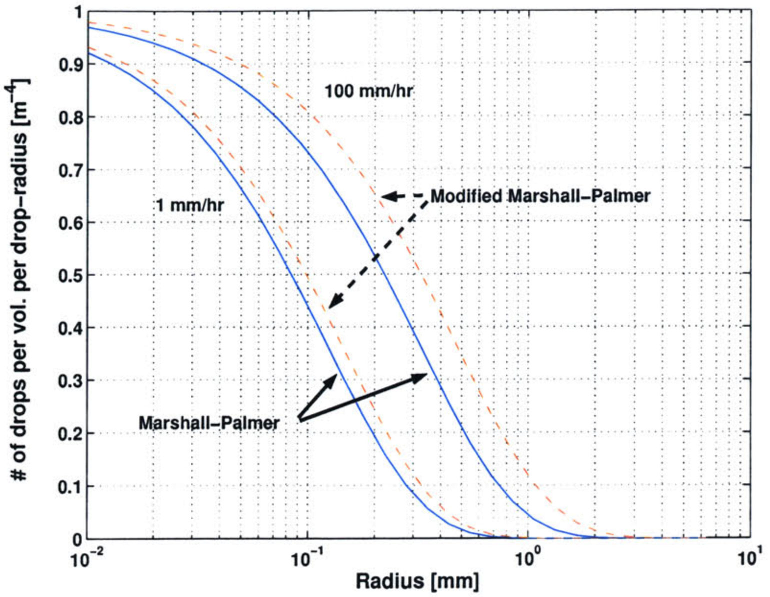

Figure 5-8: Examples of the modification to the Marshall-Palmer drop-size distribution. The traditional and modified drop-size distributions are plotted for rain rates of 1 and 100 mm/hr.

and is plotted in Figure 5-9(b). This distribution simulated the best fit to the actual brightness temperatures in an anvil cloud, and the shape was arbitrarily chosen, but was similar to other non-precipitating cloud models [67]. The non-precipitating and anvil cloud have no non-scattering cloud droplets, and the smallest diameter modeled was 0.2 μm.

There are three variables estimated in the state vector. As mentioned in Section 5.3.1, they are the precipitation cell-top altitude, rain rate, and cloud-top altitude. The precipitation cell-top altitude is defined as the altitude marked in Figure 5-7(a), but the cloud-top altitude is found in all three profiles and is defined as the highest altitude of the small cloud droplets. Cloud-top altitude is also marked in all the profiles, and it should be noticed that the cloud particles are one kilometer higher than the precipitation for all altitudes in the precipitating profiles (Figure 5-7(a)). The precipitating-cloud profile was also modeled to have a layer of cloud particles that varied from one to four kilometers thick, and the results did improve the error in a few pixels, but did not alter the overall error.

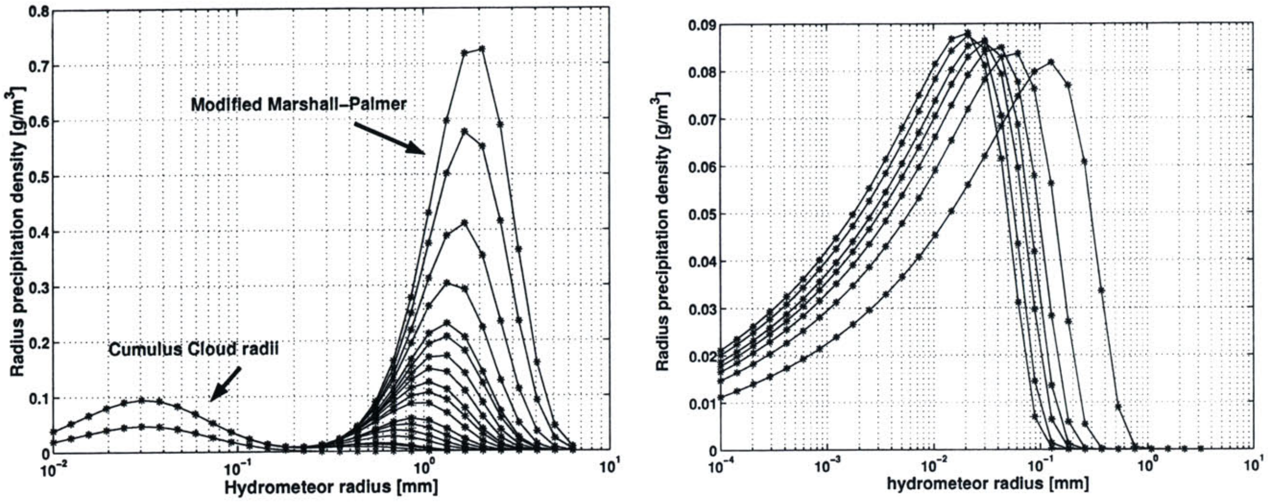

(a) Precipitating profiles' drop-size distributions

(b) Anvil profile's drop-size distributions

Figure 5-9: Drop-size distributions used in the atmospheric model.

5.3.3 Performance

This section presents two techniques to evaluate the retrieval technique before actual aircraft data is used. One quantitative technique to test the success of a statistical estimator is to compare the training data set with the truth. The other technique employs the GCE ensemble by first simulating brightness temperatures from portions of the cloud-resolving model. Then the brightness temperatures are used to retrieve precipitation parameters that allow comparisons back to the GCE model truth. Actual aircraft data from two deployments are presented as case studies in Section 5.4.

Evaluation using Training Set

To evaluate the overall estimator, the simulated brightness temperatures from the approximated cell model were used as inputs and compared with the correct output. Figure 5-10 summarizes the results for each of the state vector variables for different surface conditions. The dash-dot line is the ideal input/output relationship, *i.e.*, it has a slope of one. The solid lines represent the mean statistic from the simulation ensemble at a given truth value, then select mean values have their standard devia-

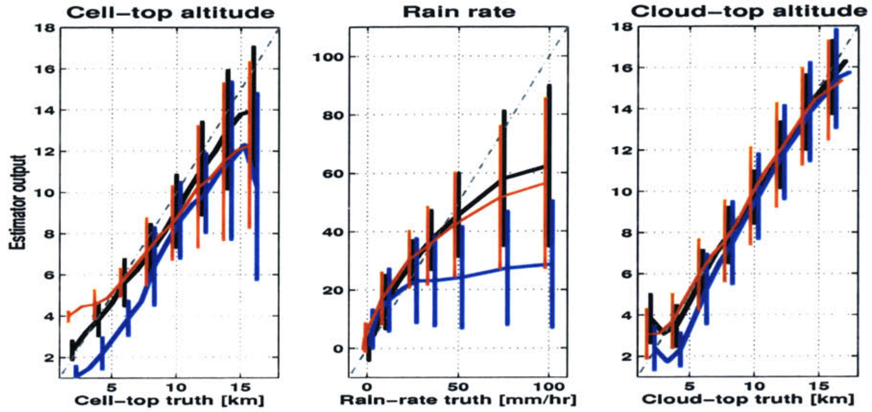

(a) water surface

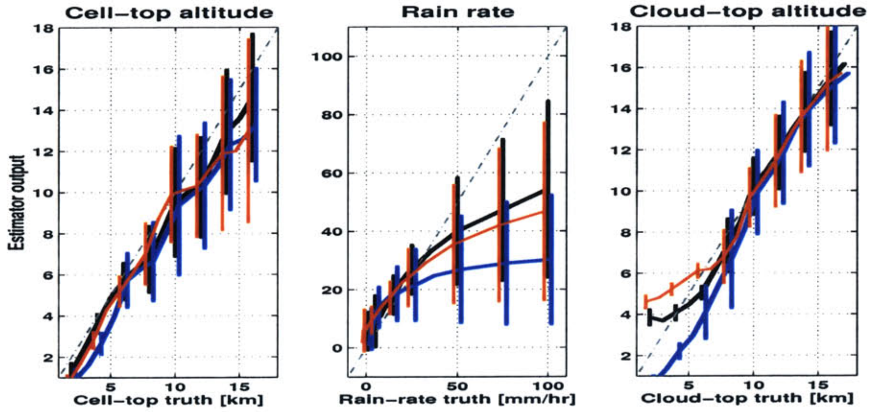

(b) water/land mix

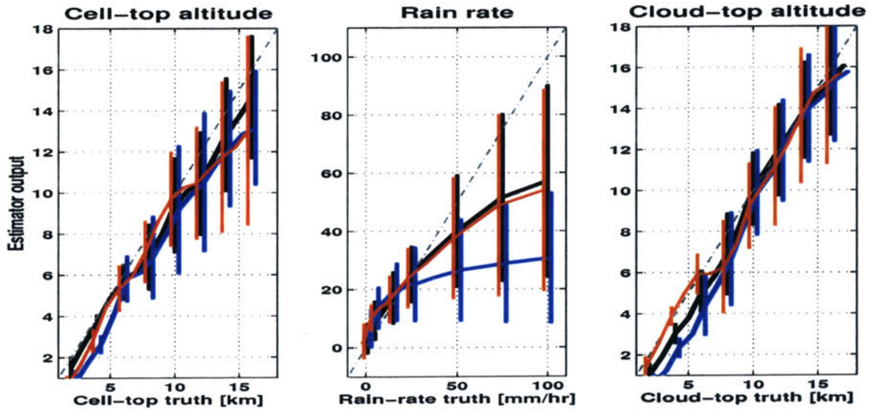

(c) land surface

Figure 5-10: Nonlinear estimator comparison between a full complement NAST-M instrument (black), an estimator limited to the 183- and 425-GHz channels (blue), estimator limited to 54- and 183-GHz (red).

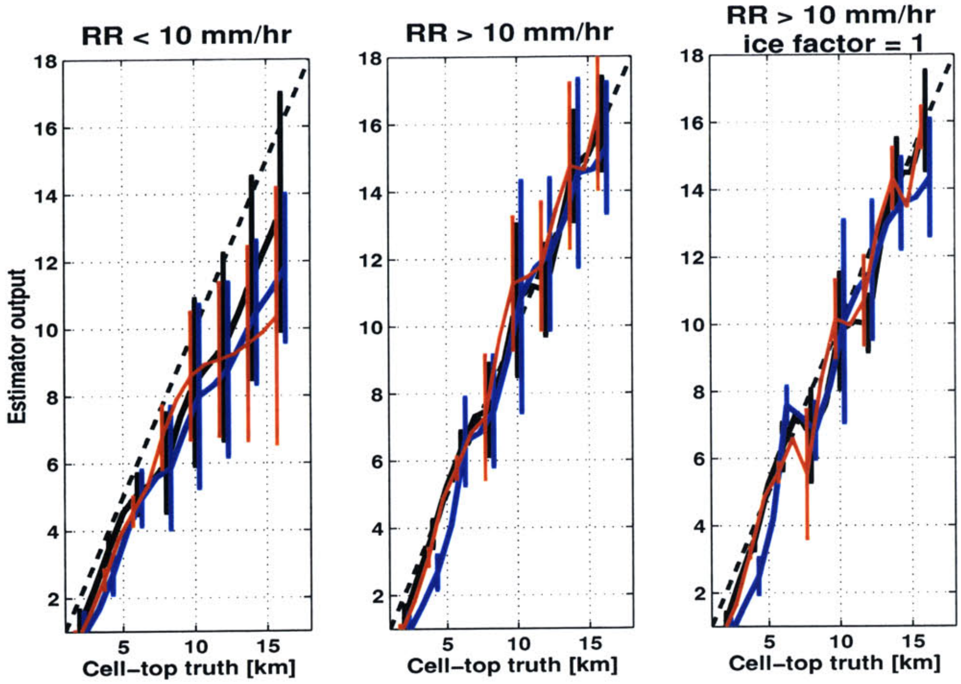

Figure 5-11: Estimation of cell-top altitude over land with a selective subsets of the training ensemble.

tion given as error bars. The different colors mark different radiometric systems. For example, the black line corresponds to a system using all of the NAST-M channels with the exception of the three most opaque 118-GHz channels (see Table 3.1, 3.2, 3.3, and 3.4). The other two systems are a 183/425-GHz system (blue line) and a presently operational AMSU-like system using the 54- and 183-GHz spectrometers. In order to limit the influence of instrument noise, each channel was given a radiometric sensitivity of 0.4 Kelvin (RMS) for this comparison. The local oscillator frequencies were set to their optimal values, and all channels were made operational with the exception of the three most opaque 118-GHz channels.

The results show that all three radiometric systems are adequate for cell-top and cloud-top altitude estimation over all the surfaces presented, but the accuracy at the higher altitudes is very poor. Figure 5-11 investigates some of the sources of these inaccuracies in measuring cell-top altitude. Some of the trouble comes from the low rain rates that have fewer and smaller hydrometeors to scatter the electromagnetic energy. The first two plots on the left-hand side divide the statistic's training-set ensemble between rain rates equal to and below 10 mm/hr and those greater than 10 mm/hr . The third plot limits the statistics to rain rates greater than 10 mm/hr and where the ice factor was set to ice. Ice has a higher reflectivity, and is very prominent in strong convective cores, which could make the precipitation easier to sense. The results show that in general these insights are true. The standard deviation of the retrieval error does decrease as the ensemble is reduced. It is realistic to assume that the convective core has rain rates greater than 10 mm/hr and that the frozen particles are ice.

Next, the estimation of rain rate will be discussed. Similar to the analysis of precipitation cell-top altitude, the rain-rate statistical ensemble was reduced and the results are plotted in Figure 5-12, but retrievals over both land and water were included. The results for retrieving rain rates over land below five kilometers were extremely poor, but remarkably better over water. This is credited to the advantage of having a very reflective surface, because the 183/425 combination did not gain much improvement with the change in surface emissivity. The window lower-frequency channels have the advantage, because the hydrometeor's emission against the reflective surface is more visible [69]. Water becomes less reflective as frequency increases. It is assumed that the retrievals have more difficulty retrieving under five kilometers because of the limited number of weighting functions that penetrate to the lowest five kilometers and the lack of the strongly scattering ice.

Evaluation using Goddard Cumulus Ensemble (GCE) Model

A qualitative evaluation of the retrieval technique was performed within a subsection of the GCE model data. The convective cell presented in Figure 5-4 was converted pixel by pixel to brightness temperature with almost the same simulation technique presented in Section 5.3.2. The main difference was that the cloud particles did not scatter, and therefore the scattering radii were limited to the precipitating hydrometeors in the M-P distribution. Also, the GCE model included three densities for the frozen particles, so a modified form of tbscat software program was used that had an independent ice factor variable for each precipitation level above freezing.

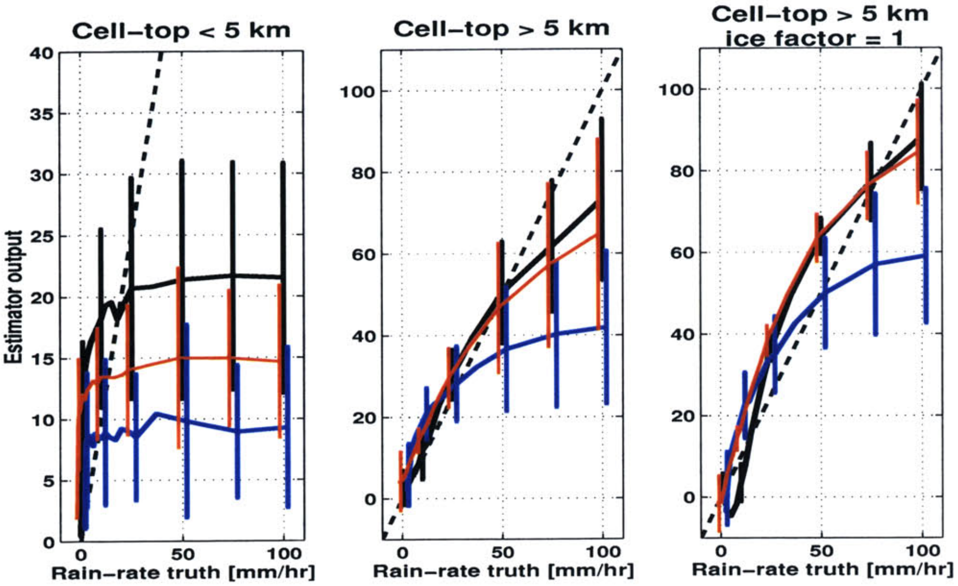

(a) land surface

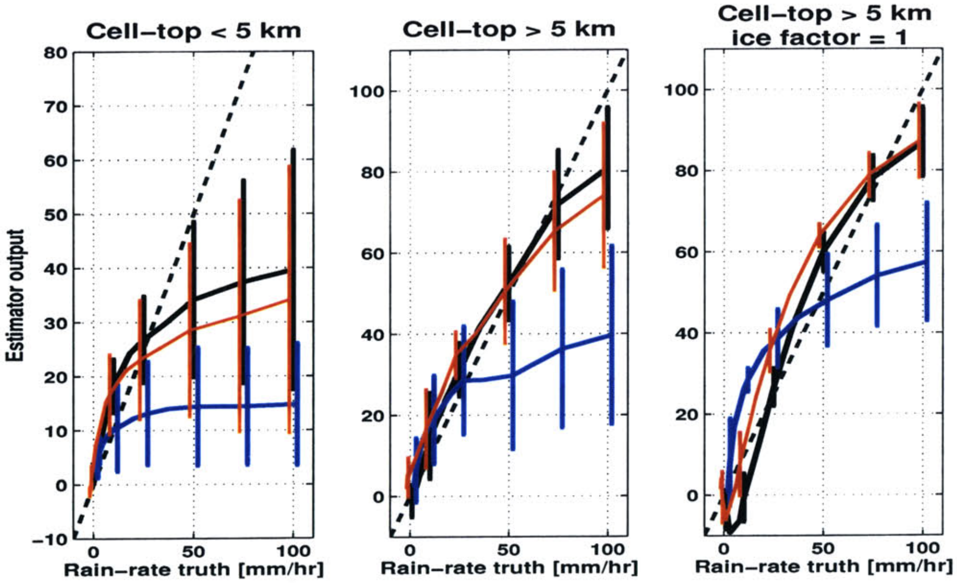

(b) water surface

Figure 5-12: Retrieval statistics of rain rate using a selective subset of the training set ensemble.

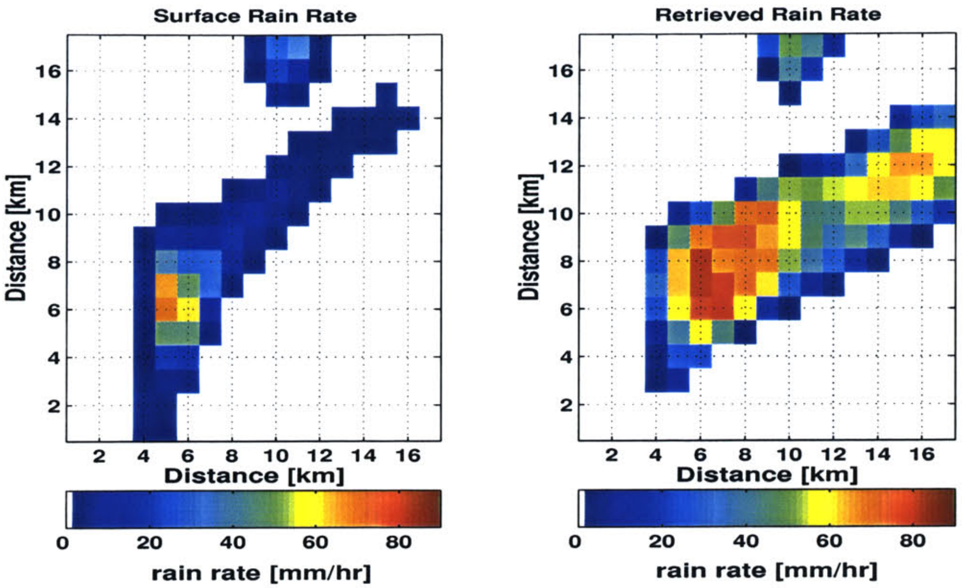

Figure 5-13: Rain-rate retrieval compared to GCE model surface rain rate.

This allowed the simulation to have a graupel layer under a snow layer, as hinted at in Figure 5-6, which is commonly encountered and often modeled in strong convection. The retrieval-technique training ensemble used with the GCE model consisted of precipitating and non-precipitating cloudy profiles, but not anvil clouds. Because the simulation lacked cloud droplet scattering, which are necessary for the 425-GHz channels, the anvil cloud profiles only confound the retrieval,*i.e.*, increase the error of the precipitation cell-top altitude.

Figure 5-13 presents the result of the rain-rate retrieval for one convective event and gives the GCE model's surface rain rate for comparison. This NAST-M retrieval technique measures the hydrometeors throughout the atmosphere, and some morphological discrepancies are expected as some precipitation has yet to reach the ground. Figure 5-4(b) and 5-4(c) show the precipitable water aloft, which is also measured by this retrieval technique. Figure 5-14 gives the GCE model's truth for the altitude of the precipitation. The hydrometeor profile's cell-top altitude does not have a well defined beginning when compared to the boxcar of the approximated profile (see Figure 5-5(b) compared to Figure 5-7(a)). The plot on the left-hand side of Figure 5-14 is the altitude at the very top of the precipitation. The general morphology is the same, but the absolute value is different. The differences are easily within the error

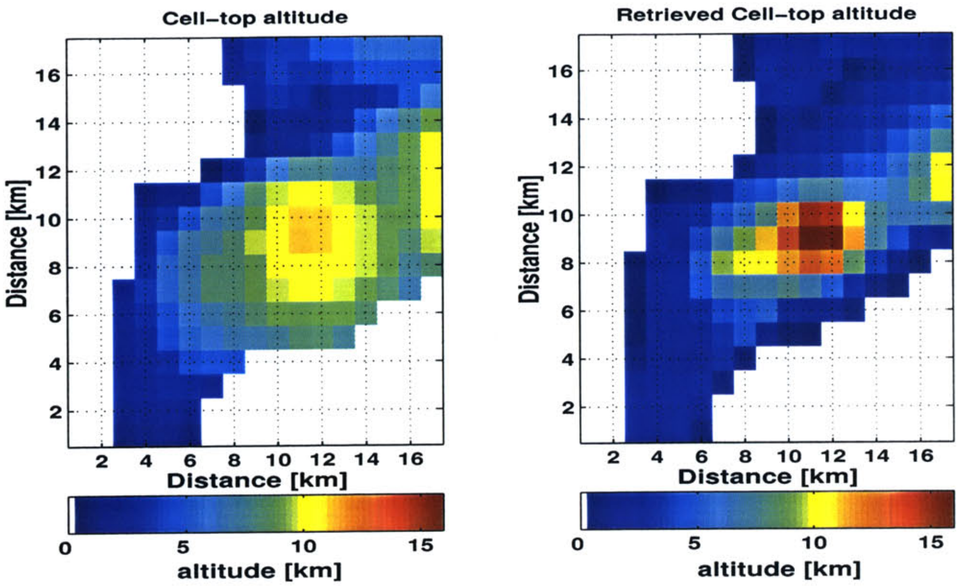

Figure 5-14: Precipitation cell-top altitude estimation compared to GCE model truth.

bars from the best-case situation in Figure 5-11.

5.4 Case Studies

This section presents case studies, which will cover two field deployments and three convective cells. NAST-M brightness temperatures and precipitation-parameter retrievals will be compared with available visible, infrared and radar imagery of clouds and precipitation. An error analysis is given for each convective cell.

5.4.1 PTOST

The NAST-M instrument flew on the ER-2 aircraft for a deployment based in Honolulu, HI. The deployment was called the Pacific THOR*pex* (THe Observing-system Research and *p*redictability *ex*periment) Observing System Test (PTOST 2003). On a transit flight during PTOST 2003, the ER-2 flew over scattered thunderstorms. This section will present retrievals and error analysis for two convective cells. First, brightness-temperature perturbations from the convective cells are presented along with the retrievals. Next, the convective cells go through actual-versus-simulated brightness temperature analysis, which categorizes the NAST-M pixels as precipitat-

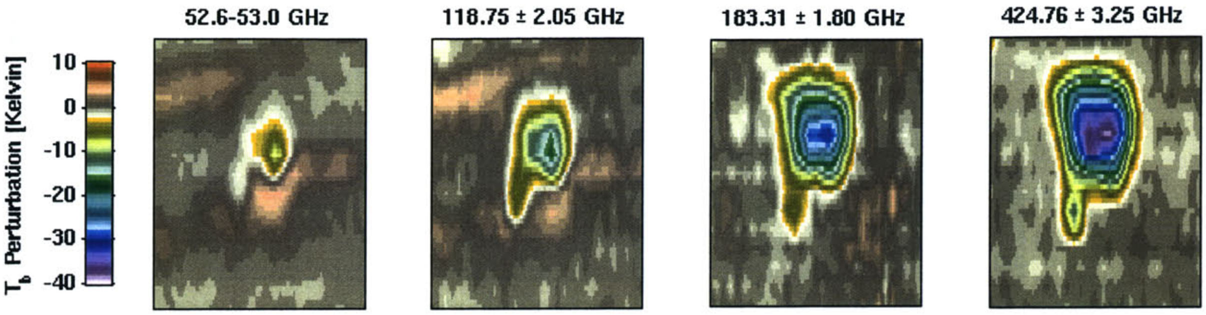

(a) Channels with similar clear-air altitude-peaking weighting functions

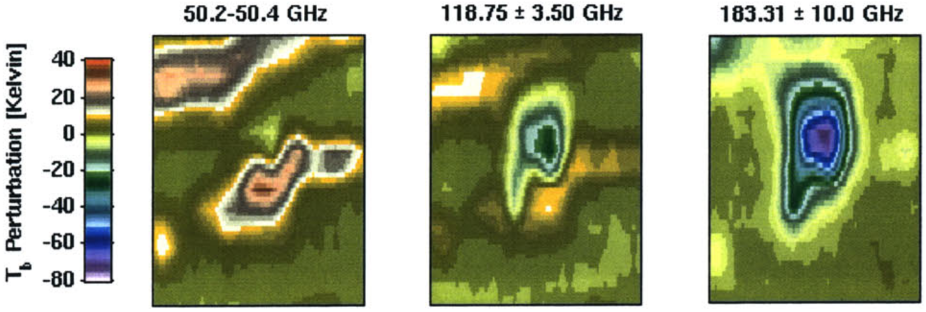

(b) Window channels

Figure 5-15: Brightness temperature perturbations for a convective cell (Cell I) on March 14, 2003 over ocean during PTOST. The vertical axis is approximately 50 km and the horizontal axis is 35 km.

ing, non-precipitating, or clear air, and quantifies the distance between the measured brightness temperature and the nearest simulated brightness temperature profile in the training set in a root-mean-squared sense. Problematic pixels are presented and discussed.

Brightness Temperature Observations

Brightness temperature perturbations are presented for Cell I in Figure 5-15 and for Cell II in Figure 5-16. A brightness-temperature baseline, from nearby clear-air data, was subtracted from the calibrated brightness-temperature image to create the perturbation images shown in the figures. In Figure 5-15(a) and Figure 5-16(a), a channel

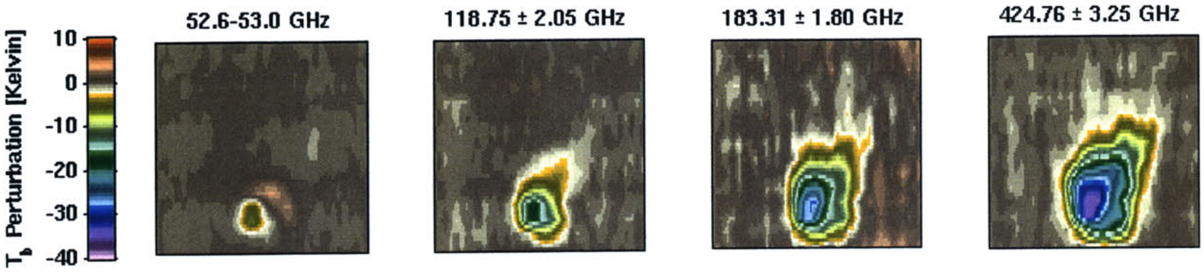

(a) Channels with similar clear-air altitude-peaking weighting functions

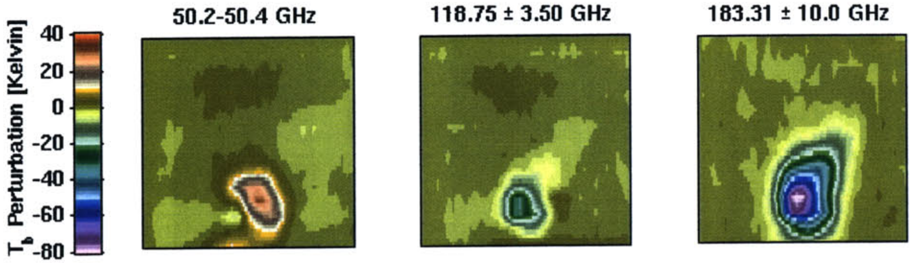

(b) Window channels

Figure 5-16: Brightness temperature perturbations for a convective cell (Cell II) on March 14, 2003 over ocean during PTOST. The vertical axis is approximately 50 km and the horizontal axis is 44 km.

from each spectrometer was chosen that matched the clear-air brightness-temperature baseline of the 425-GHz window channel, which peaks around the freezing point. This assured that the channels were viewing approximately the same clear-air altitude within the atmosphere. The window channels of the other three spectrometers were added for comparison in Figure 5-15(b) and Figure 5-16(b), respectively. The brightness-temperature images use only the inner fifteen angles of the swath (±50.4°), which covers a cross-track width of approximately 50 km. The aircraft flew across the image from left to right. Cell I is 30 scans or 35 km long, and Cell II is 38 scans or 44 km on the surface.

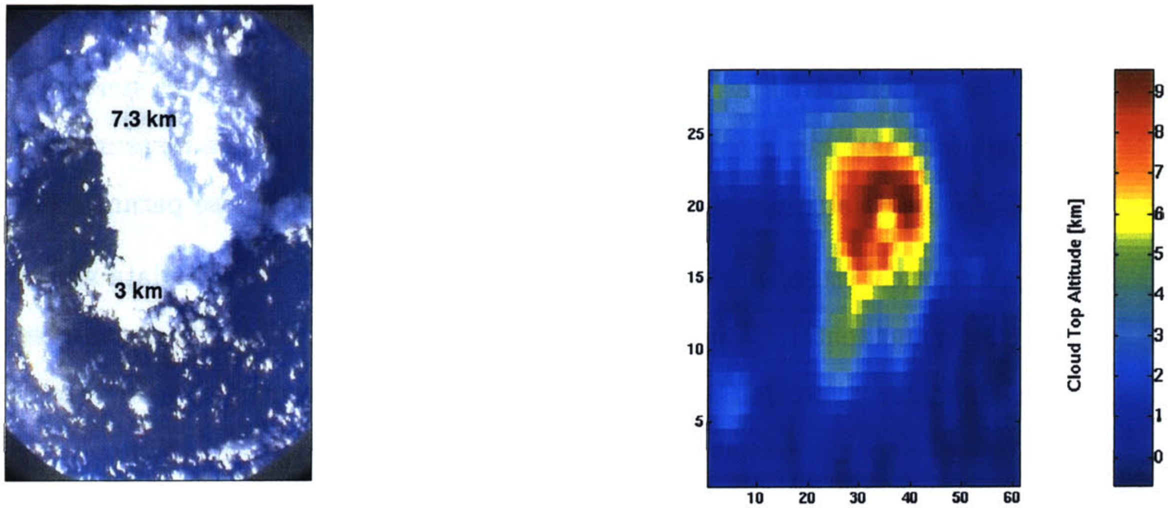

(a) NAST-M camera at

(b) Cloud-Top Estimate

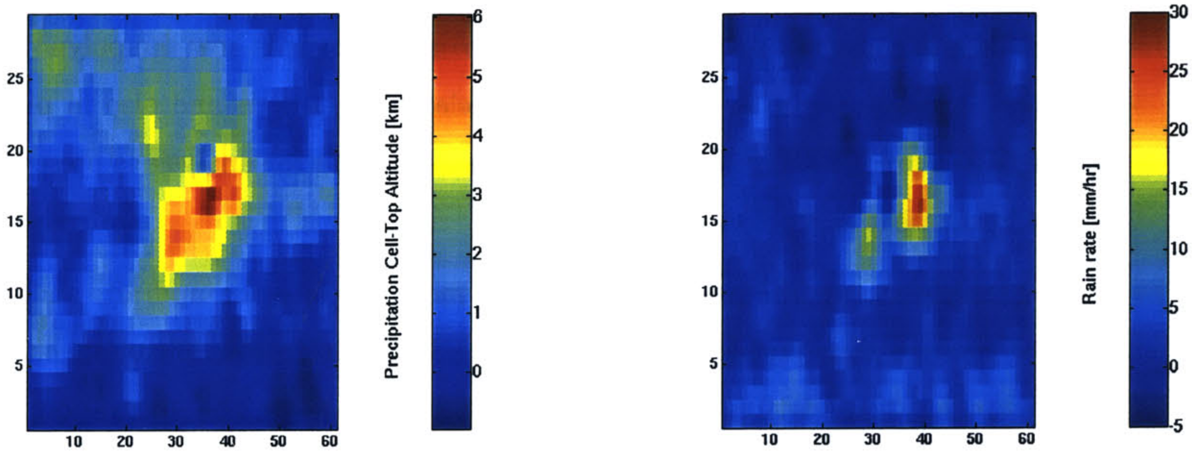

(c) Cell-Top Estimate

(d) Rain Rate Estimate

Figure 5-17: PTOST convective cell (Cell I): precipitation-parameter retrievals using the polynomial estimator. A NAST-M video image is also included.

Retrievals

The brightness temperatures for these two convective cells served as inputs to the precipitation-parameter estimators described earlier in this chapter, and they are presented in Figure 5-17 and Figure 5-18. The retrievals were bi-linearly interpolated, and then filtered with a 3x3-pixel arithmetic mean filter. Optical stereoscopy gives the approximate cloud-top altitudes, but the lack of any viable measurement of rain rate or cell-top altitude allows only qualitative analysis of those parameters.

The optical stereoscopic technique used on the NAST-M video data was evaluated against coincidental Cloud Physic Lidar (CPL) data [45], with agreement within one kilometer. For Cell I, the optical stereoscopy measured the cloud-top altitude at 7.3 km and the retrieved cloud-top altitude gives good agreement, but seems to overestimate the altitude in some areas. The Cell II retrieval generally follows the stereoscopic cloud-altitude gradient, but disagrees on the anvil blowoff altitude. The retrieval shows the anvil tail at a lower altitude, while the stereoscopy measures a gain across the cloud. The retrieval does recognize the general shape of the anvil tail, but fails to correctly measure the altitude. Another issue is how the polynomial estimator estimates negative rain rates within clear-air portions and also in pixels that register a precipitating cell. Later in this section, an error analysis is presented that addresses this issue.

In a thunderstorm, the inflow brings warm moist air into the updraft, and the hydrometeors are then pushed off the updraft and fall within the downdraft or out into the anvil. Figure 5-19 is an illustration of a squall line. In the illustration, the gust front separates the rainshaft/downdraft and the updraft while the vertical wind shear blows the anvil back over the updraft. The observed microwave brightness-temperature perturbations may also suggest the location of potential gust fronts. In Figure 5-15 and Figure 5-16, the brightness-temperature images of the 54-GHz channels over ocean show a warm perturbation next to a cold perturbation. The cold perturbation in the 54-GHz channels is due to large-diameter hydrometeors within the rainshaft, which are lacking in the warm 54-GHz perturbation (labeled the "rain-free

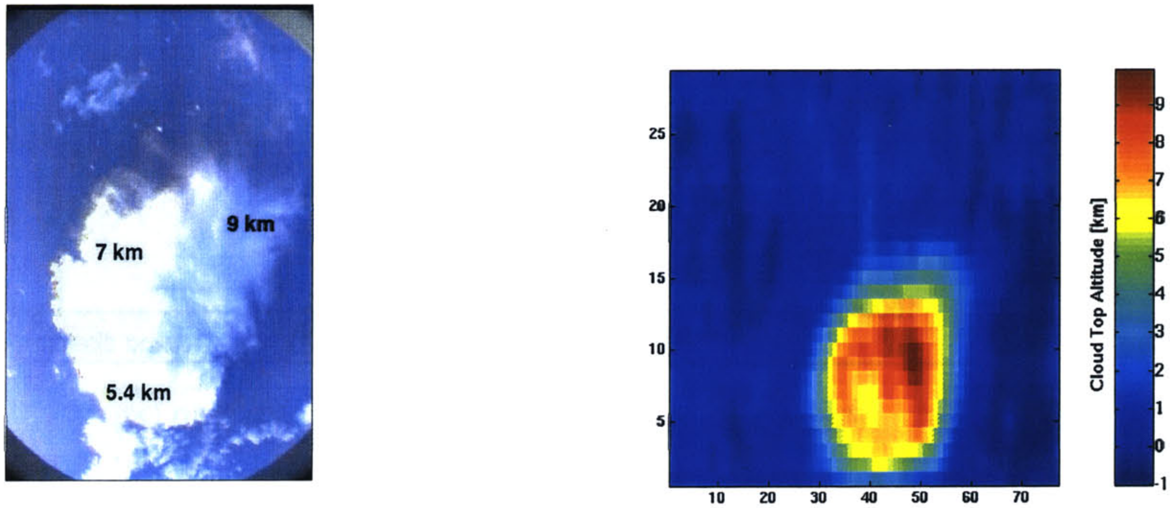

(a) NAST-M camera

(b) Cloud-Top Estimate

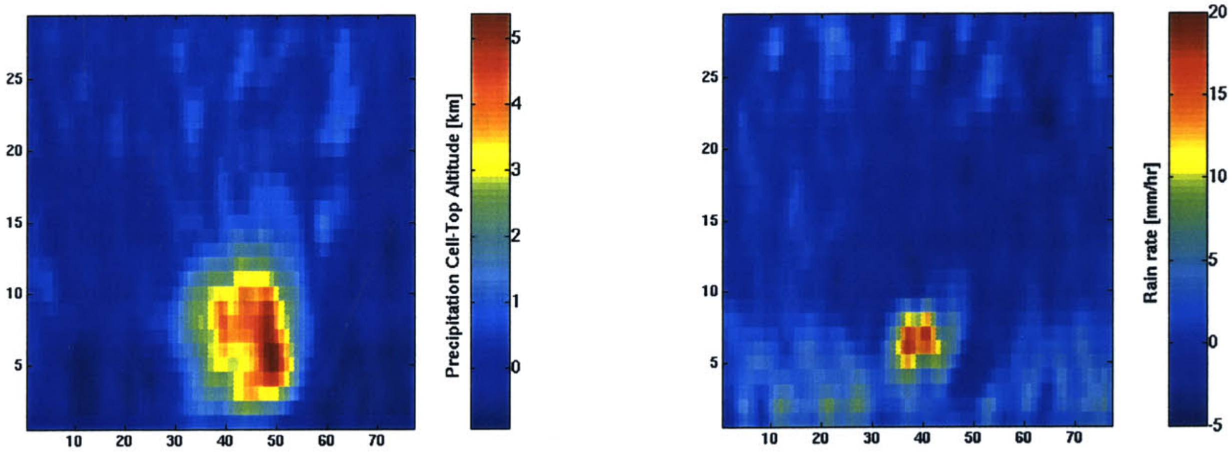

(c) Cell-Top Estimate

(d) Rain Rate Estimate

Figure 5-18: PTOST convective cell (Cell II): precipitation-parameter retrievals using the polynomial estimator. A NAST-M video image is also included.

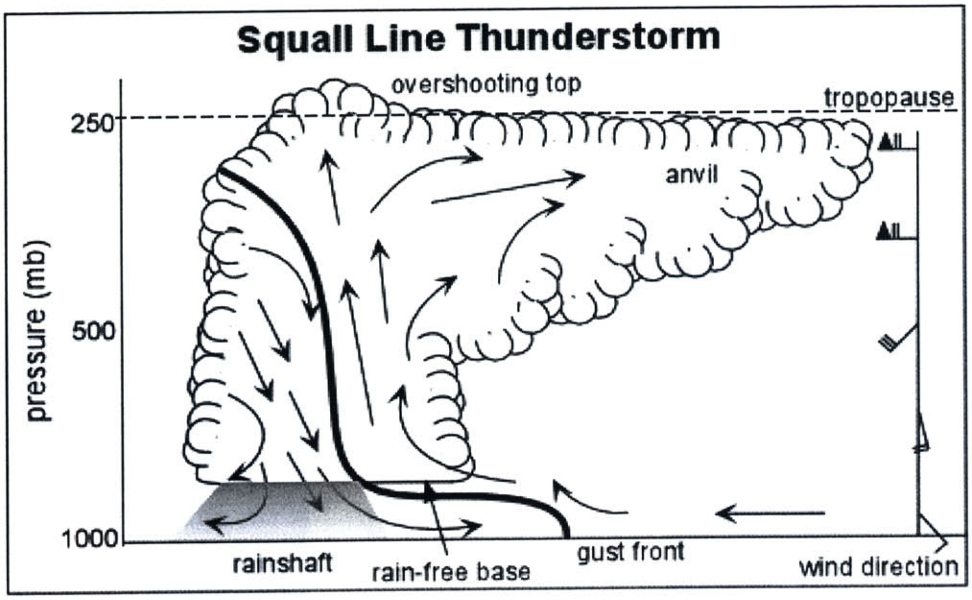

Figure 5-19: Squall line Illustration from WW2010 [27]

base" in Figure 5-19). The warm perturbation is most likely due to the emission of hydrometeors too small to significantly scatter the 54-GHz channels. The direction of the anvil blowoff seems to be different for these two cells. In Cell I, the vertical wind shear seems to go from the warm toward the cold perturbation, which is identified by the increase in the cold perturbation as frequency is increased. On the contrary, Cell II has a vertical wind shear that goes from the cold toward the warm perturbation. The higher-frequency radiometric signatures cover both perturbations, and the relatively long wavelengths of the 54-GHz are unaffected by the smaller hydrometeors and can penetrate to lower portion of the updraft. The knowledge inferred from Cell II agrees with the schematic in Figure 5-19, while Cell I follows a much weaker version of the storm in Figure 5-1. Figure 5-20 gives a closer look at the potential gust front. The opaque 54-GHz channel perturbation (dashed line) is plotted along with the rain-rate retrieval (solid line). In both images the cold perturbation goes below negative six Kelvin and the warm perturbation is approximately three Kelvin. The precipitation is retrieved within the cold perturbation and in between the minimum-maximum brightness-temperature pairs.

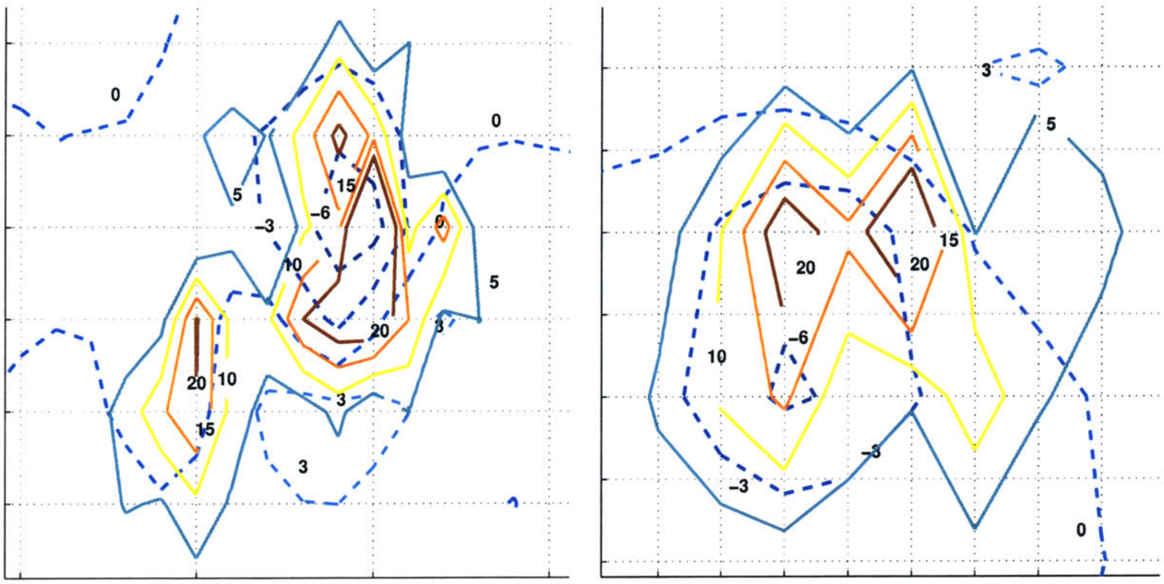

(a) Cell I

(b) Cell II

Figure 5-20: Contour plot of the brightness temperature perturbation and rain rate estimation. The dashed lines are for the perturbation from channel three of the 54-GHz system, and the solid lines are from the rain-rate estimation.

Simulation Discrepancy Analysis

A discrepancy analysis was done on the convective cells which was independent of the polynomial estimator introduced in Section 5.3.1. The discrepancy metric measures the difference between the actual flight data and the closest simulated profile. Each pixel has a brightness temperature vector consisting of 22 channels. This vector was compared with all of the simulated brightness temperature vectors $(\overline{T}^s_b)$ in the training set, and a vector $(\overline{T}^s_b)$ was chosen that:

$$\underset{\overline{T}^s_b}{\arg\min} \sqrt{\sum_{i=1}^{N} \frac{w_i}{M}(T_{b_i} - T^s_{b_i})^2}. \tag{5.6}$$

M is the sum of the all the weights ($M = \sum_{i=1}^{N} w_i$), and the weights were limited to values of either one or two. The weights (w_i) were chosen to emphasize the first three 54-GHz window channels and the first two 118-GHz window twice as much as the other channels. This was done when it was found that the unweighted metric would minimize the high-frequency channels where the simulation seem to have the most difficulty. Therefore more weight was put of the traditional precipitation-sensing window channels.

The closest brightness-temperature vector, $\overline{T}_b^s$, has an associated state vector and therefore a hydrometeor profile type; for example, it could be a precipitating profile. This allows a classification of each pixel to be either clear air, non-precipitating, or precipitating. Figure 5-21(a) and Figure 5-22(a) gives the classifications for Cell I and Cell II, respectively. Also plotted in Figure 5-21(b) and Figure 5-22(b) are the error values, which gives a metric on how far, in a weighted mean-squared error sense (WMSE), the actual brightness temperature data is from the simulations. The categorization of these two cells looks reasonable with a convective core surrounded by non-precipitating clouds. This classification could be used to increase the potential of the estimator technique by designing an estimator for a specific classification. Also, the discrepancy image allows an evaluation of how well the simulation ensemble represents the actual data. If there is a breakdown in the polynomial estimator, *e.g.*, negative rain rate, then the problem can be identified as either a defect of the estimator or as a deficit of the training ensemble.

Figure 5-21(c) compares the pixel having the largest RMS discrepancy in Figure 5-21(b) with the simulation training set. The problematic pixel lies nine pixels up and nineteen across and had an RMS discrepancy of 6.54 Kelvin. It was classified as a precipitating profile with a rain rate of 25 mm/hr and a precipitation cell-top altitude of 7 km. It should be noted that this pixel is at the "northern" boundary of the precipitating section, and it is expected that the brightness temperatures would be difficult to classify as precipitating or non-precipitating. To investigate this idea, the profiles of the closest precipitating and non-precipitating profiles were compared with the actual brightness temperatures in that pixel. The lowest discrepancy for the non-precipitating profiles was 6.86 Kelvin, while other non-precipitating profiles were very close in their discrepancy value (within 0.1 Kelvin). This particular pixel had a similar distance in discrepancy to a precipitating profile (6.54 K) as it did to a non-precipitating profile (6.86 K). The brightness temperatures for the above men-

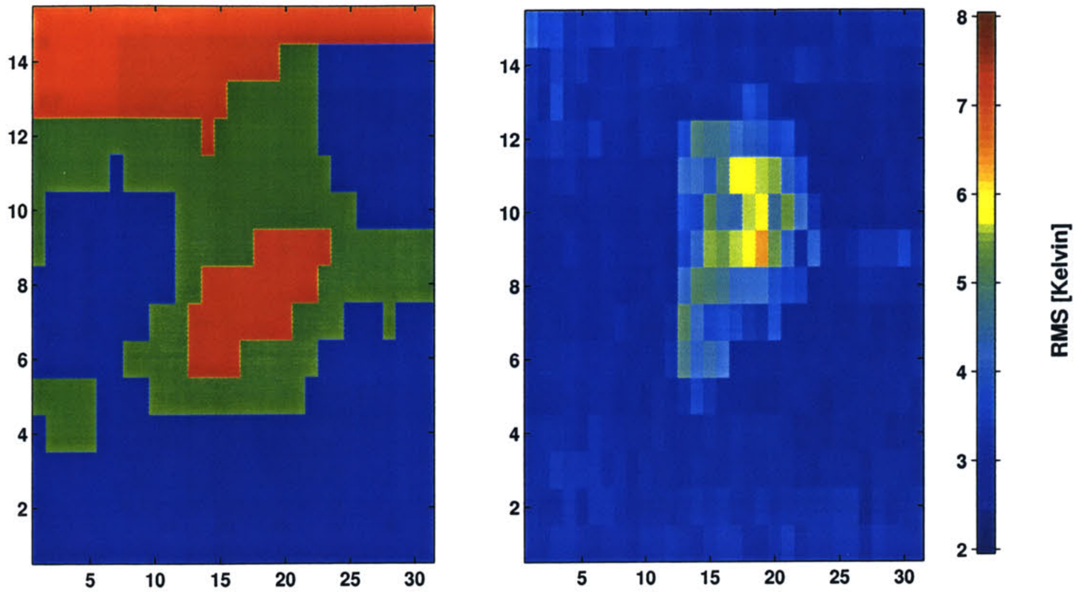

(a) Classification of flight data. Blue is clear air. Green is a non-precipitating-cloud profile. Red is a precipitating-cloud profile.

(b) Discrepancy (RMS) between the actual flight data (T_b) and the nearest training-set profile that minimizes the WMSE.

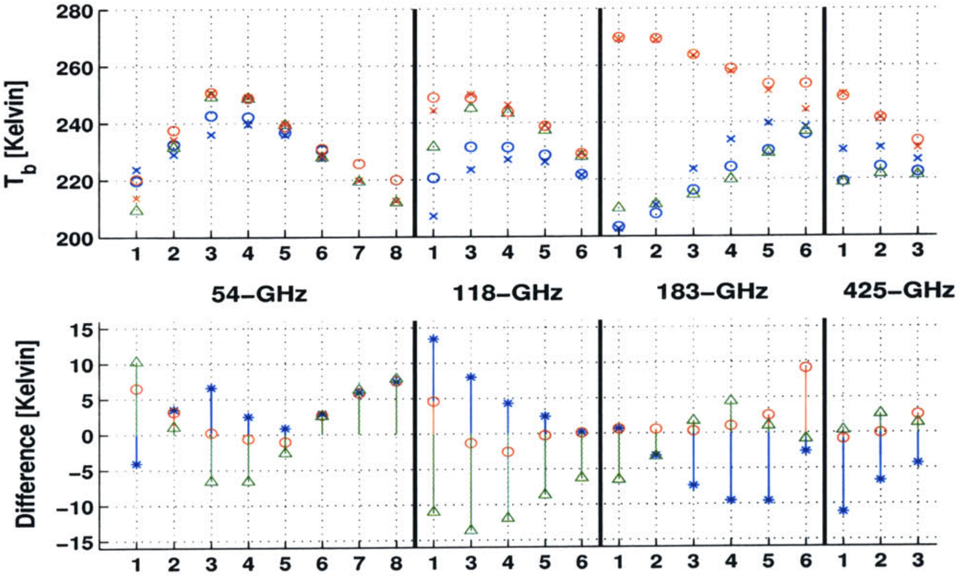

(c) The largest-discrepancy pixel is 9 up and 19 across. Training-set and flight brightness temperatures are marked with x and o, respectively. △ are the closest non-precipitating simulated profile. For reference, clear-air brightness temperatures from the training set (x) and nearby clear air (o) are included in red. The differences are between the actual T_b minus closest simulated T_b where the circle is clear air; the asterisk is a precipitating simulation; and the triangle is the closest non-precipitating simulation

Figure 5-21: Analysis of Cell I from PTOST on March 14, 2003. See text for more details.

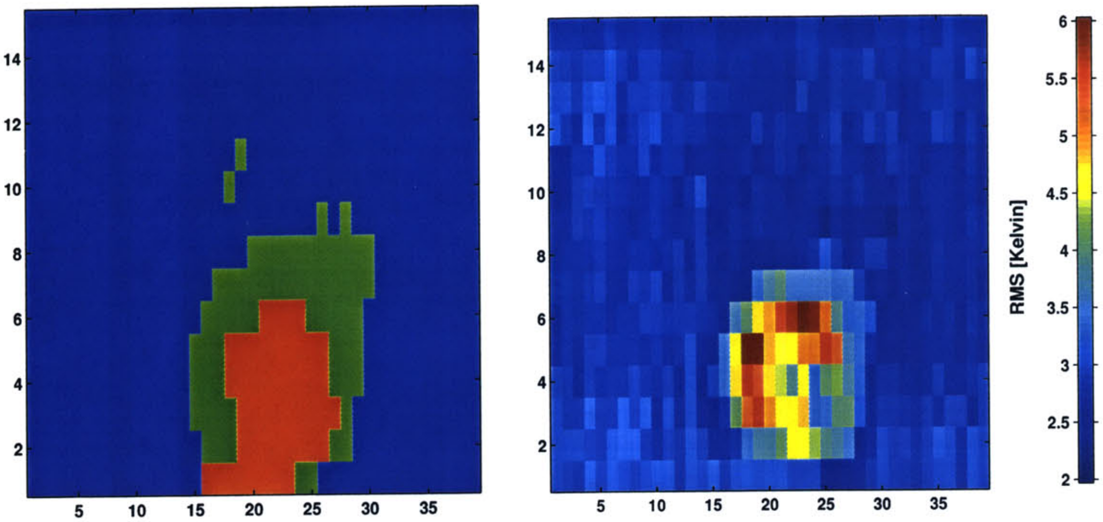

(a) Classification of flight data. Blue is clear air. Green is a non-precipitating-cloud profile. Red is a precipitating-cloud profile.

(b) Discrepancy (RMS) between the actual flight data (T_b) and the nearest training-set profile that minimizes the WMSE.

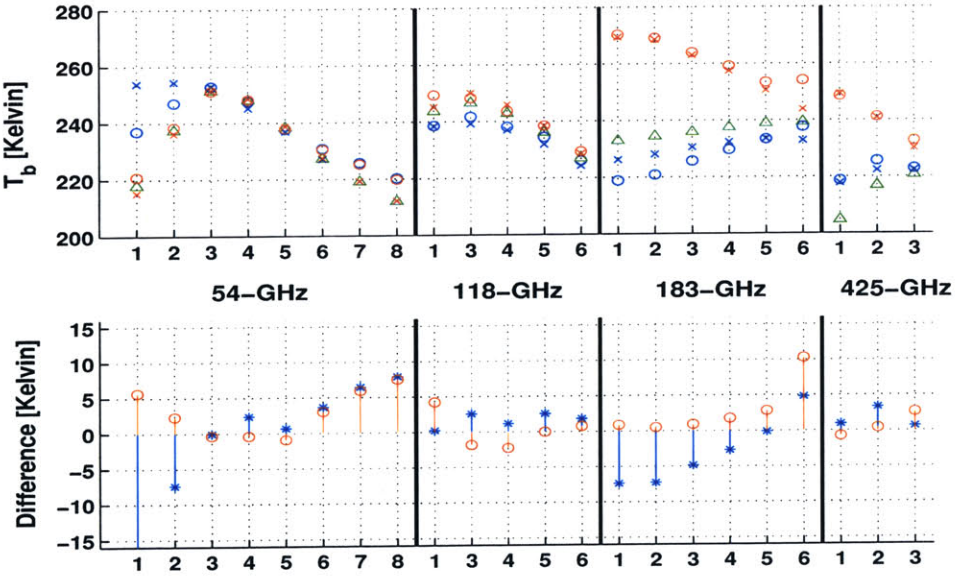

(c) The largest-discrepancy pixel is 5 up and 19 across. Training-set and flight brightness temperatures are marked with x and o, respectively. △ are the closest non-precipitating simulated profile. For reference, clear-air brightness temperatures from the training set (x) and nearby clear air (o) are included in red. The differences are between actual T_b minus the closest simulated T_b. The circle is the clear air difference, and the asterisk is the precipitating difference

Figure 5-22: Analysis of Cell II from PTOST on March 14, 2003. See text for more details.

tioned pixel and profiles are plotted in Figure 5-21(c). In the top plot, the blue circles are the absolute brightness temperatures of the problematic pixel, and the blue x's are the closest WMSE simulation, which in this case was a precipitating profile. The green triangles are the nearest simulation from exclusively the non-precipitating profile set, which had an altitude of 10 km. The red symbols are the clear-air brightness temperatures, which are included to see the clear-air discrepancy between simulation and actual data on one hand, but also to see the change that the problematic pixel introduced when compared to the clear-air conditions. The red circles are from an averaged portion of the flight deemed "cloud free" and the red x's are the average of all the simulated clear-air brightness temperatures in the training set. The bottom of Figure 5-21(c) plots the differences between the actual data and the closest corresponding simulation. For example, the green triangles in Figure 5-21(c) are the difference between the problematic pixel's brightness temperatures and the brightness temperatures from the closest simulation within the non-precipitating portion of the training set. By looking at the differences of the lowest-discrepancy precipitating (blue *) and non-precipitating profiles (green $\triangle$), the actual data suggests a layer of smaller-diameter cloud particles over the precipitation cell. The precipitating hydrometeor profiles had only modeled one kilometer of cloud droplets over the precipitation (see Section 5.3.2). Specifically to test this theory, the simulation model was redone with thicker non-precipitating clouds above the precipitation that ranged from one to four kilometers in thickness. The problematic pixel's discrepancy was reduced by one Kelvin RMS, but otherwise the discrepancy image in Figure 5-21(b) remained unchanged.

Along the same lines as the previous paragraph, the highest-discrepancy pixel presented in Figure 5-22(c) (from Cell II) was analyzed, and it lies five pixels up and nineteen across. The nearest training set profile, in the WMSE sense, was precipitating and had an RMS discrepancy of 6.06 Kelvin, while the nearest non-precipitating profile had an RMS discrepancy of 8.65 Kelvin. The precipitating profile had a rain rate of 3 mm/hr reaching an altitude of nine kilometers. Notice that this profile (simulation and actual) did not have enough large-diameter hydrometeors to scatter the downwelling electromagnetic energy. Instead, emission of the hydrometeors warmed the window channels of the 54-GHz system relative to the reflective surface. The non-precipitating profile (a cloud 8-km high and with 5 g/m^3 TWC) perturbed the 183- and 425-GHz channels, but left the 54- and 118-GHz systems nearly unchanged when compared to the clear-air brightness temperatures. In contrast to the comparison of Figure 5-21(c), the highest RMS discrepancy came from the differences between the actual data and simulations at the more transparent 54- and 183-GHz channels. The differences come from too much absorption or not enough scattering. This is not to say that the error is from the calculations of the absorption coefficients or Mie scattering efficiencies, but more likely comes from incorrect assumptions on the input parameters such as the drop-size distribution.

Using the results of the discrepancy analysis, the problems with the polynomial estimator can be revisited. The polynomial estimator's negative rain rates occur predominately in the areas where the polynomial estimator registered a cell-top, but the pixel was classified as non-precipitating. Therefore, the polynomial estimator failed to adapt to this particular brightness temperature input. The polynomial estimator results could be improved by first classifying the pixels into one of the three categories, then have a polynomial estimator specificly trained for a particular classification. Some of the negative values can be associated with surface or atmospheric variations, but the discrepancy analysis from the next case study tends to implicate the estimator, not the training set.

Additional Data

One of the main contributions of the NAST-M comes from the 425-GHz system, especially with respect to contributions the system could provide on geostationary satellite platforms [6]. The 425-GHz brightness-temperature perturbation image corresponds well to the dynamically-lifted portions of the visible cells, but exhibits little response to the surrounding lower clouds. An example of a failure to respond to lower clouds is illustrated in Figure 5-15(a) and Figure 5-17(a). At the center of the right-hand side of Figure 5-17(a) there is a cloud that stereoscopy estimates to have a cloud-top altitude of approximately three km. In Figure 5-15(a), both the 52- and 118-GHz channels exhibit ~10-20 Kelvin warming due to unglaciated precipitation or heavy clouds too low in the humid atmosphere to be sensed at 425 GHz. The limited ability of 425-GHz channels to sense low-altitude clouds is further illustrated graphically in Fig. 5-23, which presents a PTOST ferry flight over the North Pacific on March 14, 2003. The three window channels (*i.e.*, the most transparent) of the 54-, 183-, and 425-GHz systems are shown with a visible image. The 425-GHz channel has a weighting function peaking near 4-5 km due to water vapor, which is at the top of these low-lying clouds. In dry atmospheres, 183-GHz channels penetrate to sea level, whereas the 425-GHz band almost never does.

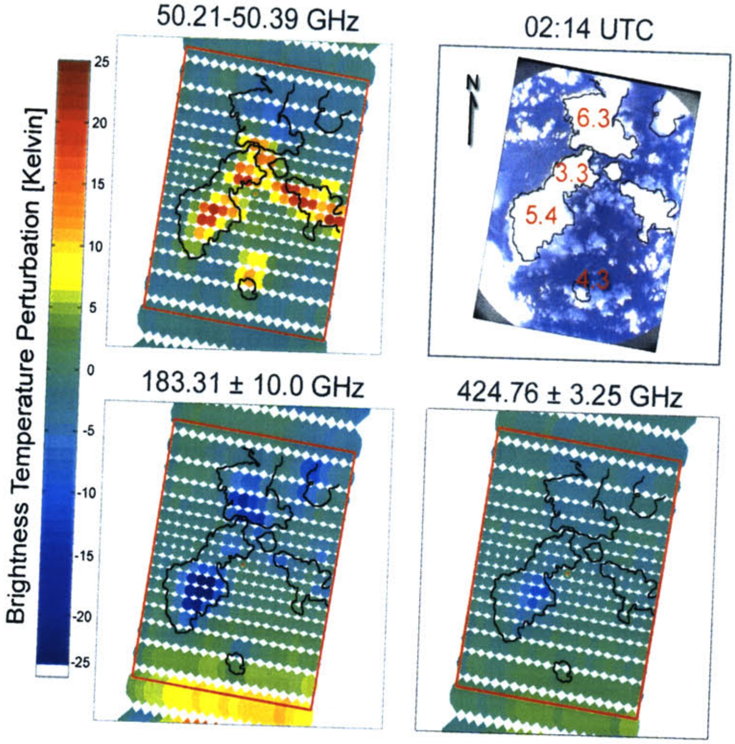

Figure 5-23: NAST-M brightness temperature perturbations for the 54-, 183-, and 425- GHz window channels with a matching NAST-M video image. The clear-air brightness temperatures at nadir (limb) were 221 (242) K, 272 (266) K, and 251 (243) K for the 54-GHz, 183-GHz, and 425-GHz channels, respectively.

To strengthen these observations and to take it one step further, Figure 5-24 is a scatterplot of the actual brightness temperatures from PTOST along with a sim-

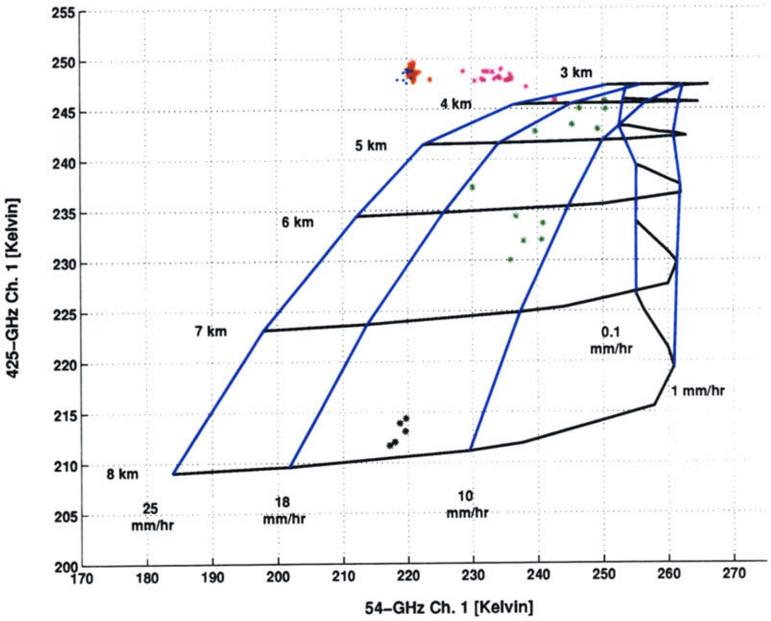

Figure 5-24: Scatterplot of the 54- and 425-GHz window-channel's brightness temperatures from the PTOST Cell I. The near-nadir pixels are classified and assigned asterisks with red as clear air, magenta as non-precipitating clouds, green as precipitating clouds, and black as precipitating clouds with cold perturbations from the clear-air baseline.

ulation cloud-model parameter grid overlaid. The figure has two parameters from the precipitating-cloud model plotted on a grid around select Cell I pixels (shown in Figures 5-15, 5-17, and 5-21). The two grid parameters are the precipitation cell-top altitude and rain rate, and the constant rain rate contours are the blue lines and the constant cell-top altitudes are the black lines. The Cell I pixels were separated by the classification technique used in Figure 5-21(a). The red asterisks are the clear air, magenta are the non-precipitating clouds, green are the precipitating clouds, and the black asterisks are the precipitating-cloud pixels that had the negative brightness temperature perturbations in Figure 5-20(a), which was assumed to have the largest hydrometeors and therefore the highest rain rate. The clear-air simulations are marked as blue dots, and they were shifted to overlap the image's clear air pixels by subtracting two Kelvin from the 425-GHz channel and by adding six Kelvin to the 54-GHz channel. These differences could be from the simulation's atmospheric profile difference, the surface-emissivity model errors, or calibration errors. The scatterplot compares the channels with the largest frequency difference and gives insight into how the two frequencies help precipitation-parameter estimation. The hydrometeors at first warm the 54-GHz channel as the diameters are still small, then scattering becomes more dominate and the 54-GHz channel starts to cool and eventually becomes colder than the reflective ocean background. The 425-GHz channel is quite different. It saturates at any amount of precipitation, but is much more sensitive to the altitude of the precipitation. The grid also shows that the sensitivity to the altitude is decreasing as the precipitation altitude decreases. At a 3-km cell-top altitude, the scattering of the 425-GHz channel is same as if it was clear air, which suggest that the 425-GHz system is blind to precipitation in the lower troposphere.

5.4.2 CRYSTAL-FACE

The Cirrus Regional Study of Tropical Anvils and Cirrus Layers-Florida Area Cirrus Experiment (CRYSTAL-FACE 2002) studied convective systems around Florida during July 2002. NAST-M flew on the Proteus aircraft and flew above a convective cell twice on July 13^{th}, which is presented in this case study.

Brightness Temperature Observations

The two passes were within minutes of each other, and both are presented in this case study. Figure 5-25 presents the first passes' data by plotting the brightness temperatures within an antenna footprint with the use of the aircraft's navigation instrumentation and GPS data. This allows a more accurate comparison with other instruments' images. Similar to the presentation of brightness temperature from the last case study, the images are of the same clear-air-altitude-peaking channels. On the right-hand side are images from the Geostationary Observational Environmental Satellite (GOES-8) at two different frequencies. The infrared image has a spatial resolution of 2 km and the visible image has 1-km resolution. The radar-reflectivity image allows relative intensity and morphology to be compared with the brightness temperatures and retrievals. Figure 5-26 and Figure 5-27 give the brightness temperatures for these two passes in the same format as the PTOST case study (Figure 5-15

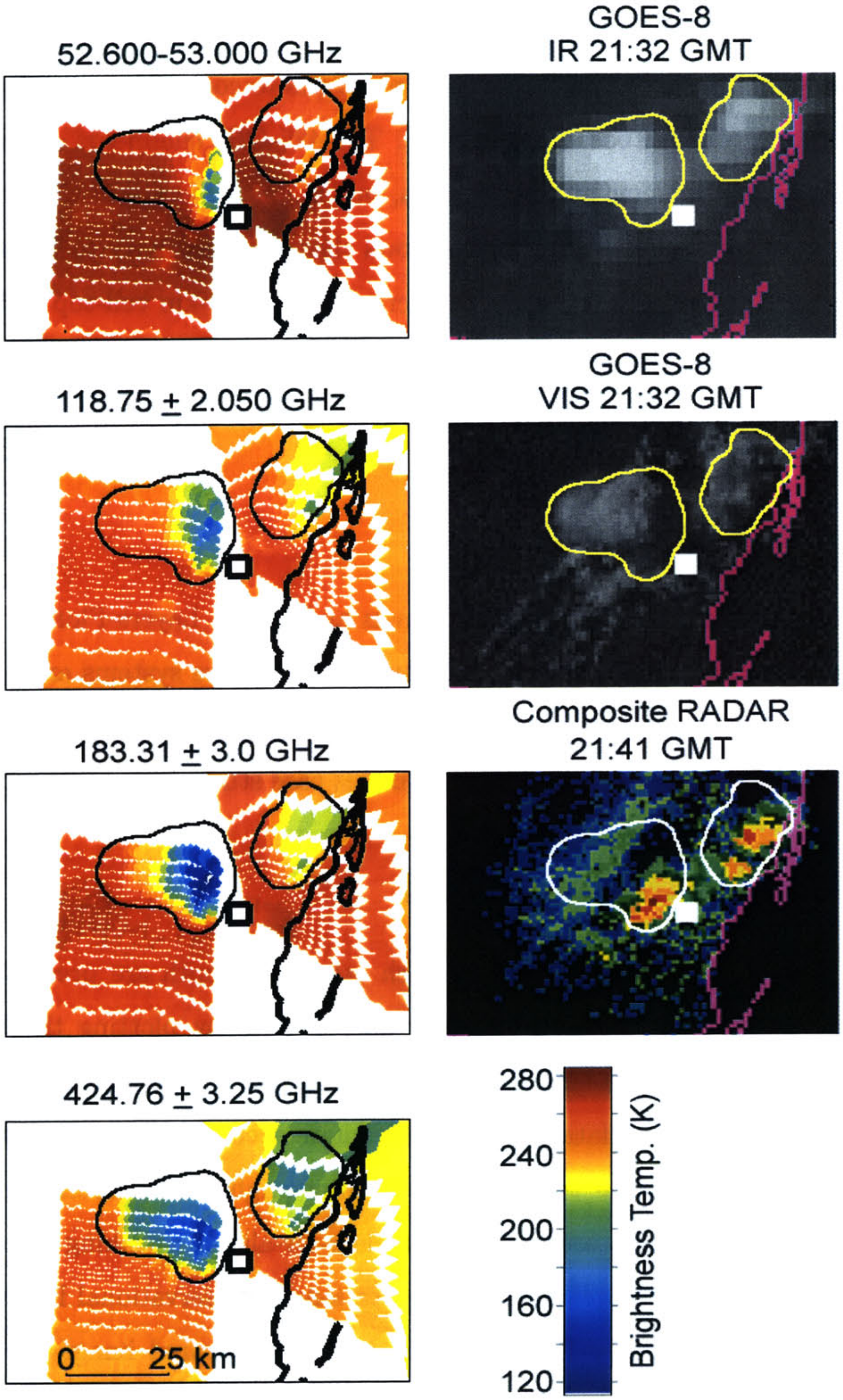

Figure 5-25: Convective cell signature from microwave to visible wavelengths and with composite radar reflectivity on July 13, 2002 during CRYSTAL-FACE. The first Proteus overpass of the convective cell's core was at 21:38 UTC.

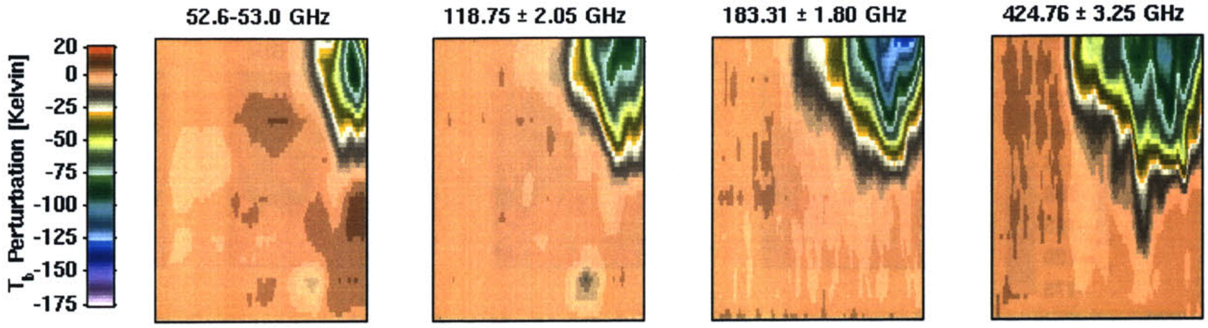

(a) Channels with similar clear-air altitude-peaking weighting functions

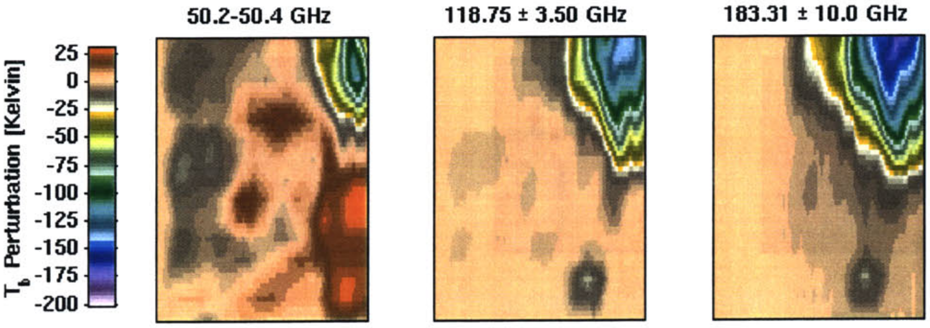

(b) Window channels

Figure 5-26: Brightness-temperature perturbation for the left-most convective cell (1^{st} pass) in Figure 5-25 on July 13, 2002 during CRYSTAL-FACE. The vertical axis is approximately 50 km and the horizontal axis is 35 km.

and Figure 5-16). The clear-air baseline was taken from the data at the far left of the image in an attempt to sample the clear air shown in the GOES images. Note that the surface emissivity for this geographic location varies because of the marshland surface.

Figure 5-25 presents images of the first pass, which flew from left to right. After a 360 degree turn, the second pass crossed the thunderstorm from right to left. In Figure 5-25, the eastern-most convective cell was imaged while the aircraft was banking and is not considered the second pass. This cell was imaged in between the two passes of the main convective cell. Because the aircraft was banking, the scattering is less prominent across all channels as the effective thickness of the atmosphere increased.

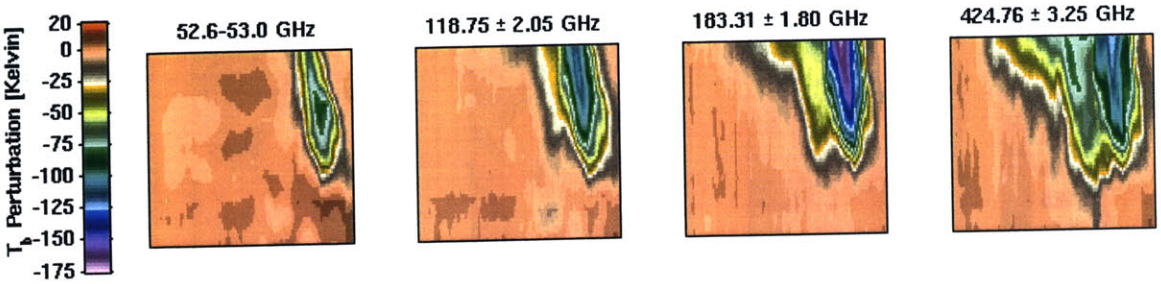

(a) Channels with similar clear-air altitude-peaking weighting functions

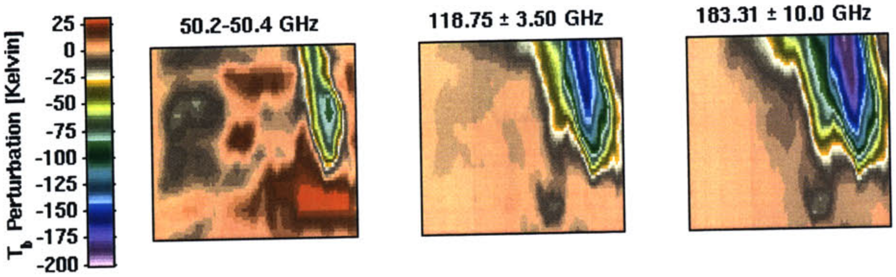

(b) Window channels

Figure 5-27: Brightness-temperature perturbation for a convective cell (2^{nd} pass) on July 13, 2002 during CRYSTAL-FACE. The vertical axis is approximately 50 km and the horizontal axis is 45 km.

The western "main" cell illustrates the sensitivity of wavelength to hydrometeor diameter. This strong convective core is identified by the strong scattering signature in the 54-GHz channel, which is due to the abundance of large-diameter hydrometeors. As frequency increases, the cell signature enlarges to the extent of the infrared image, which is the limit of the cloud droplets. The boundaries of the infrared signature are outlined on the other images. The east-to-west increase in signature size could be an indication of westward blowoff due to the vertical wind shear at the top of the updraft. The 183-GHz channel had the largest brightness-temperature perturbation, whereas the 425-GHz channel could see a high-altitude layer of small-diameter hydrometeors that don't perturb the lower frequency channels. When the microwave image is compared to the composite radar image, the 54- and 118-GHz channels match the highest-reflectivity region. While the airborne microwave instrument suggests the anvil blowoff, the ground based composite radar does not register the same precipitation aloft. These discrepancies could arise from either instruments' spatial blind spots or temporal differences.

Retrievals

Figure 5-28 is the precipitation-parameter retrieval from both passes, but also includes GOES-8 images at 21:32 UTC and composite radar at 21:42 UTC. For these retrievals, only the precipitating and anvil profiles were included in the estimator's training set, because it was found that the non-precipitating cloud profiles used in the PTOST case study only increased the estimator's distortion. The convective cells in the CRYSTAL-FACE data are much stronger than the PTOST data. For this cell on July 13^{th}, the CPL cloud radar measured the peak of the cell at 14 km and sections of the anvil at 8 km (CPL has nadir measurements only). The 54-GHz perturbations are again at the heaviest precipition, but still the polynomial estimator retrieved negative rain rates throughout most of the anvil. The discrepancy analysis that follows investigates these inaccuracies. Note that for these figures, all of the retrievals were limited to values within a reasonable range, *e.g.*, negative rain rates were capped at zero mm/hr. The cell-top and cloud-top altitude retrievals also had trouble in certain areas. The cloud-top estimate shows good agreement with the cloud's overall area and also with the absolute altitude values. The cloud-top retrievals have some of the low-lying contrail-like clouds visible in the visible image (Figure 5-28(a)), but there is also a portion of the retrieval that had large negative altitude values, which, as will be seen in the following discrepancy analysis, is in the region with the highest RMS discrepancy. That discrepancy comes from large perturbations at the 183-GHz channels that do not agree with the simulation data. A better example of the "nearest profile" retrieval is presented in Figure 5-29. A GOES-8 visible wavelength image is in Figure 5-29(a), and it has a composite radar reflectivity image overlaid. The timestamp for the GOES image is 17:02 UTC, while the timestamp for the radar image is 16:45 UTC. The aircraft crossed over the main cloud at approximately 17:00 UTC, and the "nearest

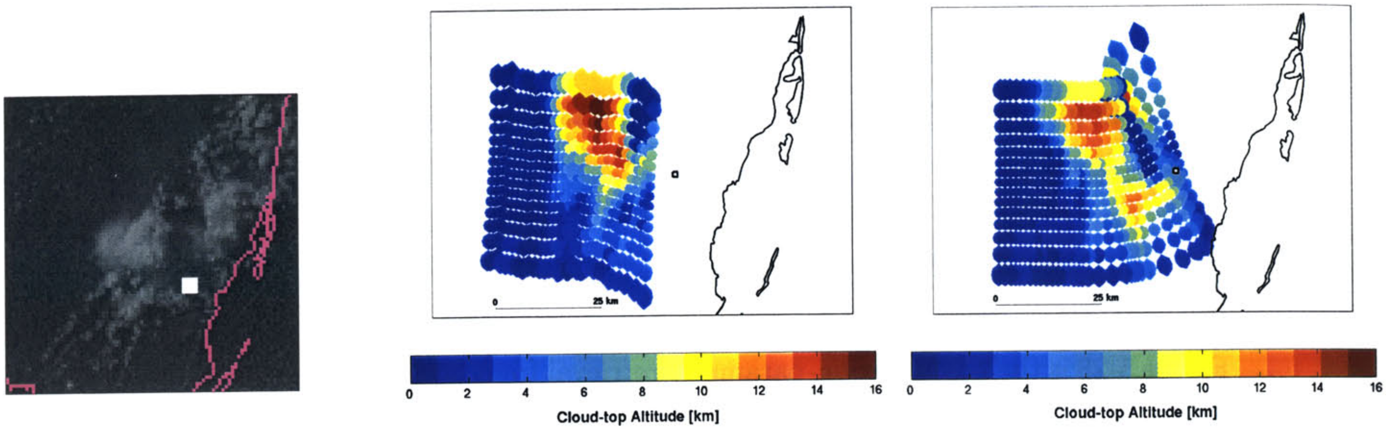

(a) GOES-8 visible wavelength

(b) Estimated Cloud-top Altitude: Pass one

(c) Estimated Cloud-top Altitude: Pass two

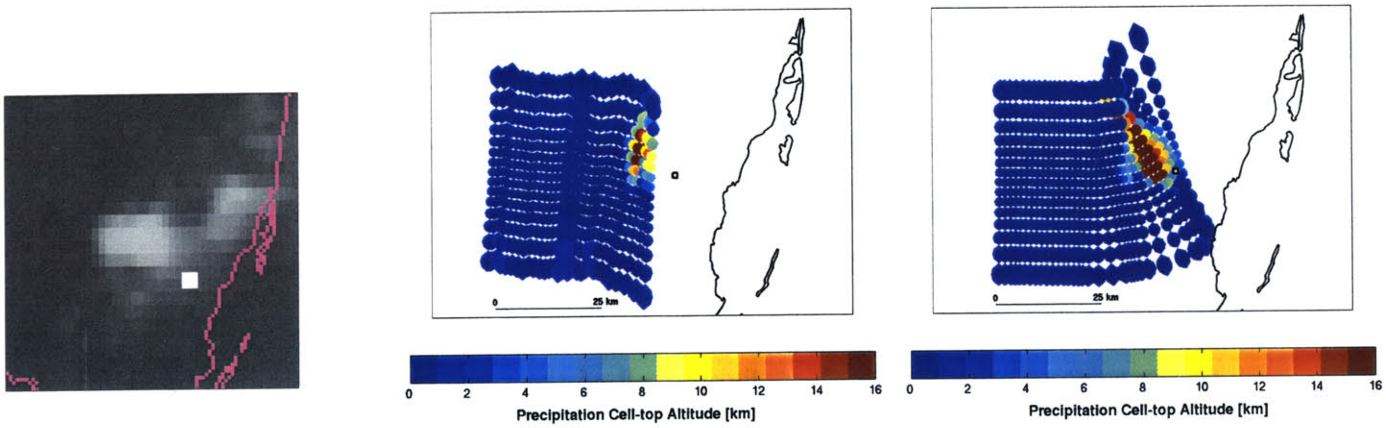

(d) GOES-8 infrared wavelength

(e) Estimated Cell-top Altitude: Pass one

(f) Estimated Cell-top Altitude: Pass two

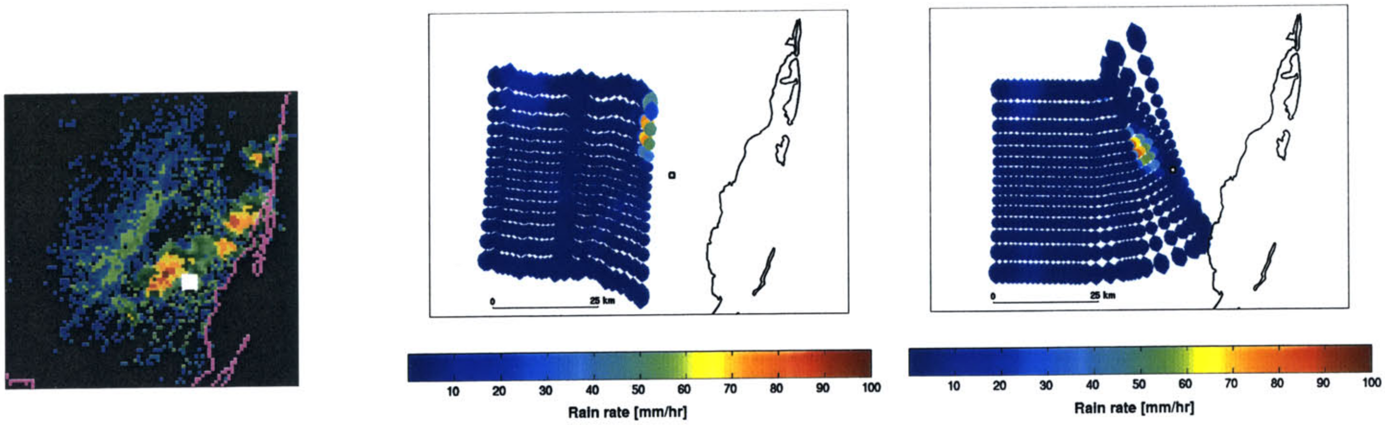

(g) Composite Radar

(h) Estimated Rain Rate: Pass one

(i) Estimated Rain Rate: Pass two

Figure 5-28: CRYSTAL-FACE convective cell on July 13, 2002.

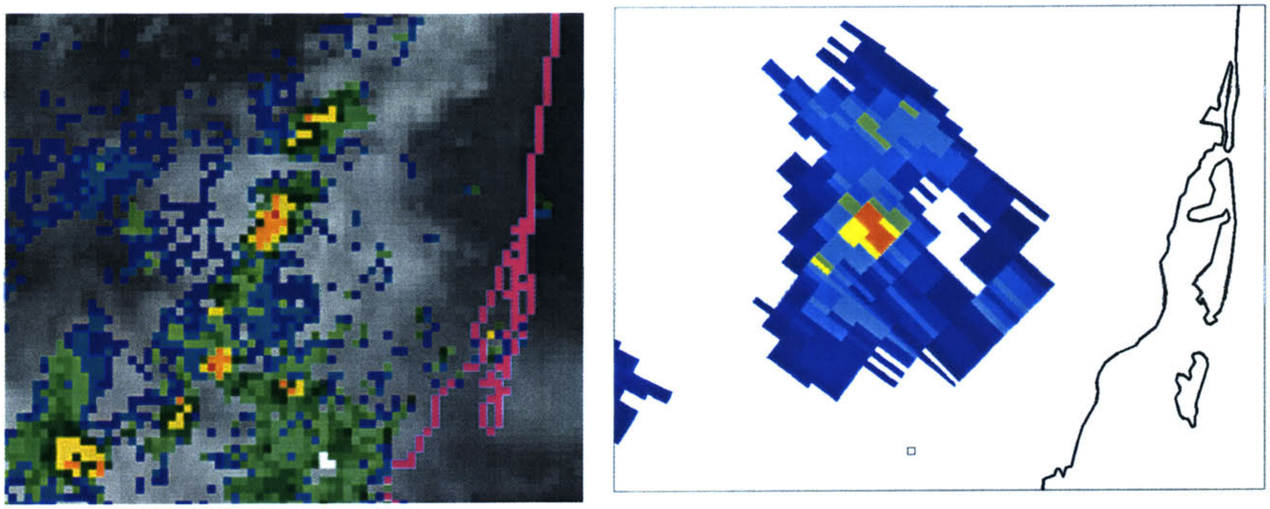

(a) GOES-8 visible image with composite radar reflectivity overlaid. GOES-8 Visible at 17:02 UTC and the composite radar is at 16:45 UTC

(b) "Nearest profile" rain-rate retrieval at approximately 17:00 UTC

Figure 5-29: Rain rate morphology comparison during CRYSTAL-FACE on July 11, 2002.

profile" retrieval is presented in Figure 5-29(b). The radar image has reflections due to ground clutter at the bottom center of the image. In Figure 5-29(a), the white square is the location of the radar antenna. The radar antenna location is marked by a black box in Figure 5-29(b).

Simulation Discrepancy Analysis

The discrepancy analysis follows the previous work that was presented in the PTOST case study. The analysis starts for both passes of the convective cell in Figure 5-30. Figure 5-30(a) and Figure 5-30(c) are the RMS discrepancies between the actual brightness temperatures and the nearest simulation in the same weighted mean-squared sense (WMSE). Figure 5-30(b) and Figure 5-30(d) are the classification of the pixels into precipitating cloud (red), non-precipitating cloud (green), or clear air (blue). Unlike the PTOST case study where the surface emissivity was uniform in the direction of flight, the C-F images had a large swing in values of surface emissivity. In Figure 5-26(b) and Figure 5-27(b), the 54-GHz window channels attests to this fact.

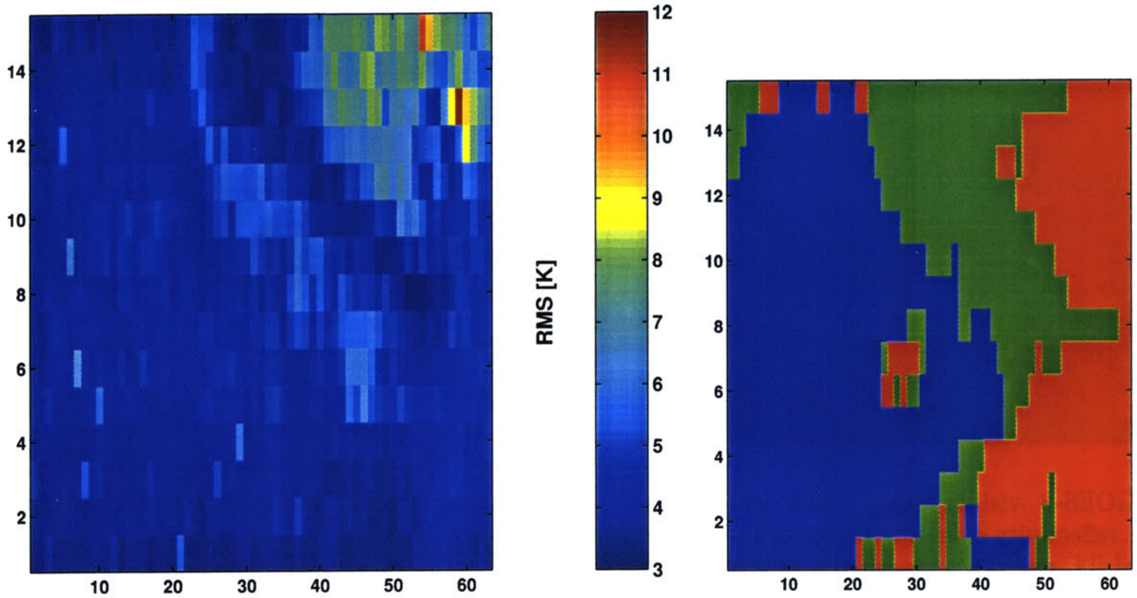

(a) Discrepancy image (RMS) of 1^{st} pass.

(b) Classification image of the 1^{st} pass at 21:38 UTC. Blue is clear air. Green is a non-precipitating-cloud profile. Red is a precipitating-cloud profile.

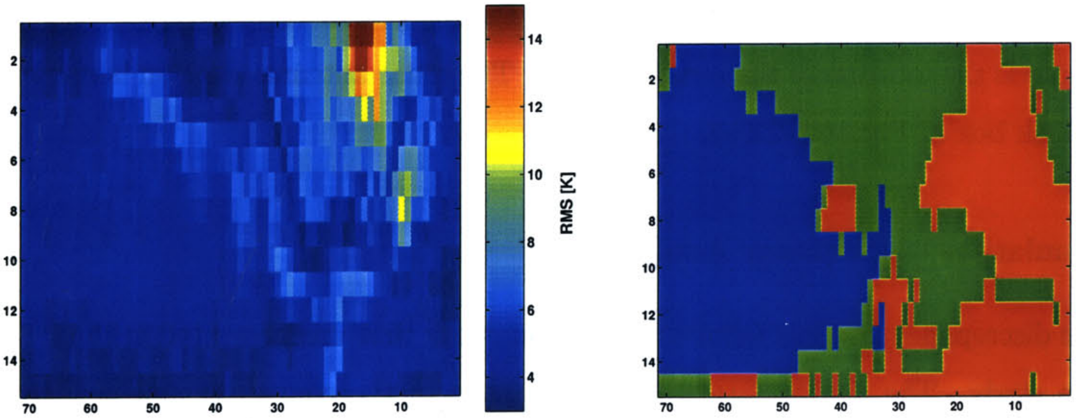

(c) Discrepancy image (RMS) of 2^{nd} pass.

(d) Classification of the 2^{nd} pass at 21:44 UTC. Blue is clear air. Green is non-precipitating-cloud profile. Red is a precipitating-cloud profile.

Figure 5-30: Classification and discrepancy images for both passes over a convective cell on July 13, 2002 (CRYSTAL-FACE).

According to maps of the area, the area is inundated with sloughs and swamps. In an attempt to model this, the training ensemble was trained as a land-water mixture with the percentage land being a uniform random variable from 40 to 70 percent. This gave the best agreement with a majority of the surface sensitive data. The lower right-hand side of the 54-GHz window-channel image in Figure 5-26(b) has the driest surface because the brightness temperatures are the warmest. A retrieval was performed on the same geographic location earlier in the flight without the precipitation, but with light cloud cover. The classification erroneously classified the dry land in the lower right-hand corner of the image as very light low-altitude precipitation. The polynomial estimator uses a noise covariance matrix, which includes the instrument noise. To help offset the wide surface variability, the window channels had an additional term added (less than 1 K) to the noise covariance matrix. This helped to alleviate the problem in the retrievals, but the error minimization technique was susceptible to classifying the warm surface as low-lying emission from hydrometeors. Measures can be taken to increase the training ensemble to include more appropriate surface emissivities, but it adds to the polynomial estimator's error. Two other techniques could help alleviate this problem. One technique could estimate the surface emissivity, and then use a precipitation-parameter estimator trained only for the narrow surface-emissivity estimated. Or a precipitation-masking technique, which uses non-surface-sensitive channels, could identify the location of precipitation before the precipitation-parameter retrievals are attempted.

Individual pixels were examined from each pass and are featured in Figure 5-31 and Figure 5-32. Figure 5-31(b) and Figure 5-32(a) characterize two pixels that were retrieved as negative rain rates by the polynomial estimator. These pixels were within the anvil, and the largest brightness temperature difference seems to come from the 54-GHz window and the 183-GHz channels. The error could be attributed to the simplicity of the polynomial estimator or the simulation profiles. The closest WMSE precipitation profile is relatively close when compared to discrepancies in other parts of the image, but the pixel seems to lie at the core-anvil boundary. As mentioned in the previous case study, this area of the storm seemed problematic. Figure 5-31(a) and

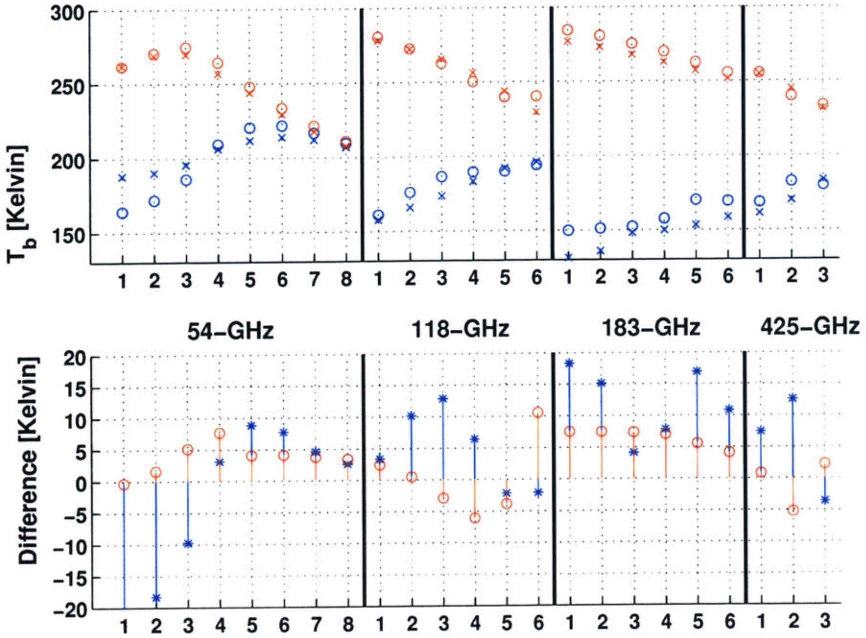

(a) T_b for the pixel 13 up and 59 across in Figure 5-30(a). This pixel had the highest discrepancy closest to the convective core.

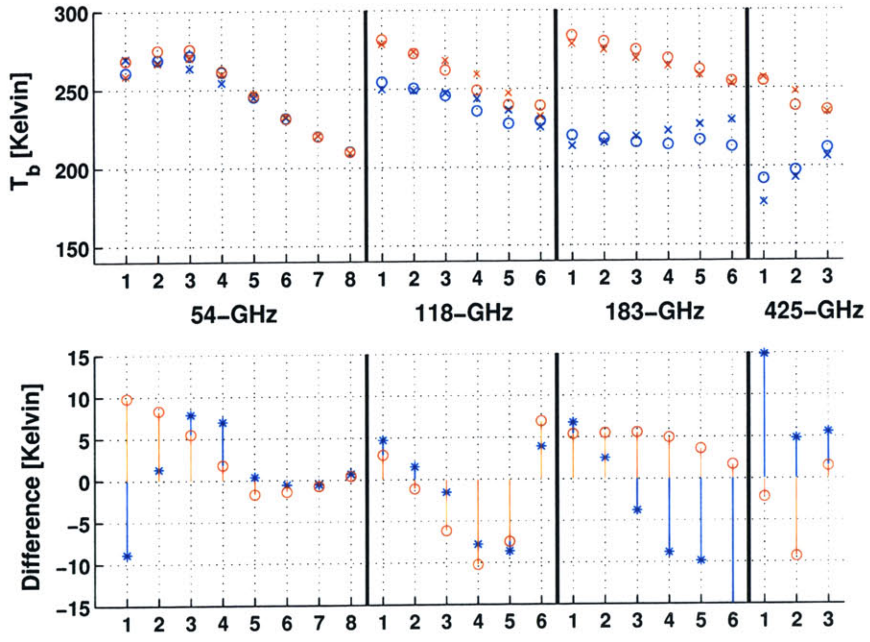

(b) T_b for the pixel 11 up and 48 across in Figure 5-30(a). This pixel retrieved a large negative rain rate.

Figure 5-31: Problematic pixels from the first pass over a convective cell on July 13, 2002 (CRYSTAL-FACE). The circles are the actual flight data, and the x's are the closest simulated data from the training set. Red symbols are clear air, and the blue symbols are problematic pixels. The differences are between simulated and actual data.

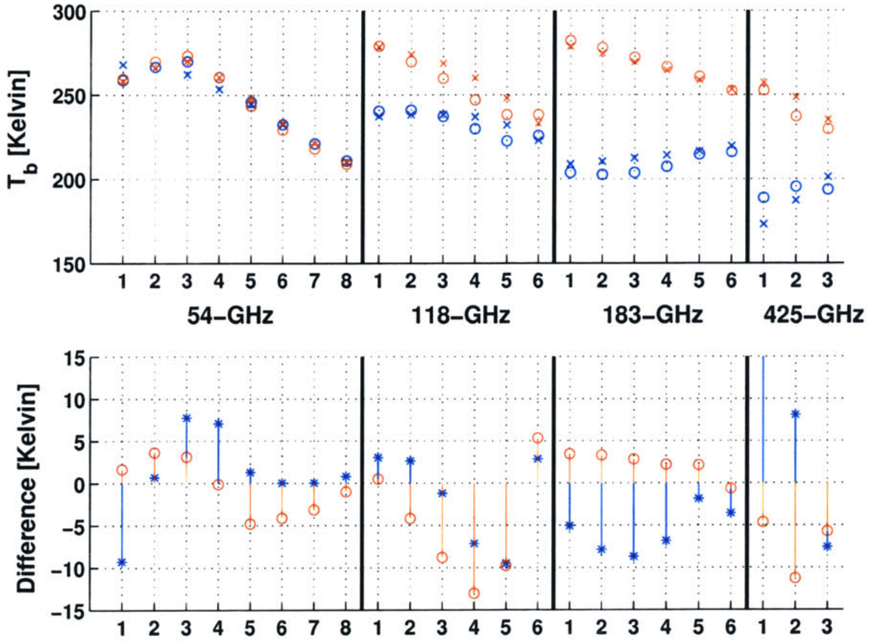

(a) T_b for the pixel 6 down and 23 across in Figure 5-30(c). This pixel had a large negative rain rate retrieved.

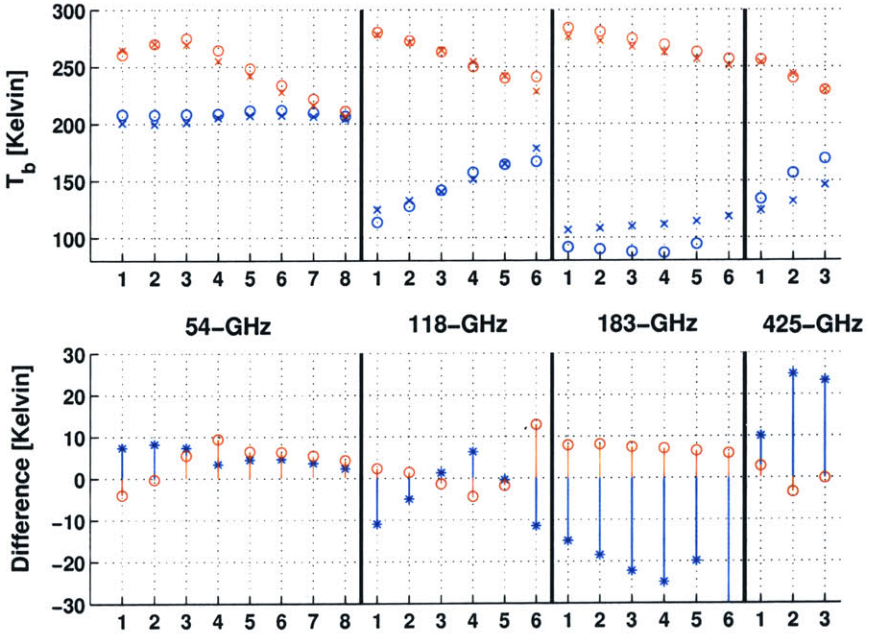

(b) T_b for the pixel 2 down and 16 across in Figure 5-30(c). This pixel is from the high discrepancy region.

Figure 5-32: Problematic pixels for the second pass over a convective cell on July 13, 2002 (CRYSTAL-FACE). The circles are the actual flight data, and the x's are the closest simulated data from the training set. Red symbols are clear air, and the blue symbols are problematic pixels. The differences are between simulated and actual data.

Figure 5-32(b) characterize the pixel with the highest discrepancy in WMSE sense. Figure 5-31(a) is the pixel with the highest discrepancy near the convective core in Figure 5-30(a). Here the transparent 54-GHz channels are still problematic, but the 183-GHz channels are now warmer than the simulations. Figure 5-32(b) is a representive pixel in the area where the cell- and cloud-top altitude estimators registered negative values just north of the convective core (*e.g.*, Figure 5-28(c)). The principal deviation in the brightness temperatures were at 183 GHz where the simulations were warm, but the 425-GHz system simulated colder brightness temperatures. One way to try to increase the 183-GHz perturbation is to increase the total water content of the hydrometeors, but this would also increase the 425-GHz perturbation, which is already too cold. A more viable option is to increase the cloud droplet diameter in an attempt to make the 183-GHz signature colder, and the scattering signature at 425 GHz probably has already saturated in the Mie or optical region and would not get much colder. Model parameter or distribution tweaking, adding a new profile type, improving the simple estimator, or some combination is needed to make this simulated training ensemble more robust.

Retrieval Technique Comparison

The next couple of figures compare the two retrieval techniques. One technique is the polynomial estimator, while the other is the "nearest-profile" estimator used in the discrepancy analysis. The training set profile that was closest to the actual brightness temperature data in a weighted-mean-squared-error sense (WMSE) is determined, and the parameters in the associated state vector are the "nearest profile" retrieval parameters. Figure 5-33 shows both retrievals of the first pass, and Figure 5-34 is the second pass. The left-hand side consists of the polynomial estimator's retrievals of the three parameters in the state vector without the exact geographic placement of the antenna footprint. On the right-hand side, the state vectors that were closest to the actual brightness temperatures are plotted, *i.e.*, "nearest profile" retrieval. The white pixels in the nearest-profile estimation (right-hand side figures) represents retrieved values that were equal to zero. The polynomial estimator often

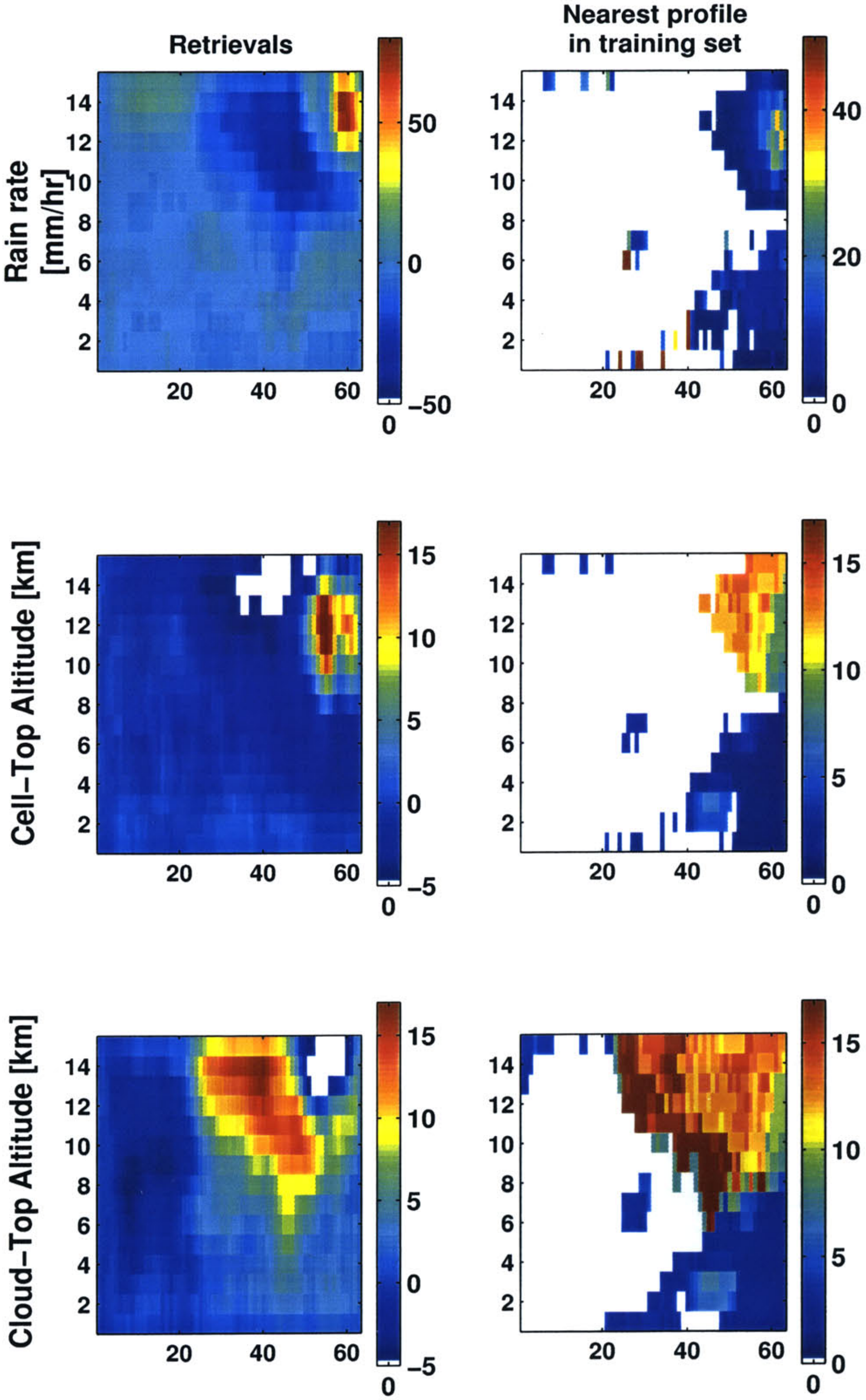

Figure 5-33: Pass 1: Retrievals from the polynomial estimator and the state vector that minimized the WMSE.

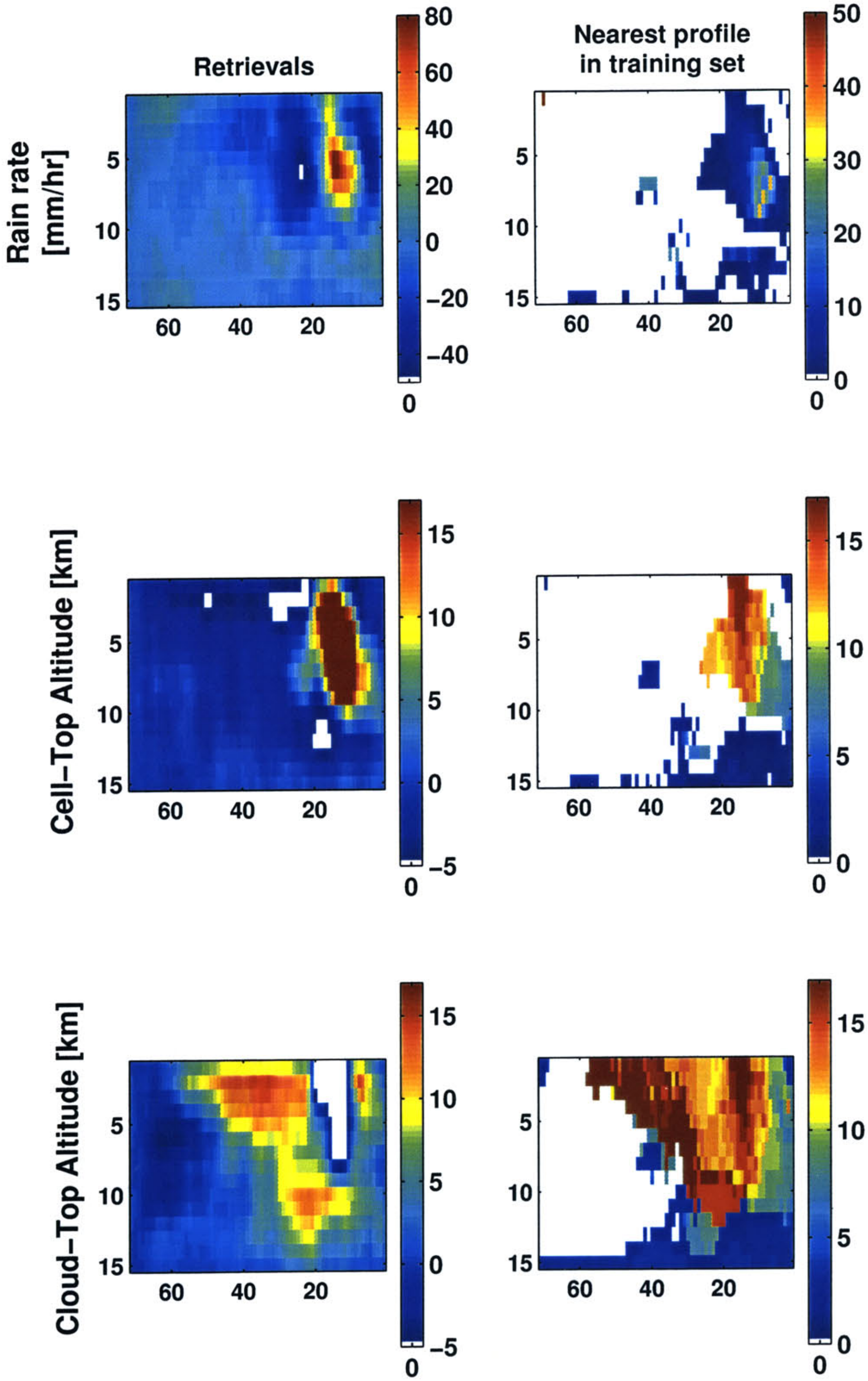

Figure 5-34: Pass 2: Retrievals from the polynomial estimator and the state vector that minimized the WMSE.

estimates negative values, and the negative values below the colorbar in the left-hand figures are replaced with white pixels. The WMSE estimations did not have the same problem with negative values, but it did yield extreme values in areas of high discrepancy. The area where the polynomial estimator retrieved cloud-top altitude as a large negative value and the cell-top altitude as an unreasonablely large value (above the aircraft's altitude) is characterized in Figure 5-31 and Figure 5-32. As previously mentioned, both estimation techniques would misclassify dry surfaces as light low-altitude precipitation, and Figure 5-33 and Figure 5-34 shows evidence of this. The high surface emissivity in the lower right-hand corner the image (also refer to Figure 5-26(b) and Figure 5-27(b)) was classified as a precipitating profile that had a low rain rate and low cell-top altitude. An earlier pass of this geographic area, when it was covered with only light clouds and no precipitation, was classified as having similar light low-altitude precipitation in approximately the same places. Therefore, the light low-altitude precipitation in the lower right-hand corner for both passes should be considered "ghost" precipitation, and highlights one of the challenges of retrieving precipitation over land.

Both techniques have their problems, but the nearest-profile technique seems to be more robust. The simulation training ensemble represents a majority of the brightness temperatures found in the convective cells presented in the case studies. Even the pixels with the largest errors, *e.g.*, Figure 5-32(b), have simulations that match the general form of the brightness temperature as a function of channel.

5.5 Conclusion

Each cloudy or precipitating flight pixel's brightness temperature vector could go through a stringent evaluation, which could lead to changes or adaptations to the training ensemble's parameters that could reduce the discrepancies. Various changes, some obvious and others abstruse, could make the training assemble more *ad hoc* and, at the very least, greatly increase the complexity of the simplified convective-cell hydrometeor-profile model. The work presented has reached a stopping point where the model represents a satisfactory portion of the data from the three convective cells. The work presented here leaves the fine tuning or improvements as future work. At the present, the case studies show success in identifying the convective core and potentially even the inner workings of some of the moderate-sized thunderstorms. The full complement of channels gives an unprecedented insight into the storm from solely the perspective of the microwave spectrum. Improvements could consist of applying a mask to the images and specializing the retrieval techniques, or the estimation technique could be upgraded, *e.g.*, by using a multilayer feedforward neural network or Bayesian retrieval algorithm [5].

Chapter 6

Cell-wide Precipitation Analysis

A useful parameter in climatology, hydrology, and hydrometeorology is the total rainfall or rain volume, which is usually in units of $km^2\,mm$. A closely related parameter is the instantaneous volumetric rain rate in units of $km^2\ mm/hr$, which has long been associated with the area of a precipitating cloud, and this relationship has been exploited by satellite (*e.g.*, [4]). In this chapter, the aggregate rain rate, *i.e.*, volumetric rain rate ($km^2\ mm/hr$), is shown to be related to the cumulative area of the NAST-M convective-cell microwave signatures. A convective cell model is discussed with the goal of giving a physical basis for the relationship.

6.1 Introduction

The relationship between a convective cell's area and rainfall has long been recognized (*e.g.*, [11]), and there is a family of precipitation techniques called the life-history methods [49] that rely on this area-rain volume relationship. To gain a perspective on the area-rain volume relationship, one method is briefly described here. The Area-Time Integral (ATI) method, introduced by Doneaud *et al.* [20], presented a simple and straight-forward estimate of the rain volume, which was eventually found applicable to satellite platforms [19, 4]. The basis of the ATI technique is to measure the area of the convective storm as it progresses through its life cycle. The parameter used to measure the dynamic area is the ATI in units of $km^2\ hr$, and is usually made discrete as $ATI = \sum_i A_i \Delta t_i$ where A_i is the storm area in image i, and the images are taken Δt_i apart in time. The ATI value is highly correlated with the total rain volume ($km^2\, mm$), and the ratio of total rain volume and ATI gives the average rain rate during the entire storm. One drawback is the necessity to view the entire duration of the storm. Doneaud *et al.* eventually developed a modified ATI technique that only required viewing the storm until just after its maximum stage [18]. Other life-history methods have also developed "nowcasting" techniques [49]. Doneaud found that the storm's maximum aggregate rain rate was highly correlated with a modified ATI parameter that integrated the area from the start to the midpoint of the storm. The midpoint was determined when the radar echo from the convective cell reached its maximum area. The strong correlation that Doneaud found between the maximum volumetric rain rate and radar echo area gives credit to a similar technique that would relate the aggregate rain rate to NAST-M's measurement of the passive 'echo' of the storm. In practice, microwave measurements from aircraft or low-earth-orbit satellites (LEOSs) would have a difficult time recognizing the peak of the evolving storm area, because of temporal coverage. But auxiliary data may be used or a geostationary-earth-orbit satellites (GEOSs) would be necessary.

In this chapter, the cell-wide aggregate rain-rate is compared with the measurements of a convective cell's passively-radiated microwave electromagnetic energy. The results show a linear relationship, but the number of usable convective cells is limited, and a correlation would be difficult to quantify. An overview of the technique starts with using NAST-M's high-resolution brightness-temperature imagery to determine a perturbation surface area for each of four frequencies. The exact procedure for measuring the surface-area of the brightness-temperature perturbations is presented in Section 6.3.1. The perturbation area of the four frequencies is summed, and then regressed against the convective cell's instantaneous aggregate rain rate. Several metrics were used, and will be discussed. The calculation of the aggregate rate rate is based on the single-pixel rain-rate retrievals from Chapter 5. Rain rate is retrieved for each pixel in a single convective cell, and the aggregate rain rate is calculated by approximating a volume integral. The details are presented in Section 6.3.3. Actual flight data is presented from convective cells over the North Pacific Ocean and the Florida peninsula during PTOST 2003 and CRYSTAL-FACE 2002, respectively. In Staelin [60], a simple three-dimensional model of a convective cell is presented, and this model can be used to help validate the physics behind the regression of aggregate rain rate and the cumulative signature area. Each cell's life-cycle classification is presented and discussed.

6.2 Convective Cell Model

It has been proposed that the area of a cell's radiometric signature at different frequencies is related to the volumetric rain rate within the individual cell. In Staelin [60], a simple three-dimensional model was proposed and is reviewed here. In equilibrium, the total precipitation from a convective cell approaches the total water vapor lofted per second (kg/s) by the updraft. Then the total water vapor flux (kg/s) is assumed, at equilibrium, to be the water vapor entering the updraft near the surface. The total water vapor flux is proportional to the product of the water vapor density (kg/m^3) and volume upflow (m^3/s) in the updraft. The water vapor density can be estimated from the integrated water vapor column density from a non-precipitating point just outside the convective cell. Alternatively, one might assume $\sim$95 percent relative humidity and use the retrieved air temperature 0-2 km away to estimate water vapor density. The volume upflow is then related to the radial velocity at the outflow, and therefore of the hydrometeors. The radiometric signatures from the different spectrometers will give a snapshot of radial distance that the different particle diameters have traveled from the convective core's center, because of the instrument's sensitivity to the hydrometeor's radius.

The frequency sensitivity of hydrometeor scattering is illustrated in Figure 6-1. The figure has plots of the product of $p(r)$ and $Q_s(r)$ used in the equation of the volume scattering coefficient (Equation 2.22), which is repeated here:

$$\kappa_s = \int_{r=0}^{r=\infty} p(r) Q_s(r) dr. \tag{6.1}$$

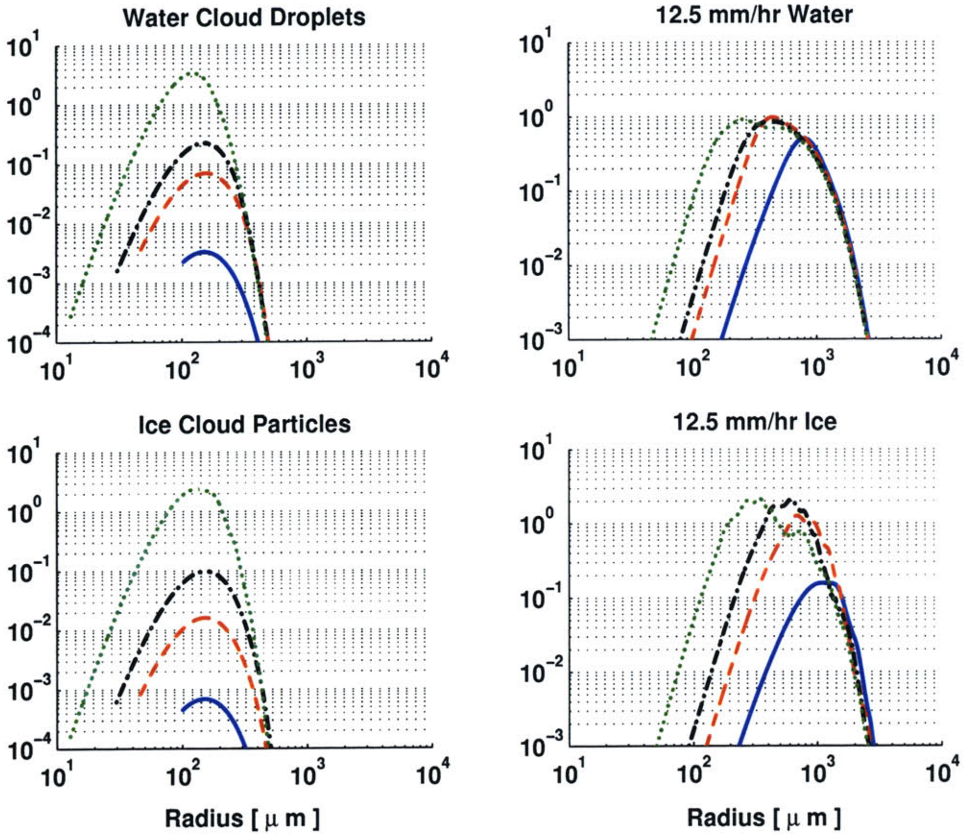

Figure 6-1: Ordinate: Number of drops per unit volume per drop-radius interval $[m^{-4}]$ multiplied by Scattering cross-section $[m^{2}]$ gives $[m^{-2}]$ Solid blue - 54 GHz, Dashed red - 118 GHz, Dashed-dot black - 183 GHz, Dotted green - 425 GHz

The plots on the left-hand side of the figure use a drop-size distribution $(p(r))$ that models cloud particles, and the right-hand side uses a drop-size distribution that models a rain rate of 12.5 mm/hr. The curves in the figure use the Marshall-Palmer [67, pg. 317] drop-size distribution for rain rate. The cloud particle drop-size distribution [67, pg. 306], the Mie scattering efficiencies [67, pg. 290], and the index of refraction are from Ulaby [67, pg. 298]. The scattering is assumed to be from water spheres, and liquid and frozen phases are only differentiated by their refractive index. The absolute values in the figure are relative when comparing the cloud droplets to the rain, but the difference of the values between the liquid and ice are useful within each of the columns in the figure.

Simple assumptions and the use of a hydrometeor's free-body diagram help develop relationships between the storm model and the microwave signature. The particles coming out of the updraft aloft are traveling in two directions. One is the radial direction away from the convective core by way of the outflow phenomena, and the other is descending downward vertically toward the surface because of gravity. In the vertical direction, the terminal velocity of the particle can be found by setting the force of gravity equal to the drag force. In general, two other forces are involved, which are buoyancy and mist drag. The buoyancy force is negligible in air, and the mist drag, which is the force of the raindrop accreting smaller mist droplets as it falls, is negligible when compared to air drag [21].

In Edwards *et al.* [21], the mist-free settling velocity (v_o) is a linear function of radius ($v_o = \delta \cdot r$) for raindrops 0.2 to 2.4 mm in diameter. The radius limitation is due to an approximation of the drag coefficient, which is a function of the Reynolds number and therefore the drop radius. The gain is equal to:

$$\delta = \frac{2}{3}\left(\frac{\rho_p}{\rho_a}\right)^{2/3}\left(\frac{g^2}{3\nu}\right)^{1/3}, \tag{6.2}$$

where ρ_a is the density of air, ρ_p is the density of the particle, g is the acceleration due to gravity, ν is the kinematic viscosity of air. At an eight kilometer altitude, the gain is equal to 10,574 sec^{-1}. Therefore, a 1-mm-diameter hydrometeor will have a "settling" velocity of 5.27 m/s, 0.4-mm-diameter hydrometeor settles at 2.11 m/s, and the 0.2-mm-diameter hydrometeor settles at 1.06 m/s . That suggests that the 0.2-mm-diameter hydrometeor will stay in the instrument's "field of view," before dropping out of the instrument's penetration horizon, for five times as long as the 1 mm-diameter hydrometeor would. The radial motion aloft depends partly on the reduction of the radial velocity as the particle gets further away for the storm's center, but the model here considers the radial velocity to be constant within the field of view.

Next the radiometer's scattering sensitivity must be considered. The Mie scattering efficiency is the ratio of the scattering cross-sectional area and cross-sectional area of the sphere. In the Rayleigh region, the formula for the scattering efficiency is [67]:

$$\xi_s = \frac{8}{3}\chi^4|K|^2; \ \chi = \frac{2\pi r}{\lambda}, \ K = \frac{n^2-1}{n^2+2}, \text{ and } |n\chi| \ll 1. \tag{6.3}$$

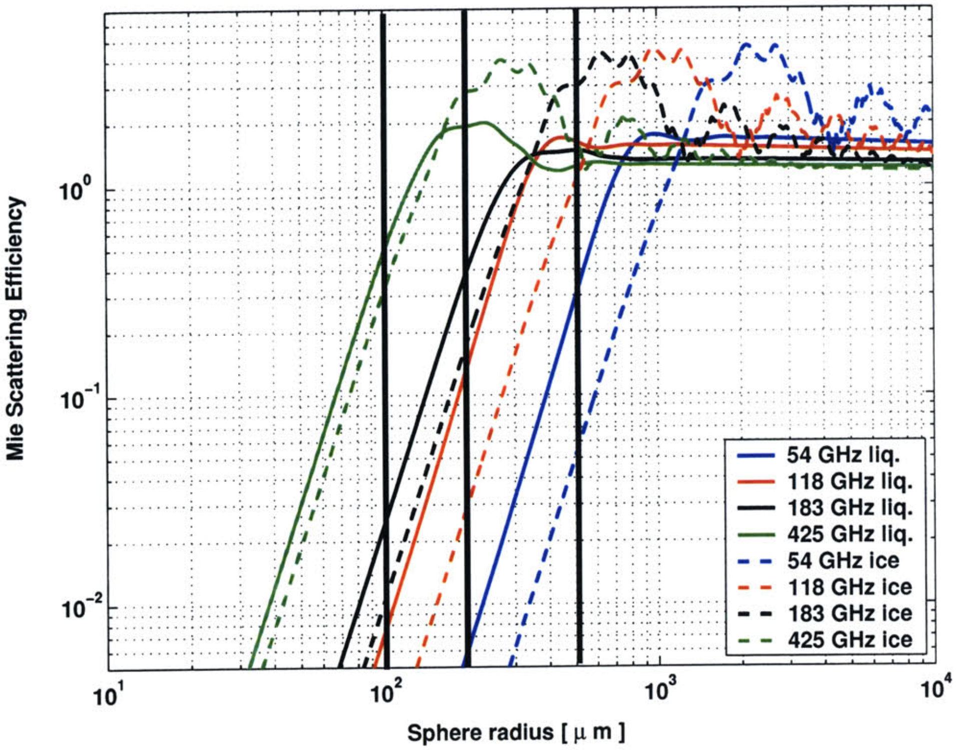

Figure 6-2: Mie scattering efficiency as a function of sphere's radius for water (solid line) and ice (dashed line): blue - 54 GHz, red - 118 GHz, black - 183 GHz, green - 425 GHz

The variables are the radius of the particle, r, the wavelength of the electromagnetic wave, λ, and the index of refraction of the particle, n. The scattering efficiency in the Rayleigh region is a function of the ratio between the particle diameter and wavelength. Figure 6-2 is the Mie scattering efficiency as a function of the sphere's radius. The three radii in this example are marked with black vertical lines. At 1-mm diameter, only the 54-GHz channel is in the Rayleigh region, and all channels are in the Rayleigh region for the 0.2-mm-diameter particle. The ratio of hydrometeor diameter to wavelength for a 1-mm-diameter particle at 50 GHz is roughly the same as the ratio of a 0.4-mm-diameter particle at 120 GHz.

$$\frac{\text{particle diameter}}{\text{wavelength}} = \frac{1\,mm}{6\,mm} = \frac{0.4\,mm}{2.5\,mm} \tag{6.4}$$

Even though the 0.4-mm-diameter particle is taking twice the amount of time to fall out of the field of view compared to the 1-mm-diameter particle, they have approxi-

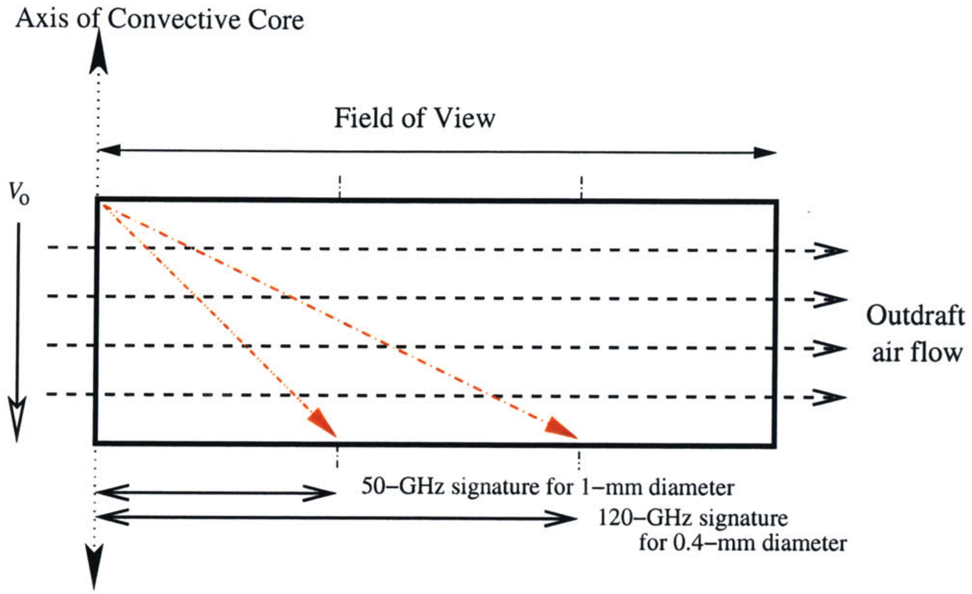

Figure 6-3: Illustration of the expected radiometric signature ratio calculations.

mately equivalent radiometric signatures. Figure 6-3 is an illustration of the particles of 0.4-mm and 1-mm diameter falling out of the anvil cloud of a convective cell. v_o is in the direction of the settling velocity. The radiometer is looking down onto the top of the outflow. Given that the ratios are equal in Equation 6.4, the radius of the 120-GHz channel's radiometric signature in the outflow region should be roughly twice the 50-GHz channel radiometric signature. With a similar argument, the 183 should have a radius approximately five times that of the 50-GHz channel (0.2-mm and 1-mm diameter particles). The 425-GHz band does not meet the criterion that $|n\chi| \ll 1$, so it is not appropriate in this set of examples. The hydrometeor drop-size distribution ($p(r)$) is modeled as an decaying exponential, and the Marshall-Palmer distribution is illustrated in Figure 5-8. As rain rate increases, the particle diameters increase. At 100 mm/hr, there are approximately 2.5 times as many 0.4-mm-diameter particles as there are 1-mm-diameter particles. The excess 0.4-mm diameter particles strengthens the argument of the equivalent radiometric signature between 50 and 120 GHz. The 0.4-mm diameter particles have to travel further away from the convective core, and therefore spread out further, but there are over twice as many of 0.4-mm-diameter particles, so they can still give a similar radiometric signature at 120 GHz as the denser 1-mm-diameter particles do at 50 GHz much closer to the core. Two mature cells from Section 6.3.1 can help validate these results. In particular, PTOST cells in Figure 6-5(c) and Figure 6-5(d) are cells that seem to be right after their peak, and therefore they are applicable to this argument. In Figure 6-5(c), from a point in the center of the 54-GHz perturbation, the radial distance to the 54-GHz 3-dB (half maximum perturbation) contour is ~ 2 km. Along the same radial direction, the 118-GHz contour is 5 km away from the center. This is close to the previous determined factor of two. The 183-GHz contour roughly follows precedent because it is 8 km away from the center. The factor of four instead of the factor of five between the 54-GHz radius and the 183-GHz radius could result from a reduction in radial velocity as the particles get further away from the center, or perhaps the storm has not yet reached maturity. In general, the greater the flow (kg/s) from the updraft, the more particles (and larger diameters) are injected into the outdraft. This model and the data collected give a basis for the relationship between the radiometric signature and aggregate rain rate. The above examples from PTOST are hardly conclusive, but it is the first step in validating the conceptual idea that relates a convective storm's strength to its microwave signature.

6.3 Field Deployment Observations

To support the theory of the relationship between aggregate rain rate and microwave radiometric signatures, empirical data was analyzed. The cells presented were chosen based on cell-image integrity, strength of scattering signature, and whether all four radiometers were working. A total of eleven cells meet the criterion from PTOST 2003 and three cells from CRYSTAL-FACE 2002. There were other potential cells from CRYSTAL-FACE, but the convective cells were in groups that made identifying the boundaries of individual cells difficult. The cells that were analyzed are summarized in Table 6.2 at the end of this section, but first the techniques for determining the perturbation area and the aggregate rain rate are presented in Sections 6.3.1 and 6.3.3, respectively.

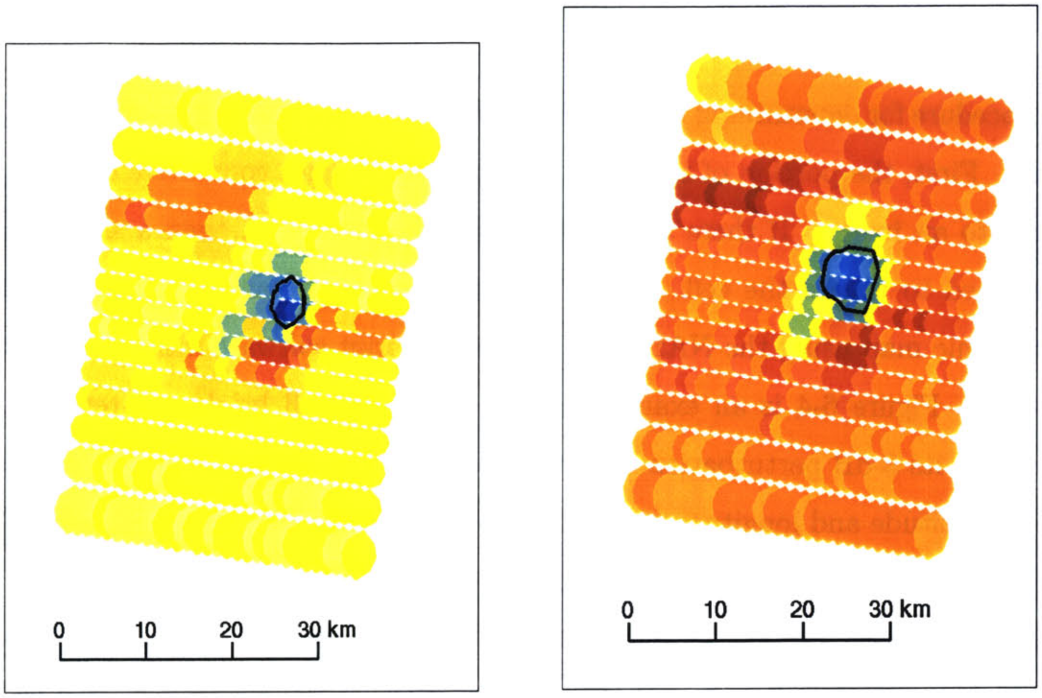

(a) 54-GHz Ch. 3 (b) 118-GHz Ch. 3

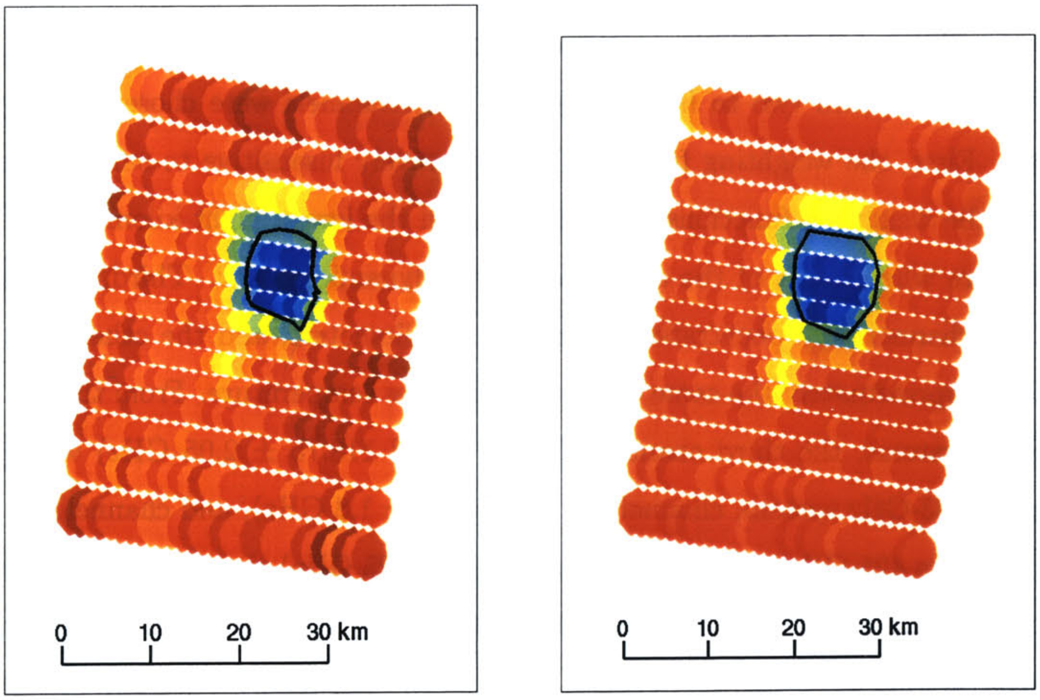

(c) 183-GHz Ch. 5 (d) 425-GHz Ch. 1

Figure 6-4: Example of the 3-dB perturbation contours over the brightness temperature image of a PTOST convective cell on March 14, 2003. (Designated C4)

6.3.1 Cell Brightness-Temperature Signatures

The procedure for determining the 3-dB brightness-temperature perturbation is straight forward. First, the portion of the flight related to the target convective cell was collected into an image. If there are multiple cells in the image, then a simple mask was applied to isolate the cell. Next the brightness temperatures were plotted on a geographic map using the NAST-M antenna-footprint software introduced in Section 3.2.1. Figure 6-4 is an example of the convective-cell brightness-temperature image with its 3-dB perturbation contours overlaid. The antenna-footprint software gives the latitude and longitude of each of the antenna spots. The coordinates of the NAST-M spots were calculated by using the GPS coordinates of the aircraft at the beginning the scan, the known scan pattern, the 3-dB antenna beamwidth, and the distance between the aircraft and the surface. The brightness-temperature images in Figure 6-4 are perturbations from a clear-air mean. A mean value was calculated for each spot from the nearest portion of clear air available. Each of the channels shown in Figure 6-4 had similar clear-air mean values and had weighting functions that peaked between two to five kilometers. The channels were chosen for several reasons. First, the weighting functions were relatively insensitive to surface effects. Second, the weighting functions generally covered the lowest eight kilometers of the atmosphere where most of the convective cloud dynamics occur. Third, the lowest 425-GHz channel only penetrated to about four kilometers, and the other channels matched approximately the same clear-air brightness temperature. From the 54- and 118-GHz systems, the third channel (52.6-53.0 and 118.75 ± 2.05 GHz) was used. From the 183-GHz system, channel five was used (± 1.8 GHz), and channel one was used from the 425-GHz system when available (± 3.25 GHz) or otherwise the second channel (± 2.15 GHz). The second channel of the 425-GHz system was used for the two cells on July 11, 2002.

The next step consisted of bilinearly interpolating the brightness-temperature perturbation and pixel coordinates twice in both directions. The cell's lowest brightness temperature was found within the interpolated image. If the perturbation was less

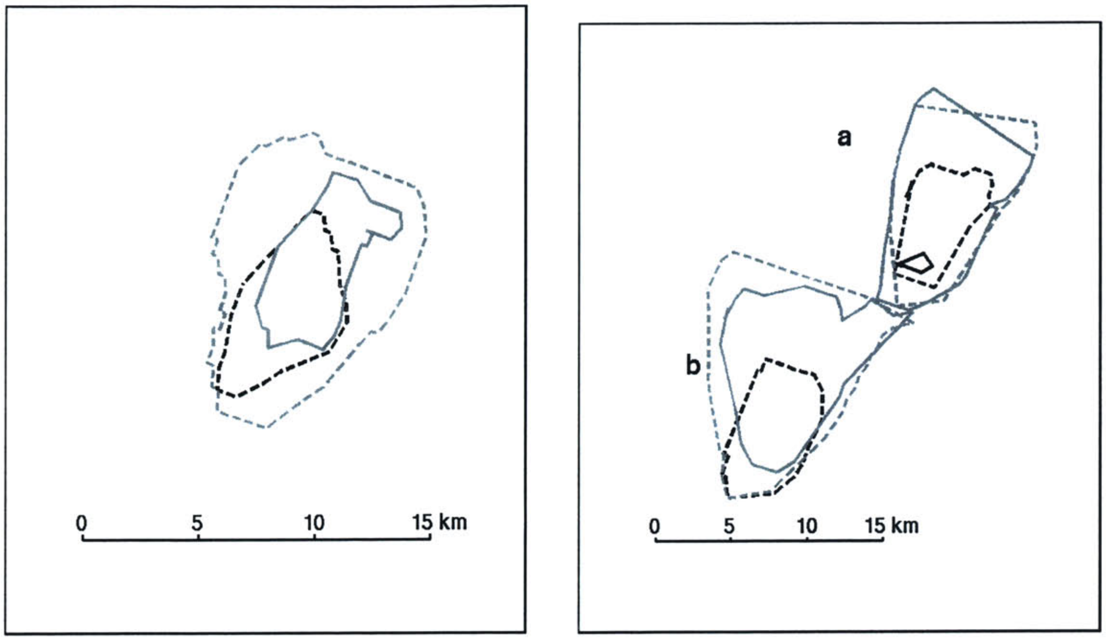

(a) PTOST: Location 1 (C1)

(b) PTOST: Location 2 (C2a, C2b)

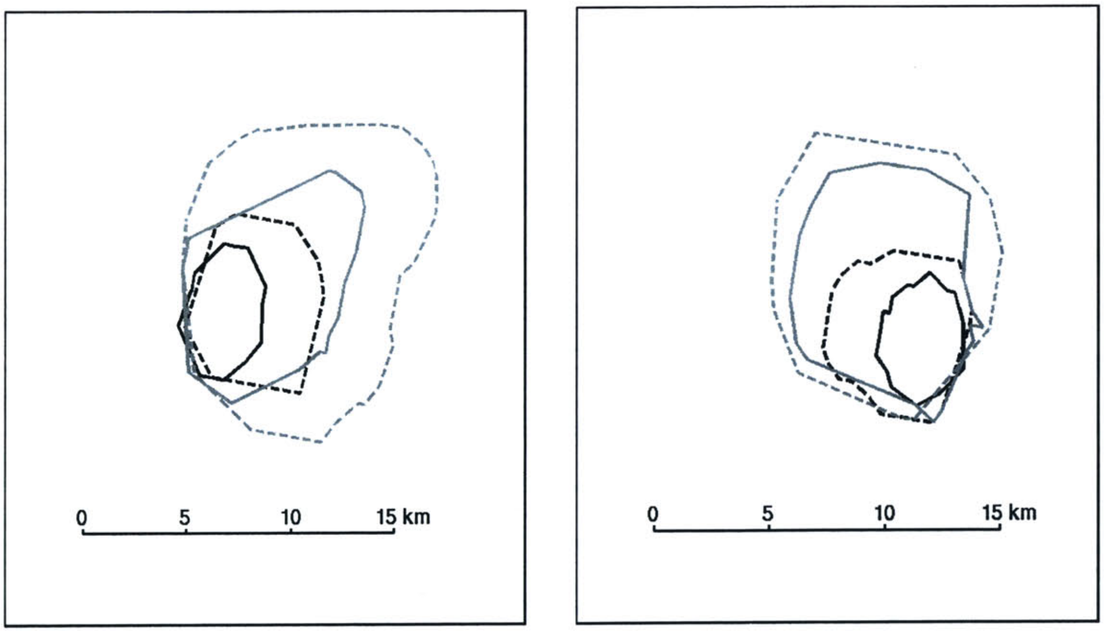

(c) PTOST: Location 3 (C3)

(d) PTOST: Location 4 (C4)

Figure 6-5: 3-dB contours of PTOST convective cells on March 14, 2003. Solid black line: 54-GHz Ch. 3; dashed black line: 118-GHz Ch. 3; solid gray line: 183-GHz Ch. 5; and the dashed gray line: 425-GHz Ch. 1.

than -1.5 K, then a search was performed within the interpolated image for all values at half of the maximum perturbation value. To ensure that enough values were found to encircle the perturbation, values typically within ±1 Kelvin of the target half-maximum perturbation were accepted. The limits were influenced by the size of the perturbation. Next, the marked interpolated pixels were related to their appropriate coordinates. The coordinates were rearranged into a polygon to allow the surface area to be calculated from a line integral approach. Examples of the results for a PTOST convective cell are drawn in Figure 6-4 as solid black lines over the brightness temperature perturbations.

6.3.2 Storm Life-Cycle Classification

Each convective cell was classified into one of three categories by inspecting the available video images, the 3-dB perturbation contour plots, and the retrieved precipitation cell-top altitude. The 3-dB contours of all fourteen convective cells are presented in Figures 6-5, 6-6, 6-7, and 6-8. The available NAST-M video images of the PTOST convective cells on March 14, 2003 are presented in Figure 6-9. The convective cell observed on July 13, 2002 during CRYSTAL-FACE was extensively examined in Chapter 5 in Section 5.4.2. Only the 3-dB contour of the second pass is presented because the first pass seemed to cover only a limited portion of the convective storm. The 3-dB contours of the second pass are presented in Figure 6-8(a). The convective cells from July 11, 2002 were not presented in Chapter 5, but Figure 6-10 presents a comparison between the GOES-8/composite radar and the NAST-M data. The brightness temperature perturbations had a baseline removed, which is presented for each channel at the bottom of the figure. There were several convective cell candidates to analyze in this image, but only two were good enough (*i.e.*, well-defined boundaries). CF2b can be easily identified as the isolated cell at 16:53 UTC, while CF2a can be identified as the only perturbation visible in the 54-GHz channel's image.

The above mentioned figures were used to classify each cell into one of three storm stages. In some cases, the convective cell had some characteristics outside its

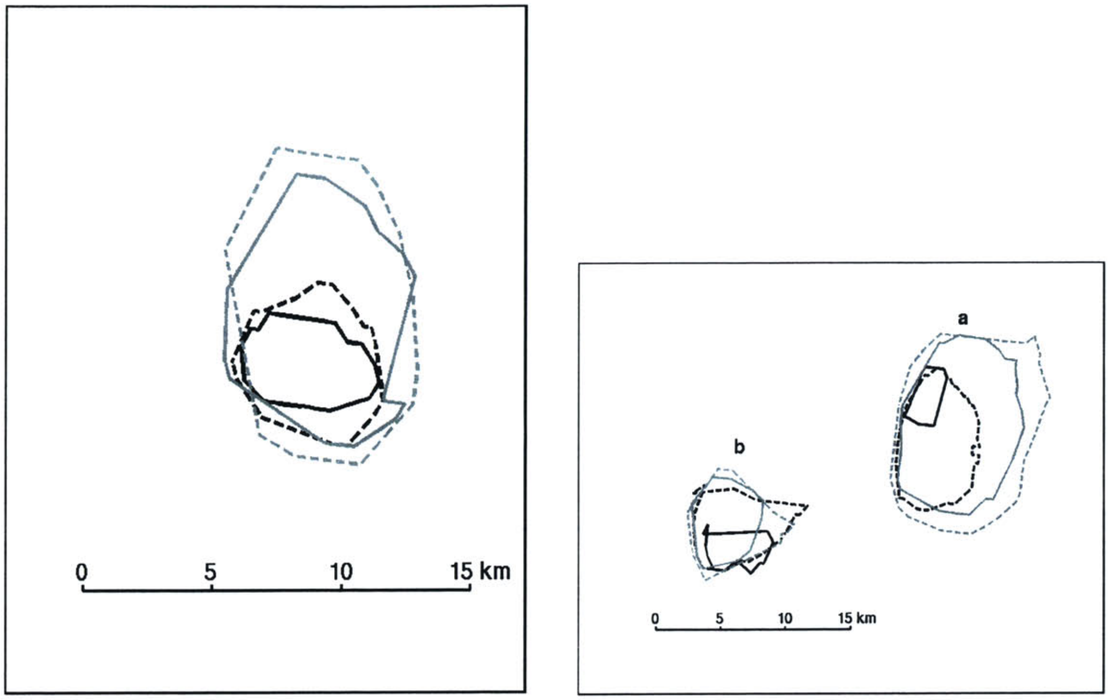

(a) PTOST: Location 5 (C5)

(b) PTOST: Location 6 (C6a and C6b)

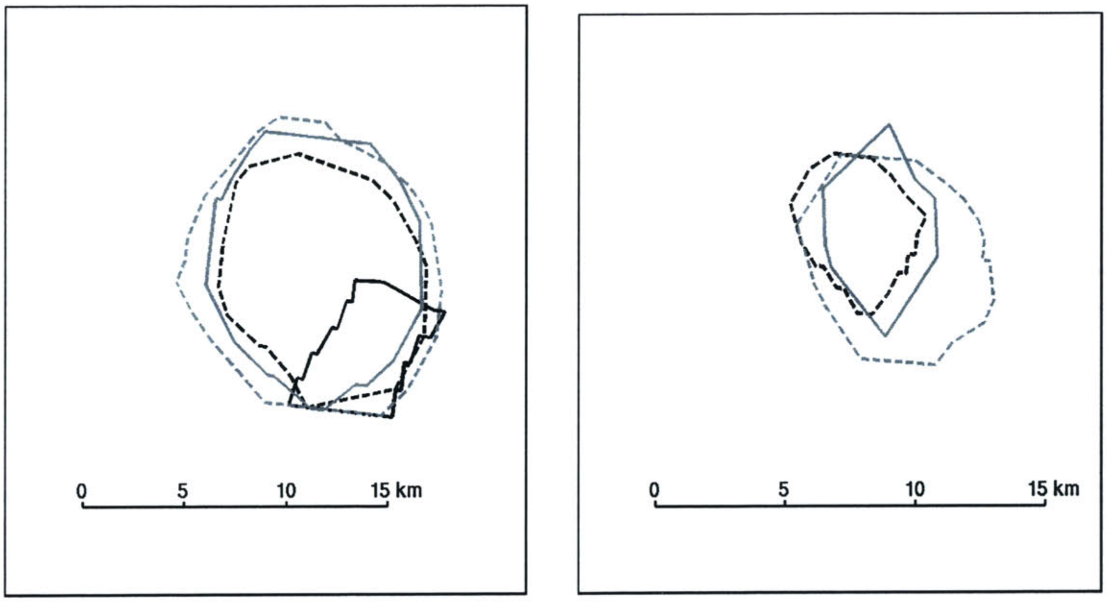

(c) PTOST: Location 7 (C7)

(d) PTOST: Location 8 (C8)

Figure 6-6: 3-dB contours of PTOST convective cells on March 14, 2003. Solid black line: 54-GHz Ch. 3; dashed black line: 118-GHz Ch. 3; solid gray line: 183-GHz Ch. 5; and the dashed gray line: 425-GHz Ch. 1.

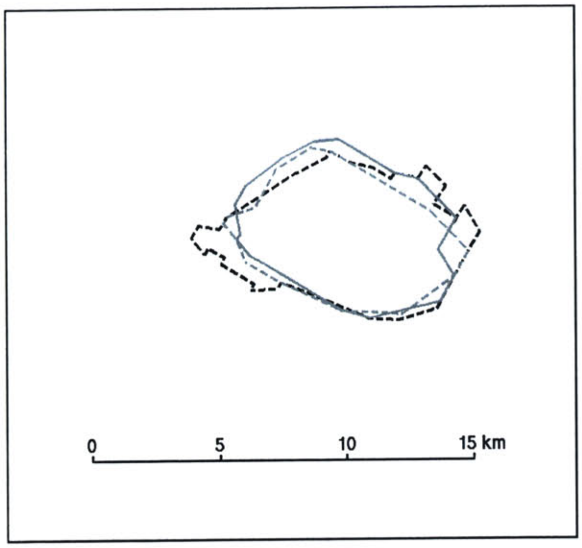

Figure 6-7: PTOST: 3-dB contours of convective cell (C9). Solid black line: 54-GHz Ch. 3; dashed black line: 118-GHz Ch. 3; solid gray line: 183-GHz Ch. 5; and the dashed gray line: 425-GHz Ch. 1.

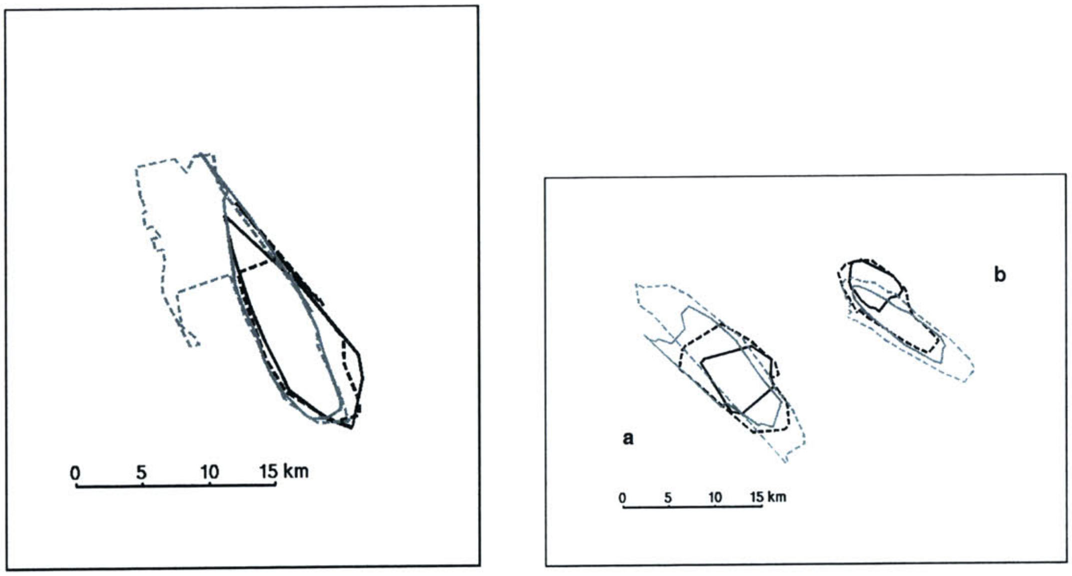

(a) July 13, 2002 (CFP2)

(b) July 11, 2002 (CF2a and CF2b)

Figure 6-8: 3-dB contours of the CRYSTAL-FACE 2002 convective cells. Solid black line: 54-GHz Ch. 3; dashed black line: 118-GHz Ch. 3; solid gray line: 183-GHz Ch. 5; and the dashed gray line: 425-GHz Ch. 1 on 13th and Ch. 2 on the 11th.

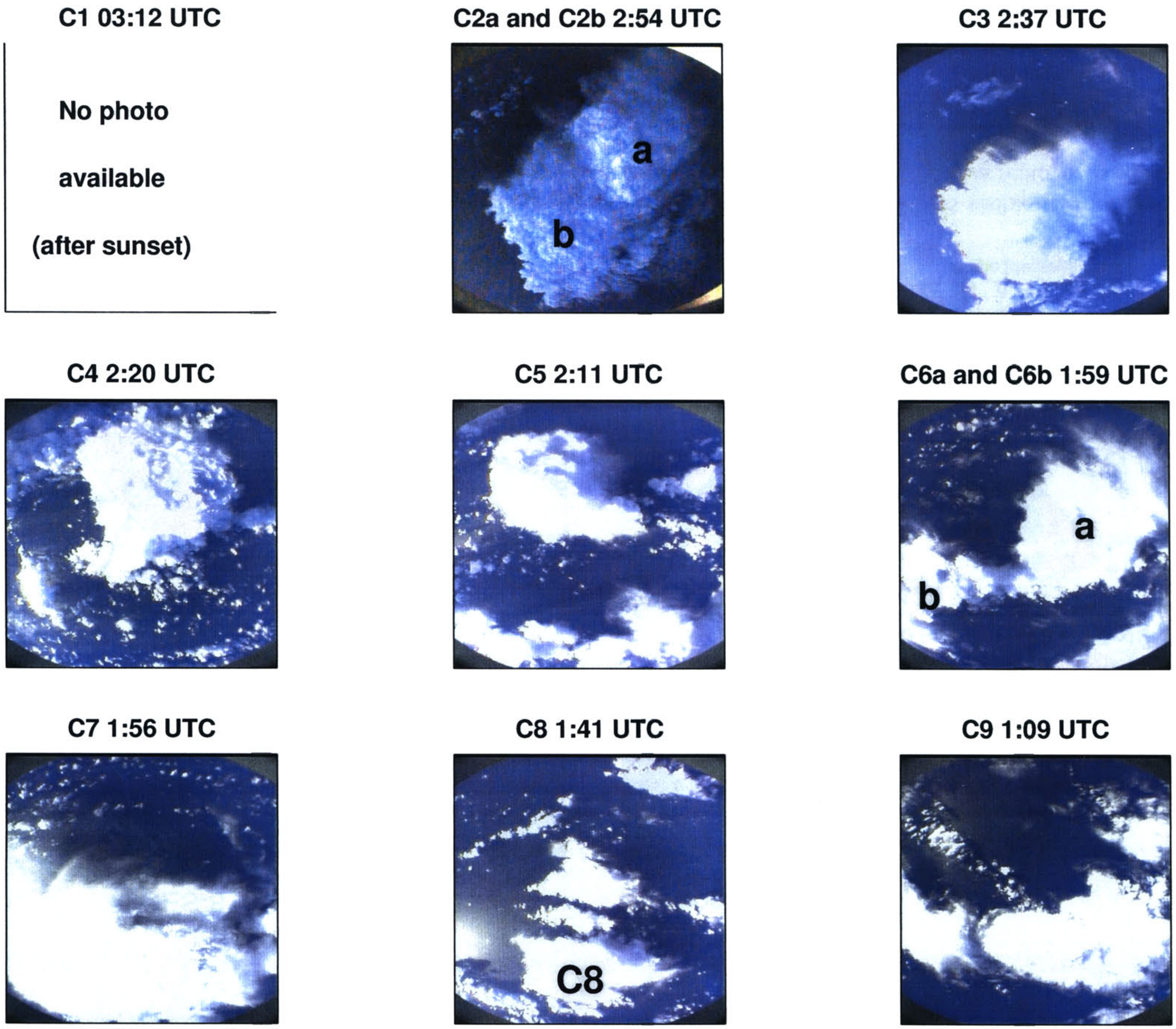

C1 03:12 UTC

No photo

available

(after sunset)

C2a and C2b 2:54 UTC

C3 2:37 UTC

C4 2:20 UTC

C5 2:11 UTC

C6a and C6b 1:59 UTC

C7 1:56 UTC

C8 1:41 UTC

C9 1:09 UTC

Figure 6-9: NAST-M video images of the eleven PTOST convective cells on March 14, 2003.

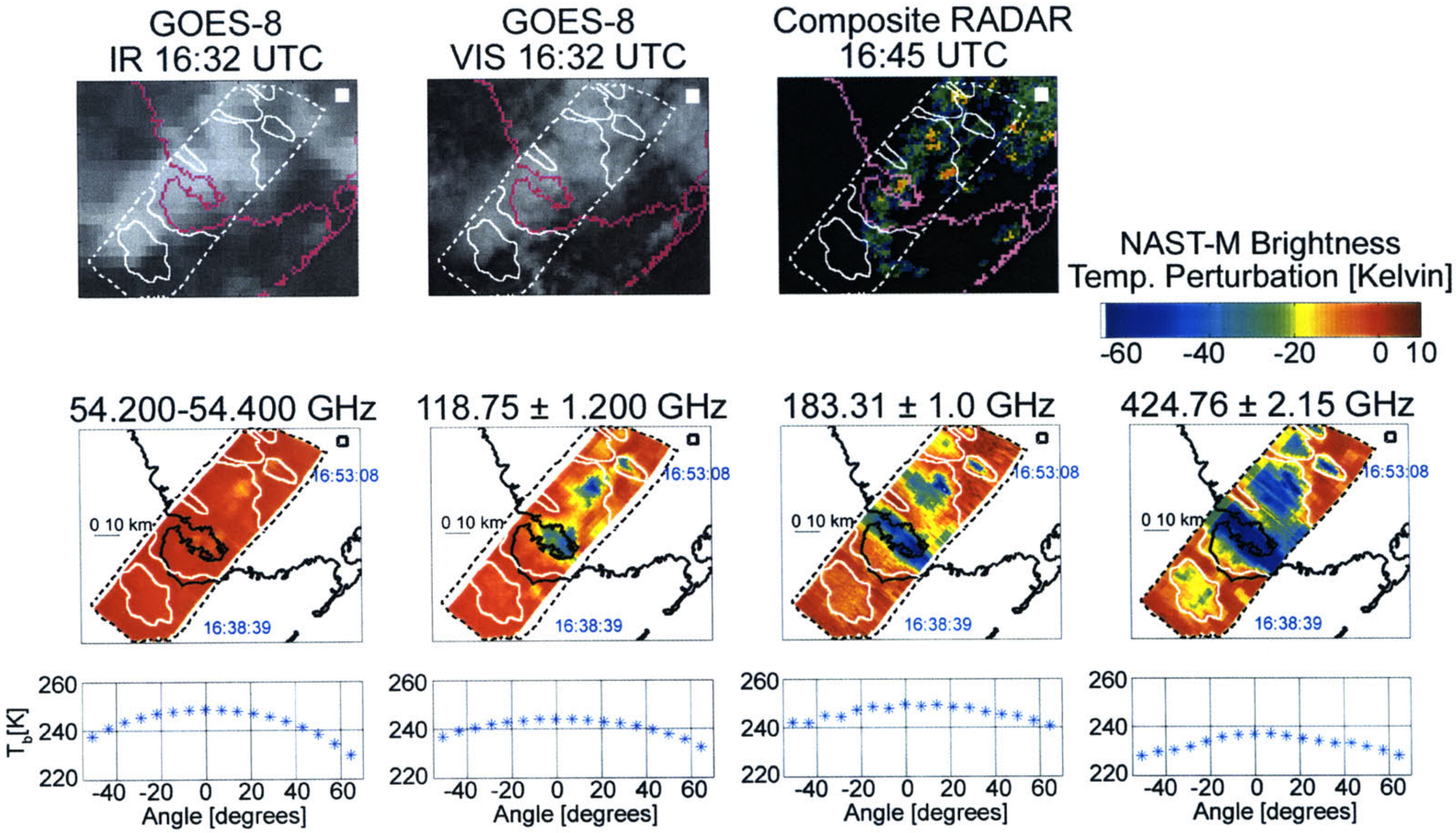

Figure 6-10: CRYSTAL-FACE: Selected NAST-M channels from July 11, 2002 along with GOES visible and infrared images and composite radar. The brightness temperature images are perturbations and the baseline that was removed is shown at the bottom for each channel.

Table 6.1: Classification of Life-Cycle Stages

No.	Category Title	Cell Identification	Figure Color	Figure Symbol
1	Growing	C2a, C5, C6b, CF2b	green	○
2	Mature	C3, C4, C6a, C7, CFP2, CF2a	red	□
3	Dissipating	C1, C2b, C8, C9	black	△

Symbols are used in Figure 6-13 and 6-14.

classification and could be debated. A storm gains intensity in its early stage (when the highest rain rates usually occur) until it reaches a peak, at which point the storm loses energy and dissipates. The cells were classified into either growing, mature (near the peak of the storm), or dissipating. The purpose of classification is to identify how the cell fits into the 3-D model presented in Section 6.2 or any trends the cells within a particular stage follow.

The characteristics that identified the growing-stage classification were equal-area perturbations between frequencies along with a relatively high cell-top altitude. A third trend were the maximum-perturbation values were similar across the radiometers. The differences of the maximum-perturbation values only marginally increased with frequency compared to the mature stage where there was a steady increase in the maximum-perturbation values with frequency (see Table 6.2). The mature stage has two additional characteristics. First the perturbation areas were steadily increasing as frequency increased, which is a sign that the sizes of the hydrometeors were decreasing in the radial direction. The retrieved cell-top altitudes were the highest. The last category had two easily identifiable characteristics. There was negligible perturbation near 54 GHz, and the area of the other channels increased with frequency. This fits with the theory that the largest hydrometeors have fallen out, while the increasing area per frequency is an indication of the smaller particles still present.

6.3.3 Aggregate Rain Rate Estimation

The calculation of aggregate rate rate is based on the single-pixel rain-rate retrievals from Chapter 5. The convective cells were separated into single pixels, and the single-pixel retrievals of rain rate were integrated to find the aggregate rain rate. The volumetric rain rate was approximated as:

$$
\begin{aligned}
V = \int_Y \int_X R(x,y)\, \delta x\, \delta y \ &\approx \ \sum_{j=1}^{M} \sum_{i=1}^{N} R(x_i, y_j)\ dx_i\, dy_j \\
&\approx \ \sum_{j=1}^{Sp} \sum_{i=1}^{Sc} R(i,j)\ area_j, \qquad (6.5)
\end{aligned}
$$

where V is the aggregate rain rate ($km^2\, mm/hr$), and $R(x,y)$ is the rain rate (mm/hr) as a function of the coordinate x and y. The single-pixel rain rate estimate is discrete and represents the rain rate within the antenna's footprint. In this application, an area similar to the antenna's footprint ($area_j$) replaces the incremental area ($dx_i\, dy_j$) in the last line of Equation 6.5. The $area_j$ is a box surrounding the antenna footprint. This assures the area of the entire image is covered. The value of Sp represents the total number of scan angles used, *i.e.*, the spots, in the image, and the value of Sc is the total number of scans in the image. The area of the antenna footprint ($area_j$) on the ground is dependent on the scan angle and altitude. The nadir antenna footprints are circular, while those at the extreme angles are elliptical in shape. Figure 6-11 is an illustration of the footprints on the surface from an altitude of 20 km while NAST-M is aboard the ER-2. On either platform, there is oversampling in the direction of the aircraft's motion as can be seen in Figure 6-11. The approximation in Equation 6.5 does not account for overlap at nadir. While on the ER-2 aircraft, the scans are split into two sets of data. The first set is represented by the solid black circles (or ellipses) in Figure 6-11, and the second set is represented by the dashed circles. Note that the antenna footprints in each individual set do not overlap. Summing the values within one set of data gives an estimate of the volumetric rain rate. The two sets of non-overlapping footprints give two estimates of the same volumetric rain rate, and they are averaged together. The Proteus aircraft travels at less than half the speed of the ER-2, and the footprint overlap is much greater. Figure 6-12 is an illustration of the nadiral Proteus footprints on the surface from an altitude of 17.5 km. The data from the Proteus required a slightly different approach. Instead of separating the pixels into two independent images, every third pixel was separated into three independent images. All three images were averaged to get the final estimate of the volumetric rain rate or aggregate rain rate.

6.3.4 Comparative Analysis

The techniques for determining the radiometric signatures and aggregated rain rate of the fourteen convective cells has been described in Section 6.3.1 and 6.3.3, respectively. Table 6.2 summarizes the results of the analysis. The precipitation cell-top altitude was estimated using the nearest-simulation technique described in Chapter 5. There are numerous metrics that can be used to relate the radiometric signature to the aggregate rain rate. Figure 6-13 gives insight into a good metric and has a curve plotted for each of the fourteen cells. They were color/symbol coded by the classification of its life-cycle stage (see Table 6.1). Some of the characteristics used to classify the cells can be seen in the Figure 6-13. For example, the mature stage has a well-developed 54-GHz signature surface area and steadily increasing perturbation surface area as frequency increases, while the growing stage curves were more level across frequency. The dissipating stage had curves with both characteristics, and this can be credited to various stages of decay. The dissipating curves did share the characteristic that the 54-GHz channel's perturbation was negligible.

These trends in the area/frequency relation led to a metric that summed the areas for all four radiometers. The results are plotted in a scatterplot in Figure 6-14. The black dashed line minimized the least-squares error. The life-cycle classification behaved as expected, with the dissipating cells tending towards the bottom left-hand corner, the mature stages in the upper right-hand corner, and the growing stage in between. The "y-intercept" of the regression is close to zero, but from these data points, the dynamic range of the regression cannot be determined. The slope is about

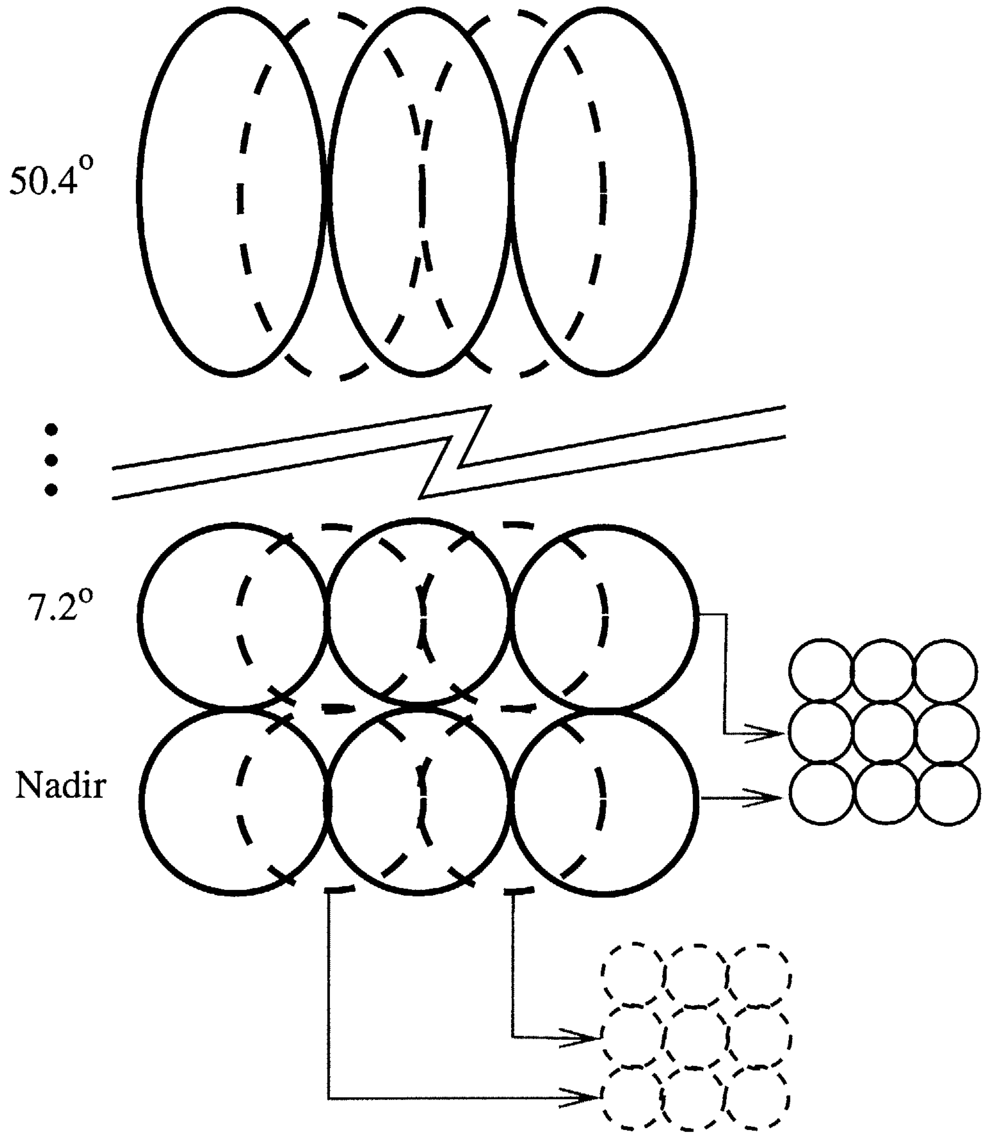

Figure 6-11: Illustration of the antenna footprints on the surface from an altitude of 20 km aboard the ER-2. The spots do begin to enlarge as the scan angle increases, so there is some overlap in the direction of flight at the extreme angles.

Table 6.2: Cell Summary

Cell #	Label	Aggregate rain rate $[km^2 \cdot \frac{mm}{hr}]$	Cell-top altitude [km]	54 GHz Ch. 3	118 GHz Ch. 3	183 GHz Ch. 5	425 GHz Ch. 1	
1	C1-△	742.9	5	1.77	-6.26	-5.69	-15.42	ΔT_b [K]
				0	25.95	24.02	80.37	Area $[km^2]$
2	C2a-○	1731.3	7.5	-3.46	-17.69	-19.86	-25.33	ΔT_b [K]
				1.53	31.80	86.42	85.98	Area $[km^2]$
3	C2b-△	939.1	6	-0.47	-11.70	-16.92	-21.83	ΔT_b [K]
				0	40.75	86.01	129.33	Area $[km^2]$
4	C3-□	1168.9	8.5	-6.45	-19.06	-27.53	-34.72	ΔT_b [K]
				19.03	42.91	66.27	128.71	Area $[km^2]$
5	C4-□	2088.0	7.5	-8.09	-17.06	-31.03	-37.19	ΔT_b [K]
				15.37	36.04	67.67	94.55	Area $[km^2]$
6	C5-○	1712.6	8.5	-7.23	-16.76	-20.85	-27.89	ΔT_b [K]
				14.57	25.43	54.02	68.88	Area $[km^2]$
7	C6a-□	2427.6	8	-2.40	-12.98	-18.86	-27.92	ΔT_b [K]
				8.99	52.88	101.76	145.05	Area $[km^2]$
8	C6b-○	613.5	7	-2.43	-12.77	-20.46	-28.72	ΔT_b [K]
				12.64	35.96	28.95	40.77	Area $[km^2]$
9	C7-□	2684.5	8	-2.81	-12.46	-19.20	-26.44	ΔT_b [K]
				28.34	94.14	107.60	137.50	Area $[km^2]$
10	C8-△	250.1	4	-0.84	-6.89	-9.64	-18.47	ΔT_b [K]
				0	20.31	22.73	45.28	Area $[km^2]$
11	C9-△	866.9	5	-1.29	-7.17	-12.55	-17.31	ΔT_b [K]
				0	44.99	42.06	38.23	Area $[km^2]$
12	CFP2-□	2317.5	14.5	-83.29	-118.55	-163.39	-125.47	ΔT_b [K]
				64.70	58.03	61.88	115.35	Area $[km^2]$
13	CF2a-□	774.6	12	-40.47	-75.78	-87.64	-64.53	ΔT_b [K]
				36.65	80.34	75.82	108.00	Area $[km^2]$
14	CF2b-○	444.9	9	-38.49	-55.57	-67.00	-55.94	ΔT_b [K]
				19.29	48.61	28.93	60.94	Area $[km^2]$

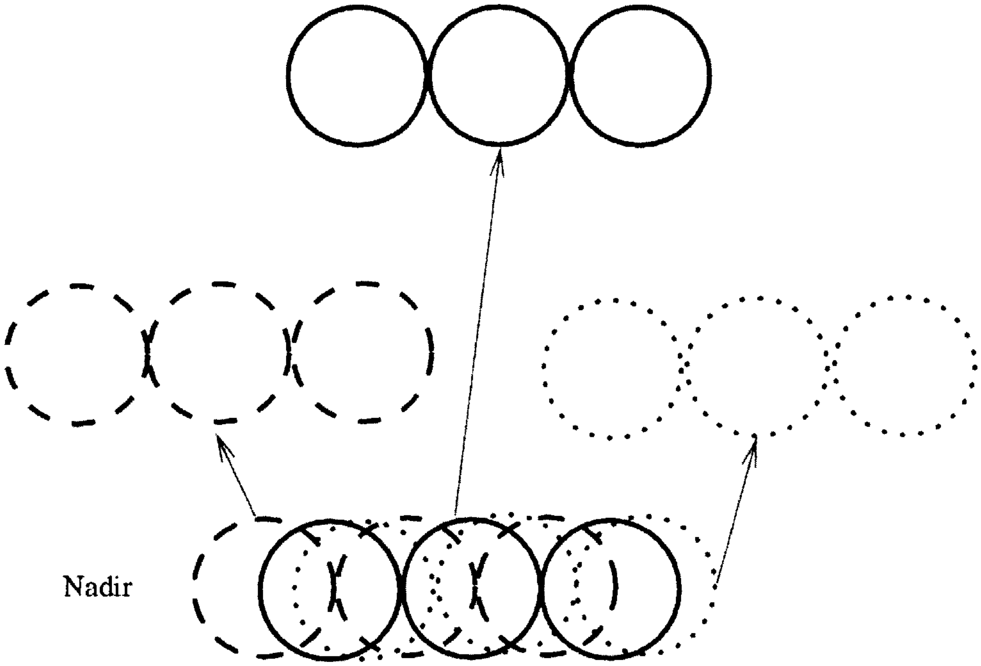

Figure 6-12: Illustration of the nadir antenna footprints on the surface from an altitude of 17.5 km aboard the Proteus.

five.

6.4 Conclusion

This chapter provides a rudimentary foundation for retrieving precipitation parameters on a storm-wide scale from the microwave radiometric signatures. First, a convective cell model was reviewed and elaborated. Next, convective cells were analyzed from data collected during two recent deployments in which convective cells were imaged. The radiometric areas were quantified for fourteen convective cells, which included convection over land and ocean. The cells were also classified within their life cycle, and characteristics unique to each classification were identified within the radiometric signatures. Finally, the aggregate rain rate was estimated using the techniques introduced in Chapter 5 as a base. The aggregate rain rate was well correlated with the cumulative area of the radiometric signatures. Other metrics were attempted beside the cumulative area, such as the sum of the ratios of the 3-dB perturbation areas by the maximum-perturbation values, or solely the area signature

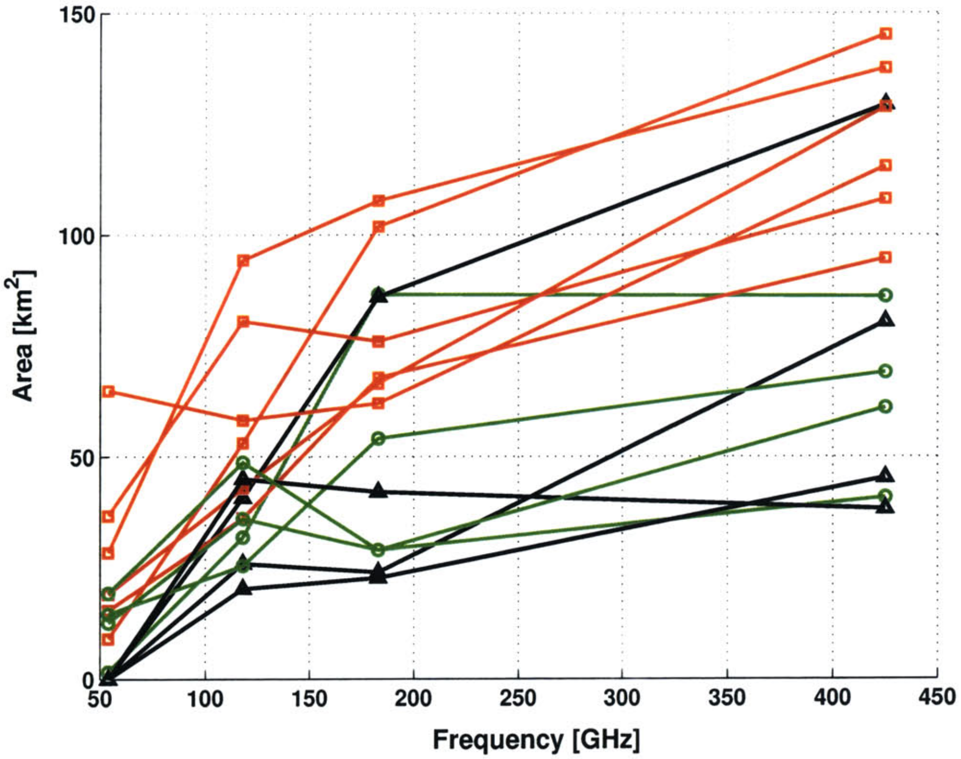

Figure 6-13: Each of the fourteen cells has a frequency versus area curve on this plot. The red squares are the cells classified as being at the mature stage. The green circles are classified as cells in the growing stage, and the black triangles are cells that are dissipating.

of the 425-GHz channel, but the cumulative sum performed the best. The cell life-cycle stages were grouped in reasonable sections of the regression, with the mature cells exhibiting higher aggregate rain rates, while the dissipating cells were positioned toward the low end.

The low aggregate rain rate of the convective cells over land caused some concern. They had the largest maximum-perturbation values, but the aggregate rain rate retrieved was relatively low. The RMS discrepancy between the actual brightness temperatures and the simulated training-ensemble brightness temperatures (*e.g.*, Figure 5-21(b)) for the land convective cells was larger than the oceanic convective cells by three Kelvin, which suggests that the nearest-profile estimate is not finding a brightness temperature profile very similar to the actual brightness temperature the instrument measured when viewing the land-based convective cells. This means that the training ensemble does not match the land-based convective cells as well as it

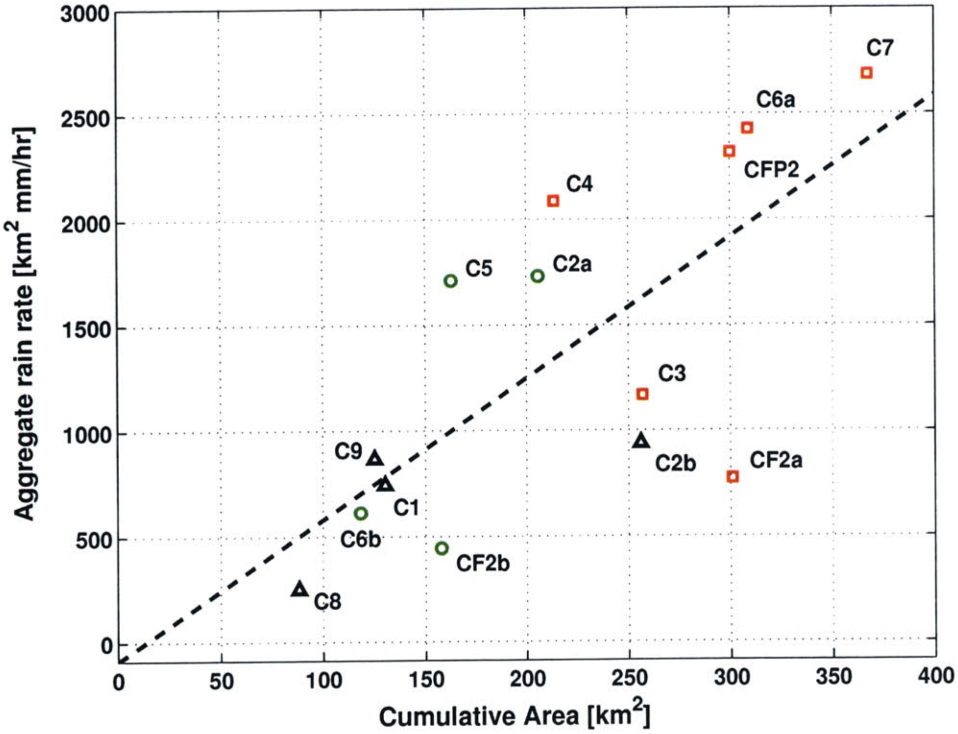

Figure 6-14: Regression of aggregate rain rate versus cumulative area for the fourteen cells. The cell labels reference Table 6.2, while the life-cycle stage are represented as black triangles for dissipating, green circles for growing, and red squares for mature. (See Table 6.1)

does the oceanic convective cells. An independent estimate of the aggregate rain rate would help validate the regression, but there are few options for measuring aggregate rain-rate for oceanic convective cells.

The life-cycle classification of a storm through its microwave signature is a testament to the ability of microwaves to penetrate a storm's internal structure. The comparison between the different frequencies only enhanced the information gained. The microwave signature component of the 3-D convective storm model presented by Staelin [60] was elaborated. Cells C3 and C4 are the ones most consistent with the 3-D convective model. The 3-D convective model made the assumption that the storm was near or closely after maturity, and the life-cycle classification of C3 and C4 was mature.

Chapter 7

Conclusion and Future Work

The conclusions are divided into three areas, which are instrumentation, validation, and science. The instrumentation section covers the present state of the 183- and 425-GHz spectrometers. The validation section discusses the results of the calibration of CRYSTAL-FACE 2002 and PTOST 2003. The science section covers both the single-pixel and cell-wide retrievals. The last section presents ideas for future work.

7.1 Instrumentation

The 183- and 425-GHz spectrometers were successfully integrated into the existing NAST-M instrument, and gave the suite the ability to sense water vapor and smaller-diameter hydrometeors. The engineering required minimum modification to the scanning assembly, while still maintaining the co-location of all four radiometer antennas. The data processing capabilities were upgraded to include the new spectrometers, and at the same time improved performance of the instrument in the field, *i.e.*, reduced the number of in-flight computer restarts.

The 183-GHz system has LO leakage that disrupts the 118-GHz system, which is not an atypical problem with receivers that upconvert from a relatively low LO frequency. Techniques must be investigated to mitigate the 183-GHz receiver's LO leakage. The 425-GHz system is a paradigm of the problem with finding high-frequency high-power oscillators that are stable in non-laboratory conditions. The 106-GHz

LO had difficulties from the beginning, because it was power starved at the target frequency of 106.19 GHz. A minimum amount of input power is necessary to properly drive the subharmonic mixer, and the Gunn oscillator was unable to maintain it. Also, the oscillator was not designed for the harsh flight conditions, and it turned out that maintaining a stable RF frequency during flight proved to be very difficult. The LO would shift frequency, which was blamed on the mechanical frequency tuner. The mechanical frequency tuner was a micrometer that would adjust a short within the Gunn diode cavity. Often, vibration would move the short, and it would have to be retuned. Even with these difficulties, NAST-M has produced the first images obtained with a 425-GHz spectrometer, and is also the only microwave suite with this collection of microwave channels.

7.2 Validation

The validation of the Cirrus Regional Study of Tropical Anvils and Cirrus Layers-Florida Area Cirrus Experiment (CRYSTAL-FACE 2002) and the Pacific THOR*pex* (THe Observing-system Research and *p*redictability *ex*periment) Observing System Test (PTOST 2003) was successful and prepared the flight data for access by the public. The various hardware issues mentioned in Sections 4.2.4 and 7.1 were identified, and a technique was devised that estimated the LO frequency for the double-sideband systems that view oxygen absorption lines through the zenith port.

The laboratory measurements provided a simple correction to be included in the standard calibration technique, but further investigation into the source of the discrepancies is needed. Two options were developed for dealing with the two-Kelvin discrepancy in the calibration load's temperature. The discrepancy was found to be across all channels. The first option adjusted the temperature of the external ambient load (used in the laboratory experiments) to match the radiometric difference, while the second option reduced the internal sensor's measurement of the load's temperature. While the first option had a more physically plausible explanation (*i.e.*, the measurement of the external Eccosorb's temperature was flawed), the second option agreed better with brightness-temperature simulations for all channels.

7.3 Science

The science contributions were twofold. First is NAST-M's improved sensitivity to hydrometeor diameters and the implications for precipitation-parameter estimation. The second contribution comes from the increase in understanding of the relation between convective precipitation and microwave signatures.

7.3.1 Convective-Cell Brightness-Temperature Modeling

A simplified hydrometeor-profile set representing convective cells was presented. The simplified hydrometeor-profile model and the radiative transfer equation allowed brightness temperatures to be simulated, which were compared to the actual brightness temperatures measured over convective phenomena during CRYSTAL-FACE and PTOST. The comparison revealed that the simplified model showed agreement over a wide range of convective activity. The results allowed each pixel to be classified as clear air, a non-precipitating cloud, or a precipitating cloud, which leads to a number of useful applications, *e.g.*, category-specific estimators. The simplified profiles produced a brightness-temperature training ensemble, which was used in two precipitation-parameter estimation techniques. The first used the ensemble to determine the coefficients of a Bayesian polynomial estimator, while the second technique found the shortest mean-squared-error distance between the actual brightness temperature and the simulated ensemble. The polynomial technique was simple, but problematic with negative rain rate and unrealistic retrievals under certain conditions. The "nearest profile" technique did not have these problems, but the retrieval technique did have quantization error. For example, the ensemble included simulations using only a finite number of rain rates, so actual rain rates in between two neighboring simulated rain rates would be limited to one or the other. The oceanic convective cells showed good retrieval results with the polynomial estimator, and most of the difficulties came from the land-based convective cells. Another result confirmed the necessity of including cloud particles in the scattering regime for millimeter wavelengths (425-GHz system). The 425-GHz system was very sensitive to cloud-particle scattering; especially to the cloud particles over precipitation.

7.3.2 425-GHz Spectrometer

There are several concerns with a geostationary 425-GHz radiometer, and the 425-GHz data presented in this thesis contributes empirical results to discussions that were previously limited to simulations and theory. First, it was evident that the window channels of the 425-GHz are blind to much of the atmospheric dynamics in the lowest three kilometers of the troposphere, and it was shown that water vapor obscures the lowest-lying clouds in the brightness temperature imagery. A combination of flight and simulation data supports the inability of the 425-GHz system to sense low-lying precipitation. Scatter plots of the simulated 54- and 425-GHz window channels, in which the simulated precipitation altitude and rain rate varied, showed that the 425-GHz brightness-temperature perturbations for the precipitation altitudes less than four kilometers were negligible and therefore indecipherable. The evaluation of the polynomial precipitation-parameter estimator using only the 183- and 425-GHz channels gave further evidence of the 425-GHz system's poor performance at low altitudes.

On the other hand, the 425-GHz channels seemed to have the greatest ability to identify convective cells from a geostationary platform. The convective cells imaged had perturbation diameters that varied with frequency, and the largest perturbation diameters came from the 425-GHz channels. The GEM/GOMAS [6] proposal presented the 425-GHz spatial resolution at 16 km for a two-meter diameter antenna, while the 183-GHz channels were at 42 km. The aircraft's 425-GHz data showed promise in being able to recognize convective cells (which were typically 15 km in diameter at 425-GHz) from a geostationary platform because the 425 GHz sensitivity to smaller hydrometeors produced a larger radiometric signature, which would be visible at the GEO's expected spatial resolution. The other lower resolution radiometers may not register a strong enough signature, under certain circumstances.

7.3.3 Cloud Structure

The millimeter wavelengths of the NAST-M suite have a unique ability to penetrate convective cells. This was demonstrated by the 54-GHz system and the rain-rate retrieval (which used all of the channels) in the possible identification of a gust front within the convective cell (see Figure 5-20). Also, a squall line is made up of several convective cells in close proximity, which can be indistinguishable to precipitation estimation techniques that rely solely on cloud-top area or temperature. The wide microwave-frequency range allows the NAST-M suite to identify individual cells underneath a single cloud canopy. Furthermore, by recognizing trends in the microwave signature, the individual cells were classified within their life cycle.

7.3.4 Radiometric Signature and Aggregate Rain Rate

Previous work related radar echos to the aggregate rain rate, *i.e.*, volumetric rain rate (m^3/s). A potentially useful contribution of this thesis is the introduction of a rudimentary basis for relating the passive microwave radiometric signature to the instantaneous volumetric rain rate and, with enough temporal coverage, the entire rain volume (m^3) of a convective cell.

7.3.5 Convective Cell 3-D Model

A three-dimensional convective cell model was elaborated, which gives a physical basis for the relationship between the radiometric signature and aggregate rain rate. The emphasis was on the microwave spectrometer's sensitivity to the hydrometeor diameter distribution as they radially disperse within the convective cell's outflow. Such sensitivity to particle diameter requires a microwave suite with a frequency range similar to NAST-M.

7.4 Future Work

The future work is divided into instrumentation and science.

7.4.1 Instrumentation

Adding radiometers to the existing NAST-M suite will require serious modifications to the instrument, which has little spare room after the 183- and 425-GHz additions. Yet, the addition of radiometers at 23.8, 31.4, and 89 GHz would better match the AMSU/HSB sounding suite and allow direct comparisons between precipitation estimation techniques on the aircraft and satellite platforms.

Achieving the present NAST-M configuration's full capability might start with redesigning the 425-GHz receiver's LO chain. This will make 425-GHz system operate at the correct target frequency, and therefore have proper temperature sounding weighting functions. Other issues include the LO leakage of both the 183- and 118-GHz radiometers. Another issue to work out is the LO switching from 183 to 166 GHz, which includes optimizing the 183-GHz mixer for both 183 and 166 GHz and determining NAST-M's radiometric response, *e.g.*, whether NAST-M exhibits output transients when the LO switches frequency.

Validation of CRYSTAL-FACE and PTOST uncovered the potential uncertainty of the onboard calibration load's temperature. Further experiments are needed, which could include retesting the emissivity of the loads at the higher frequencies or even sacrificing alternate scans to image the onboard calibration loads during a Proteus engineering flight (because the Proteus flies at such a slow speed and the surface imaging would be the least effected). Also, the new spectrometers should have their power spectral densities estimated in order to determine the 1/f noise contribution. This could help identify issues of excessive 1/f noise that could be attributing to higher radiometric sensitivity values (ΔT_{rms}), and also identify the amount of correlation between calibration load measurements.

7.4.2 Precipitation-Parameter Estimation

The single-pixel retrieval technique would gain from further refinement of the hydrometeor-profile model. Optimizing the level of complexity to reach a point of marginal improvement could be beneficial in simulating a larger range of convective profiles. The estimation technique could also be improved by using a more sophisticated estimator (*e.g.*, multi-feedforward neural network) or further development of the "nearest profile" technique by enlarging the hydrometeor-profile ensemble to cover more convective-cell profiles.

The study of the relationship between the microwave signature and rain volume is in its rudimentary stage. More convective cells must be imaged and analyzed, but the availability of pertinent data is a limitation. Satellite or simulated data might be an appropriate source to further validate the relationship. To further investigate the utility of the 425-GHz system aboard GEO, the varying spatial resolution should be taken into account.

Appendix A

Deployment Summary

Table A.1: CRYSTAL-FACE NAST-M Mission Report

Date	Total Flight Hours	Calibrated Flight Hours	UTC Start	Notes
3-Jul-02	6:15	6:15	14:18	
7-Jul-02	6:30	6:30	15:24	
9-Jul-02	7:45	7:45	14:16	183 sys. down
11-Jul-02	7:00	7:00	14:24	limited 425 sys.
13-Jul-02	6:50	6:50	16:17	limited 425 sys.
16-Jul-02	2:20	2:20	17:35	
17-Jul-02	4:50	4:50	15:32	
19-Jul-02	7:50	7:50	16:10	
21-Jul-02	5:15	5:15	17:58	
23-Jul-02	6:10	6:10	17:50	
26-Jul-02	5:15	5:15	17:14	
29-Jul-02	5:50	5:50	16:15	
30-Jul-02	7:25	7:25	12:36	ferry

Table A.2: PTOST NAST-M Mission Report

Date	Total Flight Hours	Calibrated Flight Hours	UTC Start	Notes
31-Jan-03	2:10	2:10	18:50	183 failed eng. flt.
6-Feb-03	3:15	3:15	17:50	CA
11-Feb-03	5:20	5:20	19:37	425 failed CA
19-Feb-03	6:20	6:20	18:53	425 failed ferry
21-Feb-03	5:30	3:20	20:50	425 failed
22-Feb-03	7:00	7:00	21:28	425 failed
24-Feb-03	5:40	5:40	21:19	425 failed
26-Feb-03	5:10	5:10	22:04	425 failed
1-Mar-03	4:50	4:50	22:12	
3-Mar-03	4:50	3:15	22:47	
10-Mar-03	6:30	6:30	21:40	
11-Mar-03	7:10	7:10	20:52	
12-Mar-03	7:20	7:20	20:41	
13-Mar-03	4:30	4:30	20:19	
14-Mar-03	5:45	5:45	20:45	ferry

Appendix B

Summary of Atmospheric Simulation Models

B.1 Tbarray

The Tbarray software is described in Section 2.3.5, but the assumptions are summarized here:

- Numerical Solution - Tbarray [51]
- Absorption Coefficients Model - Millimeter-wave Propagation Model (MPM) [37, 38, 39, 42, 52]
- Fresh Water Permittivity Model - Liebe *et al.* [41, 40]
- Fresh-water Ice Permittivity Model - Hufford [31]
- Oceanic Surface Emissivity Model - fastem [22]
- Frequency Resolution - thousands of frequencies across laboratory-measured passbands
- Antenna Beam - Gaussian function with nine data points that models 3-dB beamwidth of 7.5°
- Altitude Resolution - 200 meters

B.2 Tbscat

A description of the Tbscat software can be found in Section 2.3.5, but the assumptions are summarized here:

- Numerical Solution - Tbscat [50]
- Absorption Coefficients Model - Millimeter-wave Propagation Model (MPM) [37, 38, 39, 42, 52]
- Scattering Coefficient Model
  - Mie Coefficients
    - Mie region - Deirmendjian [17]
    - Rayleigh region - Wiscombe [70]
  - Drop-size Distribution - Marshall-Palmer [43]
  - Phase function - Henyey-Greenstein [28]
- Fresh Water Permittivity Model - Liebe *et al.* [41, 40]
- Fresh-water Ice Permittivity Model - Hufford [31]
- Oceanic Surface Emissivity Model - fastem [22]
- Frequency Resolution - single frequency in center of passband (one in upper and lower sidebands for double-sideband systems)
- Antenna Beam - single point at antenna beam's center
- Altitude Resolution - 500 meters

Appendix C

Selected Source Code

C.1 NAST-M Mapping Functions

```
function [LAT, LON, cmap]=Map_Tb_ftprt_CF(lat,lon,Tb,alt,turn,lim,LAT,LON)
% usage [LAT LON CMAP]=Map_Tb_ftprt_CF(lat,lon,Tb,alt,turn,lim,LAT,LON);
%
% Input:
% lat.......latitude vector relating to the aircraft's position
% lon...... longitude vector relating to the aircraft's position
% Tb........matrix of brightness temperatures for nadir-viewing
%           spotXscan [19xn] (or other variable to plot)
% alt.......vector for distance in kilometers between aircraft
%           and weighting function peak
% turn......vector with roll value at each scan
% lim.......vector with colorbar limits [min max]
%
% Optional Input:
% LAT.......matrix of latitude for each spot spotsXscan
% LON.......matrix of longitude for each spot spotsXscan
%  These optional inputs can help reduce computation time if
%  the function is called again for the same swath
```

```
%
% Output
% LAT  spotsXscans latitude values
% LON  spotsXscans longitude values
% CMAP colormap used
%
% Note: To avoid plotting any particular footprint (e.g., if the
% aircraft banks steeply or to reduce footprint overlap),
% replace the Tb value with NaN. The program will ignore it.
%
% WARNING: code removes last scan for coding convenience

% Initialize output variables
if exist('LAT')==1 & exist('LON')==1,latexist=0;else latexist=1;end
if latexist,
LAT=ones(siz(1),siz(2)-1);
LON=LAT;
end

% Prepare figure
figure
axesm('mercator')                                            axesm
gridm on
load worldhi
plotm(UnitedStatesofAmerica.lat,UnitedStatesofAmerica.long,'k', ...
      'LineWidth',1.7);
plotm(BahamasThe.lat,BahamasThe.long,'k','LineWidth',2);
plotm(Cuba.lat,Cuba.long,'k','LineWidth',2);

% find and set map limits
```

```
[latmnmx]=minmax(lat(:));
[lonmnmx]=minmax(lon(:));
setm(gca,'maplonlimit',[lonmnmx(1)+1 lonmnmx(2)-1],'maplatlimit', ...
        [latmnmx(2)-1 latmnmx(1)+1])

% Assumed NAST-M configuration for CRYSTAL-FACE or Proteus:
% step pattern + tilt in Proteus + pattern adjustment
% (adjust moves nadir spot from 3.2 degrees to 0.2 degrees)
angle_space=[-64.8:7.2:64.8]+10-3;

% get rid of NaN in turn
for i=1:length(turn);
   if isnan(turn(i)),
  turn(i)=0;
   end
end

siz=size(Tb);
ln=length(angle_space);
Tb_ln=siz(2);

% From the limits given, make a custom color map
% Notice that the lowest resolution of the colormap is one,
% but it can be increased without much effort.
cmin=lim(1);
cmax=lim(2);
cmap=jet(length([(cmin):1:cmax]));
set(gcf,'Colormap',cmap)                                              set
set(gca,'CLim',[cmin cmax])                                           set
```

```
% set half of the 3dB beamwidth
theta=(7.5/2)*(pi/180);

% For each footprint find eight points (45 degrees apart)
% on the circumference
azi=[0:45:360];
al=length(azi);

% Make a patch the size of the footprint for each spot
for i=1:siz(2)-1,
  % adjust angle for aircraft roll
  thisangle=angle_space-turn(i);
  % find the distance from nadir of each spot for this scan
  dis=abs(alt(i).*tan(thisangle.*(pi/180)));
  % find azimuth direction based on the next gps reading
  % (another option is to use INS heading, but the INS data may be
  % difficult to find)
  az(i)=azimuth(lat(i),lon(i),lat(i+1),lon(i+1));

% Determine which scan angles are to the left or right of nadir
pos=find(thisangle>0);
neg=find(thisangle<0);
zro=find(thisangle==0);

% Start plotting the positive angle footprints
  for j=1:length(pos),
 % Find the latitude and longtitude of the spot's center by using the nadir's
 % lat/lon, the distance of the spot from nadir, and the azimuth
 % (i.e., the direction of the aircraft's motion)
if latexist,
```

```
[LAT(pos(j),i),LON(pos(j),i)]=reckon(lat(i),lon(i),km2deg(dis(pos(j))),az(i)+90);
end
    % Next, determine the circumference of the footprint
    % Start by computing three of the eight distances from the spot's center
    % to the edge of the footprint
a=alt(i)*(tan(thisangle(pos(j))*(pi/180))-tan(thisangle(pos(j))*(pi/180)-theta));
b=alt(i)*(tan(theta)/cos(thisangle(pos(j))*(pi/180)));
d=sqrt((a/2)^2+0.75*b^2);
    % The footprint is symmetric, so form the distance to the eight points
    % from the three calculated distances:
dist=[a d b d a d b d a];
    % Next, the lat/lon must be calculated for each of the eight points on
    % the circumference of the footprint (These lat/lon are entered
    % into the patchm function below)
[glat,glon]=reckon('gc',LAT(pos(j),i)*ones(1,al),LON(pos(j),i)*ones(1,al),...
                   km2deg(dist),azi+az(i)+90);

% Next, determine the color of the patch from Tb and lim
bts=Tb(pos(j),i);
% This part of code will clip data to the max/min values set by lim and
% will ignore NaN values
if isnan(bts),bts=cmin-1; elseif bts<cmin,bts=cmin;elseif bts>cmax,...
      bts=cmax;else bts=bts;
end
    if bts==(cmin-1),
      % don't plot NaN
    else
patchm(glat,glon,-1,cmap(round(bts)-cmin+1,:),'EdgeColor','none');
    end
  end
```

```
% Procedure is repeated for the negative angles
  for j=1:length(neg),
if latexist,
[LAT(neg(j),i),LON(neg(j),i)]=reckon(lat(i),lon(i),km2deg(dis(neg(j))),az(i)-90);
end
a=alt(i)*(tan(abs(thisangle(neg(j)))*(pi/180))-tan(abs(thisangle(neg(j)))*(pi/180)-theta));
 b=alt(i)*(tan(theta)/cos(abs(thisangle(neg(j)))*(pi/180)));
  d=sqrt((a/2)^2+0.75*b^2);
    dist=[a d b d a d b d a];
[glat,glon]=reckon('gc',LAT(neg(j),i)*ones(1,al),LON(neg(j),i)*ones(1,al),...
                   km2deg(dist),azi+az(i)-90);

btd=Tb(neg(j),i);
if isnan(btd),btd=cmin-1; elseif btd<cmin, btd=cmin;elseif btd>cmax,...
      btd=cmax;else btd=btd;
end
    if btd==(cmin-1),
      % don't plot NaN
    else
patchm(glat,glon,-1,cmap(round(btd)-cmin+1,:),'EdgeColor','none');
    end
  end

% Procedure is repeated if there is a nadir spot
if zro >=1,
  a=alt(i)*tan(theta);
dist=[a a a a a a a a a];
[glat,glon]=reckon('gc',lat(i)*ones(1,al),lon(i)*ones(1,al),km2deg(dist),azi-az(i));
btz=Tb(zro,i);
```

```
 if isnan(btz),btz=cmin-1; elseif btz<cmin,btz=cmin;elseif btz>cmax,...
     btz=cmax;else btz=btz;
 end
   if btz==(cmin-1),
     % don't plot NaN
   else
patchm(glat,glon,-1,cmap(round(btz)-cmin+1,:),'EdgeColor','none');
   end
 end
end

% Plot markers for C-F landmarks
latec=25+39/60; % East-coast Groundsite
lonec=80+25.3/60;
latwc=25+53/60; % West-coast Groundsite
lonwc=81+19/60;
plotm(latec,-lonec,'s','MarkerFaceColor',[1 1 1],...
     'MarkerEdgeColor',[0 0 0],'Linewidth',2);
plotm(latwc,-lonwc,'s','MarkerFaceColor',[1 1 1],...
     'MarkerEdgeColor',[0 0 0],'Linewidth',2)
```

```
function [LAT, LON, cmap]=Map_Tb_ftprt_PTOST(lat,lon,Tb,alt,turn,lim,LAT,LON)
% [LAT LON CMAP]=Map_Tb_ftprt_PTOST(lat,lon,Tb,alt,turn,lim);
% Input:
% lat....... latitude vector relating to the aircraft's position
% lon....... longitude vector relating to the aircraft's position
% Tb........ matrix of brightness temperature for nadir-viewing spots
%            spotsXscan [19xn]
% alt....... vector for distance in kilometers between aircraft
%            and weighting function peak
% turn...... vector with roll at each scan
% lim....... vector with colorbar limits [min max]
%
% Optional Input:
% LAT.......matrix of latitude for each spot spotsXscan
% LON.......matrix of longitude for each spot spotsXscan
%  These optional inputs can help reduce computation time if
%  the function is called again for the same swath
%
% Output
% LAT  spotsXscans latitude value
% LON spotsXscans longitude value
% CMAP colormap used
%
% Note: To avoid plotting any particular footprint (e.g., if the
% aircraft banks steeply or to reduce footprint overlap),
% replace the Tb value with NaN. The program will ignore it.
%
% WARNING: Code removes last scan for coding convenience

% Initialize output variables
```

```
if exist('LAT')==1 & exist('LON')==1,latexist=0;else latexist=1;end
if latexist,
LAT=ones(siz(1),siz(2)−1);
LON=LAT;
end

% Prepare figure
figure
axesm('mercator')                                                      axesm
gridm on
load worldhi
plotm(UnitedStatesofAmerica.lat,UnitedStatesofAmerica.long, ...
      'k','LineWidth',1.7);
plotm(BahamasThe.lat,BahamasThe.long,'k','LineWidth',2);
plotm(Cuba.lat,Cuba.long,'k','LineWidth',2);

% find and set map limits
[latmnmx]=minmax(lat(:));
[lonmnmx]=minmax(lon(:));
setm(gca,'maplonlimit',[lonmnmx(1)+1 lonmnmx(2)−1],'maplatlimit', ...
         [latmnmx(2)−1 latmnmx(1)+1])

% assume NAST-M configuration for PTOST/ATOST or ER-2 flights
angle_space=[−64.8:7.2:64.8];

% get rid of NaN in turn
for i=1:length(turn);
   if isnan(turn(i)),
  turn(i)=0;
   end
```

```
end

siz=size(Tb);
ln=length(angle_space);
Tb_ln=siz(2);

% From the limits given, make a custom color map
% Notice that the lowest resolution of the colormap is one,
% but it can be increased without much effort.
cmin=lim(1);
cmax=lim(2);
cmap=jet(length([(cmin):1:cmax]));
set(gcf,'Colormap',cmap)                                          set
set(gca,'CLim',[cmin cmax])                                       set

% set half of the 3dB beamwidth
theta=(7.5/2)*(pi/180);

% For each footprint find eight points (45 degrees apart)
azi=[0:45:360];
al=length(azi);

% Make a patch the size of the footprint for each spot
for i=1:siz(2)-1,
  % adjust angle for aircraft roll
  thisangle=angle_space-turn(i);
  % find the distance from nadir of each spot for this scan
  dis=abs(alt(i).*tan(thisangle.*(pi/180)));
  % find azimuth direction based on the next gps reading
  % (another option is to use INS heading, but the INS data may be
```

```
 % difficult to find)
 az(i)=azimuth(lat(i),lon(i),lat(i+1),lon(i+1));

% Determine which scan angles are to the left or right of nadir
pos=find(thisangle>0);
neg=find(thisangle<0);
zro=find(thisangle==0);

% Start plotting the positive angle footprints
 for j=1:length(pos),
 % Find the latitude and longtitude of the spot's center by using the nadir's
 % lat/lon, the distance of the spot from nadir, and the azimuth
 % (i.e., the direction of the aircraft's motion)
if latexist,
[LAT(pos(j),i),LON(pos(j),i)]=reckon(lat(i),lon(i),km2deg(dis(pos(j))),az(i)+90);
end
   % Next, determine the circumference of the footprint
   % Start by computing three of the eight distances from the spot's center
   % to the edge of the footprint
a=alt(i)*(tan(thisangle(pos(j))*(pi/180))-tan(thisangle(pos(j))*(pi/180)-theta));
 b=alt(i)*(tan(theta)/cos(thisangle(pos(j))*(pi/180)));
  d=sqrt((a/2)^2+0.75*b^2);
   % The footprint is symmetric, so form the distance to the eight points
   % from the three calculated distances:
  dist=[a d b d a d b d a];
   % Next, the lat/lon must be calculated for each of the eight points on
   % the circumference of the footprint (These lat/lon are entered
   % into the patchm function below)
[glat,glon]=reckon('gc',LAT(pos(j),i)*ones(1,al),LON(pos(j),i)*ones(1,al), ...
                    km2deg(dist),azi+az(i)+90);
```

```
% Next, determine the color of the patch from Tb and lim
bts=Tb(pos(j),i);
% This part of code will clip data to the max/min values set by lim and
% will ignore NaN values
if isnan(bts),bts=cmin−1; elseif bts<cmin,bts=cmin;elseif bts>cmax, ...
      bts=cmax;else bts=bts;
end
    if bts==(cmin−1),
      % don't plot NaN
    else
patchm(glat,glon,−1,cmap(round(bts)−cmin+1,:),'EdgeColor','none');
    end
  end

% Procedure is repeated for the negative angles
  for j=1:length(neg),
if latexist,
    [LAT(neg(j),i),LON(neg(j),i)]=reckon(lat(i),lon(i),km2deg(dis(neg(j))),az(i)−90);
end
a=alt(i)*(tan(abs(thisangle(neg(j)))*(pi/180))−tan(abs(thisangle(neg(j)))*(pi/180)−theta));
 b=alt(i)*(tan(theta)/cos(abs(thisangle(neg(j)))*(pi/180)));
  d=sqrt((a/2)^2+0.75*b^2);
   dist=[a d b d a d b d a];
[glat,glon]=reckon('gc',LAT(neg(j),i)*ones(1,al),LON(neg(j),i)*ones(1,al), ...
                    km2deg(dist),azi+az(i)−90);

btd=Tb(neg(j),i);
if isnan(btd),btd=cmin−1; elseif btd<cmin, btd=cmin;elseif btd>cmax, ...
      btd=cmax;else btd=btd;
```

```
end
    if btd==(cmin-1),
      % don't plot NaN
    else
patchm(glat,glon,-1,cmap(round(btd)-cmin+1,:),'EdgeColor','none');
    end
  end

% Repeat procedure if there is a nadir spot
if zro >=1,
  a=alt(i)*tan(theta);
dist=[a a a a a a a a a];
[glat,glon]=reckon('gc',lat(i)*ones(1,al),lon(i)*ones(1,al),km2deg(dist),azi-az(i));
btz=Tb(zro,i);
if isnan(btz),btz=cmin-1; elseif btz<cmin,btz=cmin;elseif btz>cmax, ...
      btz=cmax; else btz=btz;
end
    if btz==(cmin-1),
      % don't plot NaN
    else
patchm(glat,glon,-1,cmap(round(btz)-cmin+1,:),'EdgeColor','none');
    end
 end
end
```

C.2 Calibration Code

```
function [Tb2pt] = NASTM_calib_2pt(x,rtdf,t,tspot,rtdW,Tb1st)
% usage [Tb2pt] = NASTM_calib_2pt(x,rtdf,t,tspot,rtdW,Tb1st)
% This script calibrates all four spectrometers of NAST-M
% using a two-point calibration.
%      x       -> counts 30x25xr  (30 channels, 25 spots, r scans)
%      rtdf    -> rtd temperatures 29xr (29 rtd's, r scans)
%      t       -> time stamp of scan POSIX
%      tspot   -> time stamp of each spot POSIX
%      rtdW    -> structure array
%          rtdW.H hot load rtd index
%          rtdW.A ambient load rtd index

siz=size(x);
% Determine the brightness temperature corrupting the 54-GHz system
Tnadir=squeeze(mean(Tb1st(:,[5 6 21 22],:),2));
Tsky=squeeze(mean(Tb1st(:,24:25,:),2)-2); % guess at sky pipe Tb

% From William J. Blackwell's Ph.D. Thesis
% percentages adjusted for the scan angle that the antenna views the
% calibration loads
spill_amb=[5.8 1.6;6.6 2.1;7.7 2.4;7.1 2.4;7.3 2.3;10.0 2.7; ...
          14.7 3.1;20.0 4.4]*1e-3;
spill_heat=[5.7 2.4;5.3 2.4;5.4 2.3;5.0 2.4;5.0 2.3;5.8 2.8; ...
           8 3.1;12.9 3.4]*1e-3;

% Heated load weights
% From W. J. Blackwell's Ph.D. Thesis.
w=[0.1568 0.1435 0.1402 0.1330 0.1412 0.1449 0.1402];
```

```
% Ambient Load weights
WgtA=[0.2;0.2;0.2;0.2;0.2];

Wh=zeros(30,31); %30 channels by 29+2 corruptions
Wa=Wh;

% Adjust 54-GHz weights to account for spillover
for i=1:8,
Wh(i,rtdW.H(:,1))=w.*(1-sum(spill_heat(i,:)));
Wa(i,rtdW.A(:,1))=WgtA'.*(1-sum(spill_amb(i,:)));
Wh(i,30)=spill_heat(i,2);
Wh(i,31)=spill_heat(i,1);
Wa(i,30)=spill_amb(i,2);
Wa(i,31)=spill_amb(i,1);
end

for i=9:30,
Wh(i,rtdW.H(:,1))=w;
Wa(i,rtdW.A(:,1))=WgtA';
end

% select the appropriate rtds related to each calibration load
for k=1:30,
Th(k,:)=Wh(k,:)*[rtdf';Tnadir(k,:);Tsky(k,:)];
Ta(k,:)=Wa(k,:)*[rtdf';Tnadir(k,:);Tsky(k,:)];
end

clear x_;
x_=shiftdim(x,2);
```

```
% determine the counts at the calibration spots
C54h=x_(:,:,1);               % [rx30x1]
Cotherh=x_(:,:,2);
Ca=mean(x_(:,:,[24:25]),3);
C183h=x_(:,:,3);
C183a=x_(:,:,23);

% filter counts to reduce instrument noise
C54hf=filtfiltcol(ones(1,4)/4,1,C54h);
Cotherhf=filtfiltcol(ones(1,4)/4,1,Cotherh);
Caf=filtfiltcol(ones(1,4)/4,1,Ca);
C183hf=filtfiltcol(ones(1,4)/4,1,C183h);
C183af=filtfiltcol(ones(1,4)/4,1,C183a);

% interpolate RTD and simulation temperatures to all spots
    for i=1:30,
Thi(i,:)=interp1(t,Th(i,:),tspot(:),'linear','extrap')';
Tai(i,:)=interp1(t,Ta(i,:),tspot(:),'linear','extrap')';
    end

% interpolate radiances to all spots
th54=tspot(1,:);
C54hi=interp1(th54,C54hf,tspot(:),'linear','extrap')';
thother=tspot(2,:);
Cotherhi=interp1(thother,Cotherhf,tspot(:),'linear','extrap')';
ta=mean(tspot([24:25],:));
Cai=interp1(ta,Caf,tspot(:),'linear','extrap')';
t183h=tspot(3,:);
C183hi=interp1(t183h,C183hf,tspot(:),'linear','extrap')';
```

```
t183a=tspot(23,:);
C183ai=interp1(t183a,C183af,tspot(:),'linear','extrap')';

% Implement ‘‘option 1” calibration adjustment:
% correction for the 183-GHz system
                    Thi(9:14,:)=Thi(9:14,:)-2;
                    Tai(9:14,:)=Tai(9:14,:)-0.5;
% correction for 425-GHz system
Thi(24:30,:)=Thi(24:30,:)-1;
Tai(24:30,:)=Tai(24:30,:);

% prepare parameters used in Weighted Least-Square Estimation of
% gain and baseline
% Ax=b -> Counts matrix x [gain baseline] = cal. load temp.
b=zeros(2,siz(1),siz(3)*25);
b(1,:,:)=Tai(:,:);
b(2,:,:)=Thi(:,:);

A=ones(2,2,siz(1),siz(3)*25);
A(1,1,:,:)=Cai(:,:);
A(1,1,9:14,:)=C183ai(9:14,:);
A(2,1,1:8,:)=C54hi(1:8,:);
A(2,1,9:14,:)=C183hi(9:14,:);
A(2,1,15:30,:)=Cotherhi(15:30,:);

% form optimal weight matrix C
% load delta_T_rms statistics
load NASTM_noise_01Mar03.mat

% add additional sources of noise on each of the calibration loads
```

```
th54=1; % due to spillover
ta54=0.5; % due to spillover
th118=1.0; %due to gradient on heated load
ta118=0.2; %due to gradient on ambient load
th183=1.0;
ta183=0.2;
th425=1.0;
ta425=0.2;

htloadadj=[th54.*ones(1,8) th183*ones(1,6) th118*ones(1,9) th425*ones(1,7)];
ambloadadj=[ta54.*ones(1,8) ta183*ones(1,6) ta118*ones(1,9) ta425*ones(1,7)];
adj=[ambloadadj;htloadadj];

for z=1:30,
C(:,:,z)=diag((NASTM_noise_01Mar03(2:3,z)+adj(:,z)).^(-2));
end

X=zeros(2,siz(1),siz(3)*25);
for i=[1:siz(3)*25],
if i==round((siz(3)*25/2)),
  fprintf('Half of the gains have been calculated...\n'),end
if i==round((siz(3)*25/4)),
  fprintf('Quarter of the gains have been calculated...\n'),end
if i==round((siz(3)*25*3/4)),
  fprintf('3/4 of the gains have been calculated...\n'),end
        for j=[1:siz(1)],
X(:,j,i)=inv(A(:,:,j,i)'*C(:,:,j)*A(:,:,j,i))*A(:,:,j,i)'*C(:,:,j)*b(:,j,i);
        end;
end;
```

```
for i=1:30,
x_2(:,i)=reshape(x(i,:,:),length(x)*25,1);
end



Tb1=squeeze(X(1,:,:))'.*x_2 + squeeze(X(2,:,:))';


Tb1= Tb1';
for i=1:30,
Tb2pt(i,:,:)=reshape(Tb1(i,:),25,length(x));
end

fprintf('\n NAST-M''s Corruption-Corrected ...
        Two-point Calibration is complete.\n\n')
```

```
function [Tb3pt] = NASTM_calib_3pt(x,rtdf,t,tspot,nav,rtdW,HEIGHT,Tb1st)
% usage [Tb3pt] = NASTM_calib_3pt(x,rtdf,t,tspot,nav,rtdW,HEIGHT,Tb1st)
% This script calibrates all four spectrometers of NAST-M
% using a three-point calibration.
%       x      -> counts 30x25xr  (30 channels, 25 spots, r scans)
%       rtdf   -> rtd temperatures 29xr (29 rtd's, r scans)
%       t      -> time stamp of scan POSIX
%       tspot  -> time stamp of each spot POSIX
%       nav is structure array
%            nav.d  ER-2 navigation data
%           nav.t  navigation time stamp
%       rtdW    -> structure array
%           rtdW.H heated-load rtd index
%           rtdW.A ambient-load rtd index
%        Height -> height of aircraft
%        Tb1st  -> first run at calibrating NASTM data (usually a
%                    simple two-point calibration)

siz=size(x);
% Determine the brightness temperature corrupting the 54-GHz system
Tnadir=squeeze(mean(Tb1st(:,[5 6 22 23],:),2));
Tsky=squeeze(mean(Tb1st(:,1:2,:),2));

% Spillover taken from W. J. Blackwell's Ph.D. thesis
% percentages adjusted for the scan angle that the horn views the
% calibration loads
spill_amb=[5.8 1.6;6.6 2.1;7.7 2.4;7.1 2.4;7.3 2.3;10.0 2.7; ...
          14.7 3.1;20.0 4.4]*1e-3;
spill_heat=[5.7 2.4;5.3 2.4;5.4 2.3;5.0 2.4;5.0 2.3;5.8 2.8; ...
           8 3.1;12.9 3.4]*1e-3;
```

```
% Heated load weights
% W. J. Blackwell's Ph.D. thesis
w=[0.1568 0.1435 0.1402 0.1330 0.1412 0.1449 0.1402];

% Ambient Load weights
WgtA=[0.2;0.2;0.2;0.2;0.2];

Wh=zeros(30,31);
Wa=Wh;

% Adjust 54-GHz weights to account for spillover
for i=1:8,
Wh(i,rtdW.H(:,1))=w.*(1-sum(spill_heat(i,:)));
Wa(i,rtdW.A(:,1))=WgtA'.*(1-sum(spill_amb(i,:)));
Wh(i,30)=spill_heat(i,2);
Wh(i,31)=spill_heat(i,1);
Wa(i,30)=spill_amb(i,2);
Wa(i,31)=spill_amb(i,1);
end

for i=9:30,
Wh(i,rtdW.H(:,1))=w;
Wa(i,rtdW.A(:,1))=WgtA';
end

% select the appropriate rtds related to each calibration load
for k=1:30,
Th(k,:)=Wh(k,:)*[rtdf';Tnadir(k,:);Tsky(k,:)];
Ta(k,:)=Wa(k,:)*[rtdf';Tnadir(k,:);Tsky(k,:)];
```

```
end

% usual altitude of the aircraft is 20 km
if exist('HEIGHT')~=1,HEIGHT=20.1;end;

% load statistics from zenith comparison between the standard
% atmosphere and the TIGR profile ensemble
% 1951 and 2051 represent the altitudes of the simulation (19.51
% and 20.51 km)
load NASTM_zenith_stat ZTbm_1951 ZTbm_2051

% Separate simulations were done for the 425-GHz system based on
% the LO frequency (e.g., here the frequency was at 105.95 GHz)
load zenith_stats_10595.mat ZTbm_1951_425 ...
    ZTbm_2051_425 ZTbstd_2051_425 ZTbstd_1951_425
ZTbm_1951(24:30)=ZTbm_1951_425;
ZTbm_2051(24:30)=ZTbm_2051_425;

% Interpolate the values from 19.51 and 20.51 km to the
% aircraft's altitude
Tz=ones(30,length(rtdf));
Tz1=interp1([19.51 20.51],[ZTbm_1951'; ZTbm_2051'], ...
            HEIGHT,'linear','extrap');
for i=1:30,
        Tz(i,:)=Tz(i,:).*Tz1(i)';
end;

clear x_;
% Remove zenith radiance data during aircraft rolls and replace
% it with interpolated data.
```

```
% clean_sky_rad shifts x to x_ ->[rx30x25]
x_=clean_sky_rad(x,nav,t);

% determine the counts at the calibration spots
Ch54=x_(:,:,3);           % [rx30x1]
Chother=x_(:,:,4);
Ca=mean(x_(:,:,[24:25]),3);
Cz=mean(x_(:,:,[1:2]),3);

% filter counts to reduce instrument noise
Ch54f=filtfiltcol(ones(1,4)/4,1,Ch54);
Chotherf=filtfiltcol(ones(1,4)/4,1,Chother);
Caf=filtfiltcol(ones(1,4)/4,1,Ca);
Czf=filtfiltcol(ones(1,4)/4,1,Cz);

% interpolate RTD and simulation temperatures to all spots
    for i=1:30,
Thi(i,:)=interp1(t,Th(i,:),tspot(:),'linear','extrap')';
Tai(i,:)=interp1(t,Ta(i,:),tspot(:),'linear','extrap')';
Tzi(i,:)=interp1(t,Tz(i,:),tspot(:),'linear','extrap')';
    end

% interpolate radiances to all spots
th54=tspot(3,:);
Ch54i=interp1(th54,Ch54f,tspot(:),'linear','extrap')';
thother=tspot(4,:);
Chotheri=interp1(thother,Chotherf,tspot(:),'linear','extrap')';
ta=mean(tspot([24:25],:));
Cai=interp1(ta,Caf,tspot(:),'linear','extrap')';
tz=mean(tspot([1:2],:));
```

```
Czi=interp1(tz,Czf,tspot(:),'linear','extrap')';

% Implement “option 1” calibration adjustment:
% correction for the 183-GHz system
                    Thi(9:14,:)=Thi(9:14,:)-2;
                    Tai(9:14,:)=Tai(9:14,:)-0.5;
% correction for 425-GHz system
Thi(24:30,:)=Thi(24:30,:)-1;
Tai(24:30,:)=Tai(24:30,:);

% prepare parameters used in Weighted Least-Square Estimation of
% gain and baseline
%Ax=b  -> Counts matrix x [gain baseline] = cal. load temp.
b=zeros(3,siz(1),siz(3)*25);
b(1,:,:)=Tzi(:,:);
b(2,:,:)=Tai(:,:);
b(3,:,:)=Thi(:,:);

A=ones(3,2,siz(1),siz(3)*25);
A(1,1,:,:)=Czi(:,:);
A(2,1,:,:)=Cai(:,:);
A(3,1,1:8,:)=Ch54i(1:8,:);
A(3,1,9:30,:)=Chotheri(9:30,:);

% optimal weight matrix C
% load delta_T_rms statistics
load NASTM_noise_01Mar03.mat

% add adjustment for error in using standard atmosphere above the aircraft
adj=zeros(3,30);
```

```
load NASTM_zenith_stat ZTbstd_2051 ZTbstd_1951
% adjust 425-GHz statistics for specific LO frequency
ZTbstd_1951(24:30)=ZTbstd_1951_425;
ZTbstd_2051(24:30)=ZTbstd_2051_425;

% Determine additional sources of noise on each of the calibration loads
th54=2; % due to spillover
ta54=1.5; % due to spillover
th118=1.5; %due to gradient on heated load
ta118=0.2; %due to gradient on ambient load
th183=1.5;
ta183=0.2;
th425=1.5;
ta425=0.2;

htloadadj=[th54.*ones(1,8) th183*ones(1,6) th118*ones(1,9) th425*ones(1,7)];
ambloadadj=[ta54.*ones(1,8) ta183*ones(1,6) ta118*ones(1,9) ta425*ones(1,7)];
zenloadadj=interp1([19.51 20.51],[ZTbstd_1951';ZTbstd_2051'], ...
                    HEIGHT,'linear','extrap');
adj=[zenloadadj;ambloadadj;htloadadj];

for z=1:30,
C(:,:,z)=diag((NASTM_noise_01Mar03(:,z)+adj(:,z)).^(-2));
end

X=zeros(2,siz(1),siz(3)*25);
for i=[1:siz(3)*25],
if i==round((siz(3)*25/2)),
  fprintf('Half of the gains have been calculated...\n'),end
if i==round((siz(3)*25/4)),
```

```
  fprintf('Quarter of the gains have been calculated. . .\n'),end
if i==round((siz(3)*25*3/4)),
  fprintf('3/4 of the gains have been calculated. . .\n'),end
        for j=[1:siz(1)],
X(:,j,i)=inv(A(:,:,j,i)'*C(:,:,j)*A(:,:,j,i))*A(:,:,j,i)'*C(:,:,j)*b(:,j,i);
        end;
end;


for i=1:30,
x_2(:,i)=reshape(x(i,:,:),length(x)*25,1);
end


Tb1=squeeze(X(1,:,:))'.*x_2 + squeeze(X(2,:,:))';

Tb1= Tb1';
for i=1:30,
Tb(i,:,:)=reshape(Tb1(i,:),25,length(x));
end


fprintf('\n NAST-M''s Corruption-Corrected . . .
        Three-point Calibration is complete.\n\n')
```

C.3 Storm Simulation Code (PTOST)

```
% This script will simulate the precipitating clouds for the cloud
% parameter retrieval. PTOST retrievals during Mar. 2003


% find atmospheric profile from TIGRS profile ensemble
load('/leslie2/TIGR2000/TIGR2K.mat')                                    load
THpxind=find(TIGR2K.lat<=50 & TIGR2K.lat>=20 & TIGR2K.month<=4);
altind=25; % altitude of 19.98 k
temp_=mean(TIGR2K.temp_K(:,THpxind),2);
pres_=TIGR2K.pres_mb(:,1);
relH_=mean(TIGR2K.relH(:,THpxind),2)*100;

% set simulation's altitude resolution
simaltres=[0:0.5:20];

% interpolate profile to simulation's resolution
temp=interp1(TIGR2K.alt_km(1:altind,1),temp_(1:altind),simaltres,'linear','extrap')';
pres=interp1(TIGR2K.alt_km(1:altind,1),pres_(1:altind),simaltres,'linear','extrap')';
relH=interp1(TIGR2K.alt_km(1:altind,1),relH_(1:altind),simaltres,'linear','extrap')';

% set LO frequencies
LO425=106.1*4;
LO183=183.31;
LO118=118.2;
LO54=46;
% set passband's center frequencies
freq54=[50.3 51.76 52.8 53.73 54.3 54.94 55.485 55.945];
freq118=[LO118-3.5 LO118+3.5 LO118-2.55 LO118+2.55 LO118-2.05 ...
    LO118+2.05 LO118-1.6 LO118+1.6 LO118-1.2 LO118+1.2 LO118-0.8 LO118+0.8];
```

```
freq183=[LO183−10 LO183+10 LO183−7 LO183+7 ...
    LO183−4.5 LO183+4.5 LO183−3 LO183+3 LO183−1.8 LO183+1.8 LO183−1 ...
    LO183+1];
freq425=[LO425−3.25 LO425+3.25 LO425−2.15 LO425+2.15 LO425−1.43 ...
      LO425+1.43 LO425−0.91 LO425+0.91 LO425−0.68 LO425+0.68 ...
      LO425−0.505 LO425+0.505 LO425−0.285 LO425+0.285];
freq=[freq54 freq118 freq183 freq425]';

% choose the angles
angle=[0 7.2 14.4 21.6 30 37.2 43 50 60];
secant=sec(angle*(pi/180))';

% set sea surface temperature
Tsurf=273.15+25;

% find the Tb above aircraft to use as an initial condition for tbscat
simind=[altind:length(temp_)];
[tb1,tb2,e1,e2]=tbarray(temp_(simind),pres_(simind),vapor(temp_(simind),...
relH_(simind)),zeros(length(simind),1),zeros(length(simind),1),secant,secant,freq);
Tcos=Tcosmic(freq)*ones(1,length(secant));
tbc=tb1(:,:)'+e1(:,:)'.*Tcos(:,:);

% prepare tbscat variables
icef=[0.1 0.4 0.7 1 2]; % ice density [g/cm^3] 2 flag for
                        % clear-air simulations
cldalti=[5:2:27]; % index to match cldalt
cldalt=simaltres(cldalti);

% Set rain rate based on the Marshall-Palmer distr.
RR=[0 0.1 0.3 0.5 1 3 8 10 18 25 35];
```

```
lambdaMP=4.1*RR.^(-0.21); %Marshall-Palmer distribution
rdenMP=pi*8./lambdaMP.^4;

% find radi-density distribution
radi=logspace(-2,0.8,30); % radi for scattering in precipitating clouds
radmeanMP=0.5./lambdaMP;

  for j=1:length(RR),
    for i=1:length(radi),
    denMP(i,j)=exp(-radi(i)/radmeanMP(j))*radi(i)^4;
    end
% remove the NaN caused by the zero rain rate
dx=size(denMP);
for b=1:dx(1),for r=1:dx(2),if isnan(denMP(b,r)),denMP(b,r)=0;end,end,end
  denMP(:,j)=denMP(:,j)*rdenMP(j)/sum(denMP(:,j));
end

% add cloud portion of scattering hydrometeors
cldadj= [0.8 0.8 0.8 ones(1,8)];
cldl=0.5;
for j=1:length(RR),
cumul(:,j)=exp(-47.*radi'.^0.3).*radi'.^5;
cumul(:,j)=cldadj(j)*cumul(:,j)*cldl/sum(cumul(:,j));
end

%***************************
% Start simulating scattering atmospheres

if exist('tbv')~=1,
```

```
% initial variables
cldlqd=zeros(length(temp),length(cldalti));
rlH=zeros(length(temp),length(cldalti));
wvd=zeros(length(temp),length(cldalti));

% find the emissivity of water
  for q=1:length(freq),
        for x=1:length(angle),
[ev(q,x) eh(q,x)]=fastem(freq(q),angle(x),Tsurf,15,1,1,1);
        end
  end
% make sure emissivity isn't greater than one
[ev,eh]=check_emis(ev,eh);

for k=1:length(cldalti),

  for i=1:length(RR),

% Use modified M-P.
clear den
den=zeros(length(radi),cldalti(k)-1);
for v=2:cldalti(k),
  if v<=cldalti(k)-2,
den(:,v-1)=denMP(:,i)+cumul(:,i);
  else
den(:,v-1)=cumul(:,i);
  end
end
      for j=1:length(icef),
% fluctuate the humidity and temperature profile to increase
```

```
% variability of clear air
df=size(relH);
rlHca=relH+unifrnd(−0.1,0.1,df(1),df(2)).*relH;
tempca=temp+unifrnd(−0.005,0.005)*temp;
rlH(:,k)=rlHca;


cldscale=0.05;
if temp(cldalti(k))>250,
cldb=cldalti(k);
          if cldalt(k)>=4,
clda=cldalti(k)−6;
          cldlqd(clda:cldb,k)=cldscale*triang(7);
          rlH(clda:cldb,k)=100;
          elseif cldalt(k)==3,
clda=cldalti(k)−5;
          cldlqd(clda:cldb,k)=cldscale*triang(6);
          rlH(clda:cldb,k)=100;
          else
clda=cldalti(k)−3;
          cldlqd(clda:cldb,k)=cldscale*triang(4);
          rlH(clda:cldb,k)=100;
          end
else
  cldscaleH=0.05;
cldb=17; % level where temp=260 K
clda=3;
cldlqd(clda:cldb,k)=cldscaleH*triang(15);
rlH(clda:cldalti(k),k)=100;
end
wvdca(:,k)=vapor(tempca,rlHca);
```

```
wvd(:,k)=vapor(temp,rlH(:,k));

        if (icef(j)~=2),
[tbv(:,:,k,i,j),tbh(:,:,k,i,j),status(:,k,i,j)]=tbscat(temp,pres,...
        wvd(:,k),cldlqd(:,k),1,cldalti(k),radi',den,icef(j),...
        Tsurf,tbc',freq,secant,1-ev',1-eh');
        else % for clear air
[tbv(:,:,k,i,j),tbh(:,:,k,i,j),status(:,k,i,j)]=tbscat(tempca,pres,...
        wvdca(:,k),zeros(length(temp),1),4,3,radi',zeros(length(radi),1)...
        ,icef(j)-1,Tsurf+2*randn,tbc',freq,secant,1-ev',1-eh');
        end
      end % icef
    end % RR
  fprintf('Altitude  %d \r',simaltres(cldalti(k))),
end % cldalti

% tbv(angle,freq,cldalti,RR,icef)

end % end of check if tbv exists

for v=1:8, %for each angle estimator
  clear tbvf tbhf
% merge the horiz. and vert. polarizations
tbvf=squeeze(tbv(v,:,:,:,:));
tbhf=squeeze(tbh(v,:,:,:,:));
tbf=tbvf.*sin((pi/180)*angle(v)).^2+tbhf.*cos((pi/180)*angle(v)).^2;

% script that looks at the simulation output variable 'status' and
% throws away simulations with warnings.  Next is combines upper
% and lower sideband frequencies into channels.
```

```
MieInac=0; % flag to remove simulations with Mie series inaccuracies
MieInstab=0; % flag to remove simulations with Mie series instabilities
RTSInstab=1; % flag to remove simulations with unreasonable Tb from
             % radiative transfer solution instabilities
Clean_sims

tbh54{v}=tbhn54;
tbh118{v}=tbhn118;
tbh183{v}=tbhn183;
tbh425{v}=tbhn425;

% Organize the good simulations with their perspective state vector
gj=size(tbh54{v});
tb118{v}=[];tb54{v}=[];tb183{v}=[];tb425{v}=[];S{v}=[];
for i=1:gj(1),
 for j=1:gj(2),
  for k=1:gj(3),
% skip simulation if the status reported an error.
if ~(sum(isnan(tbh54{v}(i,j,k,:)))+sum(isnan(tbh118{v}(i,j,k,:)))+ ...
     sum(isnan(tbh183{v}(i,j,k,:)))+sum(isnan(tbh425{v}(i,j,k,:)))),

tb54{v}=[tb54{v} [squeeze(tbh54{v}(i,j,k,:))]];
tb118{v}=[tb118{v} [squeeze(tbh118{v}(i,j,k,:))]];
tb183{v}=[tb183{v} [squeeze(tbh183{v}(i,j,k,:))]];
tb425{v}=[tb425{v} [squeeze(tbh425{v}(i,j,k,:))]];

   if (icef(k)~=2), % for the precipitating clouds
    if RR(j)~=0,
    S{v}=[S{v} [cldalt(i)-1;RR(j);icef(k);cldalt(i)]];
    else
```

```
        S{v}=[S{v} [0;RR(j);icef(k);cldalt(i)]];
        end
      else % for the clear air
S{v}=[S{v} [0;0;0;0]];
      end
end
    end % icef
  end % RR
end % cldalti

nwln=length(tb54{v});
for i=1:nwln,
tb{v}(:,i)=[tb54{v}(:,i);tb118{v}(:,i);tb183{v}(:,i);tb425{v}(:,i)];
end

end % end of v loop over angles
```

```
% This script will simulate the non-precipitating clouds for the cloud
% parameter retrieval. PTOST

% find atmospheric profile from TIGR profile ensemble
load('/leslie2/TIGR2000/TIGR2K.mat')                                    load
addpath /leslie2/MATLAB/
THpxind=find(TIGR2K.lat<=50 & TIGR2K.lat>=20 & TIGR2K.month<=4);

altind=25; % altitude of 19.98 k
temp_=mean(TIGR2K.temp_K(:,THpxind),2);
pres_=TIGR2K.pres_mb(:,1);
relH_=mean(TIGR2K.relH(:,THpxind),2)*100;

% set simulation's altitude resolution
simaltres=[0:0.5:20];
% interpolate profiles to simulation's resolution
temp=interp1(TIGR2K.alt_km(1:altind,1),temp_(1:altind),simaltres,'linear','extrap')';
pres=interp1(TIGR2K.alt_km(1:altind,1),pres_(1:altind),simaltres,'linear','extrap')';
relH=interp1(TIGR2K.alt_km(1:altind,1),relH_(1:altind),simaltres,'linear','extrap')';

% Set LO frequencies
LO425=106.09*4;
LO183=183.31;
LO118=118.2;
LO54=46;
% Set passband's center frequencies
freq54=[50.3 51.76 52.8 53.73 54.3 54.94 55.485 55.945];
freq118=[LO118−3.5 LO118+3.5 LO118−2.55 LO118+2.55 LO118−2.05 ...
   LO118+2.05 LO118−1.6 LO118+1.6 LO118−1.2 LO118+1.2 LO118−0.8 LO118+0.8];
freq183=[LO183−10 LO183+10 LO183−7 LO183+7 ...
```

```
    LO183-4.5 LO183+4.5 LO183-3 LO183+3 LO183-1.8 LO183+1.8 LO183-1 ...
    LO183+1];
freq425=[LO425-3.25 LO425+3.25 LO425-2.15 LO425+2.15 LO425-1.43 ...
      LO425+1.43 LO425-0.91 LO425+0.91 LO425-0.68 LO425+0.68 ...
      LO425-0.505 LO425+0.505 LO425-0.285 LO425+0.285];
freq=[freq54 freq118 freq183 freq425]';

% choose the angles
angle=[0 7.2 14.4 21.6 30 37.2 43 50 60];
secant=sec(angle*(pi/180))';

% set sea surface temperature
Tsurf=273.15+25;

% find the Tb above aircraft to initialize tbscat
simind=[altind:length(temp_)];
[tb1,tb2,e1,e2]=tbarray(temp_(simind),pres_(simind),...
    vapor(temp_(simind),relH_(simind)),zeros(length(simind),1)...
     ,zeros(length(simind),1),secant,secant,freq);
Tcos=Tcosmic(freq)*ones(1,length(secant));
tbc=tb1(:,:)'+e1(:,:)'.*Tcos(:,:);

% prepare tbscat variables
icef=[1]; % ice density [g/cm^3] 2
% set range of non-scattering cloud density
cldthk=[4:2:14]; % list range of cloud thickness
cldalti=[5:2:35]; % index to match cldalt
cldalt=simaltres(cldalti);

% set range of the scattering-cloud density
```

```
lden=[0.05 0.1 0.3 0.5 1 1.5 3 5];

% radi for the scattering in non-precipitating clouds
lradi=logspace(-3,0,30);
ldenfunc=exp(-47*lradi.^0.3).*lradi.^5;

%**************************
% Start simulating scattering atmospheres

if exist('tbv')~=1,

% initialize variables
cldlqd=zeros(length(temp),length(cldalti));
rlH=zeros(length(temp),length(cldalti));
wvd=zeros(length(temp),length(cldalti));

% find the emissivity of water
  for q=1:length(freq),
        for x=1:length(angle),
[ev(q,x) eh(q,x)]=fastem(freq(q),angle(x),Tsurf,15,1,1,1);
        end
  end

% make sure emissivity isn't greater than one
[ev,eh]=check_emis(ev,eh);

for k=1:length(cldalti),
  for i=1:length(cldthk),
      for j=1:length(lden),
% fluctuate the humidity and temperature profile to increase variability
```

```
rlH(:,k)=relH;
df=size(relH);
rlH=relH+unifrnd(−0.1,0.1,df(1),df(2)).*relH;
tempca=temp+unifrnd(−0.005,0.005)*temp;

% custom the cloud thickness range for clouds
% close to the surface (e.g., a cloud with a 4-km cloud-top
% altitude can't be 6-km thick)
cldb=cldalti(k);
        if cldalt(k)>=7,
clda=cldb−cldthk(i);
rlH(clda:cldb,k)=100;
Acldthk(k,i,j)=cldthk(i);
        elseif cldalt(k)==6,
if i<=5,
clda=cldb−cldthk(i);
rlH(clda:cldb,k)=100;
Acldthk(k,i,j)=cldthk(i);
else
xh=unidrnd(5);
clda=cldb−cldthk(xh);
rlH(clda:cldb,k)=100;
Acldthk(k,i,j)=cldthk(xh);
end
        elseif cldalt(k)==5,
if i<=4,
clda=cldb−cldthk(i);
rlH(clda:cldb,k)=100;
Acldthk(k,i,j)=cldthk(i);
else
```

```
xh=unidrnd(4);
clda=cldb−cldthk(xh);
rlH(clda:cldb,k)=100;
Acldthk(k,i,j)=cldthk(xh);
end
        elseif cldalt(k)==4,
if i<=3,
clda=cldb−cldthk(i);
rlH(clda:cldb,k)=100;
Acldthk(k,i,j)=cldthk(i);
else
xh=unidrnd(3);
clda=cldb−cldthk(xh);
rlH(clda:cldb,k)=100;
Acldthk(k,i,j)=cldthk(xh);
end
        elseif cldalt(k)==3,
if i<=2,
clda=cldb−cldthk(i);
rlH(clda:cldb,k)=100;
Acldthk(k,i,j)=cldthk(i);
else
xh=unidrnd(2);
clda=cldb−cldthk(xh);
rlH(clda:cldb,k)=100;
Acldthk(k,i,j)=cldthk(xh);
end
        else
clda=cldb−3;
rlH(clda:cldb,k)=100;
```

```
Acldthk(k,i,j)=3;
          end

wvdca(:,k)=vapor(tempca,rlH(:,k));

% form cloud scattering density matrix
lm=diff([clda cldb]);
tr=ones(lm,1);
lightden=[];
for r=1:lm,
  lightden(r,:)=ldenfunc*tr(r)*lden(j)/sum(ldenfunc);
end

[tbv(:,:,k,i,j),tbh(:,:,k,i,j),status(:,k,i,j)]=tbscat(tempca,pres,...
        wvdca(:,k),zeros(length(tempca),1),clda,cldb,lradi',lightden',...
        icef,Tsurf,tbc',freq,secant,1-ev',1-eh');
      end % lden
    end % cldden
  fprintf('Altitude  %d \r',simaltres(cldalti(k))),
end % cldalti

end % end of check if tbv exists

% tbv(angle,freq,cldalti,RR,icef)

for v=1:8, % for the different angle estimators
  clear tbvf tbhf
% merge the horiz. and vert. polarizations
tbvf=squeeze(tbv(v,:,:,:,:));
tbhf=squeeze(tbh(v,:,:,:,:));
```

```
tbf=tbvf.*sin((pi/180)*angle(v)).^2+tbhf.*cos((pi/180)*angle(v)).^2;

% script that looks at the simulation output variable ‘status’ and
% throws away simulations with warnings.  Next is combines upper
% and lower sideband frequencies into channels.
MieInac=0; % flag to remove simulations with Mie series inaccuracies
MieInstab=0; % flag to remove simulations with Mie series instabilities
RTSInstab=1; % flag to remove simulations with unreasonable Tb from
             % radiative transfer solution instabilities
clear tbhn54 tbhn118 tbhn183 tbhn425
Clean_sims

tbh54{v}=tbhn54;
tbh118{v}=tbhn118;
tbh183{v}=tbhn183;
tbh425{v}=tbhn425;

% Organize the good simulations with their perspective state vector
gj=size(tbh54{v});
tb118{v}=[];tb54{v}=[];tb183{v}=[];tb425{v}=[];S{v}=[];
for i=1:gj(1),
  for j=1:gj(2),
    for k=1:gj(3),
% skip simulation if the status reported an error.
if ~(sum(isnan(tbh54{v}(i,j,k,:)))+sum(isnan(tbh118{v}(i,j,k,:)))+ ...
     sum(isnan(tbh183{v}(i,j,k,:)))+sum(isnan(tbh425{v}(i,j,k,:)))),

tb54{v}=[tb54{v} [squeeze(tbh54{v}(i,j,k,:))]];
tb118{v}=[tb118{v} [squeeze(tbh118{v}(i,j,k,:))]];
tb183{v}=[tb183{v} [squeeze(tbh183{v}(i,j,k,:))]];
```

```
tb425{v}=[tb425{v} [squeeze(tbh425{v}(i,j,k,:))]];


S{v}=[S{v} [0;0;1;cldalt(i)]];


end
    end % lden
  end % cldthk
end % cldalti


nwln=length(tb54{v});
for i=1:nwln,
tb{v}(:,i)=[tb54{v}(:,i);tb118{v}(:,i);tb183{v}(:,i);tb425{v}(:,i)];
end


end % end of v loop over angles
```

C.4 Storm Simulation Code (CRYSTAL-FACE)

```
% This script will simulate the precipitating clouds for the cloud
% parameter retrieval.
% It was designed for Crystal-Face retrievals on 13Jul02

addpath /leslie2/MATLAB/

if exist('raob')~=1,
[raob]=read_CF_raob('/leslie2/NAST-M/13Jul02/raob/MI20020713_2044_COR.RAOB');
altind=632;
end

% Define the simulation's altitude resolution
simaltres=[0:0.5:17.5];

temp_=raob.temp_K;
pres_=raob.press_mb;
relH_=raob.rh_perc;
% Interpolate to simulation's resolution
temp=interp1(raob.alt_km(1:altind,1),temp_(1:altind,1),simaltres,'linear','extrap')';
pres=interp1(raob.alt_km(1:altind,1),pres_(1:altind),simaltres,'linear','extrap')';
relH=interp1(raob.alt_km(1:altind,1),relH_(1:altind),simaltres,'linear','extrap')';

% Set simulation LO frequencies
LO425=106.1*4;
LO183=183.31;
LO118=118.2;
LO54=46;
% Set passband centerfrequencies
```

```
freq54=[50.3 51.76 52.8 53.73 54.3 54.94 55.485 55.945];
freq118=[LO118-3.5 LO118+3.5 LO118-2.55 LO118+2.55 LO118-2.05 ...
      LO118+2.05 LO118-1.6 LO118+1.6 LO118-1.2 LO118+1.2 LO118-0.8 LO118+0.8];
freq183=[LO183-10 LO183+10 LO183-7 LO183+7 ...
    LO183-4.5 LO183+4.5 LO183-3 LO183+3 LO183-1.8 LO183+1.8 LO183-1 ...
    LO183+1];
freq425=[LO425-3.25 LO425+3.25 LO425-2.15 LO425+2.15 LO425-1.43 ...
      LO425+1.43 LO425-0.91 LO425+0.91 LO425-0.68 LO425+0.68 ...
      LO425-0.505 LO425+0.505 LO425-0.285 LO425+0.285];
freq=[freq54 freq118 freq183 freq425]';

% choose the angles (these matched the center angle of the spots
% next to nadir
angle=[0 7.2 14.4 21.6 30 37.2 43 50 60];
secant=sec(angle*(pi/180))';

% Set a surface temperature
Tsurf=273.15+25;

% find the Tb above aircraft for initial conditions in tbscat
simind=[altind:2:length(temp_)]; % for CF raob
[tb1,tb2,e1,e2]=tbarray(temp_(simind),pres_(simind),vapor(temp_(simind),...
            relH_(simind)),zeros(length(simind),1),...
                  zeros(length(simind),1),secant,secant,freq);
Tcos=Tcosmic(freq)*ones(1,length(secant));
tbc=tb1(:,:)'+e1(:,:)'.*Tcos(:,:);

% prepare tbscat variables
icef=[0.1 0.4 0.7 1 2]; % ice density [g/cm^3] 2 is a flag for
                        % clear-air  simulations
```

```
cldalti=[5:2:35]; % index to match cldalt
cldalt=simaltres(cldalti);

% set variable (rain rate) based on the Marshall-Palmer distr.
RR=[0 0.5 0.8 1 2 3 4 5 8 10 12 15 18 22 25 35 50 75 100];
% chosen from drizzel to tropical downpour
lambdaMP=4.1*RR.^(-0.21); %Marshall-Palmer distribution
rdenMP=pi*8./lambdaMP.^4;

% find radi-density distribution
radi=logspace(-2,0.8,30); % radi for scattering in precipitating clouds
radmeanMP=0.5./lambdaMP+[0 0.01 0.02 0.02 0.03 0.03 0.04 0.05 0.05 ...
                    0.06 0.06 0.07 0.08 0.09 0.09 0.1 0.12 0.14 0.15];
  for j=1:length(RR),
    for i=1:length(radi),
    denMP(i,j)=exp(-radi(i)/radmeanMP(j))*radi(i)^4;
    end
% remove the NaN caused by the zero rain rate
dx=size(denMP);
for b=1:dx(1),for r=1:dx(2),if isnan(denMP(b,r)),denMP(b,r)=0;end,end,end
  denMP(:,j)=denMP(:,j)*rdenMP(j)/sum(denMP(:,j));
  end

% add cloud portion of scattering hydrometeors
cldadj= [0.5 ones(1,18)];
cldl=0.8;
for j=1:length(RR),
cumul(:,j)=exp(-45.*radi'.^0.3).*radi'.^5;
cumul(:,j)=cldadj(j)*cumul(:,j)*cldl/sum(cumul(:,j));
end
```

```
%**************************
% Start simulating scattering atmospheres

if exist('tbv')~=1,

% initialize variables
cldlqd=zeros(length(temp),length(cldalti));
rlH=zeros(length(temp),length(cldalti));
wvd=zeros(length(temp),length(cldalti));

% model surface emissivity of land
evl=0.05*randn + 0.92*ones(length(freq),length(angle));
ehl=evl;

% find the emissivity of water
  for q=1:length(freq),
        for x=1:length(angle),
[evw(q,x) ehw(q,x)]=fastem(freq(q),angle(x),Tsurf,2,0,0,0);
        end
  end

% combine land and water emissivity for marshland
pl=0.6;% percent land
pw=1-pl; % percent water
ev=pl*evl+pw*evw;
eh=pl*ehl+pw*ehw;

% make sure emissivity isn't greater than one
[ev,eh]=check_emis(ev,eh);
```

```
for k=1:length(cldalti),

  for i=1:length(RR),

% Use modified M-P.
clear den
den=zeros(length(radi),cldalti(k)-1);
for v=2:cldalti(k),
  if v<=cldalti(k)-2,
den(:,v-1)=denMP(:,i)+cumul(:,i);
  else
den(:,v-1)=cumul(:,i);
  end
end

      for j=1:length(icef),
% fluctuate the humidity and temperature profile to increase
% variability of clear air simulations
df=size(relH);
rlHca=relH+unifrnd(-0.1,0.1,df(1),df(2)).*relH;
tempca=temp+unifrnd(-0.005,0.005)*temp;
rlH(:,k)=rlHca;

cldscale=0.1;

% adjust liquid cloud depending on cld-top altitude
if temp(cldalti(k))>250,
cldb=cldalti(k);
          if cldalt(k)>=4,
```

```
clda=cldalti(k)−6;
          cldlqd(clda:cldb,k)=cldscale∗triang(7);
          rlH(clda:cldb,k)=100;
          elseif cldalt(k)==3,
clda=cldalti(k)−5;
          cldlqd(clda:cldb,k)=cldscale∗triang(6);
          rlH(clda:cldb,k)=100;
          else
clda=cldalti(k)−3;
          cldlqd(clda:cldb,k)=cldscale∗triang(4);
          rlH(clda:cldb,k)=100;
          end
else
  cldscaleH=0.2;
  cldb=17; % level where temp=260 K
clda=3;
cldlqd(clda:cldb,k)=cldscaleH∗triang(15);
rlH(clda:cldb,k)=100;
end
wvdca(:,k)=vapor(tempca,rlHca);
wvd(:,k)=vapor(temp,rlH(:,k));

plca(k,i,j)=unifrnd(0.4,0.7);% clear-air percent land
plc=plca(k,i,j);
pwc=1−plca(k,i,j);% clear-air percent water

% find the surface emissivity of land
evlc=0.05∗randn + 0.92∗ones(length(freq),length(angle));
ehlc=evlc;
evc=plc∗evlc+pwc∗evw;
```

```
ehc=plc*ehlc+pwc*ehw;

% make sure emissivity isn't greater than one
[evc,ehc]=check_emis(evc,ehc);


        if (icef(j)~=2),
[tbv(:,:,k,i,j),tbh(:,:,k,i,j),status(:,k,i,j)]=tbscat(tempca,pres,wvd(:,k),...
  cldlqd(:,k),1,cldalti(k),radi',den,icef(j),Tsurf,tbc',freq,secant,1-evc',1-ehc');
        else % for clear air
[tbv(:,:,k,i,j),tbh(:,:,k,i,j),status(:,k,i,j)]=tbscat(tempca,pres,wvdca(:,k),...
        zeros(length(temp),1),4,3,radi',zeros(length(radi),1),...
        icef(j)-1,Tsurf+2*randn,tbc',freq,secant,1-evc',1-ehc');
        end
      end % icef
    end % RR
  fprintf('Altitude  %d \r',simaltres(cldalti(k))),
end % cldalti

% tbv(angle,freq,cldalti,RR,icef)

end % end of check if tbv exists

for v=1:8, % over eight angles
  clear tbvf tbhf
% merge the horiz. and vert. polarizations
tbvf=squeeze(tbv(v,:,:,:,:));
tbhf=squeeze(tbh(v,:,:,:,:));
tbf=tbvf.*sin((pi/180)*angle(v)).^2+tbhf.*cos((pi/180)*angle(v)).^2;

% script that looks at the simulation output variable ‘status’ and
```

```
% throws away simulations with warnings. Next is combines upper
% and lower sideband frequencies into channels.
MieInac=0; % flag to remove simulations with Mie series inaccuracies
MieInstab=0; % flag to remove simulations with Mie series instabilities
RTSInstab=1; % flag to remove simulations with unreasonable Tb from
             % radiative transfer solution instabilities
Clean_sims

tbh54{v}=tbhn54;
tbh118{v}=tbhn118;
tbh183{v}=tbhn183;
tbh425{v}=tbhn425;

% Organize the good simulations with their perspective state vector
gj=size(tbh54{v});
tb118{v}=[];tb54{v}=[];tb183{v}=[];tb425{v}=[];S{v}=[];
for i=1:gj(1),
  for j=1:gj(2),
    for k=1:gj(3),
% skip simulation if the status reported an error.
if ~(sum(isnan(tbh54{v}(i,j,k,:)))+sum(isnan(tbh118{v}(i,j,k,:)))+ ...
     sum(isnan(tbh183{v}(i,j,k,:)))+sum(isnan(tbh425{v}(i,j,k,:)))),

tb54{v}=[tb54{v} [squeeze(tbh54{v}(i,j,k,:))]];
tb118{v}=[tb118{v} [squeeze(tbh118{v}(i,j,k,:))]];
tb183{v}=[tb183{v} [squeeze(tbh183{v}(i,j,k,:))]];
tb425{v}=[tb425{v} [squeeze(tbh425{v}(i,j,k,:))]];

      if (icef(k)~=2), % for the precipitating clouds
        if RR(j)~=0,
```

```
     S{v}=[S{v} [cldalt(i)-1;RR(j);icef(k);cldalt(i)]];
    else
     S{v}=[S{v} [0;RR(j);icef(k);cldalt(i)]];
    end


  else % for the clear air
S{v}=[S{v} [0;0;0;0]];
  end
end
   end % icef
  end % RR
end % cldalti


nwln=length(tb54{v});
for i=1:nwln,
tb{v}(:,i)=[tb54{v}(:,i);tb118{v}(:,i);tb183{v}(:,i);tb425{v}(:,i)];
end


end % end of v loop over angles
```

```
% m-script to simulate the anvil blowoff or dissipating convective
% cell clouds

addpath /leslie2/MATLAB/


[raob]=read_CF_raob('/leslie2/NAST-M/13Jul02/raob/MI20020713_2044_COR.RAOB');
altind=632;

% set simulation's altitude resolution
simaltres=[0:0.5:17.5];

temp_=raob.temp_K;
pres_=raob.press_mb;
relH_=raob.rh_perc;

% Interpolate profiles to simulation's resolution
temp=interp1(raob.alt_km(1:altind,1),temp_(1:altind,1),simaltres,'linear','extrap')';
pres=interp1(raob.alt_km(1:altind,1),pres_(1:altind),simaltres,'linear','extrap')';
relH=interp1(raob.alt_km(1:altind,1),relH_(1:altind),simaltres,'linear','extrap')';

% set LO frequencies
LO425=106.1*4;
LO183=183.31;
LO118=118.2;
LO54=46;
% set passband's center frequencies
freq54=[50.3 51.76 52.8 53.73 54.3 54.94 55.485 55.945];
freq118=[LO118-3.5 LO118+3.5 LO118-2.55 LO118+2.55 LO118-2.05 ...
        LO118+2.05 LO118-1.6 LO118+1.6 LO118-1.2 LO118+1.2 LO118-0.8 LO118+0.8];
```

```
freq183=[LO183−10 LO183+10 LO183−7 LO183+7 ...
    LO183−4.5 LO183+4.5 LO183−3 LO183+3 LO183−1.8 LO183+1.8 LO183−1 ...
    LO183+1];
freq425=[LO425−3.25 LO425+3.25 LO425−2.15 LO425+2.15 LO425−1.43 ...
      LO425+1.43 LO425−0.91 LO425+0.91 LO425−0.68 LO425+0.68 ...
      LO425−0.505 LO425+0.505 LO425−0.285 LO425+0.285];
freq=[freq54 freq118 freq183 freq425]';

% choose the angles
angle=[0 7.2 14.4 21.6 30 37.2 43 50 60];
secant=sec(angle*(pi/180))';

% set surface temperature
Tsurf=273.15+25;

% find the Tb above aircraft to initialize tbscat
simind=[altind:2:length(temp_)]; % for CF raob
[tb1,tb2,e1,e2]=tbarray(temp_(simind),pres_(simind),vapor(temp_(simind),...
            relH_(simind)),zeros(length(simind),1),...
            zeros(length(simind),1),secant,secant,freq);
Tcos=Tcosmic(freq)*ones(1,length(secant));
tbc=tb1(:,:)'+e1(:,:)'.*Tcos(:,:);

% prepare tbscat variables
% disf is a parameter in the rain-density distribution
disf=[400 300 200 150 100 50 10 2];

cldalti=[15:2:35]; % index to match cldalt 7 km to 16 km
cldalt=simaltres(cldalti);
```

```
lden=[0.05 0.1 0.3 0.5 1 1.5 3 5];

%**************************
% Start simulating scattering atmospheres

if exist('tbv')~=1,

% initialize variables
cldlqd=zeros(length(temp),length(cldalti));
rlH=zeros(length(temp),length(cldalti));

for k=1:length(cldalti),
  % add random fluctuation to surface temperature
Tsurfk(k)=Tsurf+1*randn;
% find the emissivity of water
  for q=1:length(freq),
        for x=1:length(angle),
[evw(q,x) ehw(q,x)]=fastem(freq(q),angle(x),Tsurfk(k),2,0,0,0);
        end
  end

% combine land and water emissivity for marshy land
pl=0.6;% percent land
pw=1-pl; % percent water

% find the surface emissivity of land
evl=0.05*randn + 0.92*ones(length(freq),length(angle));
ehl=evl;
% account for the marshland by mixing water and land
ev=pl*evl+pw*evw;
```

```
eh=pl*ehl+pw*ehw;

% make sure emissivity isn't greater than one
[ev,eh]=check_emis(ev,eh);

rlH(:,k)=relH;

% setting this variable will make the cloud go close to the surface
cldscale=0;
clda=2;
cldb=cldalti(k);
          cldlqd(cldb-3:cldb,k)=cldscale*[1 0.75 0.5 0.25]';
          cldlqd(clda:cldb-4,k)=cldscale;
          rlH(clda:cldb,k)=100;

wvd(:,k)=vapor(temp,rlH(:,k));

    for i=1:length(lden),
% make cloud square in density
lm=diff([clda cldb]);
tr=ones(lm,1);
      for j=1:length(disf),
% radi for the scattering in non-precipitating clouds
lradi=logspace(-4,0.5,30);
ldenfunc=zeros(1,30);
ldenfunc=exp(-disf(j)*lradi.^2).*lradi.^0.3;
if lden(i)==1,
  denf(j,:)=ldenfunc*lden(i)/sum(ldenfunc);
end
for r=1:lm,
```

```
  lightden(r,:)=ldenfunc*tr(r)*lden(i)/sum(ldenfunc);
end

      if (disf(j)~=2),
[tbv(:,:,k,i,j),tbh(:,:,k,i,j),status(:,k,i,j)]=tbscat(temp,pres,...
  wvd(:,k),cldlqd(:,k),clda,cldb,lradi',lightden',1,...
  Tsurfk(k),tbc',freq,secant,1-ev',1-eh');
      else  % for clear air
% fluctuate the rel. hum. profile to account for atmospheric variability
df=size(relH);
rlHca=relH+unifrnd(-0.1,0.1,df(1),df(2)).*relH;
tempca=temp+unifrnd(-0.005,0.005)*temp;

% change emissivity for clear air profile in order to include more variety
% -combined land and water emissivity for marshy land
pl=unifrnd(0.4,0.7);% percent land
pw=1-pl; % percent water

% find the surface emissivity of land
evl=0.05*randn + 0.92*ones(length(freq),length(angle));
ehl=evl;
ev=pl*evl+pw*evw;
eh=pl*ehl+pw*ehw;

% make sure emissivity isn't greater than one
[ev,eh]=check_emis(ev,eh);

[tbv(:,:,k,i,j),tbh(:,:,k,i,j),status(:,k,i,j)]=tbscat(tempca,...
  pres,vapor(tempca,rlHca),zeros(length(temp),1),4,3,...
  lradi',zeros(length(lradi),1),1,Tsurfk(k),tbc',freq,secant,1-ev',1-eh');
```

```
        end

      end % disf
    end % lden
  fprintf('Altitude  %d \r',simaltres(cldalti(k))),
end % cldalti

end % end of Tbv check

% tbv(angle,freq,cldalti,RR,icef)

for v=1:8, % for each angle estimator
  clear tbvf tbhf
% merge the horiz. and vert. polarizations
tbvf=squeeze(tbv(v,:,:,:,:));
tbhf=squeeze(tbh(v,:,:,:,:));
tbf=tbvf.*sin((pi/180)*angle(v)).^2+tbhf.*cos((pi/180)*angle(v)).^2;

% script that looks at the simulation output variable 'status' and
% throws away simulations with warnings.  Next is combines upper
% and lower sideband frequencies into channels.
MieInac=0; % flag to remove simulations with Mie series inaccuracies
MieInstab=0; % flag to remove simulations with Mie series instabilities
RTSInstab=1; % flag to remove simulations with unreasonable Tb from
             % radiative transfer solution instabilities
Clean_sims

tbh54{v}=tbhn54;
tbh118{v}=tbhn118;
tbh183{v}=tbhn183;
```

```
tbh425{v}=tbhn425;

% Organize the good simulations with their perspective state vector
gj=size(tbh54{v});
tb118{v}=[];tb54{v}=[];tb183{v}=[];tb425{v}=[];S{v}=[];
for i=1:gj(1),
  for j=1:gj(2),
    for k=1:gj(3),
% skip simulation if the status reported an error.
if ~(sum(isnan(tbh54{v}(i,j,k,:)))+sum(isnan(tbh118{v}(i,j,k,:)))+ ...
     sum(isnan(tbh183{v}(i,j,k,:)))+sum(isnan(tbh425{v}(i,j,k,:)))),

tb54{v}=[tb54{v} [squeeze(tbh54{v}(i,j,k,:))]];
tb118{v}=[tb118{v} [squeeze(tbh118{v}(i,j,k,:))]];
tb183{v}=[tb183{v} [squeeze(tbh183{v}(i,j,k,:))]];
tb425{v}=[tb425{v} [squeeze(tbh425{v}(i,j,k,:))]];

      if (disf(k)~=2), % for the precipitating clouds
S{v}=[S{v} [0;0;1;cldalt(i)]];
      else  % for the clear air
S{v}=[S{v} [0;0;0;0]];
      end
end
    end % icef
  end % RR
end % cldalti

nwln=length(tb54{v});
for i=1:nwln,
tb{v}(:,i)=[tb54{v}(:,i);tb118{v}(:,i);tb183{v}(:,i);tb425{v}(:,i)];
```

```
end

end % end of v loop over angles
```

Bibliography

[1] R. F. Adler, R. A. Mack, N. Prasad, H.-Y. M. Yeh, and I. M. Hakkarinen. Aircraft Microwave Observations and Simulations of Deep Convection from 18 to 183 GHz. Part I: Observations. *Journal of Atmospheric and Oceanic Technology*, 7:377–391, June 1990.

[2] E. N. Anagnostou and W. F. Krajewski. Simulation of radar reflectivity fields: Algorithm formulation and evaluation. *Water Resources Research*, 33(6):1419–1428, June 1997.

[3] Baxter H. Armstrong and Ralph W. Nicholls. *Emission, Aborption and Transfer of Radiation in Heated Atmospheres.* Pergamon Press, New York, 1972.

[4] D. Atlas and T. L. Bell. The Relation of Radar to Cloud Area-Time Integrals and Implications for Rain Measurements from Space. *Monthly Weather Review*, 120:1997–2008, Sept 1992.

[5] Peter Bauer and Alberto Mugnai. Precipitation profile retrievals using temperature-sounding microwave observations. *Journal of Geophysical Research*, 108(D23):4730, December 2003.

[6] Bizzaro Bizzarri, Albin Gasiewski, and David H. Staelin. Initiatives for Millimetre/Submillimetre-Wave Sounding from Geostationary Orbit. In *Geoscience and Remote Sensing Symposium*, volume 1, pages 548–552. IGARSSS '02, 2002.

[7] W. J. Blackwell, J. W. Barrett, F. W. Chen, R. V. Leslie, P. W. Rosenkranz, M. J. Schwartz, and D. H. Staelin. NPOESS Aircraft Sounder Testbed-Microwave (NAST-M): Instrument description and initial flight results. *IEEE Transactions on Geoscience and Remote Sensing*, 39(11):2444–2453, November 2001.

[8] William J. Blackwell. *Retrieval of Cloud-Cleared Atmospheric Temperature Profiles from Hyperspectral Infrared and Microwave Observations.* PhD thesis, Massachusetts Institute of Technology, Department of Electrical Engineering and Computer Science, 2002.

[9] William J. Blackwell and David H. Staelin. Comparative performance analyses of passive microwave systems for tropospheric sounding of temperature and water vapor profiles. *Proceedings of SPIE*, 2812:472–478, 1996.

[10] V. N. Bringi, R. E. Hood, F. J. LaFontaine, F. S. Marzano, A. Mugnai, E. A. Smith, R. W. Spencer, J. Turk, and J. Vivekanandan. Active and passive remote sensing of precipitation over ocean surfaces. In *Geoscience and Remote Sensing Symposium*, volume 3 of *Better Understanding of Earth Environment*, pages 1241–1243. IGARSS '93, August 1993.

[11] H. R. Byers. The use of Radar in determining the amount of rain falling over a small area. *Trans. of Amer. Geophys. Union*, 29:187–196, 1948.

[12] S. Chandrasekhar. *Radiative Transfer.* Dover Inc., New York, 1960.

[13] F. W. Chen and D. H. Staelin. AIRS/AMSU/HSB Precipitation Estimates. *IEEE Transactions on Geoscience and Remote Sensing*, 41(2):410–417, February 2003.

[14] Dorothee Coppens, Zaid Haddad, and Eastwood Im. Estimating the uncertainity in passive-microwave rain-retrievals. In *Geoscience and Remote Sensing Symposium*, volume 4, pages 2060–2062. IGARSSS '99, 1999.

[15] D. Cousins and W. L. Smith. NPOESS airborne sounder testbed - interferometer. *Proceedings of SPIE*, 3756:323–331, 1997.

[16] Godelieve Deblonde. Evaluation of fastem and fastem2. Report, Meteorological Service of Canada, Dorval, PQ Canada, November 2000. Data Assimilation and Satellite Meteorology Division.

[17] D. Deirmendjian. *Electromagnetic Scattering on Spherical Polydispersions.* American Elsevier Publishing Co., New York, 1969.

[18] A. A. Doneaud, A. Makarau, and L. R. Johnson. A Modified ATI Technique for Nowcasting Convective Rain Volumes over Areas. *Journal of Applied Meteorology*, 27:491–502, April 1988. Notes and Correspondence.

[19] A. A. Doneaud, J. R. Miller, and L. R. Johnson. The Area-Time-Integral Technique to Estimate Convective Rain Volumes over Areas Applied to Satellite Data - A Preliminary Investigation. *Journal of Climate and Applied Meteorology*, 26:156–169, jan 1987.

[20] A. A. Doneaud, P. L. Smith, A. S. Dennis, and S. Sengupta. A simple method for estimatin rain volume over an area. *Water Resources Research*, 17:1676–1682, 1981.

[21] Boyd F. Edwards, J. W. Wilder, and E. E. Scims. Dynamics of falling raindrops. *European Journal of Physics*, 22:113–118, 2001.

[22] S. J. English and T. J. Hewison. A fast generic millimetre-wave emissivity model. In *Proceedings of SPIE*, volume 3503, pages 288–300, 1998.

[23] J. Escobar. *Base de Données pour la Restitution de Paramètres Atmosphériques à L'échelle Globale-Etude sur L'inversion per Réseaux de Neurones des Données des Sondeurs Verticaux Atmosphériques Satellitaires Présents et à venir.* PhD thesis, Ecole Polytechnique, France, 1993.

[24] A. J. Gasiewski. *Atmospheric Temperature Sounding and Precipitation Cell Parameter estimation using passive 118-GHz* O_2 *Observations.* PhD thesis, Massachusetts Institute of Technology, Department of Electrical Engineering and Computer Science, 1988.

[25] A. J. Gasiewski, G. A. Showman, and G. M. Skofronick. Application of neural nets to rain rate retrieval from simulated multichannel passive microwave imagery. In *Geoscience and Remote Sensing Symposium*, volume 3 of *Remote Sensing for a Sustainable Future*, pages 1688–1691. IGARSSS '96, May 1996.

[26] A. J. Gasiewski and G. M. Skofronick. Passive microwave mapping simulation, karhunen-loeve and precipitation retrievals. In *Proceedings of IEEE Topical Symposium on*, Combined Optical, Microwave, Earth and Atmosphere Sensing, pages 14–17, 1993.

[27] Steven E. Hall and et al. World weather 2010 project. Website, University of Illinois Urbana - Champaign, http://ww2010.atmos.uiuc.edu, September 1991. Department of Atmospheric Science.

[28] L.G. Henyey and J. L. Greenstein. Diffuse radiation in the galaxy. *Journal of Astrophysics*, 93:70–83, 1941.

[29] Michael S. Hersman and Gene P. Poe. Sensitivity of the total power radiometer with periodic absolute calibration. *IEEE Transactions on Microwave Theory and Techniques*, MTT-29(1):32–40, January 1981.

[30] Jeffrey L. Hesler, Kai Hui, Song He, and Thomas W. Crowe. A fixed-tuned 400 GHz subharmonic mixer using planar schottky diodes. In *Tenth International Symposium on Space Terahertz Technology*, pages 95–99, March 1999.

[31] G. A. Hufford. A Model for the Complex Permittivity of Ice at Frequencies Below 1 THz. *International Journal of Infrared and Millimeter Waves*, 12(7):677–682, 1991.

[32] Michael A. Janssen. *Atmospheric Remote Sensing by Microwave Radiometry.* John Wiley and Sons, Inc., New York, 1993.

[33] J. D. Kraus. *Radio Astronomy.* McGraw-Hill, New York, 1966.

[34] Christian Kummerow, I. M. Hakkaarinen, H. F. Pierce, and J. A. Weinman. Determination of Precipitation Profiles from Airborne Passive Microwave Radiometric Measurements. *Journal of Atmospheric and Oceanic Technology*, 8(1):148–158, feb 1991.

[35] Charlene C. Kuo, David H. Staelin, and Philip W. Rosenkranz. Statistical Iterative Scheme for Estimating Atmospheric Relative Humidity Profiles. *IEEE Transactions on Geoscience and Remote Sensing*, 32(2), March 1994.

[36] R. Vincent Leslie. Temperature Profile Retrievals with the NAST-M Passive Microwave Spectrometer. Master's thesis, Massachusetts Institute of Technology, Department of Electrical Engineering and Computer Science, May 2000.

[37] H. J. Liebe. An updated model for millimeter wave propagation in moist air. *Radio Science*, 20(5):1069–1089, October 1985.

[38] H. J. Liebe. A contribution to modeling atmospheric millimeter-wave properties. *Frequenz*, 41:31–36, 1987.

[39] H. J. Liebe. MPM - an atmospheric millimeter-wave propagation model. *International Journal of Infrared and Millimeter Waves*, 10(6):631–650, June 1989.

[40] H. J. Liebe, G. A. Hufford, and M. G. Cotton. Propagation Modeling of Moist Air and Suspended Water/Ice Particles at Frequencies Below 1000 GHz. In *AGARD Conference Proceedings*, pages 3–1–3–10, May 1993.

[41] H. J. Liebe, G. A. Hufford, and T. Manabe. A Model for the Complex Permittivity of Water at Frequencies Below 1 THz. *International Journal of Infrared and Millimeter Waves*, 12(7):659–675, 1991.

[42] H. J. Liebe, P. W. Rosenkranz, and G. A. Hufford. Atmospheric 60-GHz oxygen spectrum: New laboratory measurements and line parameters. *Journal of Quantitative Spectroscopy and Radiative Transfer*, 48, November 1992.

[43] J. S. Marshall and W. McK. Palmer. The distribution of raindrops with size. *Journal of Meteorology*, 5:165–166, 1948.

[44] F. S. Marzano, M. Palmacci, D. Cimini, G. Giuliani, and F. J. Turk. Multivariate Statistical Integration of Satellite Infrared and Microwave Radiometric Measurements for Rainfall Retrieval at the Geostationary Scale. *IEEE Transactions on Geoscience and Remote Sensing*, pages 1–14, 2004. accepted for publication.

[45] M. J. McGill, D. L. Hlavka, W. D. Hart, J. D. Spinhirne, V. S. Scott, and B. Schmid. The Cloud Physics Lidar: Instrument description and initial measurement results. *Applied Optics*, 41:3725–3734, June 2002.

[46] G. Mie. Beitrage zur Optik trüber Medien, speziell Kolloidaler Metaläsungen. *Ann. Physik*, 25:377, 1908.

[47] C. L. Parkinson. Aqua: An Earth-Observing Satellite Mission to Examine Water and Other Climate Variables. *IEEE Transactions on Geoscience and Remote Sensing*, 41(2):173–183, February 2003.

[48] G. E. Peckham. An optimum calibration procedure for radiometers. *International Journal of Remote Sensing*, 10(1):227–236, 1989.

[49] Grant W. Petty. The status of satellite-based rainfall estimation over land. *Remote Sensing of the Environment*, 51(1):125–137, January 1995.

[50] Philip W. Rosenkranz. Radiative Transfer Solution using Initial Values in a Scattering and Absorbing Atmosphere with Reflective Surface. *IEEE Transactions on Geoscience and Remote Sensing*, 40(8):1889–1892, August 2002.

[51] Philip W. Rosenkranz. Personal communication. MIT Research Laboratory of Electronics, Cambridge, MA, 2004.

[52] Michael J. Schwartz. *Observation and Modeling of Atmospheric Oxygen Millimeter-wave Transmittance.* PhD thesis, Massachusetts Institute of Technology, Department of Electrical Engineering and Computer Science, 1998.

[53] G. M. Skofronick and A. J. Gasiewski. Passive Microwave Precipitation Mapping and Retrieval Simulation. In *Geoscience and Remote Sensing Symposium*, volume 2, pages 1716–1718. IGARSS '92, 1992.

[54] G. M. Skofronick-Jackson, A. J. Gasiewski, and J. R. Wang. Influence of Microphysical Cloud Parameterizations on Microwave Brightness Temperatures. *IEEE Transactions on Geoscience and Remote Sensing*, 40(1):187–196, January 2002.

[55] Gail Skofronick-Jackson and Albin Gasiewski. Nonlinear statistical retrievals of ice content and rain rate from passive microwave observations of a simulated convective storm. *IEEE Transactions on Geoscience and Remote Sensing*, 33(4):957–970, July 1995.

[56] E. A. Smith, P. Bauer, F. S. Marzano, C. D. Kummerow, D. McKaque, A. Mugnai, and G. Panegrossi. Intercomparison of microwave radiative transfer models for precipitating clouds. *IEEE Transactions on Geoscience and Remote Sensing*, 40(3):541–549, March 2002.

[57] M. S. Spina, M. J. Schwartz, D. H. Staelin, and A. J. Gasiewski. Application of multilayer feedforward neural networks to precipitation cell-top altitude estimation. *IEEE Transactions on Geoscience and Remote Sensing*, 36(1):154–162, January 1998.

[58] David H. Staelin. Passive remote sensing at microwave wavelengths. *Proceedings of the IEEE*, 57(4):427–439, April 1969.

[59] David H. Staelin. *Course Notes: 6.661 Receivers, Antennas, and Signals.* MIT Department of Electrical Engineering and Computer Science, 1999.

[60] David H. Staelin. Concept for the passive microwave storm-based precipitation retrievals. Memorandum, Massachusetts Institute of Technology, Cambridge, MA, December 2002. Research Laboratory of Electronics: Remote Sensing and Estimation Group.

[61] Graeme L. Stephens. *Remote Sensing of the Lower Atmosphere: An Introduction.* Oxford University Press, New York, 1994.

[62] Gilbert Strang. *Introduction to Applied Mathematics.* Wellesley-Cambridge Press, Wellesley, 1986.

[63] W. K. Tao and J. Simpson. Modeling Study of a Tropical Squall-Type Convective Line. *Journal of Atmospheric Science*, 46(2), January 1989.

[64] D. S. Torres, J. M. Porra, and J. D. Creutin. A General Formulation for Raindrop Size Distribution. *Journal of Applied Meteorology*, 33:1494–1502, 1994.

[65] Leung Tsang, Jin Au Kong, and Robert T. Shin. *Theory of Microwave Remote Sensing.* John Wiley and Sons, New York, 1985.

[66] D. Tsintikidis, J. L. Haferman, E. N. Anagnostou, W. F. Krajewski, and T. F. Smith. A Neural Network Approach to Estimating Rainfall from Spaceborne Microwave Data. *IEEE Transactions on Geoscience and Remote Sensing*, 35(5):1079–1093, September 1997.

[67] Fawwaz T. Ulaby, Richard K. Moore, and Adrian K. Fung. *Microwave Remote Sensing Active and Passive: Volume I Microwave Remote Sensing Fundamentals and Radiometry.* Artech House Inc., Norwood, MA, 1981.

[68] Sanford Weisberg. *Applied Linear Regression.* John Wiley and Sons, New York, 1985.

[69] T. Wilheit, C. D. Kummerow, and R. Ferraro. Rainfall Algorithms for AMSR-E. *IEEE Transactions on Geoscience and Remote Sensing*, 41(2):204–214, February 2003.

[70] W. J. Wiscombe. Improved Mie scattering algorithms. *Applied Optics*, 19(9):1505–1509, May 1980.

[71] H.-Y. M. Yeh, N. Prasad, R. A. Mack, and R. F. Adler. Aircraft Microwave Observations and Simulations of Deep Convection from 18 to 183 GHz. Part

II: Model Results. *Journal of Atmospheric and Oceanic Technology*, 7:392–410, June 1990.